Université de Liège - Faculty of Applied Sciences

Development and analysis of low-order models of frame structures under blast loads

Thesis submitted in partial fulfillment of the requirements for the degree of Doctor of Philosophy in Applied Sciences by

HAMRA Lotfi, Ir.

September 2016

Members of the Doctoral Jury

Prof. Jean-Pierre JASPART (President of the Jury)
Université de Liège

Dr. Jean-François DEMONCEAU (Co-supervisor)
Université de Liège
Email: jfdemonceau@ulg.ac.be

Prof. Vincent DENOËL (Co-supervisor)
Université de Liège
Email: v.denoel@ulg.ac.be

Prof. John VANTOMME
Ecole Royale Militaire de Bruxelles, Vrije Universiteit Brussel

Prof. Dan DUBINA
Universitatea Politehnica Timişoara
Romania

Prof. Benno HOFFMEISTER
Rheinisch-Westfälische Technische Hochschule Aachen
Germany

Abstract

The main aim of this thesis is to propose an easy-to-apply tool to assess the level of damage of a structure in which one compartment is subjected to blast loading. This compartment is extracted from the structure accounting for the interaction with the part of the structure surrounding the loaded compartment, which is assumed to be elastic. Before studying the whole frame structure, the structural elements (i.e. the beam and its adjacent columns) are firstly studied separately taking into account the lateral restraint and mass offered by the indirectly affected part (IAP) of the structure. Secondly, the dynamic behaviour of a simple compartment made of pinned members and laterally braced is investigated. The material laws are assumed to be elastic-perfectly plastic, neglecting the effect of strain rate on the yield strength. The out-of-plane instabilities of the structural members are disregarded.

Two analytical models are developed to predict the dynamic response of the frame beam subjected to blast loading, including the elastic lateral restraint and inertia offered by the IAP of the structure, the development of nonlinear membrane action ($P - \delta$ effect) and also, the interaction between bending moment and axial force in the plastic hinges. The first model is based on a single degree of freedom (SDOF model) which is the transverse mid-span deflection of the beam while the second model is a two-degree-of-freedom (2-DOF) model which also includes the axial elongation of the beam. The accuracy of these two low-order models is assessed with finite element simulations. This validation stage shows that the proposed low-order models capture the physics of the problem in most cases of practical interest.

Concerning the columns, an analytical model is proposed to assess its dynamic response under constant axial compressive load and lateral blast loading. It accounts for large displacement ($P - \delta$ effect), bending moment-axial force (M-N) plastic interaction as well as its interaction with the indirectly affected part (IAP) of the structure. This model is non-smooth piecewise linear and involves two degrees of freedoms (2 DOFs) in each regime of the motion of the column (related to the possibilities of development of plastic hinges).

Subsequent to a parametric study, it is demonstrated that a good correlation is found between the results provided by the analytical model and a richer FEM model, despite some little discrepancies observed for some intermediate values of stiffness of the lateral restraint and lateral mass. As a possible improvement, adjustments to the analytical model are suggested.

Finally, the dynamic behaviour of a simple frame under constant compressive loads and lateral blast loading is studied with a last 2-DOF analytical model. A multi-layer model of the cross-section of the beam is used to derive the bending moment-axial force (M-N) plastic interaction instead of the Lescouarc'h formula and normality rule. The coupling between the beam and the adjacent columns is ensured through appropriate boundary conditions.

For the studied frame, two blast scenarios are contemplated, the first one corresponds to a quasi-static blast loading while the second one refers to a dynamic blast loading. The first

case study shows that a very good agreement is achieved between the deflections predicted by the analytical and numerical models although a discrepancy is observed in the assessment of the axial force in the column due to the shape of the inertial force distribution of the beam assumed in the model. The second case study illustrates that, in both analytical and numerical models, the columns are predicted to fail by buckling due to the $P - \delta$ effect although the axial force in the column is again inaccurately captured by the analytical model for the same reason.

Résumé

L'objectif principal de cette thèse est de proposer un outil facile à utiliser qui permet d'évaluer rapidement le niveau d'endommagement d'une structure dans laquelle un compartiment est soumis à une explosion. Ce compartiment est extrait de la structure en tenant compte de son interaction avec la partie de la structure entourant le compartiment sollicité, supposée élastique, en ayant recours à des techniques de condensation. Avant d'effectuer une analyse de l'entièreté du compartiment, les éléments structuraux (à savoir la poutre et les colonnes adjacentes) sont d'abord étudiés séparément en considérant la présence à leur extrémité d'une restreinte et d'une masse latérale associées à la partie indirectée affectée (IAP) de la structure. Dans un second temps, le comportement dynamique d'un portique simple, parfaitement contreventé et constitué d'éléments bi-articulés, est étudié. La loi de matériau est supposée élastique parfaitement plastique, l'effet de la vitesse de déformation sur la limite d'élasticité est négligé. De plus, les instabilités hors-plan des éléments de structure sont ignorées.

Deux modèles analytiques permettant de prédire la réponse dynamique de la poutre du portique soumis à chargement d'explosion sont développés, en tenant compte de la restreinte latérale élastique et de l'inertie offerte par la IAP de la structure, du développement de l'action membrane non-linéaire (effet $P - \delta$) et aussi, de l'interaction entre l'effort axial et le moment de flexion dans les rotules plastiques. Le premier modèle est basé sur un seul degré de liberté (ddl) qui est le déplacement transversal à mi-portée tandis que le second modèle (modèle à 2 ddls) inclut aussi l'allongement axial de la poutre. La précision entre ces deux modèles simplifiés est évaluée à l'aide de simulations numériques par éléments finis. Cette étape de validation montre que les modèles capturent bien la physique du problème dans la majorité des cas pratiques.

Concernant les colonnes, un modèle analytique est proposé pour évaluer leur réponse dynamique sous charge de compression axiale constante et un chargement latéral d'explosion. Il prend en compte l'effet $P - \delta$ (à grands déplacements), l'interaction plastique moment de flexion-effort axial (M-N) ainsi que l'interaction de la colonne avec la IAP de la structure. Ce modèle est linéaire par morceaux et comporte deux ddls à chaque régime du mouvement de la colonne (étape correspondant à l'apparition éventuelle de rotule(s) plastique(s)).

Suite à l'étude paramétrique, il est démontré qu'une bonne correspondance est observée entre les résultats analytiques et numériques par éléments finis en dépit de certaines petites différences observées pour des valeurs intermédiaires de rigidité de la restreinte latérale et masse latérale. Afin d'améliorer le modèle analytique, des ajustements y sont suggérés.

Pour finir, le comportement dynamique d'un portique simple sous des charges de gravité et soumis à un chargement d'explosion interne est étudié à l'aide d'un modèle analytique à 2 ddls. La section transversale de la poutre est modélisée à l'aide de ressorts afin de capturer la

courbe d'interaction M-N. Le couplage entre la poutre et les colonnes adjacentes est assurée via des lois de couplage appropriées.

Pour le portiqué étudié, deux scénarios d'explosion sont considérés dans l'étude; le premier correspond à un chargement d'explosion quasi-statique tandis que le second est plutôt dynamique. Le premier cas d'étude illustre qu'un très bon accord est obtenu entre les résultats analytiques et numériques bien qu'une anomalie est observée dans l'évaluation de la force axiale de la colonne. En effet, celle-ci dépend de la forme de la distribution des forces inertielles supposée être bi-linéaire et indépendante du temps dans le modèle analytique alors que ce n'est pas le cas d'après les prédictions du modèle numérique (par éléments finis). Le deuxième cas d'étude montre que, dans les deux modèles, les colonnes flambent à cause de l'effet $P - \delta$. La force axiale dans la colonne est à nouveau mal capturée par le modèle analytique pour la même raison.

Acknowledgements

Tout d'abord, je tiens à remercier mon promoteur et chef de travaux Jean-François Demonceau ainsi que le professeur Jean-Pierre Jaspart de m'avoir donné l'opportunité de m'investir dans un projet de recherche intéressant et novateur. Sans doute, la plus grande difficulté à laquelle j'ai été confronté pendant ma thèse (humour) a été de répondre sérieusement à la question suivante: "Pourquoi étudies-tu les explosions ?" qui était souvent accompagnée d'un large sourire... Force est de constater qu'encore aujourd'hui, malheureusement, les actes terroristes et les discours populistes continuent à alimenter notre actualité, et qu'à travers cette thèse, cela me permet de mener une lutte, certes très minime et modestement à mon échelle, contre ces fléaux.

Je tiens à remercier une nouvelle fois mon promoteur Jean-François Demonceau ainsi que mon co-promoteur Vincent Denoël pour leur patience et leurs conseils lors de ces fameuses réunions interminables. Je remercie également le professeur John Vantomme de m'avoir invité à plusieurs reprises à l'Ecole Royale Militaire à Bruxelles.

Dear members of the committee, thank you for accepting the reading and examination of the thesis. I hope your lecture will be enjoyable.

Chers collègues Clara et Hav, ce fut un plaisir de partager mon bureau à vos côtés, de pouvoir échanger nos moments difficiles mais aussi de joie ! Je vous souhaite le meilleur pour la suite de votre carrière ! C'est officiel Hav, je te lègue ma chaise de bureau confortable (héritée auparavant de Clara :D) !

Ma très chère Myriem, je te remercie de m'avoir soutenu et remonté le moral avec ta joie et ta bonne humeur. Et je remercie tous mes amis, et plus particulièrement Jérôme, d'avoir empêché les grévistes d'asperger mon bureau avec un extincteur :D. Et pour conclure, merci à ma famille et surtout à mes parents pour leur soutien inconditionnel et leur amour, sans vous je n'y serais jamais arrivé.

Contents

Nomenclature

Acronyms

2D	Two-Dimensional
3D	Three-Dimensional
AISC	American Institute of Steel Construction
ALP	Alternate Load Path
ASCE	American Society of Civil Engineers
BC	Boundary condition
DC	Dynamic Condensation
DIF	Dynamic Increase Factor
DLF	Dynamic Load Factor
DOF	Degree-Of-Freedom
GC	Guyan Condensation
IRS	Improved Reduced System
FEM	Finite Element Method
IAP	Indirectly Affected Part (of the structure)
MMF	Moment Magnification Factor
RC	Reinforced Concrete
SC	Sign Change
SDOF	Single-Degree-Of-Freedom
SEREP	System Equivalent Reduction Expansion Process
UFC	Unified Facilities Criteria

Latin lower case

a_0	Speed of sound at ambient conditions, $[LT^{-1}]$
b_f	Width of the flanges of the structural element, $[L]$

h	Depth of the cross-section of the structural element, $[L]$
h_w	Web depth, $[L]$
f_{dy}	Dynamic yield strength, $[ML^{-1}T^{-2}]$
$\mathbf{f}_{int}$	Internal forces of the whole structure, $[ML^{-1}T^{-2}]$
f_y	Static yield strength, $[ML^{-1}T^{-2}]$
$k_{c,1}$	Elastic stiffness of the beam-column, $[MT^{-2}]$
$k_{c,2}$	Elastic-plastic stiffness of the beam-column (after formation of a plastic hinge), $[MT^{-2}]$
k_r	Elastic stiffness of the real structure, $[MT^{-2}]$
k_s	Elastic stiffness of the SDOF model, $[MT^{-2}]$
k_{EA}	Elastic axial stiffness of the beam, $[MT^{-2}]$
ℓ	Half of the length of the beam, $[L]$
ℓ_h	Length of a plastic hinge, $[L]$
m	Dimensionless bending moment, $[-]$
m_c	Lineic mass of the beam-column, $[ML^{-1}]$
m_s	Lineic mass of the floor, $[ML^{-1}]$
n	Dimensionless axial force, $[-]$
p	Pressure generated by the blast loading, $[ML^{-1}T^{-2}]$
p_0	Peak overpressure of the blast loading, $[ML^{-1}T^{-2}]$
$p_{0,r}$	Peak reflected overpressure, $[ML^{-1}T^{-2}]$
$p_{0,s}$	Peak side-on overpressure, $[ML^{-1}T^{-2}]$
p_∞	Quasi-static asymptotic solution, $[ML^{-1}T^{-2}]$
p_{atm}	Ambient pressure, $[ML^{-1}T^{-2}]$
p_b	Static pressure that causes the beam plastic mechanism, $[ML^{-1}T^{-2}]$
p_c	Characteristic pressure of the column, $[ML^{-1}T^{-2}]$
p_{QS}	Peak quasi-static pressure due to gas expansion, $[ML^{-1}T^{-2}]$
$p_r(t)$	Reflected overpressure, $[ML^{-1}T^{-2}]$
$p_s(t)$	Side-on overpressure, $[ML^{-1}T^{-2}]$
$\mathbf{p}_{\Gamma_i}$	Vector of blast loading applied to beam-column in regime Γ_i, $[ML^{-1}T^{-2}]$
$\overline{p}$	Dimensionless peak overpressure of the blast loading, $[-]$
$\overline{p}_{act}$	Actual quasi-static asymptote, $[-]$
$\overline{p}_{app}$	Approximated quasi-static asymptote, $[-]$
$\tilde{\mathbf{p}}_{\Gamma_i}$	Vector of dimensionless blast loading applied to beam-column during regime Γ_i, $[-]$
$\tilde{p}$	Dimensionless peak overpressure of blast loading, $[-]$
$\mathbf{q}$	Vector of generalized displacements q_i, $[L]$
q_i	Generalized displacement, $[L]$
$\dot{q}_i$	Generalized velocity, $[LT^{-1}]$
$\mathbf{q}_{\Gamma_i}$	Vector of generalized displacement of regime Γ_i, $[L]$
$\tilde{\mathbf{q}}_{\Gamma_i}$	Vector of dimensionless generalized displacement in regime Γ_i, $[-]$
r	Radius of gyration of the beam, $[L]$
$\mathbf{r}_{\Gamma_i}$	Plastic resistance of the beam-column in regime Γ_i, $[MLT^{-2}]$
$\tilde{\mathbf{r}}_{\Gamma_i}$	Dimensionless plastic resistance of the beam-column in regime Γ_i, $[-]$
s	Constant coefficient depending on α, $[-]$

t	Time, $[T]$
t_a	Arrival time of blast wave front, $[T]$
t_d	Positive phase duration of the blast loading, $[T]$
$t_{d,r}$	Positive phase duration of the reflected blast wave, $[T]$
$t_{d,s}$	Positive phase duration of the side-on blast wave, $[T]$
t_f	Flange thickness, $[L]$
t_k	Time at which a regime transition occurs, $[T]$
t_r	Rise time of blast pressure, $[T]$
t_w	Web thickness, $[L]$
$\mathbf{v}$	Vector incorporating the values of v_i, $[LT^{-1}]$
v_i	Initial generalized velocities, $[LT^{-1}]$
w_b	Transverse displacement along the beam, $[L]$
w_c	Transverse displacement along the column, $[L]$
$\dot{w}_c$	Transverse velocity along the column, $[LT^{-1}]$
x	Abscissa, $[L]$
$\overline{x}$	Dimensionless abscissa, $[-]$
z	Ordinate, $[L]$
z_m	Ordinate of the plastic hinge in the central region of the beam-column, $[L]$
$\overline{z}$	Dimensionless ordinate, $[-]$
$\overline{z}_m$	Dimensionless ordinate of the plastic hinge in the central region of the column, $[-]$

Latin upper case

A	Area of the cross-section, $[L^2]$
A_i	Area of a layer of the beam cross-section, $[L^2]$
A_s	Total inside surface area of the structure, $[L^2]$
A_w	Area of the web, $[L^2]$
C_D	Drag coefficient, $[-]$
C_m	Coefficient dependent upon beam-column curvature caused by applied moment, $[-]$
D	Energy dissipation, $[ML^2T^{-2}]$
DLF	Dynamic load factor, $[-]$
DLF_0	Dynamic load factor in the absence of axial load ($P = 0$), $[-]$
E	Constant Young's modulus, $[ML^{-1}T^{-2}]$
E_r	Strain energy stored in the beam-column reduced by the presence of the axial load, $[ML^2T^{-2}]$
$\overline{F}_{int,b}$	Dimensionless equivalent internal force in the beam, $[-]$
F_0	Peak force of blast loading, $[MLT^{-2}]$
F_{ext}	External force due to blast loading, $[MLT^{-2}]$
F_{inert}	Equivalent inertial force of the lateral mass, $[MLT^{-2}]$
F_{int}	Total equivalent internal force in the structure, $[MLT^{-2}]$
$F_{int,b}$	Equivalent internal force in the beam, $[MLT^{-2}]$
$F_{int,K}$	Equivalent internal force in the lateral restraint, $[MLT^{-2}]$

$\mathbf{G}_v$	Matrix for initial condition on beam-column velocities, $[-]$
H	Height of the column, $[L]$
I	Momentum of the blast loading, $[ML^{-1}T^{-1}]$
I_b	Inertia of the beam, $[L^4]$
I_c	Inertia of the column, $[L^4]$
$I_{rot,b}$	Rotatory inertia of the beam, $[ML]$
I_r	Reflected impulse, $[ML^{-1}T^{-1}]$
I_s	Incident impulse, $[ML^{-1}T^{-1}]$
I_∞	Impulsive asymptotic solution, $[ML^{-1}T^{-1}]$
$\overline{I}$	Dimensionless momentum of the blast loading, $[-]$
$\overline{I}_{act}$	Actual impulsive asymptote, $[-]$
$\overline{I}_{app}$	Approximated impulsive asymptote, $[-]$
K	Kinetic energy of the system, $[ML^2T^{-2}]$
$\mathbf{K}$	Linear elastic stiffness matrix of the whole structure, $[MT^{-2}]$
K_{cr}	Buckling length coefficient of beam-column, $[-]$
$\mathbf{K}_{P,\Gamma_i}$	Geometric matrix of the beam-column in regime Γ_i, $[MT^{-2}]$
K_L	Load factor, $[-]$
K_{LM}	Load-mass factor, $[-]$
K_M	Mass factor, $[-]$
$K_{M^\star}$	Kinetic energy of the lateral mass, $[ML^2T^{-2}]$
K_S	Stiffness factor, $[-]$
K_r	Rotational kinetic energy, $[ML^2T^{-2}]$
$\mathbf{K}_\delta$	Transformed stiffness matrix of the whole structure, $[MT^{-2}]$
$\mathbf{K}_{\Gamma_i}$	Linear stiffness matrix of the beam-column in regime Γ_i, $[MT^{-2}]$
$K^\star$	Stiffness of the lateral restraint, $[MT^{-2}]$
$K_G^\star$	Stiffness of the lateral restraint (obtained from Guyan condensation), $[MT^{-2}]$
$\overline{K}_0$	Initial dimensionless kinetic energy of the beam, $[-]$
$\tilde{\mathbf{K}}_{\Gamma_i}$	Dimensionless linear stiffness matrix of the beam-column in regime Γ_i, $[-]$
L	Length of the beam, $[L]$
M	Bending moment, $[ML^2T^{-2}]$
$\mathbf{M}$	Mass matrix of the whole structure, $[M]$
M_c	Generalized mass of the beam-column, $[M]$
M_i	Bending moment associated to the shape function ϕ_i, $[ML^2T^{-2}]$
M_{pl}	Pure plastic bending resistance of the structural element, $[ML^2T^{-2}]$
$M_{pl,d}$	Dynamic plastic bending resistance, $[ML^2T^{-2}]$
$M_{pl,red}$	Plastic bending resistance reduced by the presence of axial force, $[ML^2T^{-2}]$
M_s	Generalized mass of SDOF model, $[M]$
MMF	Moment magnification factor, $[-]$
MMF_{corr}	Corrected moment magnification factor, $[-]$
$\mathbf{M}_\delta$	Transformed mass matrix of the whole structure, $[M]$
$\mathbf{M}_{\Gamma_i}$	Mass matrix of the beam-column in regime Γ_i, $[M]$
$M^\star$	Lateral mass, $[M]$
$M_G^\star$	Lateral mass (obtained from Guyan condensation), $[M]$

$\tilde{\mathbf{M}}_{\Gamma_i}$	Dimensionless mass matrix of the beam-column in regime Γ_i, $[-]$
N	Axial force, $[MLT^{-2}]$
N_{pl}	Plastic axial resistance of structural element, $[MLT^{-2}]$
$N_{b,Rd}$	Design axial buckling resistance of structural element (Eurocode),$[MLT^{-2}]$
P	Constant axial compressive load due to dead and live loads from upper stories, $[MLT^{-2}]$
$\mathbf{P}$	Dynamic external loading applied to the whole structure, $[MLT^{-2}]$
P_{cr}	Euler elastic buckling load of structural element, $[MLT^{-2}]$
P_p	Cross-sectional axial compression capacity (UFC design guide), $[MLT^{-2}]$
P_u	Ultimate compression capacity of beam-column according to UFC design guide, $[MLT^{-2}]$
Q_c	Characteristic displacement of the beam-column, $[L]$
R	Range from the charge centre, $[L]$
R_m	Plastic resistance of SDOF model, $[MLT^{-2}]$
R_r	Resistance function of SDOF model reduced by application of an axial load, $[MLT^{-2}]$
R_u	Plastic resistance corresponding to the development of beam-column plastic mechanism, $[MLT^{-2}]$
R_y	Plastic resistance corresponding to the development of the first plastic hinge, $[MLT^{-2}]$
S	Correction coefficient, $[-]$
T	Period of vibration of beam-column ($P \neq 0$) or SDOF model, $[T]$
$\mathbf{T}$	Transformation matrix, $[-]$
T_0	Period of vibration of beam-column in the absence of axial load ($P = 0$), $[T]$
T_b	Characteristic period of the beam, $[T]$
T_c	Characteristic period of the column, $[T]$
$\mathbf{T}^\star$	Transformation matrix corresponding to a reduction model, $[-]$
$\mathbf{T}^\star_D$	Transformation matrix corresponding to the dynamic condensation, $[-]$
$\mathbf{T}^\star_G$	Transformation matrix corresponding to the Guyan condensation, $[-]$
$\mathbf{T}^\star_{IRS}$	Transformation matrix corresponding to the IRS reduction model, $[-]$
$\mathbf{T}^\star_{SEREP}$	Transformation matrix corresponding to SEREP, $[-]$
U	Total strain energy stored in SDOF model, $[ML^2T^{-2}]$
U_1	Elastic strain energy stored in the structural element, $[ML^2T^{-2}]$
U_2	Energy dissipated in the plastic hinges of the structural element, $[ML^2T^{-2}]$
U_3	Elastic strain energy stored in the lateral restraint, $[ML^2T^{-2}]$
U_4	Energy dissipated axially in plastic hinges, $[ML^2T^{-2}]$
$U_{int,b}$	Total strain energy in the beam, $[ML^2T^{-2}]$
$\overline{U}_I$	Dimensionless total strain energy stored in the structure subjected to impulsive blast loading, $[-]$
$\overline{U}_p$	Dimensionless total strain energy stored in the substructure subjected to quasi-static blast loading, $[-]$
V	Shear force, $[MLT^{-2}]$
V_i	Shear force distribution associated to the shape function ϕ_i, $[MLT^{-2}]$

V_{pl}	Plastic shear resistance of the structural element, $[MLT^{-2}]$
V_s	Volume of the blast-loaded compartment of the structure, $[L^3]$
W	Mass of the spherical charge of TNT, $[M]$
W_p	Work done by the blast loading, $[ML^2T^{-2}]$
W_P	Work done by the axial load P, $[ML^2T^{-2}]$
W_{pl}	Plastic flexural modulus of the structural element, $[L^3]$
$\overline{W}_p$	Dimensionless work done by the blast loading, $[-]$
X	Vertical displacement at mid-span of the beam or displacement of SDOF model, $[L]$
$\mathbf{X}$	Nodal displacements of the whole structure, $[L]$
X_e	Vertical displacement at mid-span of the beam at first yielding, $[L]$
X_{el}	Deflection of the beam when the plastic mechanism is formed, $[L]$
X_m	Maximum deflection of the structure, $[L]$
X_{st}	Deflection of the structure under a static force F_0, $[L]$
X_y	Deflection of the beam when the plastic mechanism is formed , $[L]$
$\dot{X}$	Vertical velocity at mid-span of the beam, $[LT^{-1}]$
$\dot{X}_0$	Initial vertical velocity at mid-span of the beam, $[LT^{-1}]$
$\ddot{X}$	Vertical acceleration at mid-span of the beam, $[LT^{-2}]$
$\ddot{\mathbf{X}}$	Nodal accelerations of the whole structure, $[LT^{-2}]$
$\overline{X}$	Dimensionless vertical displacement at mid-span of the beam, $[-]$
$\overline{X}'$	Dimensionless vertical velocity at mid-span of the beam, $[-]$
$\overline{X}''$	Dimensionless vertical acceleration at mid-span of the beam, $[-]$
Y	Deflection of the beam-column, $[L]$
Y_b	Maximum deflection of the beam-column before buckling occurs, $[L]$
$Y_{b,p}$	Maximum deflection of the beam-column before buckling occurs in quasi-static regime, $[L]$
$Y_{b,i}$	Maximum deflection of the beam-column before buckling occurs in impulsive regime, $[L]$
Y_{el}	Deflection of the beam-column corresponding to the development of the plastic mechanism, $[L]$
Y_m	Maximum deflection of the beam-column, $[L]$
$\dot{Y}_0$	Initial velocity of the beam-column, $[LT^{-1}]$
Z	Scaled distance (from the charge centre), $\left[L/M^{1/3}\right]$

Greek lower case

α, β, γ	Coefficients of general M-N plastic resistance interaction, $[-]$
α_e	Ratio of vent area to wall area, $[-]$
α_{cr}	Inverse of the critical multiplier, $[-]$
α_u	Inverse of the ultimate multiplier, $[-]$
$\gamma_0, \gamma_1, \gamma_2, \gamma_3$	Coefficients of the M-N plastic interaction curve of I-shaped cross-section, $[-]$
δ	Elongation of the lateral spring, $[L]$

δ_c	Vertical displacement at the top of the column, $[L]$
$\dot{\delta}$	Velocity of the lateral mass, $[LT^{-1}]$
$\ddot{\delta}$	Acceleration of the lateral mass, $[LT^{-2}]$
$\dot{\epsilon}$	Strain rate, $[T^{-1}]$
θ	Rotation at the ends of the beam, $[-]$
θ_{bot}	Rotation at the bottom of the column, $[-]$
θ_{mid}	Rotation at $z = z_m$ from the bottom of the column, $[-]$
θ_y	Yield rotation at the ends of the beam, $[-]$
$\dot{\theta}_{bot,\Gamma_i}$	Angular velocity at the bottom of the column in regime Γ_i, $[T^{-1}]$
$\dot{\theta}_{mid,\Gamma_i}$	Angular velocity at $z = z_m$ from the bottom of the column in regime Γ_i, $[T^{-1}]$
κ	Curvature, $[L^{-1}]$
λ	Load factor, $[-]$
λ_{cr}	Critical multiplier of the column under axial load, $[-]$
λ_r	Ratio of the radius of gyration to the length of the beam, $[-]$
μ	Demand of ductility of the beam, $[-]$
ξ	Dimensionless ratio of bending to axial strengths, $[-]$
ρ	Air density, $[ML^{-3}]$
τ	Dimensionless time, $[-]$
τ_d	Dimensionless positive phase duration, $[-]$
$\tilde{\tau}$	Dimensionless time, $[-]$
$\tilde{\tau}_d$	Dimensionless positive phase duration, $[-]$
ϕ	Autobalance membrane forces, $[MLT^{-2}]$
ϕ_i	Shape function, $[-]$
χ_K	Ratio of the lateral restraint to characteristic stiffness of the beam-column, $[-]$
χ_M	Ratio of the lateral participating mass to the mass of the beam-column, $[-]$
ψ_K	Dimensionless ratio of the stiffness of the lateral restraint to the equivalent flexural stiffness of the beam, $[-]$
ψ_{KEA}	Ratio of the axial stiffness of the beam to the flexural stiffness of the beam. $[-]$
ψ_M	Dimensionless ratio of the lateral mass to the generalized mass of the floor, $[-]$
ω	Natural frequency of vibration, $[T^{-1}]$

Greek upper case

Δ	Transformed nodal displacements of the whole structure, $[L]$
Δ_0	Mean squared error between the momentum quantities at regime transition, $[ML^2T^{-2}]$
Δ_N	Axial elongation of a beam half, $[L]$
$\overline{\Delta_N}$	Dimensionless axial elongation of a beam half, $[-]$
$\ddot{\Delta}$	Transformed nodal accelerations of the whole structure, $[LT^{-2}]$
$\Phi_{p,\alpha}, \Phi_{I,\alpha}$	Integral of the dimensionless axial force according to dimensionless displacement, $[-]$
Γ_i	Symbol used for regime numbering, $[-]$

Chapter I

Introduction

I.1 Context

Since the catastrophe of Ronan Point apartment tower in London in 1968, a great concern is paid to the robustness of structures, i.e. the ability of the structures to remain as much as possible insensitive to local failures. In this accidental event, a gas explosion occurred on the 18th floor of the high-rise prefabricated concrete building which blew up and expelled the walls out of the building, resulting in a loss of supports for the upper floor concrete slab (see Fig. I.1). This loss of supports provoked the progressive collapse of the corner of the entire building, causing the death of 5 people and injuring 16 others. Some problems were found in the design of the building as well as in some construction details of connections leading to a lack of structural redundancy; these observations induced modifications of building codes [1, 2] and structural engineers are nowadays invited to think more about alternate load paths in structures in case of exceptional event leading to the loss of some key components (threat-independent approach). The final aim of these modifications is to avoid the extent of a damage to the whole structure and to allow occupants to evacuate the building.

About three decades later, a truck containing 1800 kg of ammonium nitrate/fuel oil (ANFO) mixture detonated on the North side of A. P. Murrah federal building in Oklahoma city [3]. Following this terrorist attack, more and more building owners have been concerned about how to design their building to resist to a specific blast loading (threat-dependent approach) and how to protect it from a terrorist attack. The civil structural industries struggle to determine the blast pressure time history and to assess the level of damage of structure since that kind of question is usually met in the military engineering field [4].

Blast loading is different from usual loads (dead loads, live loads, snow, wind,...) as the peak overpressure is very high and applied to the structure for an extremely short duration, requiring dynamic analyses. Due to low probability of occurrence of an explosion at the building and for economical reasons, the structural elements are not designed to respond elastically to a blast loading. Indeed, they engage their capacity to dissipate energy through inelastic deformation, which requires to consider geometric and material non-linearities at the step of structural modeling [5]. Some sophisticated software could be used to compute accurately the blast loading [6, 7, 8] or to predict the non-linear dynamic behavior of the structure [9, 10, 11]. Nevertheless, simplified procedures such as the UFC design guide [4] are generally preferred because they allow to quickly assess the level of damage of the structure with a rather good accuracy, are much less-time consuming and less expensive than commercial software.

Blast loading is very complex to assess since it depends on the nature of the explosive charge, its weight, its distance from the target structure, the geometry of the building facades, the angle of incidence of the shock front with respect to the structure, the level of confinement of the explosion, the amount of venting areas,... and a sophisticated software such as ConWep [12] is required to get an accurate estimation of blast pressure distributions around the building. However, some simplified methods to compute external blast loading around a rectangular box-shaped building and internal blast pressure due to a detonation occuring inside a compartment of the building are available in the literature and are described

in Section I.4.1. Another phenomenon which can be associated to blast loading is the fragmentation of structural components and missiles which can hurt people inside the building but also significantly damage the structure [13]; however, this effect will be neglected in this thesis.

Concerning the dynamic response of blast-loaded structural elements, the UFC design guide [4] assumes that all the structural elements (beam, slab, column,...) are featured by simple support conditions and their mode of failure is flexural. The structural elements are isolated from the rest of the structure and are analyzed as a single-degree-of-freedom (SDOF) non-linear model. The simplified method is based on energy conservation [14] and enables to quickly assess the required ductility of these individual elements and to compare them to the deformation limits proposed in Section I.4.4. However, their interaction with the rest of the structure is neglected although it could substantially affect their dynamic behaviour. For instance, the stability of beam-columns is influenced by the restraints and inertia offered by the surrounding structure and assuming simple supports conditions at the ends of the beam-columns could be conservative in some cases but unconservative in some other structural configurations. Also, the fact of neglecting the coupling effects between the studies element and the rest of the structure may lead to an underestimation of the forces reported in the structure. These observations raise the necessity to propose some easy-to-apply tools to study the dynamic interaction of these structural elements with the rest of the structure, which is the main goal of this thesis.

Figure I.1: Ronan Point apartment building progressive collapse (May 1968).

I.2 Objective and methodology

The purpose of this thesis is to study the dynamic behavior of the structure under internal blast loading as illustrated in Fig. I.2-a or of a simple moment resisting industrial frame subjected to an external explosion as shown in Fig. I.2-b. The main purpose is to develop some quick assessment tools to determine the level of damage of the structure, which could vary from superficial damage to the entire collapse of the building. To do so, we develop a low order model of the problem and analyze it. The type of the structure considered in the conducted investigations is a skeleton frame made of beams and columns which does not include walls and slabs. Indeed, the blast overpressures distributed on these elements are substituted by their resultants which are directly applied to the beams and columns of the frame.
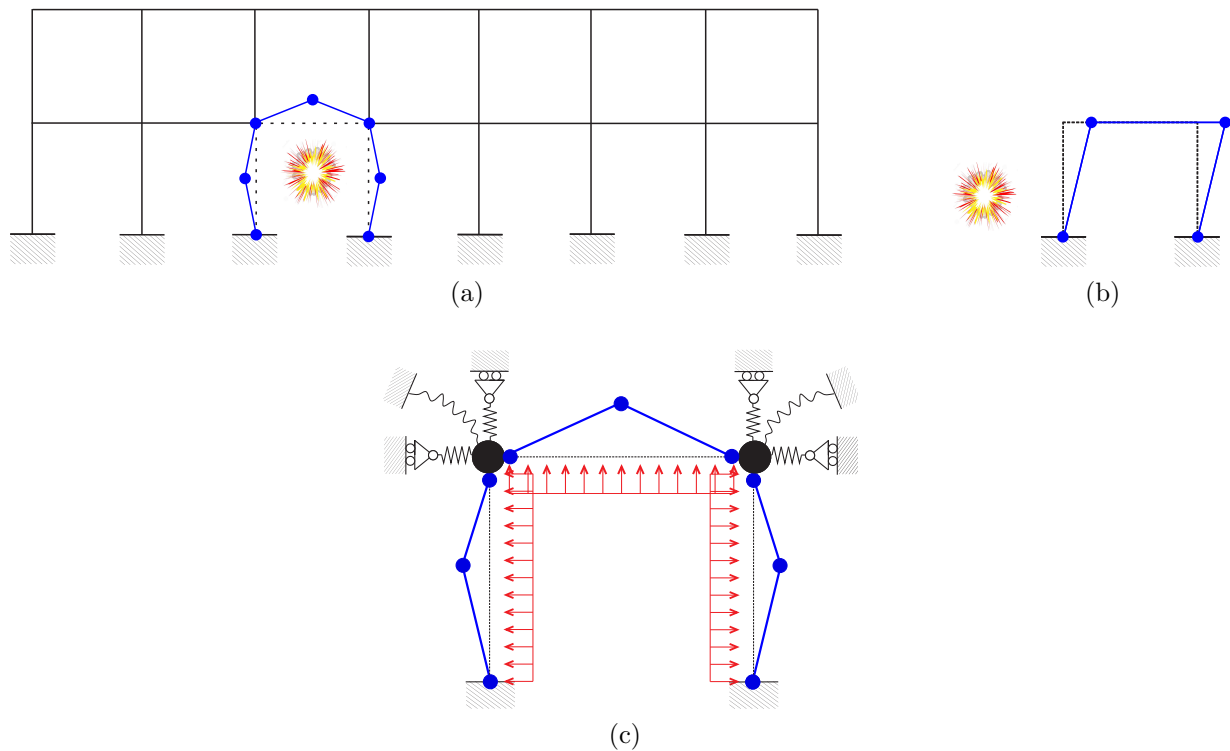
Figure I.2: Sketch of structures under (a) internal and (b) external blast loadings. (c) Extraction of the blast-loaded compartment from a whole frame structure.

The proposed model relies on the extraction of the blast-loaded compartment of the structure by using some condensation techniques to simulate the influence of the *indirectly affected part* (IAP) of the structure (i.e. the part of the structure surrounding the loaded compartment) by equivalent springs and masses (see Fig. I.2-c). There are several reduction methods that enable to determine the elastic stiffness's of the equivalent springs and the corresponding masses in the literature. However, it is difficult to derive the non-linear behavior of the

structure in the plastic regime since the failure of the IAP of the structure could be due to the plastic mechanism of a part of the structure or buckling of columns, beams or even local web or flange buckling in the rest of the structure. In addition, the capacity of deformation of the rest of the structure remains unknown so far but should be further investigated in the future.

Concerning the blast loading, it is assumed that the blast pressure is uniformly distributed along each structural member since the explosion is quite far from them although actually, it depends on the distance from the explosion centre. The type of explosion could be a deflagration due to gas combustion or detonation due to chemical reaction throughout explosive charge such as TNT, which involves different shapes of pressure-time relationship. All the analytical models that are developed in this thesis are valid for both types of explosion though they have been only formalized for the detonation without taking into account the level of confinement provided by the structure. In addition, the simplified approach developed in this thesis remains valid for a simple frame subjected to external blast loading (see Fig. I.2-b) since only the signs of the pressure distributions and the load sequences of structural elements should change compared to what is shown in Fig. I.2-c.

As stated earlier, the analysis of the structure should be carried out in large displacement, taking into account the eventual yielding of the structural elements. The beam could exhibit a significant membrane force in large displacement while the columns could eventually buckle due to the $P-\delta$ effect and lateral blast loading. The out-of-plane instabilities of the structural elements are supposed to be prevented as well as local buckling.

For a further sake of simplicity, the vertical and the rotational springs are disregarded in this thesis and the structural elements are firstly studied independently (see Figs. I.3-a and -b) to highlight the effect of the surrounding structure on the dynamic behaviour of these elements. In a second step, the dynamic interaction between the beam and the adjacent beam-columns is investigated as illustrated in Fig. I.3-c in order to emphasize the effect of inertia of the beam on the stability of the beam-column. In this last case study, the surrounding structure is substituted by lateral simple supports and the structural elements are therefore simply supported, only some compressive loads due to service and dead loads from upper stories are applied at the top of these columns.
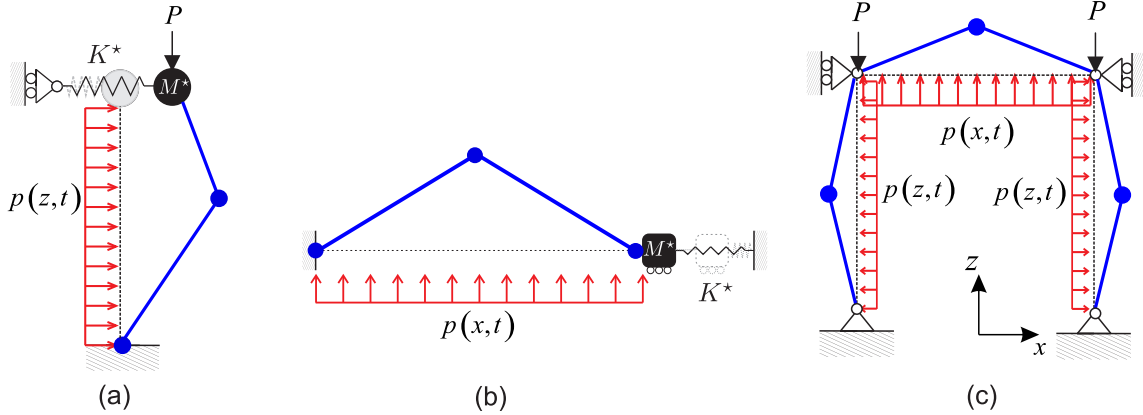
Figure I.3: Extracted structural elements.

I.3 Organization of the dissertation

The present manuscript is divided into five chapters as follows :

Chapter I contains the objective of the thesis and a literature review describing the way to compute blast pressures for internal explosion and the dynamic response of structures under blast loading, how to take into account the effect of strain rate on design strengths, the deformation limits for different structural elements and finally the condensation techniques to reduce the size of the analytical model.

Chapter II describes the analysis of a frame beam under blast loading, considering the effect of elastic lateral restraint and mass offered by the IAP of the structure. Two analytical models are developed in two stages, firstly by considering one single-degree-of-freedom (SDOF) which is the transverse mid-span deflection and secondly by incorporating another degree-of-freedom (DOF) which is the axial elongation of the beam. Both analytical models are compared through a parametric study by varying the set of key structural parameters in their practical range. In order to validate the two degree-of-freedom (2-DOF) model, the results predicted by the analytical model are also compared to those obtained with FEM model and discussed.

Chapter III is dedicated to the dynamic behaviour of the beam-column under blast loading, interacting with the rest of the structure through lateral restraint and mass. This column is subjected to a constant axial load due to dead and live loads from upper stories. In a first step, the procedure to derive the 2-DOF model of the beam-column is detailed as well as transitions of regime (from elastic to plastic regime or the opposite). For extreme cases, when the stiffness of the lateral restraint is very large (or small), a single-degree-of-freedom (SDOF) model is sufficient to accurately predict the response of the column and enables to establish the asymptotic quasi-static or impulsive solutions. Secondly, the numerical validation of the analytical model is again carried out with the help of FEM models, and a comparison is made between the analytical model and the moment magnification approach suggested in the UFC

design guide. Finally, a parametric study is performed through pressure-impulse diagrams by varying the key structural parameters in their practical ranges.

Chapter IV deals with the dynamic behaviour of a frame under internal blast loading where the blast-loaded beam interact with the adjacent blast-loaded columns. Two case studies are analyzed to highlight the effect of transverse inertia of the beam on stability of the beam-columns.

In **Chapter V**, the general conclusions of the thesis are drawn and recommendations for future investigations are given.

The glossary of symbols and initials used in the thesis is reported in the nomenclature on page on page xvii.

I.4   Literature review

I.4.1   Blast loading

I.4.1.1   Explosion

Explosion is difficult to define rigorously but one of his plausible definitions found in [15] is:

"Explosion is the rapid transformation of a material system, accompanied by a strong release of gas. These gases are more or less compressed if they are generated in a confined space or if they are released to the air in a short period of time. Their relaxation can lead to mechanical effects and in particular a sound wave more or less intense."

Another definition given by Baker and Strehlow [16] is the following one:

"In general, an explosion is said to have occurred in the atmosphere if energy is released over a sufficiently small time and in a sufficiently small volume so as to generate a pressure wave of finite amplitude traveling away from source. This energy may have originally been stored in the system in a variety of forms; these include nuclear, chemical, electrical or pressure energy, for example. However, the release is not considered to be explosive unless it is rapid enough and concentrated enough to produce a pressure wave that one can hear. Even though many explosions damage their surroundings, it is not necessary that external damage be produced by the explosion. All that is necessary is that the explosion is capable of being heard."

Section 5 of Eurocode 1991-1-7 [17] dedicated to internal explosions, which does not include solid high explosives, defines the explosion as "a rapid chemical reaction of dust, gas or vapour in air. It results in high temperatures and high pressures. Explosion pressures propagate as pressure waves."

The definitions above refer to explosions in air but they can also occur in other media such as water or underground although, in this thesis, our attention is paid to explosions in air.

There are two main types of explosion: the deflagration and the detonation. The deflagration corresponds to a combustion process of explosive material (gas, dust, vapour cloud, oil)

at a rate much below the speed of sound in the material which leads to the liberation and the propagation of the heat of reaction. Detonation is the explosive reaction of a solid material (TNT, nitroglycerin, RDX, HMX, Semtex) which produces instantaneously a high intensity shock wave front featured by large pressure and temperature gradients. The reaction rate lies between about 1500 and 9000 m/s which is appreciably faster than propagation by the thermal processes observed in deflagration [18].

Physical explosions exist and correspond to an energy released by a physical process. Examples are multiple [15]:

- ○ Pneumatic explosion, i.e. the bursting of a recipient containing a gas under high pressure;

- ○ Electrical explosion, i.e. the bursting of an electrical arc between two points;

- ○ Nuclear explosion, nuclear fusion and fission.

In this chapter, we will classify explosives, describe the phenomenology of the explosion and finally bring out the influence parameters of the explosion.

Blast-loading categories

The UFC design guide [4] propose to divide blast loads into two main groups based on the confinement of the explosive charge (unconfined and confined explosions). Explosions are unconfined when the expansion can occur freely, without preventing their displacement. These explosions (see Fig. I.4) can be qualified as:

- ○ Free-air-burst (1): the initial shock wave reaches directly the structure;

- ○ Air-burst (2) : the initial shock wave is subjected to reflections in contact with the ground before reaching the structure;

- ○ Surface-burst (3): the charge is placed close to or on the ground. Its effects are amplified by the reflections in contact with the ground.

When explosions are confined (4):

- ○ Fully vented explosions will be produced within a structure with one or more frangible surfaces open to the atmosphere (windows for example). The initial shock wave is amplified by the reflection on the nonfrangible portions of structure, but propagates away from the structure due to venting areas;

- ○ Partially confined explosions will occur in the case of structure with a limited size of openings and number of frangible surfaces. The initial shock wave is amplified by the reflections and a quasi-static pressure is build up inside the structure, this pressure has a long duration in comparison to that of the shock pressure;

○ Fully confined explosions: the structure is totally closed, the quasi-static pressure decreases very slowly and the propagation of the shock wave outside of the structure is quasi no existent.
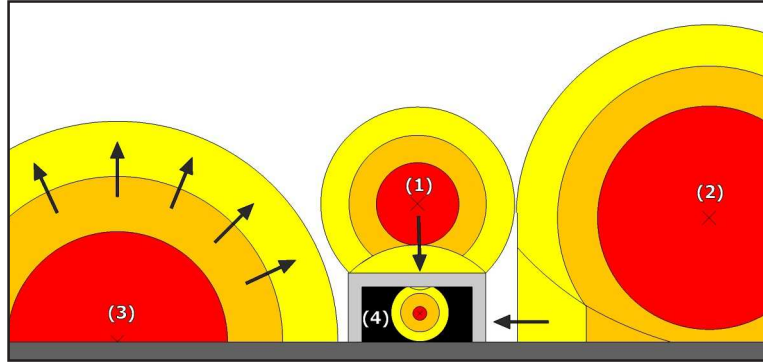
Figure I.4: Unconfined or confined explosions. (Inspired from Ref. [4])

Phenomenology of explosion

A detonation releases a great amount of energy during a very short time. The energy transfer occurs in the form of radial propagation of a shock wave accompanied by gases under high pressure and temperature and followed by an air displacement (compression of air) beyond the discontinuity front. The shock wave travels at supersonic velocity, his magnitude decreases with time to degenerate in sound wave featured by an overpressure of zero and no shock front. Due to the expansion of gases, the gas pressure falls to atmospheric pressure as the shock wave moves outwards from the source and even becomes smaller than the atmospheric pressure because of the cooling of gases (Fig. I.5). As a result, the air blown beyond the discontinuity front moves in the same direction as the shock wave, and returns to the centre of the explosion when the suction phase occurs.[15]

Thermal radiation effects are generally neglected except for gas mixtures or nuclear explosions. Also, fragments are projected at very high speed, their kinetic energy is transformed into dynamic effects on structure and can also provoke permanent damages (eventual perforation of some structural elements) [15].

At any point away from the centre of explosion, the pressure-time curve for a detonation has the shape illustrated in Fig. I.5. The shock front arrives at a given location at a time t_a involving an instantaneous rise of the pressure $p_{0,s}$ which is defined as the peak side-on overpressure. Then, the incident pressure $p_s(t)$ decreases to the ambient pressure p_{atm} at time $t_a + t_{d,s}$ and even becomes smaller than p_{atm} for a duration $t_{d,s}^-$ which is usually much longer than the positive phase duration $t_{d,s}$. The negative phase is usually less important in the design and is generally neglected. The positive incident specific impulse I_s corresponds to the area under the pressure-time curve in the positive phase

$$I_s = \int_{t_a}^{t_a+t_{d,s}} (p_s(t) - p_{atm})\, dt, \tag{I.1}$$

and is shown later to be a key parameter in the blast resistant design of structures [4].

High explosive charges detonate to create shock waves accompanied by very high pressure during a short time whereas low explosives deflagrate during the positive phase, produce pressure of smaller amplitude and longer duration than detonations without any suction phase (see Figure I.6). A great concern is paid to detonation in this thesis, but all the analytical models remain valid in case of structures under deflagration.
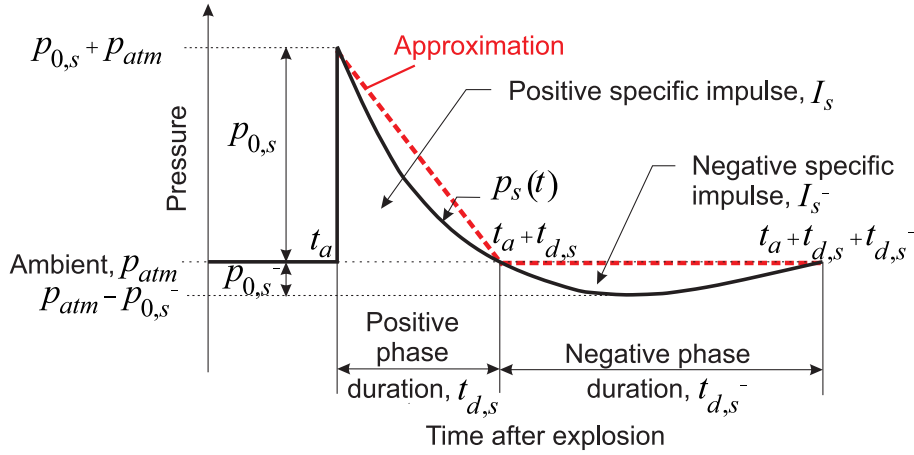
Figure I.5: Pressure-time curve for a detonation where $p_s(t)$: pressure function, p_{atm}: ambient pressure, $p_{0,s}$: peak incident overpressure, $p_{0,s}^-$: peak negative side-on pressure, t_a: arrival time of the shock wave, $t_{d,s}$: positive phase duration, $t_{d,s}^-$: negative phase duration, $I_s = \int_{t_a}^{t_a+t_{d,s}} (p_s(t) - p_{atm}) \, dt$: specific impulse of the positive phase, $I_s^- = \int_{t_a+t_{d,s}}^{t_a+t_{d,s}+t_{d,s}^-} (p_s(t) - p_{atm}) \, dt$: specific impulse of the negative phase. (graph inspired from Ref. [4])
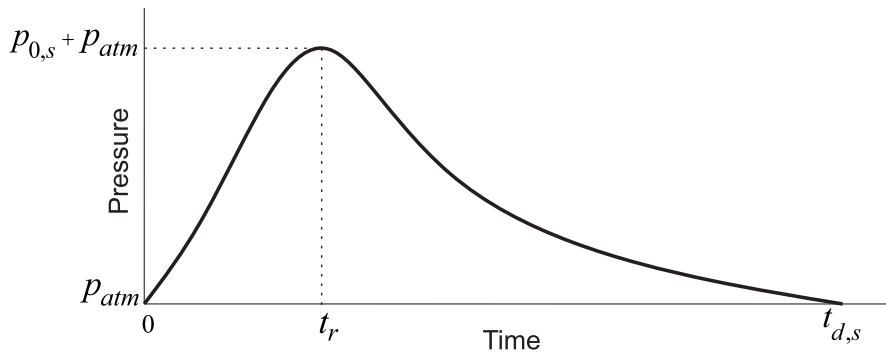

Figure I.6: Pressure-time curve for a deflagration where t_r: rise time, $p_{0,s}$: peak overpressure and $t_{d,s}$: positive phase duration. (graph inspired from Ref. [18])

Blast wave parameters

To describe the pressure-time history of a blast wave (see Fig. I.5), Friedlander equation

can be used for the positive phase $(t_a \leq t \leq t_a + t_{d,s})$

$$p_s(t) = p_{atm} + p_{0,s}\left(1 - \frac{t - t_a}{t_{d,s}}\right)\exp\left\{-b\frac{t - t_a}{t_{d,s}}\right\} \tag{I.2}$$

where b is called the wavefront parameter and is given in Ref. [4]. However, it is commonly accepted in the literature to assume a linear decay by neglecting the exponential factor

$$p_s(t) = p_{atm} + p_{0,s}\left(1 - \frac{t - t_a}{t_{d,s}}\right) \tag{I.3}$$

which is conservative for the blast resistant design of structure (see interrupted red line in Fig. I.5).

The corresponding incident specific impulse is therefore given by

$$I_s = \frac{p_{0,s}t_{d,s}}{2}. \tag{I.4}$$

To characterize all the blast parameters, a scaling of the blast wave laws must be conducted. Hopkinson and Cranz [19, 20] establish a law which states that two explosions are characterized by the same blast wave parameters provided their scaled distance $Z = R/W^{1/3}$ are identical. Indeed, their studies reveal that the energy liberated by an explosion is proportional to the mass of the explosive charge W, but also proportional to the volume of gas V. In addition, they demonstrate that the charge W is proportional to the volume of gas V, and thus to the cubic of the range R from the centre of the explosive charge. Thus, the constant of proportionality corresponds to the scaled distance $Z = R/W^{1/3}$ where the variables R and W respectively refer to the distance from the centre of a spherical charge and the charge mass of equivalent TNT (respectively expressed in meters and kilograms in the formulas below).

Theoretically, for a given type of chemical high explosive, the peak side-on overpressure reads

$$p_{0,s} = \frac{K_1}{Z^3} \tag{I.5}$$

where K_1 is a constant which depends on the quantity of the explosive charge (see Ref. [21]).

The analysis due to Brode [22] leads to the following results for peak side-on overpressure:

$$p_{0,s} = \begin{cases} \frac{6.7}{Z^3} + 1 & \text{for } p_{0,s} > 10\,\text{bar}, \\ \frac{0.975}{Z} + \frac{1.455}{Z^2} + \frac{5.85}{Z^3} - 0.019 & \text{for } 0.1 < p_{0,s} \leq 10\,\text{bar}. \end{cases} \tag{I.6}$$

Kinney and Graham [23] propose the following formula for the incident overpressure $p_{0,s}$ [kPa] and the positive phase duration $t_{d,s}$ [ms]

$$\frac{p_{0,s}}{p_{atm}} = \frac{808\left(1 + (Z/4.5)^2\right)}{\sqrt{1 + (Z/0.048)^2}\sqrt{1 + (Z/0.32)^2}\sqrt{1 + (Z/1.35)^2}} \tag{I.7}$$

and

$$\frac{t_{d,s}}{W^{1/3}} = \frac{980 \left(1 + (Z/0.54)^{10}\right)}{\left(1 + (Z/0.02)^3\right) \left(1 + (Z/0.74)^6\right) \sqrt{1 + (Z/6.9)^2}},\tag{I.8}$$

where $p_{atm} = 103.25\,\text{kPa}$ is the atmospheric pressure.

Figure I.7 summarizes the analytical laws describing the spatial and time evolution of the blast wave pressure.
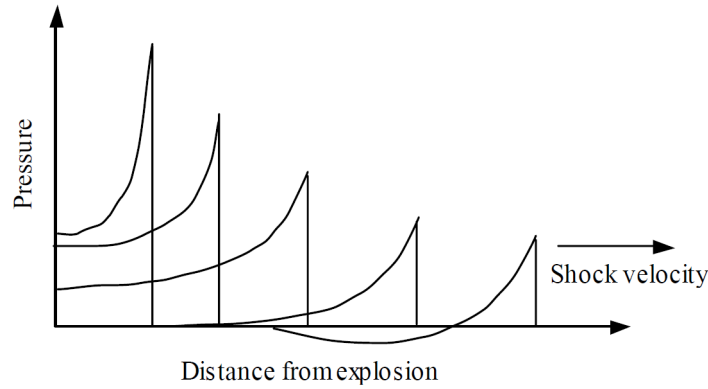
Figure I.7: Blast wave propagation (from Ref. [24]).

In addition to the side-on pressure, the maximum dynamic pressure q due to rapid air flow associated with the motion of the shock wave should be considered [25]

$$q = \frac{1}{2}\rho u^2 = \frac{5p_{0,s}^2}{2\left(p_{0,s} + 7p_{atm}\right)}\tag{I.9}$$

where ρ and u correspond to the air density and the velocity of the air flow. The UFC design guide [4] proposes to use the graph illustrated in Fig. I.8 to determine the peak dynamic pressure q according to the peak incident pressure $p_{0,s}$.

The scaled distance is defined on the basis of a spherical TNT charge as a reference but in order to quantify blast waves from other sources than TNT, Table I.1 should be used to multiply the mass of the explosive charge W by a conversion factor based on the ratio of its specific energy to that of TNT Q_x/Q_{TNT}. For instance, one kilogram of HMX is converted to 1.256 kilogram of TNT due to the ratio of their specific energies. For fuel-air or vapor cloud explosions, TNT equivalence is difficult to be accurately established although it is known that the factor of conversion varies from 0.4 to 0.6 [18].

The pressure/distance characteristics are defined on the basis of the spherical charge in air, but the shape of the charge could be cylindrical, a plane sheet or a line source. Refs. [26, 27] propose to take into account this effect on the peak side-on overpressure.
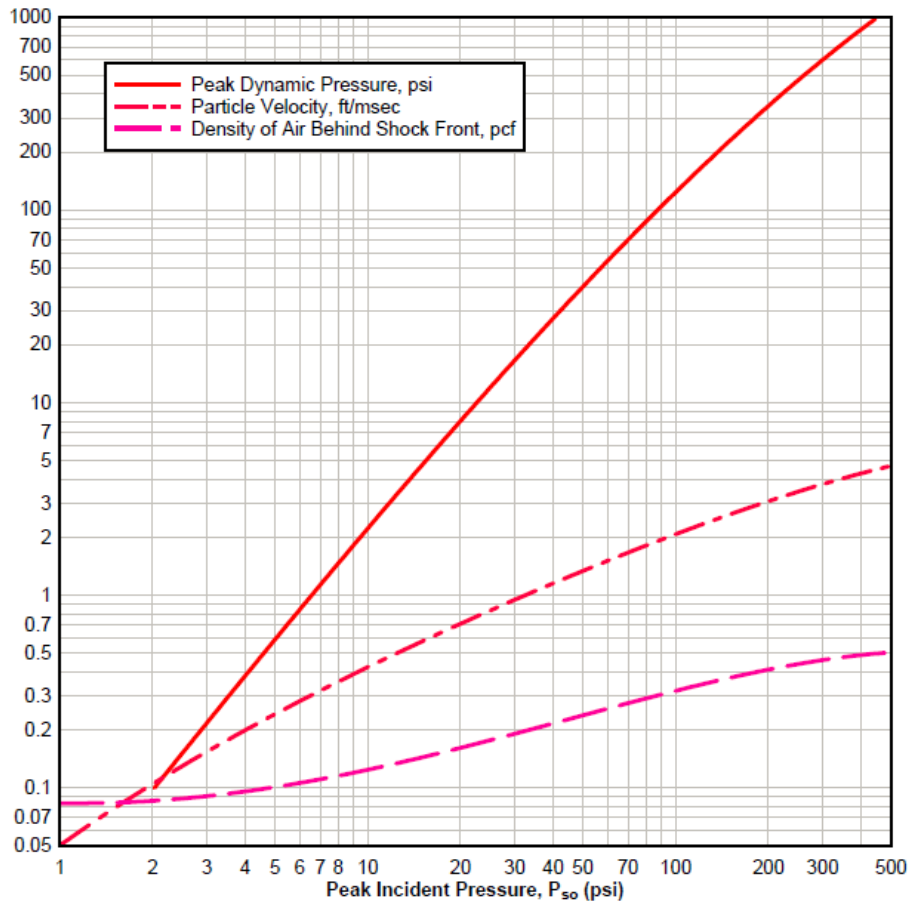
Figure I.8: Peak incident pressure versus peak dynamic pressure, density of air behind the shock front and particle velocity (from Ref. [4]).

Explosive	Mass specific energy Q_x [kJ/kg]	TNT equivalent Q_x/Q_{TNT}
Compound B	5190	1.148
RDX (Cyclonite)	5360	1.185
HMX	5680	1.256
Nitroglycerin (liquid)	6700	1.481
TNT	4520	1.000
Blasting gelatin	4520	1.000
60% Nitroglycerin dynamite	2710	0.600
Semtex	5660	1.250

Table I.1: Conversion factors for explosives extracted from [28].

Until now, a spherical free-air burst is assumed (see (1) in Fig. I.4) but when the explosive

charge lies on the ground (undeformable surface), this assumption is no longer valid. All the energy of the explosion is concentrated in a half space and so, its energy must be doubled in comparison to a free-air detonation (see (3) in Fig. I.4). Nevertheless, as the surface absorbs a quantity of energy, the mass of the explosive charge is multiplied by 1,8 when a crater is formed [15].

Only in some specific configurations, the free-field or hemispherical air bursts represent the real dynamic loading applied to structures. Indeed, the blast loading strongly depends on the orientation, the geometry and the size of the structures which the blast waves encounter. The structure prevents air molecules to move further; they are immobilized and the shock wave compresses them leading to an overpressure which is greater than the incident pressure. This phenomenon is commonly known as reflection. Generally, it is assumed that the initial shock waves are decoupled from the response of the structures, and therefore these last ones can be treated as rigid bodies which cause processes such as reflection and diffraction, and alteration of flow behind shock front [28].

Assuming that the air behaves as a real gas, Rankine and Hugoniot [29] derived a formula to get the reflected overpressure

$$p_{0,r} = 2p_{0,s} \left(\frac{7p_{atm} + 4p_{0,s}}{7p_{atm} + p_{0,s}} \right) \tag{I.10}$$

when for air, the specific heat ratio γ is set equal to 1.4. The reflection coefficient C_r, defined as the ratio of $p_{0,r}$ to $p_{0,s}$, has a lower limit equal to 2 if the incident pressure $p_{0,s}$ is significantly lower than the ambient pressure p_{atm} and an upper limit equal to 8 if $p_{0,s}$ is much greater than the ambient pressure. However, according to experimental measurements, the reflection coefficient can even reach a value of 20 because of gas dissociation effects at very close range [18]. The UFC design guide [4] proposes to determine the main blast wave parameters for spherical charges of TNT in free air using the graphs plotted against the scaled distance Z as illustrated in Fig. I.9.
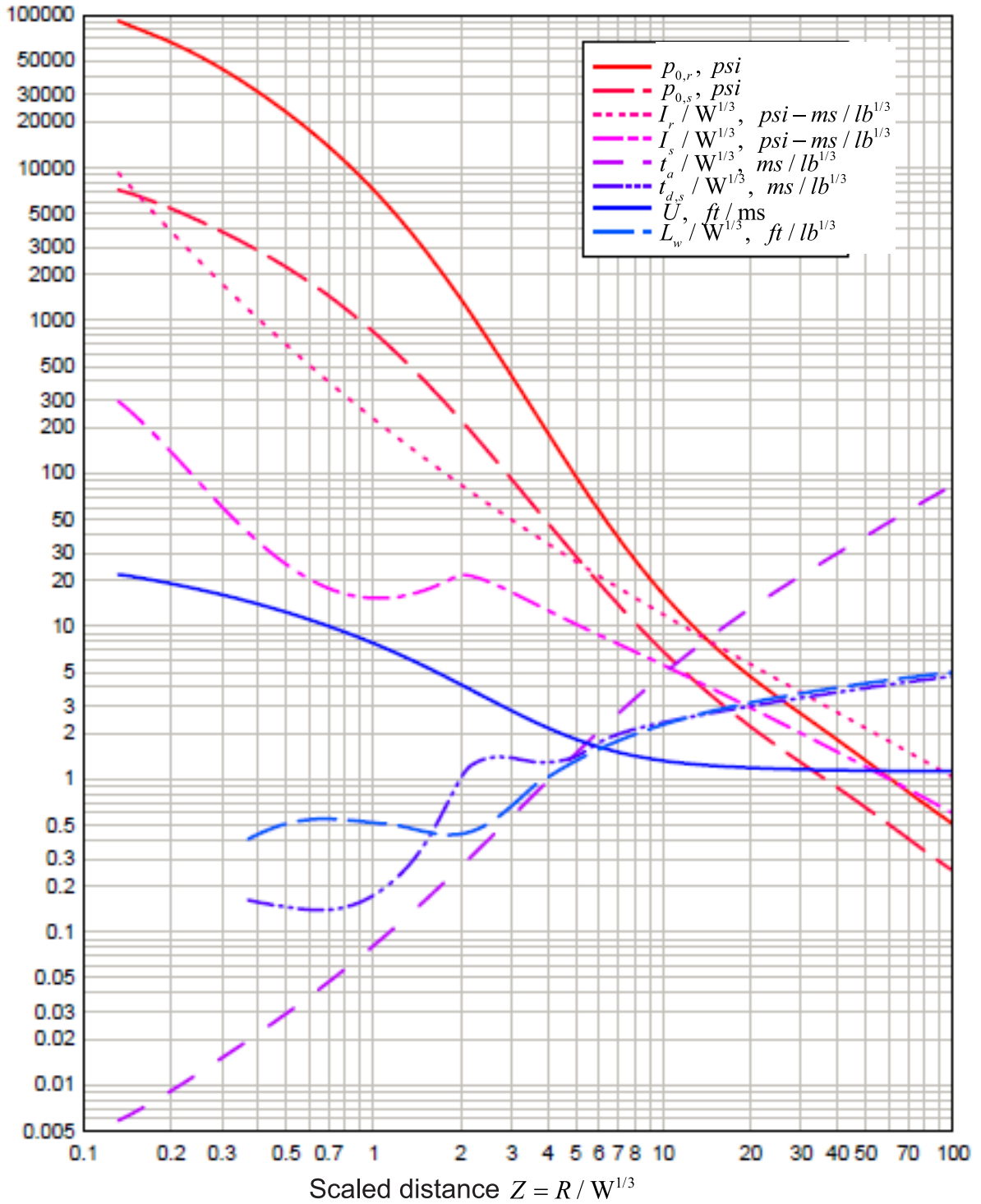
Figure I.9: Positive phase shock wave parameters for spherical charges of TNT in free air at sea level. (from Ref. [4])

I.4.1.2   Structural loading

This section is widely inspired from Refs. [30, 18].

Internal blast loading of structures

When an explosion occurs inside a structure, the blast waves are reflected several times by the walls resulting in an increase of internal pressure. However, the internal pressure could be mitigated by the breaking of venting areas (e.g. windows, doors) which enables the shock waves to dissipate their energy. The venting areas is beneficial for the protection of the structure against blast but their fragment could hurt people around the building.

The detonation of high explosive inside a structure produces two loading phases. Firstly, due to the confinement provided by the structure, a re-reflection occurs leading to a train of blast waves of decaying amplitude. The second loading phase corresponds to the build-up pressure of gas released after explosion which is more complex to assess (Fig. I.10).
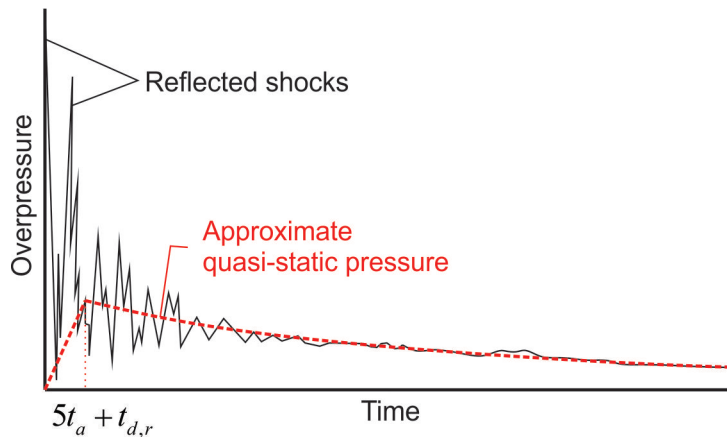
Figure I.10: Typical pressure-time profil for internal blast loading of a partially vented structure. (inspired from Ref. [18])

For the first phase of loading, the reflected pressure-time history is assumed to be linear

$$p_r\left(t\right) = p_{0,r}\left(1 - \frac{t}{t_{d,r}}\right) \tag{I.11}$$

where $t_{d,r} = 2I_r/p_{0,r}$ is the positive phase duration of the initial reflected blast wave. The reflected blast wave parameters $(p_{0,r}, I_r)$ could be determined by using Fig. I.9.

To quantify subsequent reflections, Baker *et al.* [28] assume that the peak pressure is halved on each re-reflection as well as the impulse (i.e. the duration of the pulse is supposed to remain constant) as illustrated in Fig. I.11. The reverberation time defined as the time between each blast wave arriving on the internal surface of the structure is assumed constant and equal to $2t_a$ (where t_a is the arrival time of the first blast wave at the reflecting surface). In Ref. [31], the authors compare time-pressure profile of an explosion inside a wooden box between Baker's approach, experimental and numerical tests. They show that the first peak overpressure as well as the elapsed time between successive pulses are overestimated (for the

studied case) and the negative phase of blast loading is conservatively neglected. Graphically, it seems that the total positive specific impulse predicted by Baker *et al.* is much greater than those of experimental and numerical tests, confirming that the analytical approach is therefore conservative for this case study provided the natural period of the structure is much longer than the positive phase duration of the blast loading (impulsive loading) [18].

While the pressure due to several reflections of shock waves is decreasing, the gas pressure which depends on the venting areas, the volume of the compartment and the properties of the explosive charge is developing (see interrupted red curve in Fig. I.10). Baker *et al.* [28] propose to approximate the gas pressure with a decreasing exponential function as

$$p_g\left(t\right) = \left(p_{QS} + p_{atm}\right)\exp\left\{-2.13\frac{\alpha_e A_s a_0}{V_s}t\right\} \tag{I.12}$$

where p_{QS} is peak quasi-static pressure which can be obtained from Fig. I.12, α_e is the ratio of vent area to wall area, A_s is the total inside surface area of the structure, V_s is the structure volume and $a_0 = 340\,\text{m/s}$ is the speed of sound at ambient conditions. Equation (I.12) is only valid for the part of the decaying curve as illustrated by the dashed line in Fig. I.10. The rise of the gas pressure is assumed to be linear and tops out at a time corresponding to the end of the reverberation phase $5t_a + t_{d,r}$.
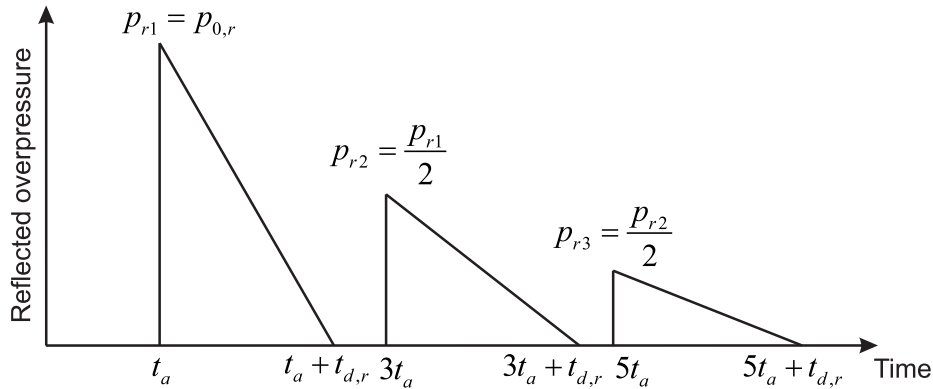
Figure I.11: Simplified blast wave reflections (t_a and $t_{d,r}$ respectively correspond to the arrival time of the first blast wave at the reflecting surface and its positive phase duration). (sketch inspired from Ref. [18])
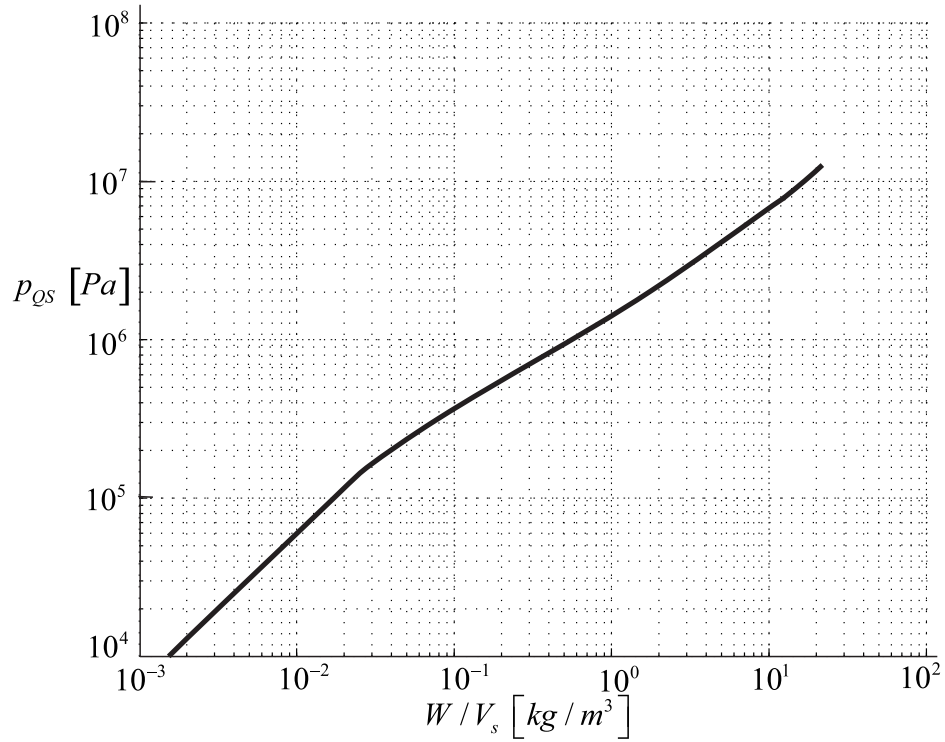
Figure I.12: Peak quasi-static pressure p_{QS} according to the ratio of the mass of the TNT equivalent explosive charge W to the volume of the structure V_s. (from Ref. [4])

The procedure to compute pressure time-history of a explosive charge detonating inside a structure is described as follows:

1. Computation of the blast wave overpressure taking into account the re-reflection of shock waves:

   (a) Estimation of the reflected blast wave parameters $p_{0,r}$ and I_r as well as the arrival time of the shock wave t_a by using the scaled distance curves shown in Fig. I.9;

   (b) Computation of the positive phase duration assuming a triangular impulse as $t_{d,r} = 2I_r/p_{0,r}$;

   (c) Drawing of the graph as illustrated in Fig. I.11;

2. Computation of the gas pressure:

   (a) Knowing the mass of the explosive charge W and the volume of the compartment V_s, the peak quasi-static pressure p_{QS} can be determined by using Fig. I.12;

   (b) After computing the ratio of vent area to wall area α_e and total inside surface area of the structure A_s, the gas pressure time history can also be drawn with Equ. (I.12);

(c) Correction of the to gas pressure time history for $t \leq 5t_a + t_{d,r}$ by assuming that the pressure increases linearly until reaching the approximated curve as illustrated in Fig. I.10.

The Section 2-14 of the UFC design guide [4] describes a similar procedure to compute an internal detonation although it proposes about one hundred graphs to determine more accurately the reflected blast wave parameters, taking into account the number of walls of the blast-loaded compartment and the exact location of the explosive charge inside the compartment.

Blast wave external loading on structures

Considering the action of a shock front on a rectangular box-shaped structure from a distant detonation (see Fig. I.13-a), the shock wave can be assumed to be planar and impacts the front face normally (the incident angle between them is equal to zero). The blast wave will engulf and crush the structure by exerting overpressure on every exposed faces of the building (see blue forces in Fig. I.13-b) while the air blow generates dynamic pressures all around the building, creating depression on the top, side and rear faces of the building (see red forces in Fig. I.13-c).

When the shock wave encounters the front face, it is reflected and causes an instantaneous peak overpressure $p_{0,r}$ (see red forces in Fig. I.13-d). Then the blast reflected overpressure $p_r(t)$ decreases because the blast wave is passing over and around the structure; the pressure is coming back to an overpressure $p_s(t)$ (with an angle of incidence between the shock wave and the faces equal to 90°) which is smaller than $p_r(t)$. The blast wave pressure on front face is accompanied by a drag force due to air blow which pushes the structure to the right with a drag coefficient C_D equal to 1. Concerning the top, side and rear faces, a suction force related to air blow is applied on the top, side and rear faces with a drag coefficient C_D equal to -0.3. The drag coefficient C_D depends on the geometry of the structure and is given in Ref. [28] for other shapes of structure.

The reader is invited to consult the Section 2-15 of UFC design guide [4] to get further information about how to compute the pressures applied to each face of the building.
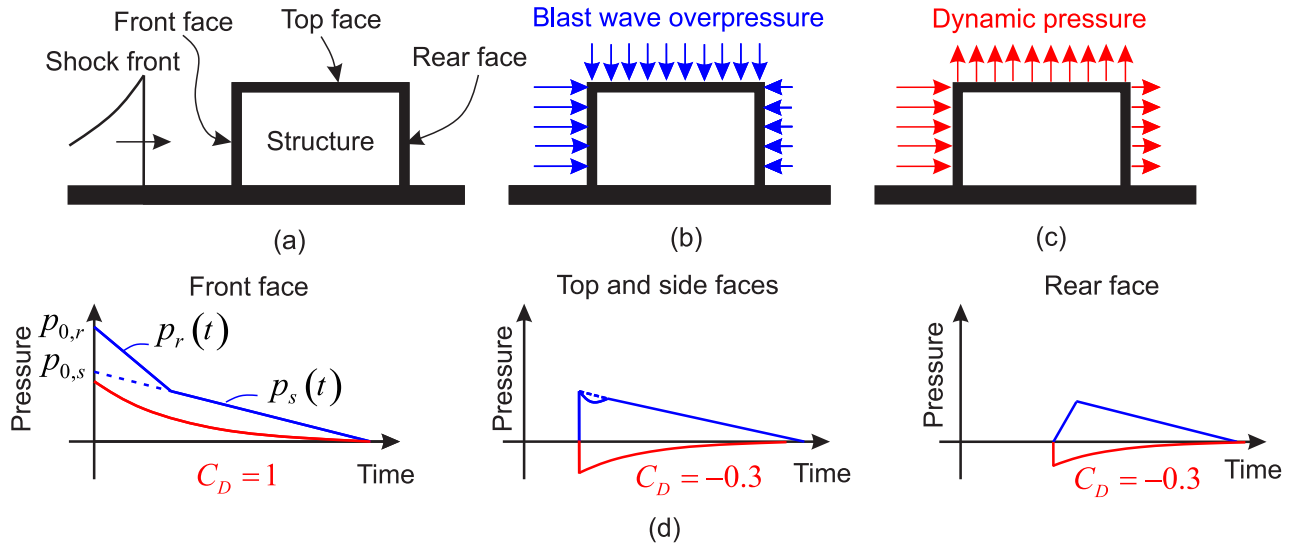
Figure I.13: Blast wave external loading on structures. (a) Elevation view of the structure subjected to a shock wave, (b) blast wave overpressure around the building, (c) dynamic pressures due to air blow around the building, (d) diffraction and drag loads applied on each face of the structure (inspired from Ref. [30]).

I.4.2 Structural response to blast loading

This section is widely inspired from Refs. [30, 18].

I.4.2.1 Elastic SDOF structure

Elastic response spectrum

A structure which can be idealized as a single-degree-of-freedom (SDOF) elastic structure with a mass M_s and a stiffness k_s is considered. The structure is subjected to an idealized triangular blast loading with a peak force F_0 and a positive phase duration t_d. The pressure time-history and the corresponding impulse are respectively described by

$$F(t) = \begin{cases} F_0 \left(1 - \frac{t}{t_d}\right) & \text{for } 0 \le t \le t_d, \\ 0 & \text{for } t_d < t. \end{cases} \tag{I.13}$$

and

$$I = \frac{1}{2} F_0 t_d. \tag{I.14}$$
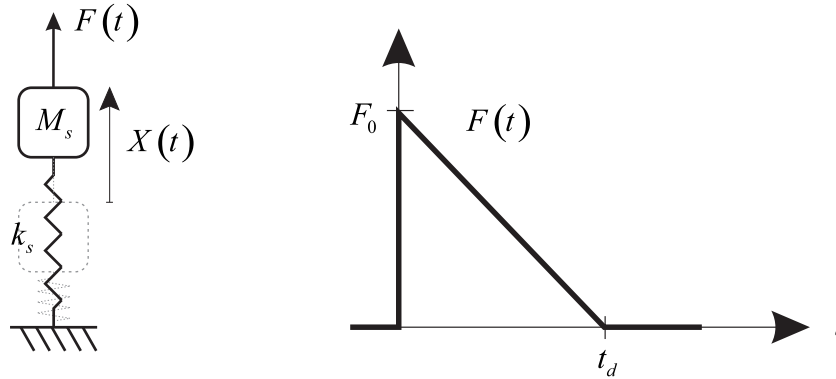
Figure I.14: Single degree of freedom (SDOF) elastic structure subjected to idealized blast impulse. (sketch inspired from Ref. [18])

The equation of motion of the structure, considering no damping effect, is

$$M_s \ddot{X} + k_s X = F(t) \tag{I.15}$$

and the solution can be written as follows

$$\frac{X(t)}{X_{st}} = \begin{cases} (1 - \cos \omega t) + \frac{1}{t_d}\left(\frac{\sin \omega t}{\omega} - t\right) & \text{for } 0 \leq t \leq t_d, \\ \frac{1}{t_d \omega}\left(-t_d \omega \cos \omega t + \sin \omega t - \sin \omega (t - t_d)\right) & \text{for } t_d \leq t, \end{cases} \tag{I.16}$$

where $\omega = \sqrt{k_s/M_s} = 2\pi/T$ is the natural circular frequency of vibration of the structure (T is the natural period of vibration) and $X_{st} = F_0/k_s$ is the static response of the structure under a static force F_0.

For instance, let us consider a structure characterized by a mass M_s of 1 kg and a natural period of vibration T of 2 s (elastic stiffness k_s is equal to π^2 N/m) that is subjected to an idealized triangular pulse featured by a peak force F_0 of 1 N and a positive phase duration t_d equal to T. The static displacement X_{st} is equal to 0.1 m. Fig. I.15-a illustrates the displacement time-history of the structure which presents a maximum dynamic amplification of 1.55 before the end of the positive phase duration. When the blast loading is ended, the structure keeps vibrating indefinitely elastically because no damping is considered in Equ. (I.15). The natural period T corresponds to the time between two successive peaks of displacement during this free regime.

It can be shown that the dynamic load factor (DLF), defined as the ratio of the maximum dynamic displacement X_m to the static displacement X_{st}, only depends on the ratio of the positive phase duration t_d to the natural period of vibration T of the structure as illustrated in Fig. I.15-b. The above example is represented by a red dot at $(1, 1.55)$ $(= (t_d/T, X_m/X_{st}))$.

Evaluation of the limits of response

In the case of quasi-static blast loading, the positive phase duration t_d is much longer than the natural period of vibration of the structure T so that the load can be considered as
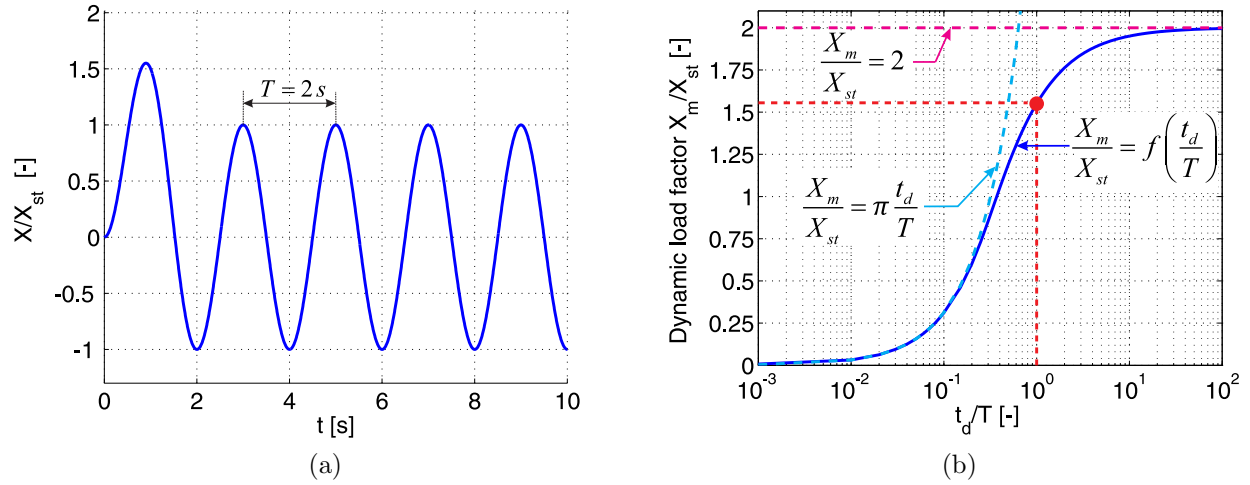
Figure I.15: (a) Dynamic displacement of the structure characterized by a mass $M_s = 1\,\mathrm{kg}$, an elastic stiffness k_s of $\pi^2\,\mathrm{N/m}$ ($T = 2\,\mathrm{s}$) subjected to a peak force $F_0 = 1\,\mathrm{N}$ and a positive phase duration $t_d = 2\,\mathrm{s}$. (b) Dynamic load factor (DLF) according to the ratio of the blast positive phase duration t_d to natural period of the structure T.

constant (and equal to the peak force F_0) while the structure reaches its maximum deflection. Based on the principle of conservation of energy, the strain energy U stored in the structure until reaching the maximum deflection X_m is equated to the work done W_p by the blast loading

$$U = \frac{1}{2}k_s X_m^2 = W_p = F_0 X_m \tag{I.17}$$

leading to the following relationship

$$\frac{X_m}{X_{st}} = 2. \tag{I.18}$$

Equation (I.18) represents the dynamic load factor (DLF) which gives the upper bound of response and is called the quasi-static asymptote (see Fig. I.15-b).

   In the case of impulsive blast loading where t_d is much smaller than T, the structure does not have time to respond significantly during the positive phase duration of blast loading. Indeed, the deformation occurs at times greater than t_d. However, the blast loading is so fast that an impulse $I = \frac{1}{2}F_0 t_d$ is delivered to the initially stationary structure, which induces an initial velocity to the structure given by the momentum conservation of the structure (see Fig. I.15-b)

$$\dot{X}_0 = \frac{I}{M_s}. \tag{I.19}$$

Therefore, the initial kinetic energy K_0 of the structure can be written as

$$K_0 = \frac{1}{2}M_s\dot{X}_0^2 = \frac{I^2}{2M_s} = \frac{F_0^2 t_d^2}{8M_s}. \tag{I.20}$$

The kinetic energy will be converted into strain energy until reaching the maximum displacement

$$K_0 = U = \frac{1}{2}k_s X_m^2 \tag{I.21}$$

which, after some rearrangement, yields the impulsive asymptote of the response (see Fig. I.15-b)

$$\frac{X_m}{X_{st}} = \frac{1}{2}\omega t_d = \pi\frac{t_d}{T}. \tag{I.22}$$

The relative errors between these analytical asymptotic solutions and response spectrum curve remain bounded to 1% when $t_d/T \leq 0.1$ for the impulsive regime and $t_d/T \geq 25$ for the quasi-static regime (see Fig. I.15-b). The structure is under a dynamic regime if the positive phase duration has the same order of magnitude as the natural period of vibration of the structure ($0.1 \lesssim t_d/T \lesssim 25$).

I.4.2.2 Elastic-perfectly plastic SDOF structure

Elastic-perfectly plastic response spectrum
Consider a SDOF structure characterized by an elastic-perfectly plastic resistance with a elastic stiffness k_s and a plastic resistance R_m. The equation of motion can be written in its general form:

$$M_s\ddot{X} + R(X) = F(t) \tag{I.23}$$

where the resistance of the system is described by

$$R(X) = \begin{cases} k_s X & \text{for } X \leq X_y, \\ R_m & \text{for } X_y < X, \end{cases} \tag{I.24}$$

and $X_y = R_m/k_s$ is the deflection of the structure at yielding.

Graphical solutions for a triangular blast loading are presented in Fig. I.16, the ductility μ defined as the ratio of the maximum displacement X_m to the yield displacement X_y is plotted against the ratio t_d/T according to R_m/F_0. Analytical solutions of Equ. (I.23) and corresponding response spectrum for triangular and exponential blast loading taking into account the negative part of the pressure-time history are available in Ref. [32].
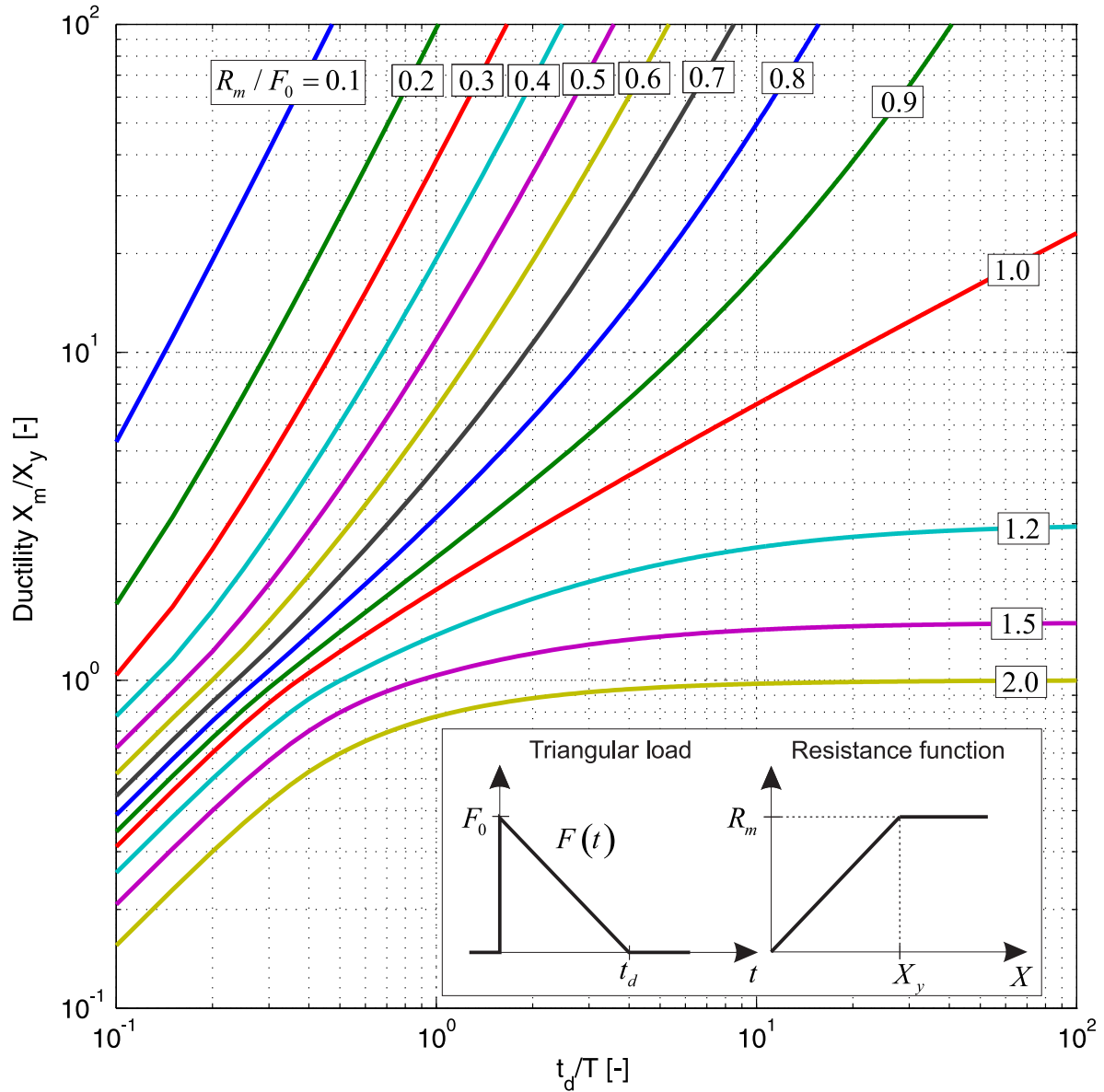
Figure I.16: Maximum response of elastic-plastic SDOF system for a triangular load.

Evaluation of the limits of response

As explained earlier, the analytical asymptotic solutions can be determined on the basis of the principle of conservation of energy. The procedure is identical to that for the elastic response spectrum except for the strain energy in the plastic regime (for a ductility ratio $\mu = X_m/X_y > 1$) which becomes

$$U = \frac{1}{2}k_s X_y^2 + R_m \left(X_m - X_y \right). \tag{I.25}$$

The quasi-static asymptotic solutions reads

$$\mu = \frac{X_m}{X_y} = \begin{cases} \frac{2}{R_m/F_0} & \text{for } \mu \leq 1 \, (\text{or } 2 \leq \frac{R_m}{F_0}), \\ \frac{R_m/F_0}{2(R_m/F_0 - 1)} & \text{for } \mu \geq 1 \, (\text{or } 1 < \frac{R_m}{F_0} \leq 2). \end{cases} \quad \text{(I.26)}$$

For instance, when the ratio of the plastic resistance to the peak force of blast loading R_m/F_0 is equal to 1.2, the ductility is equal to 3 for large value of t_d/T as illustrated in Fig. I.16 whereas the ductility tends to infinity when the ratio R_m/F_0 tends to 1. In this case, it involves that the structure could not find a stable configuration for a peak quasi-static force F_0 greater or equal to the plastic resistance R_m.

The impulsive asymptotic solutions reads

$$\mu = \frac{X_m}{X_y} = \begin{cases} \pi \left(\frac{1}{R_m/F_0} \right) \left(\frac{t_d}{T} \right) & \text{for } \mu \leq 1, \\ \frac{1}{2} + \frac{\pi^2}{2} \left(\frac{1}{R_m/F_0} \right)^2 \left(\frac{t_d}{T} \right)^2 & \text{for } \mu \geq 1. \end{cases} \quad \text{(I.27)}$$

For instance, when the ratios R_m/F_0 and t_d/T are equal to 0.1, the ductility is equal to 5.43 as illustrated and validated by the elastic-plastic response spectrum (Fig. I.16).

I.4.2.3 Pressure-impulse diagram

The first pressure-impule (P-I) diagram was established experimentally based on a study of some houses which were damaged by bombs dropped on the UK [33]. The axes of the curves are simply the side-on peak overpressure $p_{0,s}$ and specific impulse I_s as shown in Fig. I.17. The curves indicate the level of damage of the structure under the combination of load and impulse. Five categories of damage are considered (A, B, C_b, C_a and D) : category A corresponds to almost complete demolition of the building while category D refers to damage calling for urgent repair but it is not severe enough to make the building inhabitable. Further analysis allows to incorporate additional 'range-charge weight' curves to P-I diagram that enable to assess the potential damage of the structure in terms of stand-off distance (distance between the explosive charge and the target structure) and mass of the explosive charge [30].

Other P-I diagrams were also developed for human response to blast loading with categories of injury. The first category of injury is linked to direct effect of blast overpressure, the second one to the impact of fragments from weapons' casing whereas the third one refers to rapid motion of the body which may impact some obstacles [28].
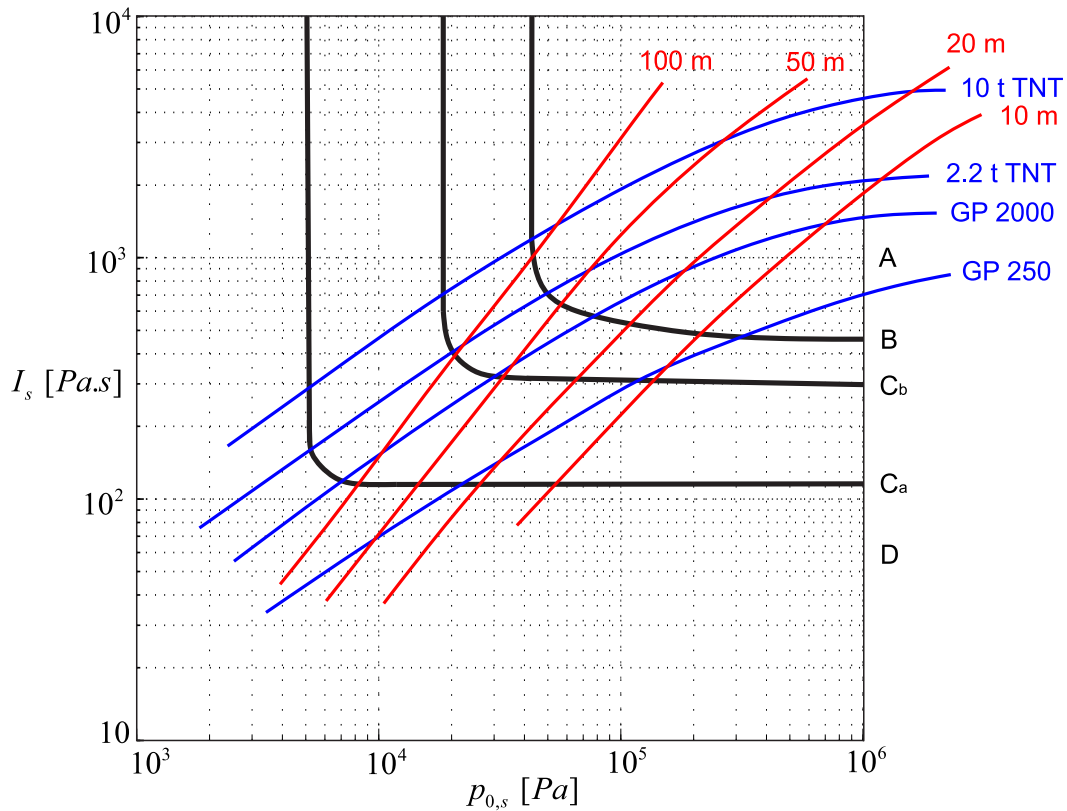
Figure I.17: Iso-damage curves with range-charge weight overlay for brick built houses. (from Ref. [30])

Fig. I.18-a illustrates a pressure-impulse (P-I) diagram for an elastic-perfectly plastic SDOF structure as described in Section I.4.2.2, with an iso-damage curve corresponding to a ductility ratio μ equal to 1. In the case of point that is below or on the left of this curve, it indicates that the structure remains elastic after explosion has occurred ($\mu < 1$) whereas it experiments a plastic deformation beyond this curve ($\mu > 1$). The typical profile of a P-I diagram is composed of two asymptotes pertaining to the fast (impulsive) and the slow (quasi-static) dynamics. The transition between these two extremes corresponds to a dynamic regime, where the duration of the loading interacts with the timescales of the structure.

Fig. I.18-b illustrates a complete p-I diagram which enables to assess quickly, with a simple reading, the level of ductility demand of the structure according to the pressure and impulse delivered to the structure. The greater the impulse or the pressure is, the greater the required ductility of the structure is. When the required ductility exceeds the maximum allowable limit of deformation, the structure is likely to fail.
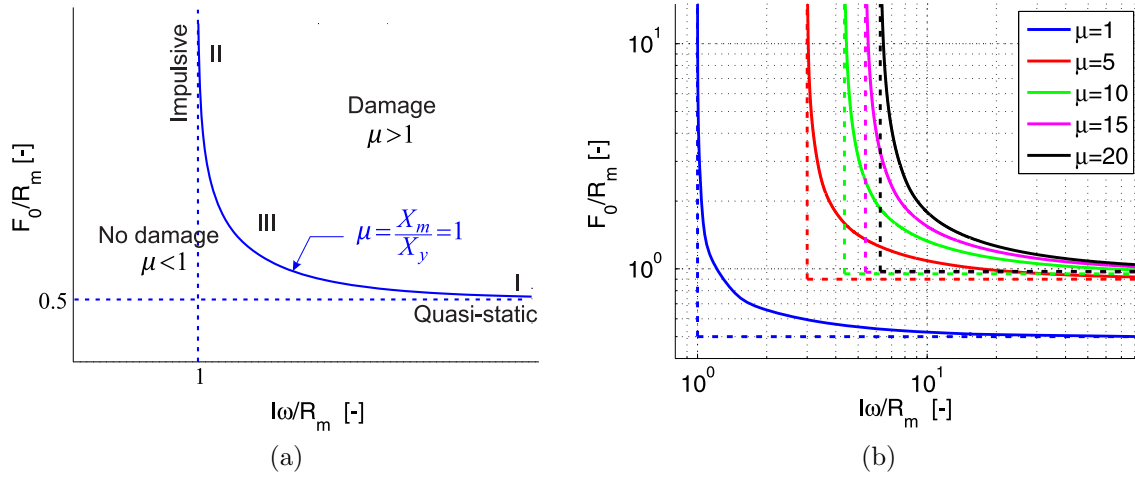
Figure I.18: (a) Regions of pressure-impulse diagram. (b) Pressure-impulse diagram of an elastic-perfectly plastic SDOF structure.

Concerning the asymptotic solutions of p-I diagram, they can be determined from Equs. (I.26) and (I.27) after some rearrangement as follows

$$\frac{F_0}{R_m} = 1 - \frac{1}{2\mu} \tag{I.28}$$

and

$$\frac{I\omega}{R_m} = \sqrt{2\mu - 1}. \tag{I.29}$$

The two asymptotes are shown in Fig. I.18-b. For a ductility ratio μ of 20, the quasi-static and impulsive asymptotic values are respectively given by 0.975 and 6.24.

More sophisticated P-I diagrams are also avalaible in the literature [28] such as the one presented in Fig. I.19 which illustrates a non-dimensional pressure-specific impulse diagram for beams under a uniformly distributed blast loading. The contours of the P-I diagram indicate the maximum strain ϵ_m, while the coordinates correspond to peak overpressure p_0 and the corresponding specific impulse $I = p_0 t_d / 2$. The material law is assumed to be elastic-perfectly plastic and different boundary conditions can be considered by inserting the appropriate ψ coefficients from the Table in upper right corner of Fig. I.19. Once strain has been obtained graphically from Figure I.19, the maximum deflection X_m is obtained by solving the equation in the lower left corner. [28]
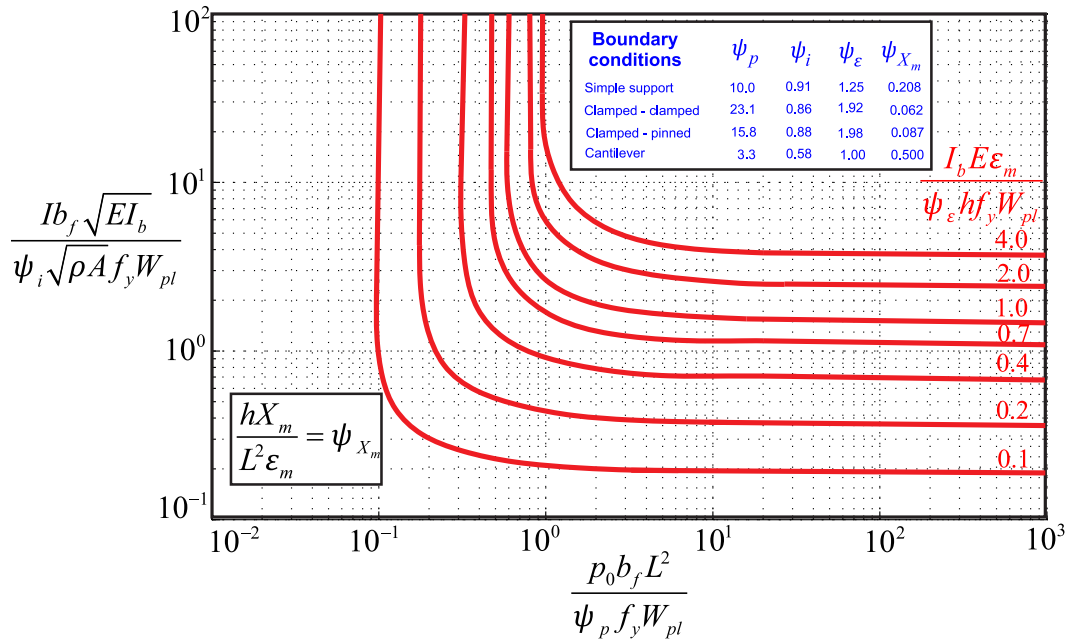
Figure I.19: Elastic-plastic solution for bending of blast loaded beams. p_0 and $I = p_0 t_d / 2$ are the peak applied pressure and specific impulse of the blast loading respectively, L is the length of the beam, b_f and h are the width and the total depth of the beam, ρ is the mass density, A is the cross-sectional area, E is the elastic modulus, f_y is the yield stress, I_b is the second moment of area and W_{pl} is the plastic section modulus of the beam (graph inspired from Ref. [28]).

I.4.2.4 Real and equivalent structural systems

To study the dynamic behaviour of real structures as illustrated in Fig. I.20, a multi-degree-of-freedom (MDOF) model may be required to provide an accurate response of some structures. However, this method is complex, time-consuming and not easy to apply in a common design office. The topic of this subsection is the substitution of the real structure by an equivalent SDOF system characterized by a generalized coordinate. The degree-of-freedom could be the mid-span deflection of a simply supported beam (see Fig. I.20-a) or the lateral deflection of a portal frame (see Fig. I.20-b). The equivalency between the real structure and the equivalent system is usually carried out by equating their energies (strain and kinetic energies, work done by the blast loading) [30, 18] or writing their equations of motion as in this section. In the following, the suffixes r and e respectively mean real and equivalent.
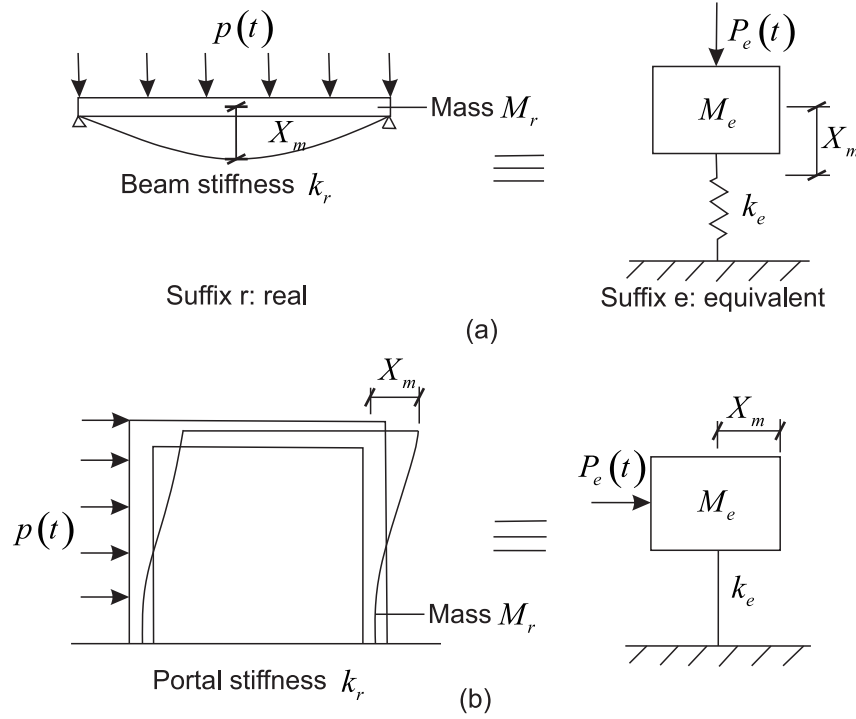
Figure I.20: Real and equivalent structural systems (sketch inspired from Ref. [18]).

In the context of transverse vibration of a beam, writing the equilibrium between inertial, internal and external forces of the beam leads to the following partial differential equation of motion [34]

$$m_b \frac{\partial^2 w(x,t)}{\partial t^2} - \frac{\partial^2 M(x,t)}{\partial x^2} = p(x,t) \tag{I.30}$$

where m_b is the lineic mass of the beam, $w(x,t)$ is the transverse displacement of the beam, $M(x,t)$ is the bending moment distribution of the beam, $p(x,t)$ is the uniformly distributed blast loading, x and t are respectively the abscissa (origin at the left support of the beam) and time variable.

In the elastic regime, the bending moment in the beam is given by

$$M(x,t) = -EI_b \frac{\partial^2 w(x,t)}{\partial x^2} \tag{I.31}$$

where E is the Young modulus and I_b is the inertia of the beam.

For example, let us consider a simply supported beam responding elastically as shown in Fig. I.20-a. After performing modal analysis, the particular solution of Equ. (I.30) in the elastic regime can be written as follows

$$w(x,t) = \sum_{i=1}^{+\infty} q_i(t) \, \phi_i(x) \tag{I.32}$$

where $\phi_i(x) = \sin\frac{i\pi x}{L}$ corresponds to i$^{\text{th}}$ mode of vibration of the beam and q_i is the corresponding generalized displacement.

Multiplying the two members of Equ. (I.30) by $\phi_k(x)$ and integrating it with respect to x along the length of the beam, we obtain

$$\int_0^L \phi_k(x) \left[m_b \frac{\partial^2 w(x,t)}{\partial t^2} + EI_b \frac{\partial^4 w(x,t)}{\partial x^4} \right] dx = \int_0^L \phi_k(x) p(x,t) dx \qquad \text{(I.33)}$$

which can also be re-written as

$$\sum_{i=1}^{+\infty} \underbrace{\left(\int_0^L m_b \phi_k(x) \phi_i(x) dx \right)}_{M_k^* \delta_{ki}} \ddot{q}_i(t) + \sum_{i=1}^{+\infty} \underbrace{\left(\int_0^L EI_b \phi_k(x) \phi_i''''(x) dx \right)}_{k_k^* \delta_{ki}} q_i(t) = \underbrace{\int_0^L \phi_k(x) p(x,t) dx}_{P_k^*(t)}$$

$$\text{(I.34)}$$

by using Equ. (I.32). The symbols " $'$ " and " $\cdot$ " respectively represent differentiation with respect to the abscissa x and time t. The partial differential equation (I.30) has been transformed into decoupled modal equations which read

$$M_k^* \ddot{q}_k(t) + k_k^* q_k(t) = P_k^*(t) \quad \forall k \in \mathbb{N}, \ k \geq 1 \qquad \text{(I.35)}$$

where the generalized mass, stiffness and loading are respectively given by

$$M_k^* = \int_0^L m_b \sin^2 \frac{k\pi x}{L} dx = \frac{m_b L}{2}, \qquad \text{(I.36)}$$

$$k_k^* = \int_0^L EI_b \left(\frac{k\pi}{L} \right)^4 \sin^2 \frac{k\pi x}{L} dx = EI_b \left(\frac{k\pi}{L} \right)^4 \frac{L}{2} \qquad \text{(I.37)}$$

and

$$P_k^*(t) = \frac{L - L\cos\pi k}{\pi k} p(t). \qquad \text{(I.38)}$$

Equation (I.35) represents a multi-degree-of-freedom (MDOF) model where the displacements q_k are the generalized coordinates of the system. The higher the number of modes of vibration conserved in the model is, the more accurate the dynamic response of the beam is. However, we decide to select only the first modal contribution of the dynamic response of the beam under blast loading

$$w(x,t) = X(t) \sin \left(\frac{\pi x}{L} \right) \qquad \text{(I.39)}$$

leading to a SDOF model characterized by the following equation of motion

$$M_e \ddot{X}(t) + k_e X(t) = P_e(t) \qquad \text{(I.40)}$$

where $X(t) (= q_1(t))$ is the mid-span transverse displacement of the beam. The equivalent mass $M_e (= M_1^*)$, stiffness $k_e (= k_1^*)$ and loading $P_e (= P_1^*)$ of the SDOF model can be expressed in terms of real mechanical properties of the beam as follows

$$
\begin{aligned}
M_e &= K_M M_r \\
k_e &= K_S k_r \\
P_e(t) &= K_L P_r(t)
\end{aligned}
\tag{I.41}
$$

where $M_r = m_b L$ is the total mass of the beam, $k_r = 384EI_b/5L^3$ is the stiffness of the beam under a uniformly distributed load and $P_r(t) = p(t)L$ is the resultant of blast loading applied to the beam. The mass factor K_M, stiffness factor K_S and load factor K_L are respectively equal to 0.5, 0.634 and 0.636. Since the stiffness and load factors are very similar, it is commonly assumed that $K_S = K_L$ (see Refs. [4, 18]).

Therefore, the equation of motion of the equivalent SDOF system can be rewritten as

$$
K_M M_r \ddot{X} + K_L k_r X = K_L P_r(t)
\tag{I.42}
$$

or

$$
K_{LM} M_r \ddot{X} + k_r X = P_r(t)
\tag{I.43}
$$

where $K_{LM} = K_M/K_L$ is defined as the load-mass factor and is equal to 0.785 for an elastic simply supported beam under uniformly distributed blast loading.

For the plastic regime, the deformed shape describing the transverse displacement of the beam is selected as a bi-linear function (see Fig. I.21)

$$
w(x,t) = \begin{cases} \left(\frac{2x}{L}\right)X & \text{for } 0 \leq x \leq L/2, \\ 2\left(1 - \frac{x}{L}\right)X & \text{for } L/2 \leq x \leq L, \end{cases}
\tag{I.44}
$$

although more complex shape functions could be used to predict the dynamic behavior of the beam at high frequencies in the plastic regime.

Substituting Equ. (I.44) into Equ. (I.30), integrating it twice with respect to x and satisfying these following conditions on shear force and bending moment at mid-span of the beam

$$
V(L/2, t) = \left.\frac{\partial M(x,t)}{\partial x}\right|_{x=L/2} = 0
\tag{I.45}
$$

and

$$
M(L/2, t) = M_{pl},
\tag{I.46}
$$

lead to the following equation of motion

$$
K_{LM} M_r \ddot{X} + R_m = P_r(t)
\tag{I.47}
$$

where $K_{LM} = 2/3$ is the load-mass factor of the simply supported beam in the plastic regime and $R_m = 8M_{pl}/L$ is the plastic resistance of the beam (M_{pl} is the pure plastic bending resistance of the beam).

   Table I.2 provides the load-mass factors, the stiffnesses and resistances for beams having other boundary conditions than simple supports. The blast loading P_r and the mass M_r are respectively given by pL and $m_b L$ for all the beams. The same procedure can be applied for other loads (e.g. concentrated load at mid-span) and for other structural element (e.g. plate) (see Ref. [4]).
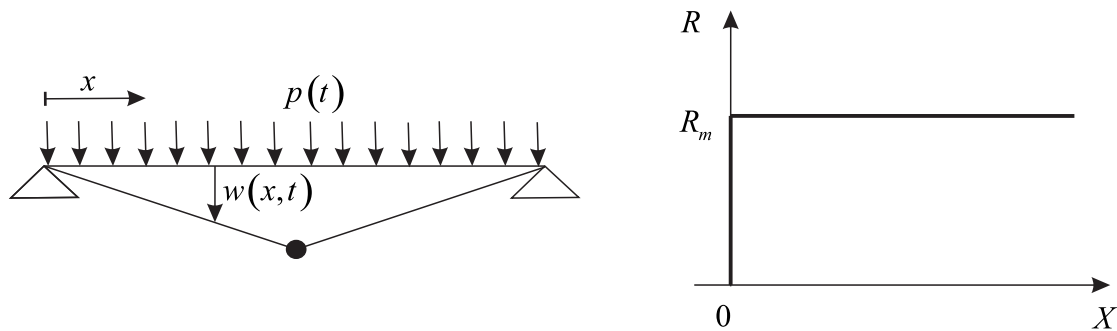
Figure I.21: Simply supported beam with a plastic hinge at mid-span and subjected to a uniformly distributed load (inspired from Ref. [15]).
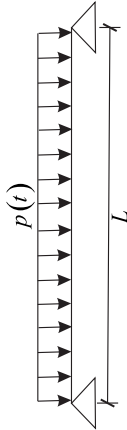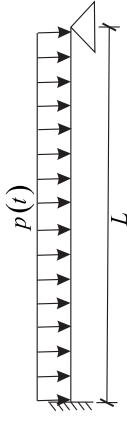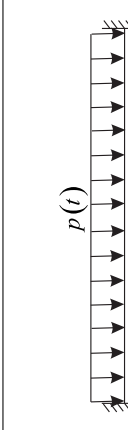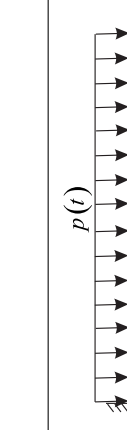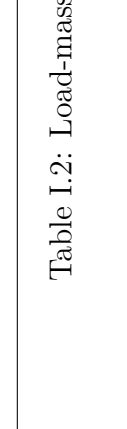
Support conditions and loading diagrams	Range of behaviour	Load-mass factor K_{LM}	Stiffness k_r	Resistance R_m
$p(t)$, L (simply supported)	Elastic	0.78	$\frac{384EI_b}{5L^3}$	0
	Plastic	0.66	0	$\frac{8M_{pl}}{L}$
$p(t)$, L (propped cantilever)	Elastic	0.78	$\frac{185EI_b}{L^3}$	0
	Elastic-plastic	0.78	$\frac{384EI_b}{5L^3}$	$\frac{8M_{pl}}{L}$
	Plastic	0.66	0	$\frac{12M_{pl}}{L}$
$p(t)$, L (fixed both ends)	Elastic	0.77	$\frac{384EI_b}{L^3}$	0
	Elastic-plastic	0.78	$\frac{384EI_b}{5L^3}$	$\frac{12M_{pl}}{L}$
	Plastic	0.66	0	$\frac{16M_{pl}}{L}$
$p(t)$, L (cantilever)	Elastic	0.65	$\frac{8EI_b}{L^3}$	0
	Plastic	0.66	0	$\frac{2M_{pl}}{L}$

Table I.2: Load-mass factors, stiffnesses and resistances for one-way elements (Ref. [18]).

I.4.3 Resistance interaction laws for cross-sections

Under blast loading, cross-sections of the loaded elements can be subjected to a combination of bending, axial and shear loads. The bending moment-axial force-shear force (M-N-V) plastic interaction for I-shaped steel beams (see Fig. II.15-c) reads

$$M_{pl,red} = M_{pl}\beta_v\beta_n \tag{I.48}$$

where $M_{pl} = W_{pl}f_y$ is the pure plastic bending resistance (W_{pl} is the plastic flexural modulus and f_y is the static yield strength). The reduction coefficients β_n and β_v taking into account the influence of axial force N and shear force V on plastic bending resistance are given by

$$\beta_n = \begin{cases} 1 - \gamma_0 \left|\frac{N}{N_{pl}}\right|^2 & \text{for } 0 \leq \left|\frac{N}{N_{pl}}\right| \leq \frac{A_w}{A}, \\ 1 - \gamma_1 - \gamma_2 \left|\frac{N}{N_{pl}}\right| - \gamma_3 \left|\frac{N}{N_{pl}}\right|^2 & \text{for } \frac{A_w}{A} \leq \left|\frac{N}{N_{pl}}\right| \leq 1, \end{cases} \tag{I.49}$$

and

$$\beta_v = \begin{cases} 1 & \text{for } 0 \leq \left|\frac{V}{V_{pl}}\right| \leq \frac{1}{2}, \\ 1 - \left(2\left|\frac{V}{V_{pl}}\right| - 1\right)^2 \frac{A_w^2}{4t_w W_{pl}} & \text{for } \frac{1}{2} \leq \left|\frac{V}{V_{pl}}\right| \leq 1, \end{cases} \tag{I.50}$$

where $N_{pl} = Af_y$ and $V_{pl} = A_v f_y/\sqrt{3}$ are respectively the plastic axial and shear resistances, $A_w = h_w t_w$, A and A_v are respectively the web area, the total area and the shear area of the cross-section.

The coefficients γ_0, γ_1, γ_2 and γ_3 depend on the geometric properties of the cross-section and are given as follows

$$\begin{aligned} \gamma_0 &= \frac{1}{2\left(\frac{h-t_f}{h-2t_f}\right)\left(1 - \frac{A_w}{A}\right)\frac{A_w}{A} + \left(\frac{A_w}{A}\right)^2}, \\ \gamma_1 &= \frac{A_w}{4W_{pl}}\left(\frac{A_w}{b_f} - h_w\right), \\ \gamma_2 &= \frac{h_w A}{2W_{pl}}\left(1 - \frac{t_w}{b_f}\right), \\ \gamma_3 &= \frac{A^2}{4b_f W_{pl}}, \end{aligned} \tag{I.51}$$

where h, b_f, t_f, h_w and t_w are respectively the depth of the cross-section, the width and thickness of the flanges, the depth and thickness of the web (see Fig. I.22-a).

The M-N plastic interaction law (I.49) was developed by Lescouarch' [35] and is valid only if the fillets are neglected while the M-V plastic interaction law (I.50) is available in Eurocode 3, Part 1-1 [36]. The ratio of the web to the cross-section areas A_w/A in Equ. (I.49) corresponds to the value of the non-dimensional axial force at which the plastic neutral axis moves from the web to the flange. For a rectangular cross-section, the ratio A_w/A and the coefficient γ_0 are equal to 1.

The M-N-V plastic interaction surface for an IPE 270 steel profile is illustrated in Fig. I.22-b, and shows that the plastic bending moment resistance decreases when the axial force or the shear force increases. The plastic bending moment resistance is equal to 0 when the axial force is equal to the axial plastic resistance, and is subjected to a reduction of 23 % when the shear force equals the associated plastic resistance, irrespective of the value of the axial force.

(a)   (b)
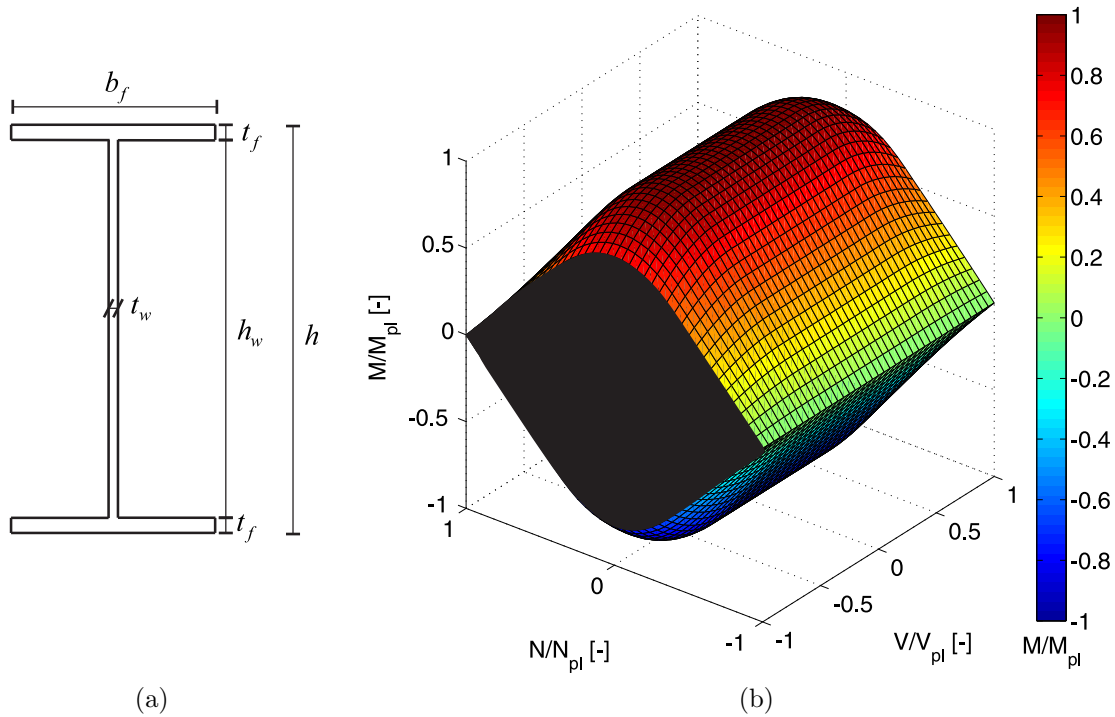
Figure I.22: (a) Geometrical properties of an I-shaped profile. (b) Bending moment-axial and shear force plastic interaction (for an IPE 270 steel profile).

I.4.4   Blast resistant design

The main objective of blast resistant design of structural elements consists of allowing them to deform significantly in order to dissipate blast-related energy by forming plastic hinges. The ductility demand of the structure is then compared to a maximum level of damage, based on several blast test programs available in the literature, which does not necessary correspond to real capacity of deformation of the studied structural element. The deformation criteria is generally based on flexural plastic deformation and assumes that any shear failure or local instability are prevented. Concerning the design resistance of the structural elements, it should be based on the ultimate state [18].

I.4.4.1 Design strengths

Strain-rate-sensitive behaviour of materials (widely inspired from Ref. [37])

The yield criteria defined in Section I.4.3 are assumed to be independent of the strain rate $\dot{\epsilon}$ which may develop in the element material under blast loading. However, the plastic flow of some materials is sensitive to strain rate as illustrated in Fig. I.23-a which shows the stress (σ) - strain (ϵ) curves for mild steel specimens that are tested at various uni-axial compressive strain rates [38]. The effect of strain rate on strength is positive since the yield and ultimate strengths of material increase with the strain rate although the associated fracture strain decreases with increase in strain rate [39], meaning that the material becomes more brittle at higher strain rates. Young's modulus remains insensitive to the strain rate.

Cowper and Symonds [40] suggested the following constitutive equation to take into account the effect of strain rate

$$\frac{f_{dy}}{f_y} = 1 + \left(\frac{\dot{\epsilon}}{D}\right)^{1/q} \tag{I.52}$$

where f_{dy} is the dynamic flow stress at a uni-axial plastic strain rate $\dot{\epsilon}$, f_y is the associated static flow stress and D and q are constants for a particular material. These last parameters are respectively equal to $40.4\,\mathrm{s^{-1}}$ and 5 for mild steel [41], meaning that the yield strength is doubled when the strain rate is equal to $40.4\,\mathrm{s^{-1}}$.

Under bending moment, the stresses and strains varies over the depth of a cross-section leading to a non-constant strain rate profile. Aspden and Campbell [42] illustrate the effect of angle rates on bending moment in Fig. I.23-b. Based on Cowper-Symonds constitute equation (I.52) and assuming that the plane cross-sections remain plane, the dynamic plastic bending resistance $M_{pl,d}$ can be predicted by the following relationship

$$\frac{M_{pl,d}}{M_{pl}} = 1 + \frac{2q}{2q+1}\left(\frac{h\dot{\theta}}{2DL}\right)^{1/q} \tag{I.53}$$

where M_{pl} is the plastic bending moment of rectangular section, h is the depth of cross-section, $\dot{\theta}$ is the angular change across a beam of length L subjected to a pure bending moment $M_{pl,d}$ [37].

Effect of strain rate on local instability of steel elements

A compact cross-section should not be affected to any local buckling of flanges or web during the yield redistribution of the cross-section to reach the plastic bending resistance. However, the increase of yield strength due to high strain rate generated by the blast loading may affect the section classification, involving that the member could experience a local buckling before achieving the plastic bending resistance or being subjected to a global instability as observed in [43, 44, 45].
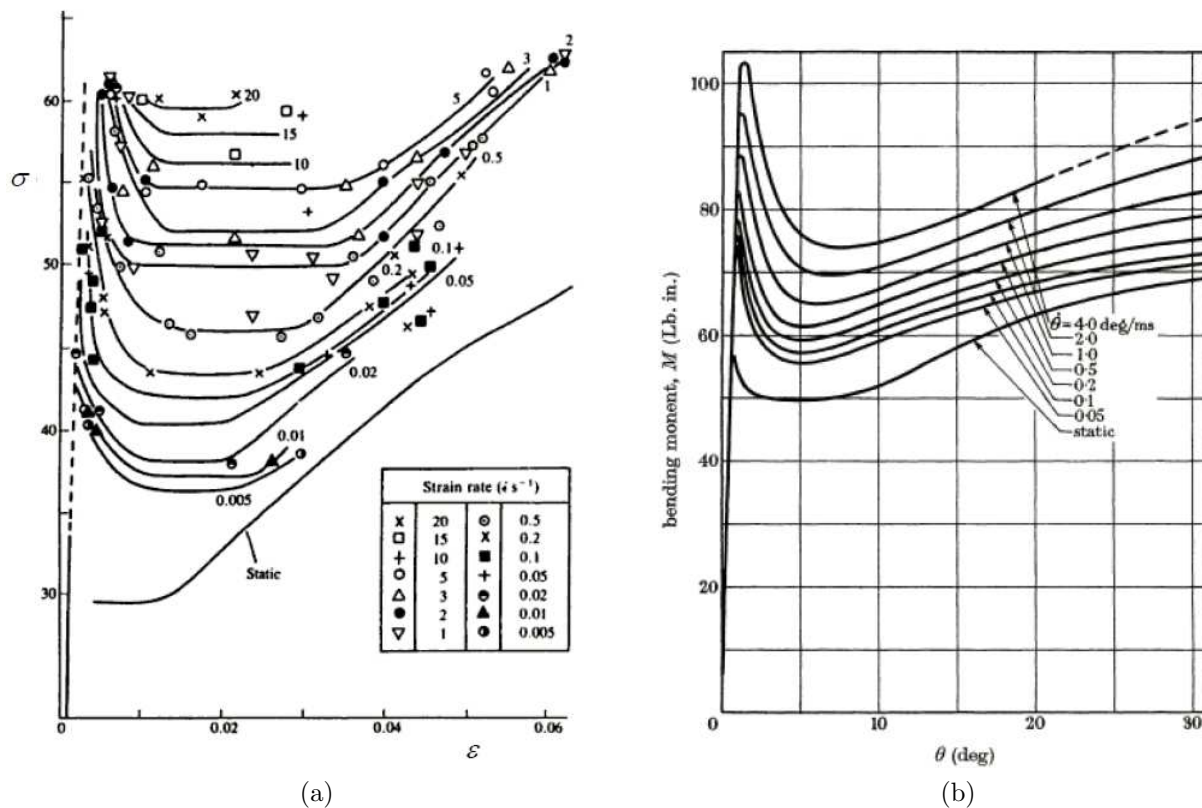
Figure I.23: (a) Stress σ-strain ϵ curves for mild steel at various uni-axial compressive strain rates according to Marsh and Campbell [38]. 1 unit of ordinate is 10^3 lbf/in^2 or 6.895 MN/m^2. (b) Dynamic bending moment-rotation curves for various values of rotation rate $\dot{\theta}$ for mild steel [42]. 1 unit of ordinate is 1 lbf or 0.113 N.m.

UFC design guide

The dynamic increase factor (DIF) is defined as the ratio of the dynamic stress to the static stress taking into account the strain rate effect. Typical values of DIF for given structural steel and reinforced concrete are respectively given in Tables I.3-a and -b (from Ref. [4]), assuming given strain rates. However, the DIF value is based on averaged strain rate value over the cross-section while the strain rate is time-dependent and varies over the depth of cross-section and along the beam. The DIF values are also independent of the blast scenario, and could therefore be unconservative in some cases.

To ensure that the steel structural members will develop the full plastic resistance and reach the ductility demand at plastic hinges locations, the flanges and web of the cross-section should respect minimum thickness requirements to prevent a local buckling failure. UFC design guide has adopted the design requirements of the American Institute of Steel Construction (AISC) specification [46]. Table I.4 and Equ. (I.54) respectively provide the slenderness limits for flange under compression and web under combined bending moment and compression

$$\frac{d}{t_w} \leq \begin{cases} \frac{412}{f_y}\left[1 - 1.4\left|\frac{P}{N_{pl}}\right|\right] & \text{for } \left|\frac{P}{N_{pl}}\right| \leq 0.27, \\ \frac{257}{f_y} & \text{for } \left|\frac{P}{N_{pl}}\right| > 0.27, \end{cases} \tag{I.54}$$

where P is the applied compressive load and d and t_w are respectively the depth and the thickness of the web.

Although these recommendations are established for members subjected to static loading, they remain applicable and even conservative for dynamic loading of short duration due to the positive effect of lateral inertial forces of these members on local buckling which is neglected in this section classification [4].

In this thesis, the strain-rate effects will be neglected. The implementation of these effects in the developed models constitutes a perspective of the present thesis.

Material	Bending		Tension or compression		
	Low Pressure ($\dot{\epsilon} = 0.1\,\text{s}^{-1}$)	High Pressure ($\dot{\epsilon} = 0.3\,\text{s}^{-1}$)	Low Pressure ($\dot{\epsilon} = 0.02\,\text{s}^{-1}$)	High Pressure ($\dot{\epsilon} = 0.05\,\text{s}^{-1}$)	
	f_{dy}/f_y				f_{du}/f_u
A36	1.29	1.36	1.19	1.24	1.10
A588	1.19	1.24	1.12	1.15	1.05
A514	1.09	1.12	1.05	1.07	1.07

(a)

Type of stress	Far design range			Close-in design range		
	Reinforcing bars		Concrete	Reinforcing bars		Concrete
	f_{dy}/f_y	f_{du}/f_u	f_{dcu}/f_{cu}	f_{dy}/f_y	f_{du}/f_u	f_{dcu}/f_{cu}
Bending	1.17	1.05	1.19	1.23	1.05	1.25
Direct shear	1.10	1.00	1.10	1.10	1.00	1.10
Compression	1.10	−	1.12	1.13	−	1.16

(b)

Table I.3: Dynamic increase factors (DIF) for design of (a) structural steel and (b) reinforced concrete elements. f_y and f_u are respectively the yield stress and ultimate tensile strength of structural steel or steel reinforcement bars and f_{cu} is the compressive strength of concrete. The subscript $'d'$ denotes the dynamic properties of material (from Ref. [4]).

f_y [ksi]	36	42	45	50	55	60	65
$b_f/2t_f$ [−]	8.5	8.0	7.4	7.0	6.6	6.3	6.0

Table I.4: Slenderness limits for flange under compression where f_y is the static yield strength in ksi, b_f and t_f are the width and thickness of the flanges (from [4]).

I.4.4.2 Design loads

The blast loading has a low probability of occurrence and thus, it is appropriate to set the corresponding partial safety factor to 1. Dead loads, storage and other permanent loads should be assigned a partial safety factor equal to unity while the variable loads are likely to be a small portion of their design loads when acting simultaneously with blast loading, involving a partial safety factor of 0.3 (for residential and office areas), as recommended in Eurocode 1 Part 1-1 [47].

UFC design guide does not provide any information about safety factors for the combinations of loads when the structure is subjected to blast loading. However, the AISC specification mention that the safety factors for dead and live loads are respectively equal to 0.9 (or 1.2) and 0.5 for structures under accidental fire.

The other loads than blast loading can induce a reduction of the effective resistance of the structural elements but their associated masses may play a positive role in the dynamic behaviour of the structure as a result of their inertia effects [18]. In this thesis, only masses due to permanent loads are considered in the analysis of structures under blast loading but the methodology remains unchanged if the effect of additional static loads are considered.

I.4.4.3 Deformation limits/capacity

The controlling criterion in the blast resistant design of structural elements is normally based on the deformation or the deflection of the element. There are two ways to assess the level of damage, firstly by computing the support rotation θ or secondly, by determining the demand of ductility of the structural element $\mu = X_m/X_y$ (see Fig. I.24).

Two categories of protection are considered in the UFC design guide [4]. The first category of protection corresponds to the protection of staff and equipment from blast waves, to shield them from fragments and falling parts of the structure. The second level of protection consists in avoiding the collapse of the structural element subjected to blast loading. Table I.5 provides the maximum level of damage permitted for beams. For frame structures, the maximum member end rotation and the maximum side-sway deflection are respectively limited to 2° and 1/25 of the storey height (see Fig. I.24).

| | Protection category | | | |
| | 1 | | 2 | |
	θ	μ	θ	μ
RC beams and slabs	2° $\simeq$ 35 mrad	/	4° $\simeq$ 70 mrad	/
Steel beams and plates	2° $\simeq$ 35 mrad	10	12° $\simeq$ 210 mrad	20

Table I.5: Maximum values of ductility μ and rotation θ for steel and concrete structural elements according to two levels of protection defined by the UFC design guide (from Ref. [4]).

The document "Design of blast resistant buildings in petrochemical facilities" published by the American society of civil engineers (ASCE) [48] considers three levels of damage of structural elements subjected to blast loading :

○ High level of damage: the component has not failed but it has significant permanent deflections, causing it to be unrepairable.

○ Medium level of damage: the component has some permanent deflection. It is generally repairable, if necessary, although replacement may be more economical and aesthetic.

○ Low level of damage: the component has none to slight visible permanent damage.

Table I.6 provides response criteria in terms of maximum ductility ratio and/or support rotation for each response level. Response critera are defined for different components (beams, slabs, walls, masonry...) and are different for primary and secondary structural elements. Primary structural elements are members which would affect a number of other components supported by this member and as a result, affect the stability of the building in the area of loss. Secondary members are the components supported by these primary structural elements. For members under compression, the compressive axial load becomes significant when it is greater than 20 % of the dynamic axial capacity of the member.

It should be noted that for moment resisting structural steel frames, the maximum side-sway deflection is respectively limited to 1/50, 1/35 and 1/25 of the height of a storey for low, medium and high response criteria.
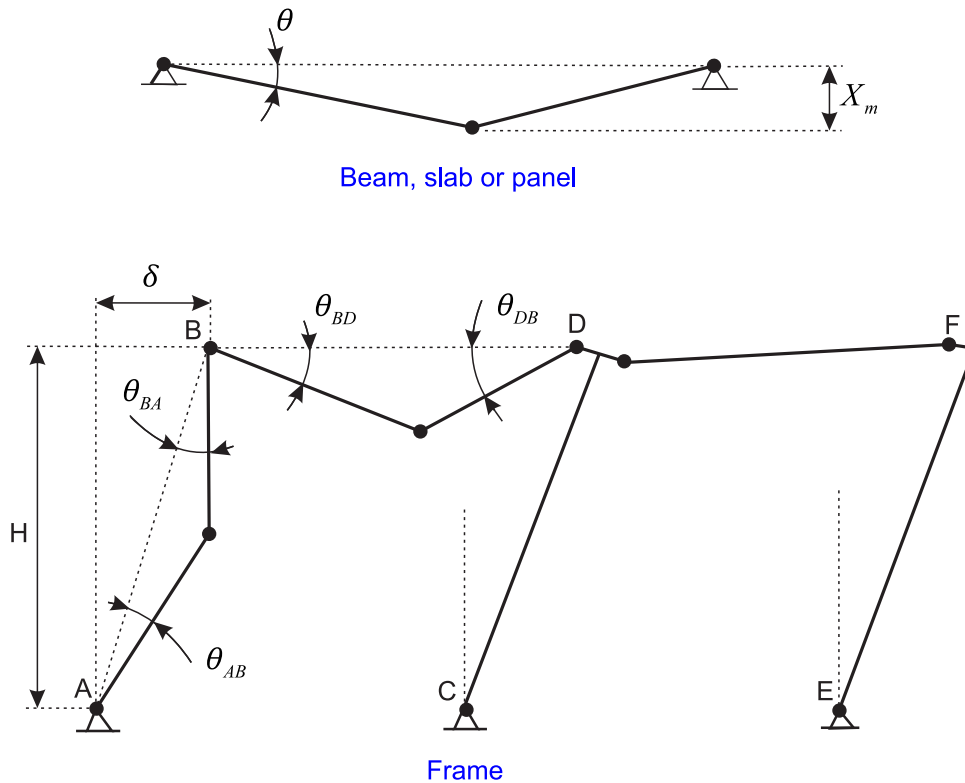
Figure I.24: Member end rotations for beams and frames (from Ref. [4]).

	Level of damage					
	Low		**Medium**		**High**	
	θ	μ	θ	μ	θ	μ
Hot-rolled steel compact secondary members (beams, girts, purlins)	2°	3	6°	10	12°	20
Steel primary frame members (with significant compression)	1°	1.5	1.5°	2	2°	3
Steel primary frame members (without significant compression)	1°	1.5	2°	3	4°	6
RC beams, slabs and wall panels (no shear reinforcement)	1°	/	2°	/	5°	/
RC walls, slabs and columns (in flexure and axial compression load)	1°	/	2°	/	2°	/

Table I.6: Response criteria for steel and reinforced concrete components (from Ref. [48]).

I.4.5   Condensation techniques

The objective of condensation techniques is to reduce the number of degrees-of-freedom of the original model by retaining only a limited set of degrees-of-freedom while maintaining as much as possible the dynamic characteristics of the structure. The equation of motion of the indirectly affected part of the structure which is assumed to remain elastic linear is given by

$$\mathbf{M}\ddot{\mathbf{X}} + \mathbf{K}\mathbf{X} = \mathbf{F} \tag{I.55}$$

where $\mathbf{K} = \begin{bmatrix} \mathbf{K}_{SR} & \mathbf{K}_{SR} \\ \mathbf{K}_{RS} & \mathbf{K}_{RR} \end{bmatrix}$, $\mathbf{M} = \begin{bmatrix} \mathbf{M}_{SR} & \mathbf{M}_{SR} \\ \mathbf{M}_{RS} & \mathbf{M}_{RR} \end{bmatrix}$, $\mathbf{X} = \begin{bmatrix} \mathbf{X}_S \\ \mathbf{X}_R \end{bmatrix}$ and $\mathbf{F} = \begin{bmatrix} \mathbf{F}_S \\ \mathbf{F}_R \end{bmatrix}$ are respectively the stiffness and the mass matrices, the degrees-of-freedom of the indirectly affected part (IAP) of the structure and the external loads applied to the IAP of the structure. The vector $\mathbf{X}_S$ collects all the degrees-of-freedom at the interface between the blast-loaded compartment and the IAP of the structure

$$\mathbf{X}_S = \begin{bmatrix} X_{1h} & X_{1v} & X_{1\theta} & X_{2h} & X_{2v} & X_{2\theta} \end{bmatrix}^T \tag{I.56}$$

as illustrated in Fig. I.25-a and $\mathbf{X}_R$ contains all other degrees-of-freedom that should be condensed.

Assuming that no dynamic loads is applied to the IAP of the structure (except for the reactions of the blast-loaded compartment) implies that

$$\mathbf{F}_R = \mathbf{0}. \tag{I.57}$$

We may apply the model reduction technique in order to downsize the dynamical system to a limited set of degrees-of-freedom $\mathbf{X}_S$. These techniques assume that the degrees-of-freedom of IAP of the structure $\mathbf{X}$ are expressed as an affine transformation of the master degrees-of-freedom $\mathbf{X}_S$,

$$\mathbf{X} = \mathbf{T}^{\star}\mathbf{X}_S, \tag{I.58}$$

where $\mathbf{T}^{\star}$ is a transformation matrix, selected in accordance with the type of model reduction. After reduction, the governing equation reads

$$\mathbf{M}^{\star}\ddot{\mathbf{X}}_S + \mathbf{K}^{\star}\mathbf{X}_S = \mathbf{F}^{\star} \tag{I.59}$$

where $\mathbf{M}^{\star} = \mathbf{T}^{\star T}\mathbf{M}\mathbf{T}^{\star}$, $\mathbf{K}^{\star} = \mathbf{T}^{\star T}\mathbf{K}\mathbf{T}^{\star}$ and $\mathbf{F}^{\star} = \mathbf{T}^{\star T}\mathbf{F}$ are the mass and stiffness matrices and the blast loading vector of the reduced model of the IAP of the structure. The assumption made in Equ. (I.58) seems to be strong as it expresses all degrees-of-freedom as a combination of six degrees-of-freedom $\mathbf{X}_S$. Model reduction techniques may however preserve an accurate quasi-static response (Guyan) or oscillatory response resulting from one or several modes of vibration of the structure, as seen below with four different examples of reduction.

First, a classical procedure to reduce a finite element model is the Guyan (or static) condensation [49], which is formally only valid in case of linear elastic systems. Nothing however prevents its use in a nonlinear setting. The set of equations (I.55), disregarding inertial terms, is described by

$$\mathbf{K}\left[\begin{array}{c} \mathbf{X}_S \\ \mathbf{X}_R \end{array}\right] = \left[\begin{array}{c} \mathbf{F}_S \\ \mathbf{0} \end{array}\right] \tag{I.60}$$

where the degrees-of-freedom to be condensed can be expressed as follows

$$\mathbf{X}_R = -\mathbf{K}_{RR}^{-1}\mathbf{K}_{RS}\mathbf{X}_S \tag{I.61}$$

and the Guyan transformation is finally given by

$$\mathbf{T}_G^{\star} = \left[\begin{array}{c} \mathbf{I} \\ -\mathbf{K}_{RR}^{-1}\mathbf{K}_{RS} \end{array}\right] \tag{I.62}$$

where $\mathbf{I}$ is the identity matrix.

Second, the Improved Reduced System (IRS) reduction process adjusts the Guyan condensation by adding some corrective terms in order to better represent the mass associated with the discarded degrees-of-freedom [50]. The IRS transformation is given by

$$\mathbf{T}_{IRS}^{\star} = \mathbf{T}_G^{\star} + \mathbf{S}\mathbf{M}\mathbf{T}_G^{\star}\mathbf{M}_G^{\star -1}\mathbf{K}_G^{\star} \tag{I.63}$$

where $\mathbf{M} = \left[\begin{array}{cc} \mathbf{M}_{SS} & \mathbf{M}_{SR} \\ \mathbf{M}_{RS} & \mathbf{M}_{RR} \end{array}\right]$, $\mathbf{S} = \left[\begin{array}{cc} 0 & 0 \\ 0 & \mathbf{K}_{RR}^{-1} \end{array}\right]$, $\mathbf{M}_G^{\star} = \mathbf{T}_G^{\star T}\mathbf{M}\mathbf{T}_G^{\star}$ and $\mathbf{K}_G^{\star} = \mathbf{T}_G^{\star T}\mathbf{K}\mathbf{T}_G^{\star}$ are the reduced mass and stiffness resulting from the Guyan condensation. This process is known to improve the accuracy of the results obtained with the Guyan condensation for higher modes of the system.

Third, if the global model vibrates mainly according to one mode shape, a dynamic condensation selecting that mode shape as a basis for the transformation matrix $\mathbf{T}^{\star}$ is more appropriate as it conserves one eigen mode and eigenvalue of the original model [51]. For the

simple degree-of-freedom condensation under consideration here, the transformation matrix is readily obtained as

$$\mathbf{T}_D^\star = \left[\begin{array}{c} \mathbf{I} \\ \left(- \left(\mathbf{K}_{RR} - \omega^2 \mathbf{M}_{RR} \right)^{-1} \left(\mathbf{K}_{RS} - \omega^2 \mathbf{M}_{RS} \right) \right) \end{array} \right] \qquad (I.64)$$

where ω represents the natural frequency of the eigen mode of interest.

The System Equivalent Reduction Expansion Process (SEREP) [52] is a fourth method that preserves several natural frequencies of the global model. The response of the IAP of the structure $\mathbf{X}$ can be expressed as a combination of six modes of vibration amplified by generalized displacements as follows

$$\mathbf{X} = \Phi \mathbf{q} = \left[\begin{array}{c} \mathbf{\Phi}_S \\ \mathbf{\Phi}_R \end{array} \right] \mathbf{q} \qquad (I.65)$$

where Φ is a matrix that contains six modes of vibration and $\mathbf{q}$ is the corresponding vector of generalized displacements. Six modes of vibration are selected as the most representative to predict the dynamic behavior of the IAP of the structure subjected to dynamic reactions of the blast-loaded compartment as illustrated in Fig. I.25-b.

It can be shown that the transformation matrix $\mathbf{T}_{SEREP}^\star$ is given by

$$\mathbf{T}_{SEREP}^\star = \Phi \left(\mathbf{\Phi}_S^T \mathbf{\Phi}_S \right)^{-1} \mathbf{\Phi}_S^T. \qquad (I.66)$$

The natural frequencies and corresponding modes of vibration of the reduced system are identical to those of the global model and do not depend on the location nor the number of points preserved in the reduced model.
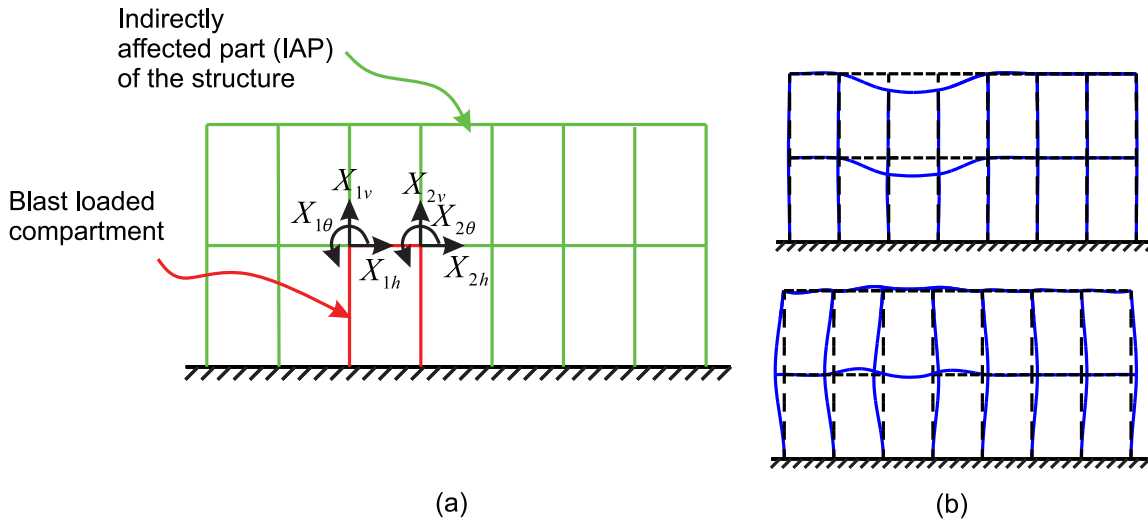
Figure I.25: (a) Degrees-of-freedom at the interfaces between the blast-loaded compartment and the indirectly affected part of the structure; (b) Sketch of two modes of vibration of the structure.

I.5   Conclusions

The purpose of this thesis is firstly described in Section I.2 and consists in studying the dynamic behavior of structures under internal blast loading although the analytical models developed in this thesis are also valid for moment resisting frames subjected to external blast loading.

In Section I.4.1, the blast loading is shown to be complex to assess since it depends on the nature of the explosive charge, its weight, its distance from the target structure, the geometry of the building facades, the angle of incidence of the shock front with respect to the structure, the level of confinement of the explosion (e.g. amount of frangible components)...but a practical procedure to compute shock overpressures and gas pressure due to a detonation occurring inside the compartment of a structure is described in detail.

Concerning the structural response to blast loading, a MDOF model may be required to provide an accurate response of some structures but is complex, time-consuming and not easy to apply in a common design office. Therefore, the substitution of the real structure by an equivalent SDOF system characterized by a generalized coordinate is carried out in Section I.4.2 by projecting the equation of motion in a given deformed shape of the structure. Then, the pressure-impulse diagram for elastic-perfectly plastic SDOF structure is defined and described, this diagram allowing assessing the ductility demand of the structure according to the pressure and impulse to it. The ductility is obviously a key element when assessing the vulnerability of a structure to blast loading as the ductility is strongly influencing the capacity of the structure to dissipate the energy injected by the blast action (Section I.4.4).

Under blast loading, the plastic bending resistance of cross-sections of the loaded elements can be reduced due to the presence of axial and shear forces as reminded in Section I.4.3 and may be affected by the strain rate effects. With the present work, the yield criterion is assumed to be independent of the strain rate which may develop in the element material under blast loading. Knowing that, the strain rate is shown to have a positive effect on yield and ultimate strengths of material although the material becomes more brittle at higher strain rates.

Finally, several techniques of condensation are described in Section I.4.5. The Guyan (static) condensation is accurate for the assessment of the stiffness of the IAP of the structure but the inertia forces are not preserved. The IRS reduction process adjusts the Guyan condensation by adding some corrective terms for higher modes of the system. The dynamic condensation enables to preserve only one natural frequency of the global model of the structure whereas the SEREP maintains the dynamic properties of the entire structure by saving several natural frequencies of the IAP of the structure.

At the end of this Chapter, it is possible to list the main assumptions on which the thesis developments will be founded

○ The blast pressure is supposed to be uniformly distributed along each structural member although actually, it depends on the distance from the explosion centre;

○ All the analytical models that are developed in this thesis are applicable for deflagration

or detonation though they have been only formalized for the detonation inside a structure without taking into account the level of confinement provided by the structure;

○ The out-of-plane instabilities of the structural elements are supposed to be prevented as well as local buckling;

○ The effects of the strain rate and shear force on the plastic interaction curve is neglected in the developments;

○ The indirectly affected part (IAP) of the structure (i.e. the part of the structure surrounding the loaded compartment) is assumed to remain in the elastic regime;

○ In Section II.2.3.2, the Guyan (static) condensation technique is shown to be more convenient for the extraction of the beam under blast loading. However, in general practice, the SEREP is more appropriate to be used for the extraction of the whole compartment from the structure since it allows to preserve several natural frequencies of the global model of the entire structure.

Chapter II

Analysis of a non-linear frame beam

II.1 State-of-the-art on beams under blast loading

The pressure-impulse (p-I) diagram is commonly used to design elements or structures for a given blast loading as mentioned in Section I.4.2.3. It consists of contour sets of damage for structural elements [30, 18, 28]. The damage index could be the required ductility for beams or slabs in bending [4], the ratio of the residual to the design axial resistances for columns [53] or the ultimate rotation for joints [54]. This chapter focuses on the determination of the required ductility of frame beams subjected to a blast loading considering the effects of lateral inertia and elastic restraint offered by the IAP of the structure through the development of p-I diagrams.

The pulse shape of the loading influences the dynamic response of structural elements. Younghdal [55] proposed to eliminate this effect by using the correlation parameters and his approach was validated theoretically in Ref. [56]. A unique effective pressure-impulse diagram independent of the pulse loading shape was established empirically, depending on Younghdal's correlation parameters [57]. This procedure was extended to elastic-perfectly plastic single degree of freedom (SDOF) systems in Ref. [58] and recently to continuous beams with semi-rigid support conditions [59]. Recent works on simply-supported circular plates subjected to localized blast loading also incorporate the spatial pulse shape effect [60, 61] whereas the analytical models deal with only distal charges, considering a spatially uniformly distributed blast loading. Moreover, the pulse shape of the blast loading is assumed to be triangular, neglecting any re-reflections of the shock waves inside the compartment as well as the build-up of quasi-static pressure due to gas expansion. However, the analytical developments remain valid for other pulse shapes.

Concerning the structural response, the conversion of a continuous beam to an equivalent single degree of freedom (SDOF) system is a common practice in order to assess the required ductility of the beam and develop its corresponding p-I diagram as described in Section I.4.2.4. The mass, the stiffness and the applied load are multiplied by some lumping factors, usually assuming a bending behavior of the beam [30, 18, 28, 4]. However, the effects of shear and membrane forces can be significant in some cases [37, 62, 63, 64, 65, 66].

R. Vaziri *et al.* [67] and N. Jones [37] looked into the development of the membrane force and the M-N interaction for a simply supported or fixed beam. In Refs. [68, 69, 70], an analytical model of a beam subjected to blast loading is proposed, dealing with semi-rigid connections and including the development of the membrane force. Langdon and Schleyer [70] compared the response of that model with the experimental results of the post-critical response of a corrugated steel wall panel subjected to blast loading with welded double angle connections at its ends. In Ref. [71], they incorporate the effect of the composite patch which strengthens the blast wall in its center.

Fallah and Louca [72] derived a p-I diagram for equivalent softening and hardening SDOF models substituting the structural behavior of the corrugated steel wall by an equivalent bilinear resistance-displacement curve. They also propose analytical equations of the asymptotes expressed as a function of the so-called hardening/softening index. Dragos and Wu [73] have recently proposed a full analytical procedure based on an empirical approach to derive the

p-I diagram of a bilinear SDOF model.

The specificity of the analytical models developed in this Chapter is to consider the effect of the elastic IAP of the structure on the dynamic behaviour of the frame beam under blast loading. The models also include the effect of nonlinear membrane actions and the bending moment-axial (M-N) plastic resistance interaction curve of the beam. The material law of the beam is assumed to be elastic-perfectly plastic, it does not include the strain rate nor hardening effects. The position of plastic hinges are assumed to be fixed and the shear failure is not considered. The beam-to-column joints are perfectly rigid; the elements connected to the ends of the beam are supposed to be rigid enough, so that their elastic rotation is negligible in comparison with the maximum plastic rotation of the beam ends.

Two analytical models are developed in this chapter, both analytical models include as a degree-of-freedom (DOF) the transverse mid-span deflection but they differ from each other with respect to the consideration of the axial elongation of the beam. In Section II.2, the axial elongation of the beam is neglected resulting in a SDOF model while in Section II.3, both DOFs are kept. This 2-DOF model is validated through comparisons with results predicted by the finite element software FinelG developed by the University of Liège in Section II.4. The conclusions of the Chapter are drawn in Section II.5 and the perspectives to improve the analytical model are detailed in Section II.6.

II.2 Single-degree-of-freedom model

The kinematics of the proposed model is first introduced in Section II.2.1.1. The reduction techniques to extract a beam from a whole structure are described in Section II.2.1.2. In Section II.2.1.3, the structural behavior of the beam with lateral mass and elastic spring is analyzed. Energy conservation consideration are invoked in Section II.2.1.4 to derive the nonlinear governing equation of motion of the substructure, which is presented in Section II.2.1.5. A scaling of the equation of motion is carried out in Section II.2.1.6. The dimensionless parameters are listed, described and their practical range is provided for steel structures. In Section II.2.2, an inexpensive iterative analytical scheme is derived for the expressions of the p-I diagram asymptotes. Some numerical simulations of frame beams subjected to a given blast loading are presented in Section II.2.3; a comparison between the reduced and global models is realized and the graphical results are discussed. A dimensionless parametric study according to four structural variables is also performed in Section II.2.4 followed by a conclusion. The results of this extensive analysis provide the necessary information to make this model a ideal tool for rapid and simple conceptual design. The content of this Section II.2 was published in the literature [74].

II.2.1   Problem formulation

II.2.1.1   Description of the problem

The considered problem consists in the establishment of the structural dynamic response of a beam under a uniformly distributed blast loading $p(x,t)$, see Figure II.1. The beam has a length 2ℓ and is characterized by a lineic mass m_s and an equivalent elastic bending stiffness k_s assumed to result from a first-order model. Specific to this problem is the lateral restraint $K^\star$ and the mass $M^\star$ that materialize respectively a horizontal restraint and a participating mass; they model the passive interaction of this beam with the indirectly affected part (IAP) of the structure and result from a dynamic condensation as stated in the next paragraph II.2.1.2. The loading is assumed to develop synchronously along the beam and is idealized as a triangular pulse, see Fig. II.1-b, so that

$$p(x,t) = p_o \left(1 - \frac{t}{t_d} \right) \quad \text{for } 0 \le t \le t_d \tag{II.1}$$

where t represents the time variable, p_o is the peak blast pressure and t_d is the positive phase duration. The impulse I associated with this pressure field is thus given by

$$I = \frac{p_o t_d}{2}. \tag{II.2}$$

Consistently with common practice in impact engineering, the loading is parametrized by (p_o, I) in the sequel, rather than (p_o, t_d). The maximum response of the beam under this parametric blast loading is then represented in a (p_o, I) diagram for various blast durations and intensities.

Although the initial configuration is asymmetric because of the lateral restraint and the additional mass, the beam is assumed to deform symmetrically, transversely. This is motivated by the rapid development of three plastic hinges, as illustrated in Fig.II.1-a, in the configurations of typical practical interest, *i.e.* where the required ductility is around 20. It is further assumed that the central hinge does not travel. Also, mainly first floor beams, where membrane forces develop in one floor only are considered. The material law is elastic-perfectly plastic but, in order to simplify the kinematics, the deflection in the elastic regime is neglected so that the deformed configuration of the beam, after plasticity has installed, consists of two straight elastic portions connected by a plastic hinge. Two additional plastic hinges also develop at the end supports of the beam. The kinematics are thus fully described by the mid-span displacement X or equivalently by the rotation $\theta = X/\ell$ of each portion of the beam, which makes this model a single degree-of-freedom system.

The presence of the lateral restraint and mass generates membrane (axial) forces in the beam. They are captured in the model thanks to a second-order large displacement/small rotation model, writing the equilibrium equations in the deformed configuration but yet assuming moderate rotations, i.e. keeping second order terms as

$$\sin\theta \simeq \tan\theta \simeq \theta = \frac{X}{\ell} \quad ; \quad \cos\theta \simeq 1 - \frac{\theta^2}{2} = 1 - \frac{X^2}{2\ell^2} \tag{II.3}$$
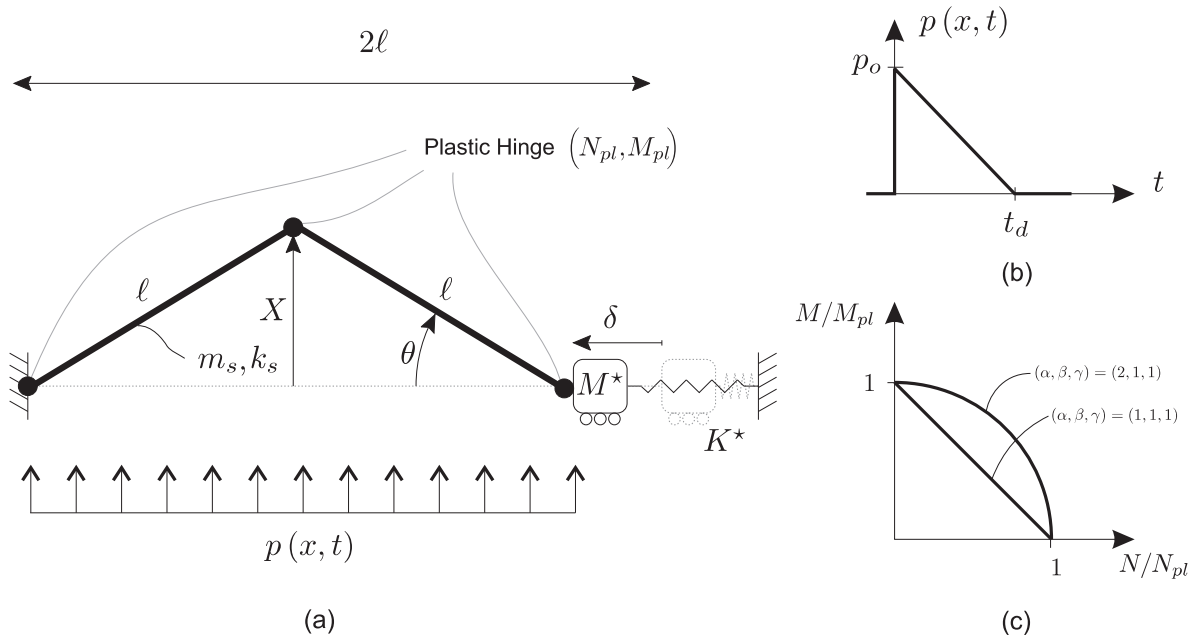
Figure II.1: (a) Sketch of the considered problem, (b) Idealized blast loading, (c) Axial force-bending moment interaction law

so that the elongation of the lateral spring reads

$$\delta = 2\ell\left(1 - \cos\theta\right) = \frac{X^2}{\ell}. \tag{II.4}$$

The formulation of rotation in Equ.(II.3) does not include the elastic deformation of the beam. In appendix VI.1, this approximation is demonstrated to be valid since the analytical model focuses on beam under membrane forces, involving large displacements.

Using an overhead dot to indicate differentiation with respect to time t, the shortening velocity and acceleration of the chord thus read

$$\dot{\delta} = \frac{2}{\ell}X\dot{X} \quad ; \quad \ddot{\delta} = \frac{2}{\ell}\left(\dot{X}^2 + X\ddot{X}\right). \tag{II.5}$$

Because of the membrane force $K^\star\delta$ increasing quadratically in the lateral spring as the transverse displacement X increases, the plastic bending moment M_{pl} that could, otherwise, be borned by the plastic hinge might drop during blasting. Accordingly the model developed in the sequel incorporates the $M-N$ interaction law between the bending moment M and the axial force N into the beam, which might be reduced on an inclusive basis in order to account for some partially resistant connections. For the sake of generality in the developments, the considered interaction law is

$$\left(\frac{M}{M_{pl}}\right)^\beta + \gamma\left(\frac{N}{N_{pl}}\right)^\alpha = 1 \tag{II.6}$$

where N_{pl} is the plastic axial resistance of the beam cross-section. Symbols α, β and γ refer to some parameters of the model (Fig. II.1-c), which should be selected in accordance with

the considered application. They might take on different values ($\alpha \geq 1$, $\beta \geq 1$ and $\gamma \geq 0$) depending on the constitutive material in the structure, namely involving steel, concrete or composite structures [75, 36, 76, 77, 78] and the cross-section shape and dimensions. Notice parameters α and β must be greater than 1 to ensure the convexity of the yield surface.

II.2.1.2 Extraction of the beam from the structure

This section discusses the extraction of the beam from the whole structure in order to study the simplest configuration represented in Figure II.1. The main challenge of dynamic condensation is to reproduce the important dynamic signature of the global finite element model after reduction of the IAP of the structure to a lateral equivalent mass and spring. No unique solution exists; some are discussed in this Section and illustrated in the applications.

In a finite element context, the equation of motion of the structure reads

$$\mathbf{M}\ddot{\mathbf{X}} + \mathbf{f}_{int}(\mathbf{X}) = \mathbf{P} \tag{II.7}$$

where $\mathbf{M}$, $\mathbf{f}_{int}$, $\mathbf{X} = \begin{bmatrix} X_{1h} & X_{2h} & \mathbf{X}_R \end{bmatrix}^T$ and $\mathbf{P}$ respectively represent the mass matrix, the internal forces, the nodal displacements (see Figure II.2) and the external loading.
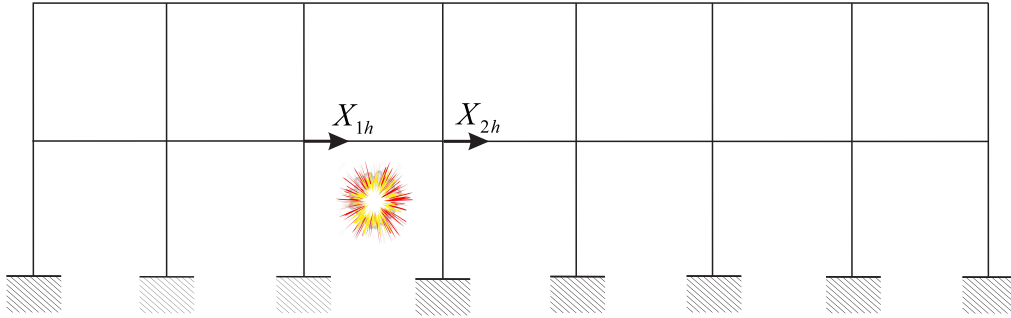
Figure II.2: Horizontal displacements at the ends of the blast loaded beam.

The internal forces can be decomposed into two parts

$$\mathbf{M}\begin{bmatrix} \ddot{X}_{1h} \\ \ddot{X}_{2h} \\ \ddot{\mathbf{X}}_R \end{bmatrix} + \mathbf{K}\begin{bmatrix} X_{1h} \\ X_{2h} \\ \mathbf{X}_R \end{bmatrix} + \phi(X_{1h} - X_{2h}; p)\begin{bmatrix} 1 \\ -1 \\ 0 \end{bmatrix} = 0, \tag{II.8}$$

namely the elastic restoring forces in the structure, expressed in terms of the stiffness matrix $\mathbf{K}$ and the auto-balanced membrane forces $\phi(X_{1h} - X_{2h}; p)$ associated with the kinematic quantities X_{1h} and X_{2h} corresponding to the horizontal displacements of the ends of the beam.

The extraction of the considered beam as sketched in the free body diagram of Fig. II.1-a requires the explicit introduction of the axial elongation $X_{1h} - X_{2h}$. Other degrees of freedom are not included in the low-dimensional model. Indeed, the rotations of the elastic elements of the IAP connected to the ends of the beam should in principle be conserved too,

since connections are perfectly rigid. However, these rotations are negligible compared to the maximum rotations of the plastic hinges. Furthermore, Nassr *et al.* have developed a SDOF model to determine the effect of axial load on column strength and stability during a blast event, and have validated their model by comparison with experimental blast tests on full scale steel columns and FEM simulations with the commercial software LS-DYNA. They show that the columns remain stable as long as the ratio of the axial load to the Euler buckling load is bounded [79, 80]. In this chapter, the supporting columns are supposed to remain stable after explosion. The beam is thus considered as vertically supported at its ends. In addition, the contribution of the adjacent columns in the computation of the lateral restraint is conservatively neglected.

Accordingly, only the horizontal displacements X_{1h} and X_{2h} are specified in the decomposition of equation (II.8). The change of variables

$$\mathbf{\Delta} := \begin{bmatrix} \delta \\ X_h \\ \mathbf{X}_R \end{bmatrix} = \begin{bmatrix} X_{1h} - X_{2h} \\ X_{1h} + X_{2h} \\ \mathbf{X}_R \end{bmatrix} = \begin{bmatrix} 1 & -1 & 0 \\ 1 & 1 & 0 \\ 0 & 0 & \mathbf{I} \end{bmatrix} \mathbf{X} \Longleftrightarrow \mathbf{X} = \begin{bmatrix} \frac{1}{2} & \frac{1}{2} & 0 \\ -\frac{1}{2} & \frac{1}{2} & 0 \\ 0 & 0 & \mathbf{I} \end{bmatrix} \mathbf{\Delta} := \mathbf{T}\mathbf{\Delta} \quad (II.9)$$

explicitly introduces the relative elongation $X_{1h} - X_{2h}$ via the transformation matrix $\mathbf{T}$.

Substitution of (II.9) into (II.8) and multiplication by $\mathbf{T}^T$ projects the equation of motion in a new coordinate system composed of the chord elongation of the beam δ, the average horizontal displacement X_h and the displacements of the other nodes of the model. It reads

$$\mathbf{M}_\delta \ddot{\mathbf{\Delta}} + \mathbf{K}_\delta \mathbf{\Delta} = -\phi\left(\delta; p\right) \begin{bmatrix} 1 \\ 0 \\ 0 \end{bmatrix} \qquad (II.10)$$

where $\mathbf{M}_\delta = \mathbf{T}^T \mathbf{M} \mathbf{T} = \begin{bmatrix} M_{\delta\delta} & \mathbf{M}_{\delta R} \\ \mathbf{M}_{R\delta} & \mathbf{M}_{RR} \end{bmatrix}$ and $\mathbf{K}_\delta = \mathbf{T}^T \mathbf{K} \mathbf{T} = \begin{bmatrix} K_{\delta\delta} & \mathbf{K}_{\delta R} \\ \mathbf{K}_{R\delta} & \mathbf{K}_{RR} \end{bmatrix}$. We may now recourse to known model reduction techniques in order to lump this dynamical system to the single degree-of-freedom δ. These techniques assume that the lumped degrees-of-freedom are expressed as an affine transformation of the master degree-of-freedom δ,

$$\mathbf{\Delta} = \mathbf{T}^\star \delta, \qquad (II.11)$$

where $\mathbf{T}^\star$ is a transformation matrix, selected in accordance with the type of the model reduction (see Section I.4.5). After reduction, the scalar governing equation reads

$$M^\star \ddot{\delta} + K^\star \delta = -\phi(\delta; p) \qquad (II.12)$$

where $M^\star = \mathbf{T}^{\star T} \mathbf{M}_\delta \mathbf{T}^\star$ and $K^\star = \mathbf{T}^{\star T} \mathbf{K}_\delta \mathbf{T}^\star$.

Later in Section II.2.3.2, one of the condensation techniques described in Section I.4.5 is shown to be more appropriate for the frame under blast loading, and thus, that last one is selected to present all our numerical results.

II.2.1.3 Structural behavior

The structural behavior of the equivalent single degree-of-freedom oscillator is sketched in Fig. II.3. It illustrates, under a blast loading, the total internal force F_{int} in the nonlinear oscillator as a function of the generalized coordinate X. It is composed of the internal forces in the beam resulting from the elastic-plastic deformations and of the nonlinear restoring forces in the horizontal spring. This illustration is provided qualitatively here, while the equivalence between the continuous structure depicted in Fig. II.1-a and this single degree-of-freedom oscillator is formally developed later, based on an energy equivalence and displacement-based approach. Figure II.3-c shows the free body diagram of the equivalent oscillator, indicating the balance of internal forces F_{int}, external forces F_{ext} and inertial forces $M_s \ddot{X} + F_{inert} \left(M^\star \ddot{\delta} \right)$ where M_s is a generalized mass and F_{inert} is the additional inertia force due to the lateral mass, as discussed later.
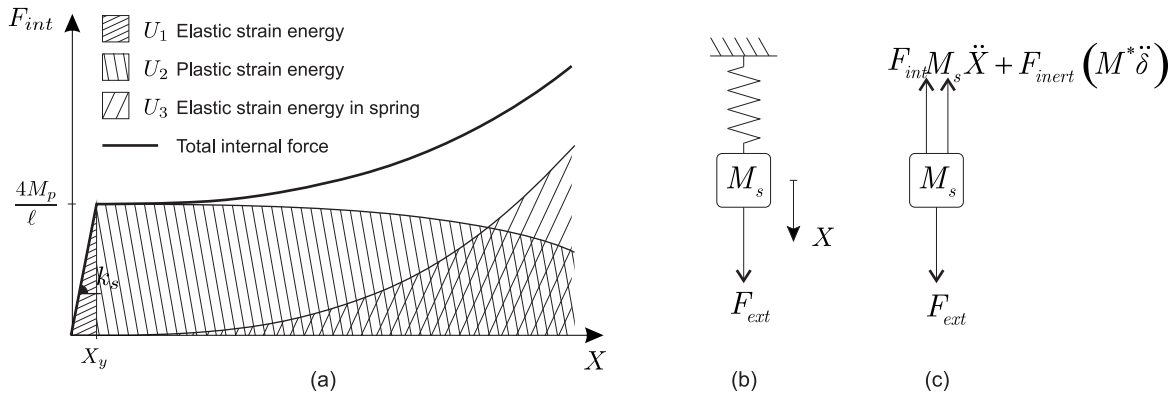
Figure II.3: (a) Sketch of the structural behavior of the equivalent single degree-of-freedom oscillator, (b) equivalent single degree-of-freedom oscillator, (c) free body diagram of the equivalent oscillator.

After a linear elastic regime extending to a yield displacement $X_y = \frac{M_{pl} l^2}{3EI_b}$ (where I_b and E are respectively the inertia of the beam and the Young's modulus of the material), the elastic strain energy stored in the system is U_1. This energy is recovered in a reversible manner during the unloading regime. Although there is a slight shift in their occurrence, it is assumed that all three plastic hinges of the problem form at the same time, after the mid-span displacement has reached X_y and for a distributed pressure p_b equal to $\frac{4M_{pl}}{\ell^2}$ corresponding, actually, to occurrence of the third plastic hinge. The secant stiffness in the elastic regime is thus $k_s = \frac{p_b \ell}{X_y} = \frac{12EI_b}{\ell^3}$.

After yielding has occurred, the beam enters a dissipative plastic regime where some strain energy U_2 is dissipated in the plastic hinges. In an elastic-perfectly plastic model, one would expect a horizontal plateau associated with the plastic bending moment in the plastic hinges. However, the maximum allowable bending moment accepted by the plastic hinges is initially M_{pl} but this value is more or less rapidly affected (depending on the spring stiffness $K^\star$ and the mass $M^\star$) as the axial force in the beam grows. It then features a smooth and gentle

decrease, as seen in Fig. II.3-a, as membrane forces develop. Notice they might be estimated as follows. We consider that the plastic hinges have already developed at that stage, i.e. the shear force in the beam is equal to $2M(N)/\ell$ where $M(N)$ represents the reduced allowable bending moment, as per the interaction law (see Equation (II.6)). For sake of simplicity, it can be approximated by $2M_{pl}/\ell$ and multiplied by the (small) rotation X/ℓ in order to obtain the component of the shear force along the chord of the beam, which contributes to the internal force in the lateral spring. This approximation results in an overestimation of the membrane force in the beam. The axial force in the beam is obtained by the horizontal equilibrium at the right end of the beam. It reads

$$
\begin{aligned}
N &\simeq -\phi\left(\delta;p\right) + \frac{2M_{pl}}{\ell}\frac{X}{\ell} \\
&\simeq \frac{2}{\ell}\left[\left(\dot{X}^2 + X\ddot{X}\right)M^\star + \frac{X^2}{2}K^\star + M_{pl}\frac{X}{\ell}\right].
\end{aligned}
\tag{II.13}
$$

II.2.1.4 Governing equations

Energy conservation states that the sum of kinetic energy K and elastic-plastic strain energy $U = U_1 + U_2 + U_3$ is equal to the work done by the external forces

$$
K + U_1 + U_2 + U_3 = W_p.
\tag{II.14}
$$

The elastic energy U_1 stored in the beam is given by

$$
U_1 = \frac{1}{2}k_s X^2
\tag{II.15}
$$

where k_s is the equivalent elastic bending stiffness of the beam, see Figure II.3. This expression is valid for $X \in [0; X_y]$ and should be set equal to $\frac{1}{2}k_s X_y^2$ for values of X out of this interval. Taking into account the reduction of the maximum allowable bending moment, the energy dissipated in the plastic hinges is equal to zero for $X \in [0; X_y]$ and expressed as

$$
U_2 = 4\int_{X_y/\ell}^{X/\ell} M\left[N\left(\theta,\dot{\theta},\ddot{\theta}\right)\right]d\theta = \frac{4}{\ell}\int_{X_y}^{X} M\left[N\left(\frac{\mathcal{X}}{\ell},\frac{\dot{\mathcal{X}}}{\ell},\frac{\ddot{\mathcal{X}}}{\ell}\right)\right]d\mathcal{X}
\tag{II.16}
$$

for $X \geq X_y$ and $\dot{X} \geq 0$. Since we mainly focus on the determination of the maximum displacement and internal forces, the configurations corresponding to the quadrants $\left(X,\dot{X}\right) \in [X_y;+\infty] \times [-\infty;0]$ or $\left(X,\dot{X}\right) \in [-\infty;0] \times \mathbb{R}$ are of secondary importance. Third, the energy stored in the lateral spring is given by

$$
U_3 = \int_0^\delta K^\star\Delta\,d\Delta = \int_0^X K^\star\frac{\mathcal{X}^2}{\ell}\frac{2\mathcal{X}}{\ell}\,d\mathcal{X} = \frac{1}{2}K^\star X^2\frac{X^2}{\ell^2}.
\tag{II.17}
$$

The total kinetic energy reads

$$K = \frac{1}{2}M_s \dot{X}^2 + \frac{1}{2}M^\star \dot{\delta}^2 + \frac{1}{2}\left(2\int_0^\ell I_{rot,b}\dot{\theta}^2\, dx\right) = \frac{1}{2}\left(M_s + 4M^\star\frac{X^2}{\ell^2} + 2\frac{I_{rot,b}}{\ell}\right)\dot{X}^2 \quad \text{(II.18)}$$

where $M_s = 2m_s\ell/3$ is the generalized mass corresponding to the assumed kinematics [18], $I_{rot,b} = m_s r^2$ is the mass moment of inertia (per unit length) and r is the radius of gyration. The last term of Equ. (II.18) corresponds to the rotational kinetic energy, and is based on the kinematic model illustrated in Figure II.1. The appendix VI.2 shows that the rotational kinetic energy for the elastic regime is of the same order of magnitude as that associated with the plastic regime. Nevertheless, in Section II.2.1.6, it is observed that the rotational inertia is negligible for practical ranges of parameters.

The external work done by the blast loading is given by

$$W_p = 2\int_0^\ell \int_0^X p\left(1 - \frac{x}{\ell}\right) d\mathcal{X}dx = 2\int_0^\ell pX\left(1 - \frac{x}{\ell}\right) dx = p\ell X \quad \text{(II.19)}$$

so that, finally, the energy conservation reads

$$\frac{1}{2}\left(M_s + 4M^\star\frac{X^2}{\ell^2} + 2\frac{I_{rot,b}}{\ell}\right)\dot{X}^2 + U_{int,b} + \frac{1}{2}K^\star X^2 \frac{X^2}{\ell^2} = p\ell X \quad \text{(II.20)}$$

with

$$U_{int,b} = \begin{cases} \frac{1}{2}k_s X^2 & \text{for } X \leq X_y, \\ \frac{1}{2}k_s X_y^2 + \frac{4}{\ell}\int_{X_y}^X M\left[N\left(\mathcal{X},\dot{\mathcal{X}},\ddot{\mathcal{X}}\right)\right] d\mathcal{X} & \text{for } X > X_y \text{ and } \dot{X} \geq 0. \end{cases} \quad \text{(II.21)}$$

II.2.1.5 Equation of motion

The equation of motion of the generalized problem is derived by differentiating the energy conservation law with respect to time and then dividing this conservation of power by the velocity $\dot{X}$.

The first term of the equation (II.20) provides the inertial force of the beam

$$\frac{1}{\dot{X}}\frac{dK}{dt} = \left(M_s + 4M^\star\frac{X^2}{\ell} + 2\frac{I_{rot,b}}{\ell}\right)\ddot{X} + 4M^\star\frac{X\dot{X}^2}{\ell^2} \quad \text{(II.22)}$$

The time derivative of the strain energy induced in the beam gives

$$F_{int,b} := \frac{1}{\dot{X}}\frac{dU_{int,b}}{dt} = \begin{cases} k_s X & \text{for } X \leq X_y, \\ \frac{4}{\ell}M\left[N\left(X,\dot{X},\ddot{X}\right)\right] & \text{for } X > X_y \text{ and } \dot{X} \geq 0 \end{cases} \quad \text{(II.23)}$$

where $F_{int,b}(t)$ is the equivalent internal force in the beam.

The third term of equation (II.20) provides the force in the lateral restraint

$$F_{int,K} := \frac{1}{\dot{X}}\frac{dU_3}{dt} = 2K^\star\frac{X^3}{\ell^2} \qquad (\text{II.24})$$

where $F_{int,K}(t)$ is the equivalent internal force in the lateral restraint. Finally, the term associated with the external force provides

$$F_{ext} = \frac{1}{\dot{X}}\frac{dW_p}{dt} = p\ell \qquad (\text{II.25})$$

where $F_{ext}(t)$ is the equivalent force due to blast loading.

All in all, the equation of motion reads

$$\left(M_s + 4M^\star\frac{X^2}{\ell^2} + 2\frac{I_{rot,b}}{\ell}\right)\ddot{X} + 4M^\star\frac{X\dot{X}^2}{\ell^2} + F_{int,b}\left(X,\dot{X},\ddot{X}\right) + 2K^\star\frac{X^3}{\ell^2} = p\ell \qquad (\text{II.26})$$

This is the nonlinear equation (with time-varying equivalent mass) that needs to be solved in order to determine the maximum displacement, and so the required ductility, of the system.

II.2.1.6   Scaling and dimensionless formulation

A natural timescale of the problem is the characteristic period of the elastic beam without lateral restraint and inertia $T_b = \sqrt{M_s/k_s}$. The characteristic pressure $p_b = 4M_{pl}/\ell^2$ corresponds to the static pressure at which the plastic beam mechanism is formed, while the characteristic displacement definitely corresponds to the yield displacement $X_y = p_b\ell/k_s$. The dimensionless version of the equation of motion is obtained by rescaling the time by the characteristic time, and dividing both sides of the equation of motion by the characteristic force $k_s X_y = p_b\ell$,

$$\left(1 + \psi_M\theta_y^2\overline{X}^2 + \lambda_r^2\right)\overline{X}'' + \psi_M\theta_y^2\overline{X}\overline{X}'^2 + \overline{F}_{int,b}\left(\overline{X},\overline{X}',\overline{X}''\right) + 2\psi_K\theta_y^2\overline{X}^3 = \overline{p}\left(1 - \frac{\tau}{\tau_d}\right) \qquad (\text{II.27})$$

where $\overline{X} = X/X_y$ is the dimensionless displacement and the prime symbol ' represents differentiation with respect to the dimensionless time $\tau = t/T_b$. Main parameters of the problem naturally appear as the ratio τ_d of the duration of blasting over the characteristic timescale, the ratio ψ_M of the lateral participating mass to the generalized mass of the beam and the ratio ψ_K of the lateral restraint to the stiffness of the beam which are respectively given by

$$\tau_d = t_d/T_b \quad ; \quad \psi_M = 4M^\star/M_s \quad ; \quad \psi_K = K^\star/k_s. \qquad (\text{II.28})$$

Other parameters are the yield rotation $\theta_y = X_y/\ell$, the ratio $\lambda_r = \sqrt{3}r/\ell$ of the radius of gyration to the length of the beam, the dimensionless peak overpressure of the blast loading $\overline{p} = p_0/p_b$ and the dimensionless internal forces defined as

$$\overline{F}_{int,b} = \frac{F_{int,b}}{p_b \ell} = \begin{cases} \overline{X} & \text{for } \overline{X} \leq 1, \\ m\left[n\left(\overline{X}, \overline{X}', \overline{X}''\right)\right] & \text{for } \overline{X} > 1 \text{ and } \overline{X}' \geq 0. \end{cases} \tag{II.29}$$

The dimensionless axial force $n := N/N_{pl}$ and its interaction with the dimensionless bending moment $m := M/M_{pl}$ are respectively given by

$$n = 4\xi\theta_y\overline{X} + 8\xi\theta_y\psi_K\overline{X}^2 + 4\psi_M\xi\theta_y\left(\overline{X}'^2 + \overline{X}\overline{X}''\right) \tag{II.30}$$

$$m^\beta + \gamma n^\alpha = 1 \tag{II.31}$$

where $\xi = (M_{pl}/2\ell)/N_{pl}$ is the ratio of bending to axial strengths. The demand in ductility

$$\mu = \max_{t \in \mathbb{R}^+}\overline{X}(t) = \frac{X_m}{X_y}, \tag{II.32}$$

where X_m represents the maximum displacement of the beam, is only ruled out by the seven dimensionless numbers of this problem, namely $\psi_K, \psi_M, \xi, \theta_y, \bar{p}, \tau_d$ and λ_r.

The scope of this work is to analyze how the demand of ductility μ is related to these parameters. There is no closed-form solution of the governing equation of the problem (II.27), taking into account (II.29) and (II.30)-(II.31). We will therefore limit the study to the influence of the problem parameters on the demand in ductility. As the influence of some parameters such as the duration of the blasting are relatively well understood, we mainly focus on the influence of ψ_K and ψ_M as they are specific to this model.

As mentioned in Section I.4.4.3, according to the UFC design guide, the ductility demand should not exceed 10 to protect staff and equipment (first level of protection) whereas the collapse of the structural element is avoided provided that the demand of ductility is smaller than 20 (see Table I.5).

The dimensionless parameters ψ_K and ψ_M depend, respectively, on the stiffness and the inertia offered by the IAP and result from reduction models. In Figure II.4-a, the structure has no lateral restraint nor additional inertia because, as explained earlier, the bending stiffness of the columns is neglected and the weight of the columns is negligible. Therefore, parameters ψ_K and ψ_M are equal to zero. At the opposite, the braced frame in Figure II.4-d offers a large stiffness to the relative chord elongation of the beam. Of course, the more lateral columns and bracings, the more rigid the lateral restraint offered to the beam.

Table II.1 gives the values of these parameters for the four structures illustrated in Figure II.4. Since they immediately represent scaled versions of $K^\star$ and $M^\star$, which depend on the reduction technique, results obtained with the different reduction models are used. The mode required for the dynamic condensation and the SEREP is selected such as it is the first mode that exhibits a relative horizontal displacement at the ends of the beam. These aforementioned reduced models have the advantage to contain one natural frequency of the global model.

To cover a wide range of cases, the dimensionless parameter ψ_K and ψ_M are assumed to vary from 0 to 4 and from 0 to 20 respectively (in Figure II.4). The Guyan process is more

appreciated if the IAP of the structure is loaded quasi-statically by the membrane force in the beam. Otherwise, the dynamic condensation or the SEREP are preferred.
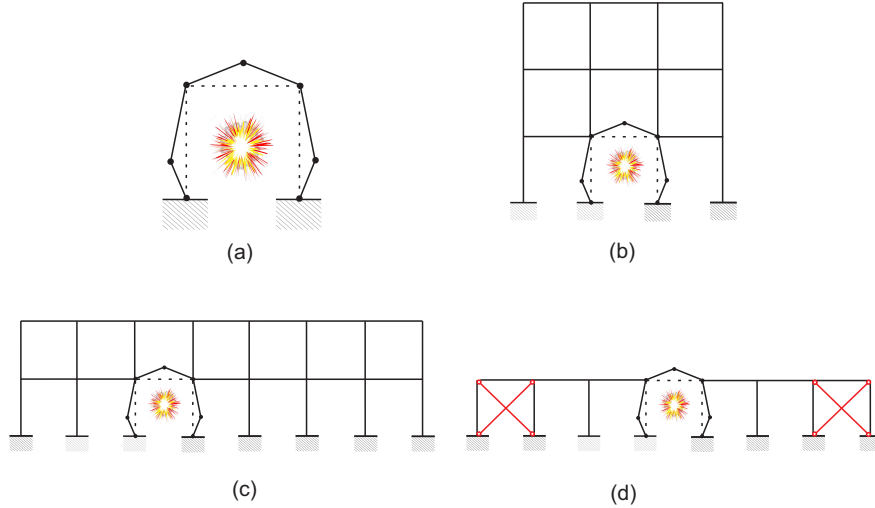
Figure II.4: Steel structure configurations with IPE 270 beams (5.4 m), HEA 240 columns (4.5 m), CHS 175x5 braces and a linear mass of the floor equals to 2500 kg/m.

	Guyan cond.		Dyn. cond.		IRS		SEREP	
Structure	$\psi_K\,[-]$	$\psi_M\,[-]$	$\psi_K\,[-]$	$\psi_M\,[-]$	$\psi_K\,[-]$	$\psi_M\,[-]$	$\psi_K\,[-]$	$\psi_M\,[-]$
(b)	0.3	6.2	0.3	6.3	0.3	6.3	0.23	6.3
(c)	0.64	14.8	0.68	16.4	0.71	25.0	0.68	16.4
(d)	2.91	8.7	3.81	13.6	3.52	13.1	4.36	15.8

Table II.1: Values of the dimensionless parameters ψ_K and ψ_M for different structures obtained by different reduction models.

The dimensionless parameters ξ and θ_y depend only on the properties of the profile and its span. Figure II.5 represents, in a scatter plot, the relation between these two parameters according to the span-to-depth ratio of the beam for any class-1 S355 steel-grade steel profiles in the ArcelorMittal catalogue (such as I, H-shaped or tubular profiles). They are found to be inversely proportional to each other in the range of interest as indicated by the upper and lower envelopes represented by dashed lines. Indeed we observe that the dimensionless group

$$\xi\theta_y = \frac{1}{8}\frac{M_{pl}^2}{N_{pl}EI_b} \tag{II.33}$$

lies in the tiny range $[2.29\,10^{-4}; 2.63\,10^{-4}]$ for the (rather wide) set of considered steel profiles. The parameters ξ and θ_y vary from 4.2 % to 1.1 % and 6.2 mrad to 22 mrad respectively as the ratio $2\ell/h$ increases from 10 to 30 (Table II.2).
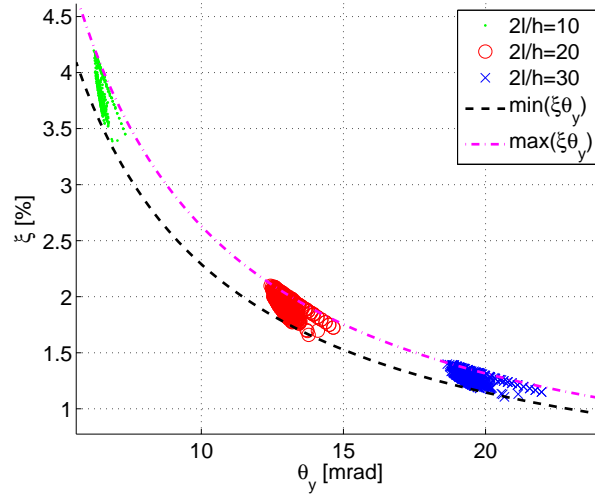
Figure II.5: Relation between ξ and θ_y for steel beams with S355 steel grade according to different ratios $2l/h$.

Ratio $2\ell/h$	10	20	30
$\min(\xi)$ [%]	3.3	1.7	1.1
$\max(\xi)$ [%]	4.2	2.1	1.4
$\min(\theta_y)$ [mrad]	6.2	12.4	18.7
$\max(\theta_y)$ [mrad]	7.3	14.6	22

Table II.2: Minimum and maximum values of the dimensionless parameters ξ [%] and θ_y [mrad] for steel beams with S355 steel grade according to different ratios $2\ell/h$.

Note that the dimensionless parameter ξ for the M-N plastic interaction is analogous to the dimensionless parameter ν for the M-V plastic interaction in [66], which is defined as a dimensionless ratio of the bending to shear strengths.

The parameter $\lambda_r = \sqrt{3}r/\ell$ depends on the radius of gyration r of the beam and its span. Table II.3 shows that λ_r takes its maximum value 7.6 % for $2\ell/h = 10$. Therefore, the rotational inertia effects are negligible for applications of interest since the parameter λ_r enters in the equation of motion (II.27) at the second power ($\max(\lambda_r^2) \simeq 5.8 \cdot 10^{-3}$) and is in competition with a unit term. In the following illustrations, we thus consider $\lambda_r = 0$.

$2\ell/h$	10	20	30
$\min(\lambda_r)$ [%]	6.3	3.2	2.1
$\max(\lambda_r)$ [%]	7.6	3.8	2.5

Table II.3: Minimum and maximum values of the dimensionless parameter λ_r for steel beams according to different ratios $2l/h$.

Three regimes can be observed according to the parameter τ_d, i.e. how fast the blasting develops according to the natural timescale of the structure. For the impulsive ($\tau_d \ll 1$) and

quasi-static ($\tau_d \gg 1$) regimes, some asymptotic analytical solutions are derived for the level of required ductility; they are provided in the following section. In the intermediate dynamic regime ($\tau_d \approx 1$), where the timescales of the loading and of the response interact, the set of equations (II.27), (II.30) and (II.31) must be solved.

II.2.2 Asymptotic solutions

II.2.2.1 The quasi-static solution (p asymptote)

In the case of the quasi-static loading ($\tau_d \gg 1$), the work done by external forces is equal to the strain energy stored in the lateral restraint and dissipated through plastic deformation at maximum displacement [30]. In the quasi-static loading regime, the dimensionless work done by the blast loading until the maximum displacement is reached is

$$\overline{W}_p = \frac{W_p\left(X_m\right)}{2U_1\left(X_y\right)} = \frac{p_0 \ell X_m}{k_s X_y^2} \tag{II.34}$$

where we have taken $2U_1\left(X_y\right) = k_s X_y^2$ as a characteristic work. Furthermore, assuming $\beta = 1$ in order to develop (II.31) analytically, the dimensionless total strain energy at maximum displacement $\overline{U}_p$ reads

$$\overline{U}_p := \frac{U}{2U_1\left(X_y\right)} = \frac{1}{2} + \left[\left(\mu - 1\right) - \frac{\gamma}{\theta_y}\left(\Phi_{p,\alpha}\left(\mu\right) - \Phi_{p,\alpha}\left(1\right)\right)\right] + \frac{\psi_K \mu^4 \theta_y^2}{2} \tag{II.35}$$

with

$$\Phi_{p,\alpha}\left(\bar{X}\right) = \int_0^{\bar{X}} n\left(\overline{\chi}, \overline{\chi}', \overline{\chi}''\right)^\alpha d\overline{\chi}. \tag{II.36}$$

The first term of Equ. (II.35) corresponds to the elastic strain energy of the beam, the second term in square brackets refers to the plastic energy dissipated in plastic hinges while the last one is related to the strain energy stored in the lateral spring.

Neglecting the contribution of the velocity and acceleration terms in the dimensionless axial force n, i.e. $n\left(\overline{\chi}, \overline{\chi}', \overline{\chi}''\right) \simeq n\left(\overline{\chi}, 0, 0\right)$, the function $\Phi_{p,\alpha}$ becomes

$$\Phi_{p,\alpha}\left(\bar{X}\right) \simeq \int_0^{\bar{X}} n\left(\overline{\chi}, 0, 0\right)^\alpha d\overline{\chi} = A_1^\alpha \frac{\bar{X}^{\alpha+1}}{\left(1+\alpha\right)} {}_2F_1\left(-\alpha; \alpha+1; \alpha+2; -\frac{A_2}{A_1}\bar{X}\right) \tag{II.37}$$

where $A_1 = 4\xi\theta_y$, $A_2 = 8\psi_K \xi\theta_y$ and ${}_2F_1\left(-\alpha; \alpha+1; \alpha+2; -\frac{A_2}{A_1}\bar{X}\right)$ is a hypergeometric function. In particular cases where $\alpha = 1$ or 2, the function $\Phi_{p,\alpha}\left(\bar{X}\right)$ further simplifies to

$$\Phi_{p,1}\left(\bar{X}\right) = \left(\frac{A_2}{3}\bar{X}^3 + \frac{A_1}{2}\bar{X}^2\right) \quad ; \quad \Phi_{p,2}\left(\bar{X}\right) = \left(\frac{A_2^2}{5}\bar{X}^5 + \frac{A_1^2}{3}\bar{X}^3 + \frac{A_2 A_1}{2}\bar{X}^4\right). \tag{II.38}$$

Equating the dimensionless work in equation (II.34) to the dimensionless strain energy in equation (II.35) gives

$$\frac{p_0 \ell X_m}{k_s X_y^2} = \overline{U}_p \left(\mu, \psi_K, \xi, \theta_y \right) \tag{II.39}$$

or

$$\overline{p} := \frac{p_0}{p_b} = \frac{1}{\mu} \overline{U}_p \left(\mu, \psi_K, \xi, \theta_y \right). \tag{II.40}$$

Since the loading rise time is equal to zero and because of the lateral mass, the assumption $n \left(\overline{\chi}, \overline{\chi}', \overline{\chi}'' \right) \simeq n \left(\overline{\chi}, 0, 0 \right)$ is a bit coarse, since inertial effects associated with the motion of the lateral mass are neglected. An explicit consideration of those terms does not result in a closed-form integral. In order to obtain an analytical formulae, the quasi-static asymptote is therefore expressed as a correction of the quasi-static solution obtained by neglecting the inertia terms in the integral (II.37). The corrected normalized pressure reads

$$\overline{p} = \frac{S \left(\mu, \psi_K, \psi_M \right)}{\mu} \overline{U}_p \left(\mu, \psi_K, \xi, \theta_y \right) \tag{II.41}$$

where the correction factor S, fitted from numerical simulations for parameters in the following ranges $\psi_K \in [0; 3]$, $\psi_M \in [0; 20]$, $2l/h \in [10; 30]$, $\beta = \gamma = 1$ and $\mu \in [0; 20]$, is given by

$$S = \left(1 - s \psi_K \left(\frac{\psi_M}{20} \right) \left(\max \left(\frac{\mu}{10}; 1 \right) - 1 \right) \right) \tag{II.42}$$

$$s = \begin{cases} 2.5/100 & \text{for } \alpha = 1 \\ 2/100 & \text{for } \alpha = 2 \end{cases}. \tag{II.43}$$

The results in Section II.2.4 will illustrate the accuracy of this formula.

The relation (II.41) does not involve the impulse of the loading. This indicates that, in the quasi-static regime, the response μ only depends on the magnitude of the loading $\overline{p}$, not its duration. Consequently the level set representation of the ductility demand features horizontal asymptotes in the p-I diagram.

II.2.2.2 The impulsive solution (I asymptote)

At the fast timescale, for short duration of blasting compared to the natural period of the structure ($\tau_d \ll 1$), conservation of momentum over the short period of loading provides the initial structural velocity to be considered for the free response taking place after the loading has stopped. In this case, $\dot{X}_0 = I\ell/M_s$ is the initial velocity at mid-span, since the additional mass $M^\star$ does not participate in the balance of momentum during this short loading phase, as the velocity $\dot{\delta}$ is proportional to the (small) generalized displacement X, see Equ. (II.5).

In the subsequent elastic-plastic free vibration problem, the maximum displacement is determined by equating the initial kinetic energy corresponding to this initial velocity and the strain energy in the system [30]. The initial dimensionless kinetic energy is given by

$$\overline{K}_0 := \frac{\frac{1}{2}M_s\dot{X}_0^{\,2}}{k_sX_y^2} = \frac{1}{2}\frac{I^2\ell^2}{k_sM_sX_y^2}. \tag{II.44}$$

Thus, equating this dimensionless kinetic energy to the dimensionless strain energy gives

$$\frac{I^2\ell^2}{k_sM_sX_y^2} = 2\overline{U}_I\left(\mu, \psi_K, \psi_M, \xi, \theta_y\right) \tag{II.45}$$

where the dimensionless total strain energy at maximum displacement $\overline{U}_I$ for impulsive loading can be written as below (assuming $\beta = 1$)

$$\overline{U}_I = \frac{U}{2U_1\left(X_y\right)} = \frac{1}{2} + \left[(\mu - 1) - \frac{\gamma}{\theta_y}\left(\Phi_I\left(\mu\right) - \Phi_I\left(1\right)\right)\right] + \frac{\psi_K\mu^4\theta_y^2}{2} \tag{II.46}$$

with

$$\Phi_{I,\alpha}\left(\bar{X}\right) = \int_0^{\bar{X}} n\left(\overline{\chi}, \overline{\chi}', \overline{\chi}''\right)^\alpha d\overline{\chi} = \int_0^{\bar{X}} \left(4\xi\theta_y\overline{\chi} + 8\xi\theta_y\psi_K\overline{\chi}^2 + 4\psi_M\xi\theta_y\left(\overline{\chi}'^2 + \overline{\chi}\overline{\chi}''\right)\right)^\alpha d\overline{\chi}. \tag{II.47}$$

In case where $\beta \neq 1$, the expression for $\Phi_{I,\alpha}$ should be substituted with an appropriate numerical integration. The major difference between $\Phi_{I,\alpha}$ and $\Phi_{p,\alpha}$ concerns the consideration of the terms related to velocity and acceleration in the expression of the internal axial force.

Finally, the impulsive asymptote can be derived

$$\overline{I} := \frac{\overline{p}\tau_d}{2} = \frac{I\ell}{\sqrt{k_sM_sX_y}} = \sqrt{2\overline{U}_I\left(\mu, \psi_K, \psi_M, \xi, \theta_y\right)} \tag{II.48}$$

where $\overline{I}$ is the dimensionless momentum associated with the blast loading. As this response does not depend on $\overline{p}$, the level set of the demand in ductility features a vertical asymptote in the p-I diagram.

The integral in (II.47) is rather complex and requires, *a priori*, numerical integration. However, the function $\Phi_{I,\alpha}\left(\bar{X}\right)$ could be simplified. Observing that the transverse velocity $\bar{X}'$ varies from $\overline{I}$ to 0 as the displacement $\overline{X}$ increases from 0 to μ, we suggest to use the rough approximation

$$\bar{X}' \simeq \overline{I}\left(1 - \frac{\bar{X}}{\mu}\right) \tag{II.49}$$

in order to simplify (II.47). This very simple model of the dynamics implies $\bar{X} = \mu\left(1 - e^{-\overline{I}\tau/\mu}\right)$ which is quite far from the actual dynamics, especially in the fully elastic regime. However, we observe later that this assumption fits pretty well the elastic-plastic response.

Moreover, further assuming that $\overline{\ddot{X}\dot{X}} \ll \overline{\dot{X}}^2$, the function $\Phi_{I,\alpha}\left(\bar{X}\right)$ simplifies into

$$\Phi_{I,\alpha}\left(\bar{X}\right) \simeq \int_0^{\bar{X}} n\left(\overline{\chi},\overline{\chi}',\overline{\chi}''\right)^\alpha d\overline{\chi} = \int_0^{\bar{X}} \left(A_1\overline{\chi} + A_2\overline{\chi}^2 + A_3\left(1 - \frac{\overline{\chi}}{\mu}\right)^2\right)^\alpha d\overline{\chi} \qquad \text{(II.50)}$$

where $A_3 = 4\psi_M\xi\theta_y\overline{I}^2$. In particular cases such as $\alpha = 1$ or 2, the function $\Phi_{I,\alpha}\left(\bar{X}\right)$ can be written as:

$$\Phi_{I,1}\left(\bar{X}\right) = \frac{A_2}{3}\bar{X}^3 + \frac{A_1}{2}\bar{X}^2 + \frac{A_3}{3\mu^2}\bar{X}^3 - \frac{A_3}{\mu}\bar{X}^2 + A_3\bar{X} \qquad \text{(II.51)}$$

$$\begin{aligned}
\Phi_{I,2}\left(\bar{X}\right) &= \frac{\bar{X}^3\left(A_1^2\mu^2 - 4A_1A_3\mu + 2A_2A_3\mu^2 + 6A_3^2\right)}{3\mu^2} + \frac{\bar{X}^4\left(A_1\mu - 2A_3\right)\left(A_2\mu^2 + A_3\right)}{2\mu^3} \\
&\quad - \frac{A_3\bar{X}^2\left(2A_3 - A_1\mu\right)}{\mu} + \frac{\bar{X}^5\left(A_2\mu^2 + A_3\right)^2}{5\mu^4} + A_3^2\bar{X}.
\end{aligned} \qquad \text{(II.52)}$$

Thus, the equation (II.48) becomes

$$\overline{I}^2 \simeq 2\overline{U}_I\left(\mu,\psi_K,\psi_M\overline{I}^2,\xi,\theta_y\right). \qquad \text{(II.53)}$$

An iterative procedure should be used to obtain the impulsive solution. A first approximation of the solution can be obtained by neglecting the effects of the lateral inertia in equation (II.53), imposing therefore that $\psi_M = 0$, in which case a simple analytical expression is obtained. A fixed point algorithm then provides a convenient recursive relation

$$\overline{I}^2_{(k+1)} \simeq 2\overline{U}_I\left(\mu,\psi_K,\psi_M\overline{I}^2_{(k)},\xi,\theta_y\right) \qquad \text{(II.54)}$$

for the iterative correction of the first estimation.

II.2.3 Parametric analysis

II.2.3.1 Description of the numerical method

The set of equations (II.27), (II.30) and (II.31) is solved with a nonlinear solver generalized from the high-order implicit scheme developed in Ref. [81]. This unconditionally stable scheme is fourth order accurate, while commonly used integration schemes (like Newmark or HHT) are only second order accurate in a nonlinear setting. Furthermore, a simple numerical dissipation may be introduced, in which case the order of accuracy drops to three, but is very convenient for the filtering of spurious high frequency components that develop because of the zero-rising time of the loading and, more generally, in case of fast dynamics and rapid development of the plastic mechanism. Furthermore, the integration scheme has a level-2 symmetric formulation which makes it really efficient from a numerical point of view [82].

II.2.3.2 Illustrative examples

Consider a structure composed of a steel beam IPE 270 with a S355 steel grade and a length $2\ell = 5.4\,\mathrm{m}$. The linear mass of the reinforced concrete floor m_s is equal to $2500\,\mathrm{kg/m}$. The coefficients α, β and γ are assumed to be equal to 2, 1 and 1 which is known to correspond rather well to strong axis bending. The peak overpressure and the positive phase duration of the blast loading are respectively equal to $306\,\mathrm{kN/m}$ and $105\,\mathrm{ms}$. The characteristic displacement, force are respectively given by

$$X_y = 0.034\,\mathrm{m} \quad ; \quad p_b\ell = 255\,\mathrm{kN} \quad ; \quad T_b = 25\,\mathrm{ms}, \tag{II.55}$$

they scale the results shown in Fig. II.6.

The dimensionless numbers of this problem obtained with a Guyan condensation of the IAP, as illustrated in Figure II.4-c, are

$$\psi_K = 0.64\,; \; \psi_M = 14.8\,; \; \xi = 2\,\%\,; \; \theta_y = 13\,\mathrm{mrad}\,; \; \overline{p} = 3.25\,; \; \tau_d = 5\,; \; \overline{I} = 8.125. \tag{II.56}$$

A value of τ_d close to 2π indicates that the duration of the loading is very similar to the natural period of the structure. The dimensionless pressure $\overline{p}$ larger than 0.5 indicates that some plasticity could develop. The objective is to determine the maximum displacement.

Figure II.6-(a) illustrates the time evolution of the response. Figure II.6-(b) shows the evolution of the internal forces in the force-displacement portrait. Four points labeled A, B, C and D are used to describe the different stages of the response of the beam.

First, at point A, the plastic mechanism of the beam has just been formed, meaning that $\overline{X} = 1$. The sum of the internal forces is close to 1 since the effect of the lateral restraint is still negligible at this stage. At point B, the maximum dimensionless displacement (ductility demand) increases to 18.3, a bit after the moment where the blast loading stops. Between points A and B, the internal force in the beam first decreases as the membrane force increases. Then, it increases before reaching point B since the membrane force decreases because of the deceleration of the system, see (II.30). The equivalent internal force in the lateral restraint increases to reach a value close to the static plastic resistance of the beam.

After reaching the maximum displacement, the beam is subjected to an elastic unloading in the opposite direction. Indeed, the lateral restraint returns a part of its elastically stored energy to the beam. At point C, the plastic mechanism is developed in the opposite direction. Finally, at point D, the beam starts vibrating indefinitely elastically.

The displacements of the beam obtained with reduced models, i.e. the Guyan condensation (G.C.) and the dynamic condensation (D.C.), seem to coincide as they provide values of ψ_K and ψ_M that are very close. Also, these curves fit well the dash-dot curve obtained by solving the multi-degree-of-freedom finite element model of the whole IAP of the structure. Each structural element of the IAP is modeled by two beam finite elements and the time step $d\tau$ is chosen equal to $\tau_d/1000 = 5.10^{-3}$.

This detailed example corresponds to only one point in a (p-I) diagram, namely a required ductility of 18.3 for the couple $\left(\overline{p}; \overline{I}\right) = (3.25; 8.125)$. This point is represented by a red dot in Figure II.8-a.

Figure II.6: (a) Displacement versus time – comparison of reduced and global models and (b) internal forces versus displacement for a given example considering the following parameters : $\psi_K = 0.64$; $\psi_M = 14.8$; $\xi = 2\,\%$; $\theta_y = 13\,\mathrm{mrad}$; $\bar{p} = 3.25$; $\tau_d = 5$; $\bar{I} = 8.125$ (Guyan condensation).

For the braced structure (Figure II.4-d), the values of the characteristic period T_b, the plastic resistance $p_b l$ of the beam as well as the blast loading do not change from the last example. Therefore, the structural parameters ξ and θ_y as well as the pressure and impulse of the blast loading $(\bar{p}, \bar{I})$ are preserved. This modification is made on purpose in order to highlight the influence of parameters ψ_K and ψ_M only. The static response of the structure for the static condensation does not correspond exactly to the selected high-frequency mode shape of vibration used for the dynamic condensation, which results in a large discrepancy in values of the parameters ψ_K and ψ_M .

In Figure II.7-a, the displacement shows the same behavior until the first peak. However, the post-failure response computed with the dynamic condensation reduction technique is now different from the response obtained with the full finite element model of the structure, meaning that the response of the IAP of the structure is rather quasi-static than dynamic. Indeed, the IAP of the structure is loaded by the membrane force in the beam which is quasi-static as it mainly depends on the response of the beam and not directly on the blast loading. The braced system significantly mitigates the effect of the blast loading on the response of the beam thanks to its (elastic) stiffness; the maximum displacement drops to 15.2 as shown in Figure II.7-b.

II.2.4   Analysis of the model

II.2.4.1   Influence of parameter ψ_K

In order to draw the p-I diagram, Krauthammer *et al.* developed three different search algorithms and presented their disadvantage in terms of the numerical stability, computational
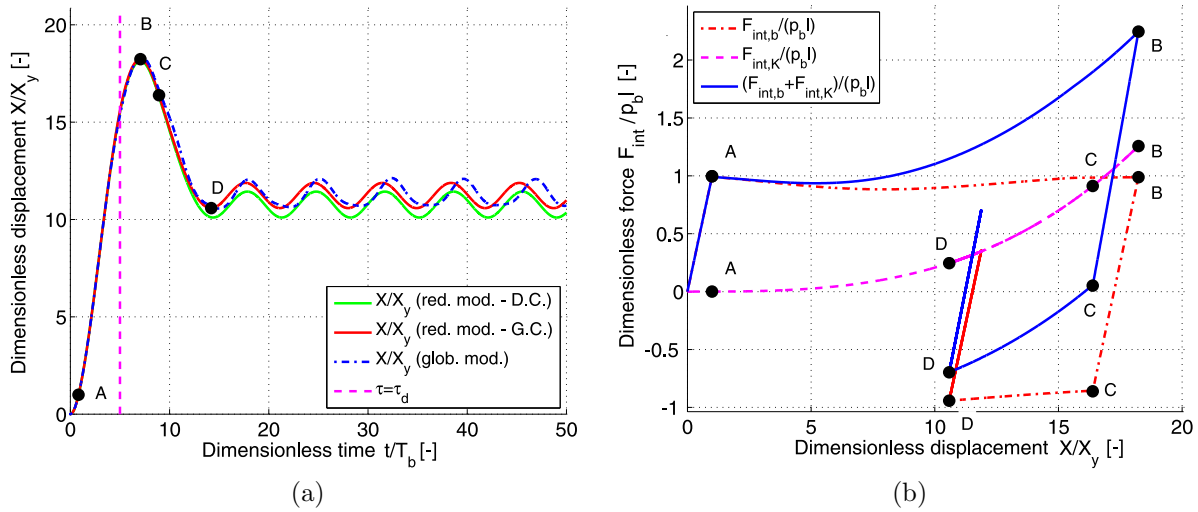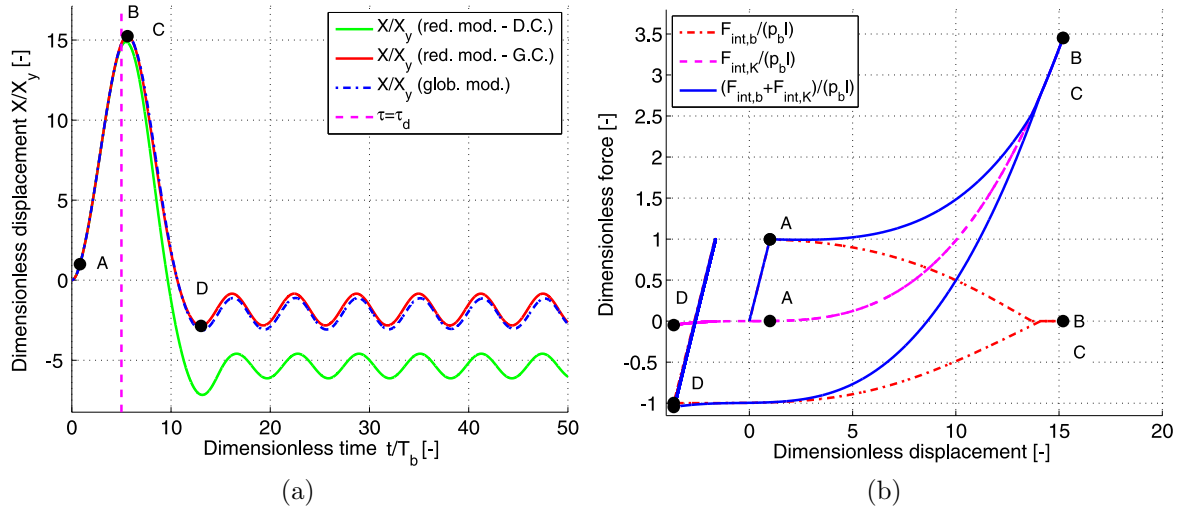
Figure II.7: (a) Displacement versus time – comparison of reduced and global models and (b) internal forces versus displacement for a given example considering the following parameters: $\psi_K = 2.91$; $\psi_M = 14.8$; $\xi = 2\%$; $\theta_y = 13\,\text{mrad}$; $\overline{p} = 3.25$; $\tau_d = 5$; $\overline{I} = 8.125$ (Guyan condensation).

efficiency, generality of the method and compared the numerical results with tested structural elements [83]. Among these methods, it turns out that Blasko's procedure based on a polar coordinate system and the bisection method are appropriate for the needs of our study.

P-I diagrams are represented for $\psi_K = 0.64$ (Figure II.8-a) and $\psi_K = 0$ (Figure II.8-b), while other parameters are chosen as $\psi_M = 14.8$; $\xi = 2\%$; $\theta_y = 13\,\text{mrad}$. Each curve represents the required ductility for design. The asymptotes represented with solid lines are obtained with the analytical procedures developed in Section II.2.2; on the other hand, black dots are obtained with the numerical simulation of the governing equations of the problem. The good agreement between these results obtained with two different approaches, in the asymptotic cases, serves as a validation of the numerical code.

For a particular blast load ($\overline{p} = 3.25$, $\overline{I} = 8.125$), comparison of Figs. II.8-a and II.8-b shows that the required ductility is reduced from 23.7 to 18.3 when the lateral restraint is considered. The case $\psi_K = 0$ corresponds to an elastic-perfectly plastic beam model as the membrane force is negligible (the effect of ψ_M is much less influential when ψ_K is low). As a result, the quasi-static loading can not exceed the plastic resistance of the beam; in other words, the p-asymptote satisfies $\overline{p} < 1$. On the contrary, in the presence of a lateral restraint, the quasi-static asymptote might be significantly higher than $\overline{p} = 1$, and the lateral stiffness could therefore significantly affect the ductility demand for longer blast loads with smaller peak pressure.

Figure II.9 illustrates the required ductility obtained with the analytical asymptotic approach as a function of parameter ψ_K ($\xi = 2\%$ and $\theta_y = 13$ mrad). It is represented as a function of (a) the pressure in the quasi-static regimes and (b) of the blast impulse in the impulsive regime. In Figure II.9-(a), the curve AB corresponding to $\overline{p} = 1$ presents a vertical
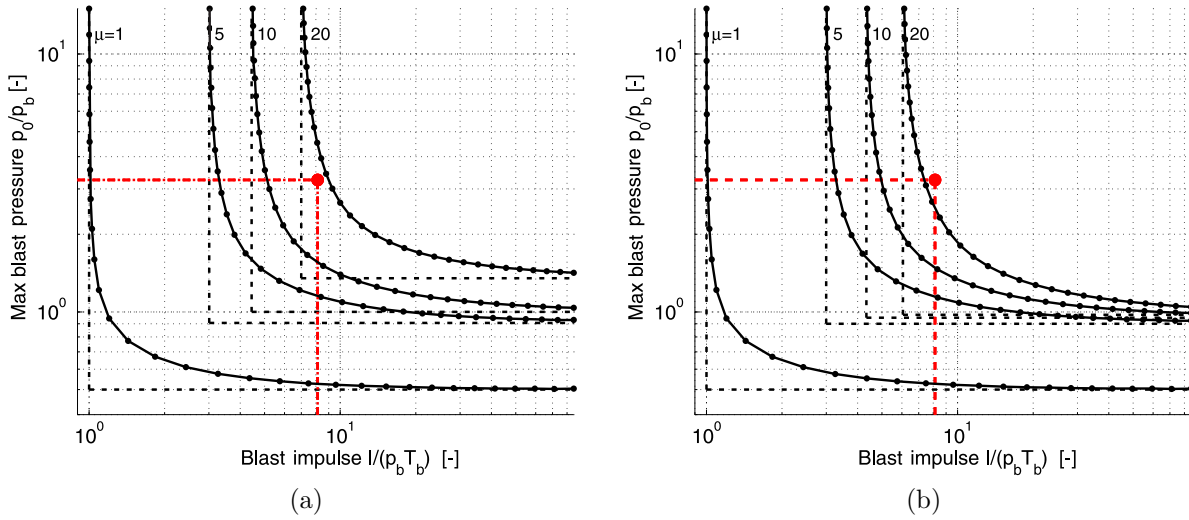
Figure II.8: Normalized p-I diagrams in logarithmic axes for (a) $\psi_K = 0.64$ and (b) $\psi_K = 0$. Other parameters are ($\psi_M = 14.8$; $\xi = 2\%$; $\theta_y = 13\,\mathrm{mrad}$).

asymptote at $\psi_K = 0$. Indeed, for an elastic-perfectly plastic model, the ductility demand tends to infinity since the quasi-static loading approaches the plastic resistance; the only load that can be borne statically by the beam has to be smaller than $\overline{p} = 1$. For low blast loads, it is seen that the stiffness of the horizontal restraint has few influence on the required ductility. In fact the required ductility is so low that the transverse displacement of the beam is small and the membrane forces are almost not activated. On the contrary, Figure II.9-(a) shows that for large (quasi-static) blast loads the membrane action significantly reduces the required ductility. As to the impulsive asymptote, the lateral restraint is globally ineffective in contributing to the global resistance of the structure. One need a dimensionless impulse of more than $\overline{I} = 5$ to observe an influence on demand in ductility. This is explained, as discussed in Section II.2.1.1, by the quadratic relation between the spring elongation and the transverse displacement of the beam. Notice that these influences on ψ_K on the asymptotic behaviors are also observable on the diagrams of Fig. II.8.

For the first protection category ($\mu = 10$), the maximum acceptable blast loading can be increased by up to 17\% and 7\% for quasi-static and impulsive loading respectively when the lateral restraint is taken into account. For the second protection category ($\mu = 20$), these gains can reach up to 150\% and 50\% respectively.
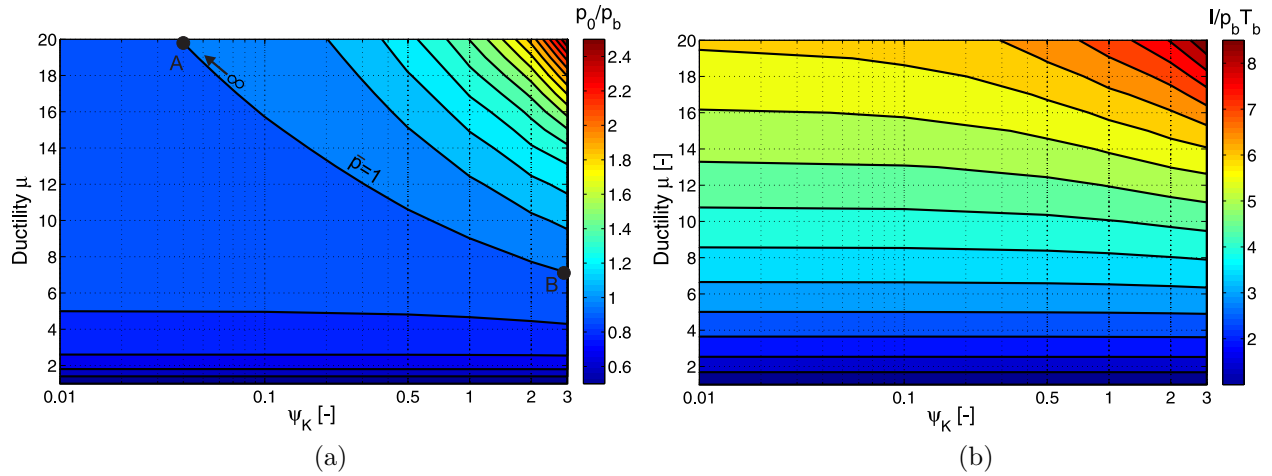
Figure II.9: Required ductility ($\psi_M = 10$; $\xi = 2\%$; $\theta_y = 13$ mrad and ψ_K variable) in the asymptotic regimes (a) for quasi-static loading $\overline{p} = p_0/p_b$ ($\tau_d \gg 1$) and (b) for impulsive loading $\overline{I} = I/(p_b T_b)$ ($\tau_d \ll 1$).

II.2.4.2 The case of large membrane forces

Figures II.10-a and -b illustrate, respectively, the structural behavior of the SDOF model and the quasi-static asymptotic solution (see Equation (II.41)) for the following structural parameters $\psi_K = 3$; $\psi_M = 0$; $\xi = 4\%$; $\theta_y = 7$ mrad. As the value of parameters ψ_K and ξ are high, the initial structural behavior is an elastic-perfectly plastic softening model until the axial force in the beam resulting from the membrane restraint reaches the axial plastic resistance (Figure II.10-a). At this last stage, the plastic hinges are fully articulated and the remaining resistance component in the SDOF model is the lateral restraint. The force-displacement response therefore features a slope discontinuity, see red dash-dot line, which translates into a similar discontinuity in the total internal force (in blue), which itself is however allowed to increase again owing to the elastic nature of the restraint. Because of this softening-hardening behavior, equating the work of external forces and the strain energy stored in the structure yields several solutions as shown in Figure II.10-b where the vertical line at $\overline{p} = 0.9$ meets the quasi-static asymptotic solution at three points. In a "dynamic" step-by-step solution starting from initial conditions at rest, the physical solution is the first point of intersection between the vertical line and the quasi-static pressure curve since it would correspond to the first crossing, in time. A snap-through is observed (from $\mu = 8$ to $\mu = 18$) for $\overline{p} = 0.94$; the equilibrium solution of the structure is unstable in between.

II.2.4.3 Assessment of the asymptotic solutions

Equation (II.53) gives an analytical approximation of the required impulsive loading $\overline{I}_{app}$ to reach a given level of damage. In a design stage, this level of damage can be chosen as one of the target values corresponding to the two levels of protection described in Table I.5. The relative error of this approximation is defined as the following ratio $\left(\overline{I}_{act} - \overline{I}_{app}\right)/\overline{I}_{app}$
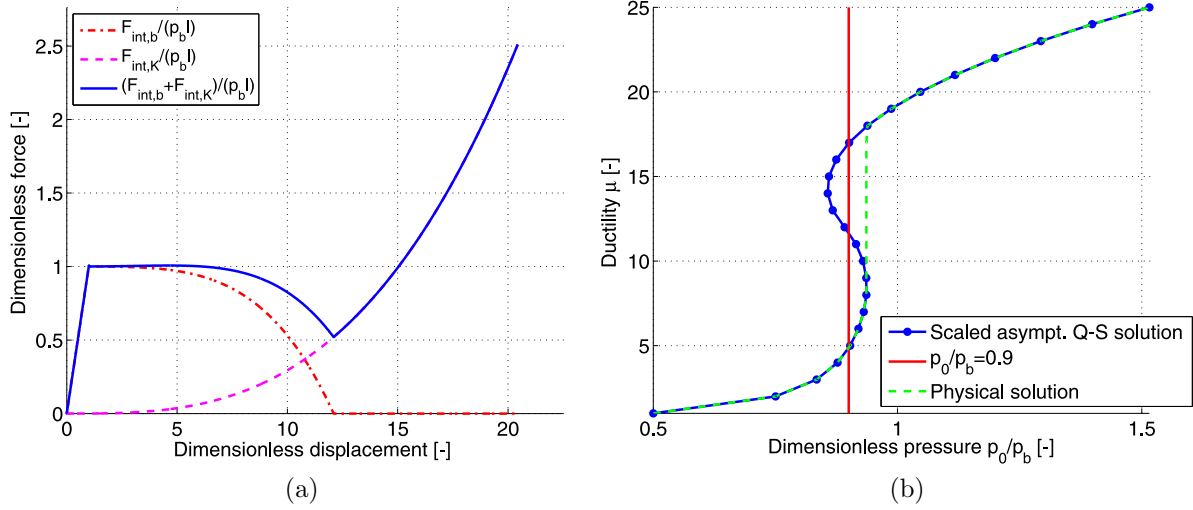
Figure II.10: (a) Structural behavior for $\xi = 4\,\%$; $\theta_y = 7\,\mathrm{mrad}$, $\psi_M = 0$ and $\psi_K = 3$; (b) Multiple solutions for a given quasi-static loading $\overline{p} = 0.9$.

where $\overline{I}_{act}$ is the actual impulsive asymptote of the corresponding iso-damage curve of the p-I diagram.

All the dimensionless parameters are varied in their practical range, the parameter ψ_K varies from 0 to 3, the M-N plastic interaction parameters are $\alpha = 2$, $\beta = 1$ and $\gamma = 1$ and the other parameters ξ and θ_y are approximately the mean values of range boundaries for three different ratios of $2\ell/h$ detailed in Table I.5. The last parameter ψ_M takes its maximum value, i.e. 20, corresponding to the highest relative error.

For the first category of protection ($\mu = 10$), the relative error is less than $1.5\,\%$ (figure II.11-a). However, for the second category of protection ($\mu = 20$), the relative error reaches a maximum value of about $6\,\%$ (figure II.11-b). If the parameter α is equal to 1, the relative error is below $5.5\,\%$.

(a)

(b)
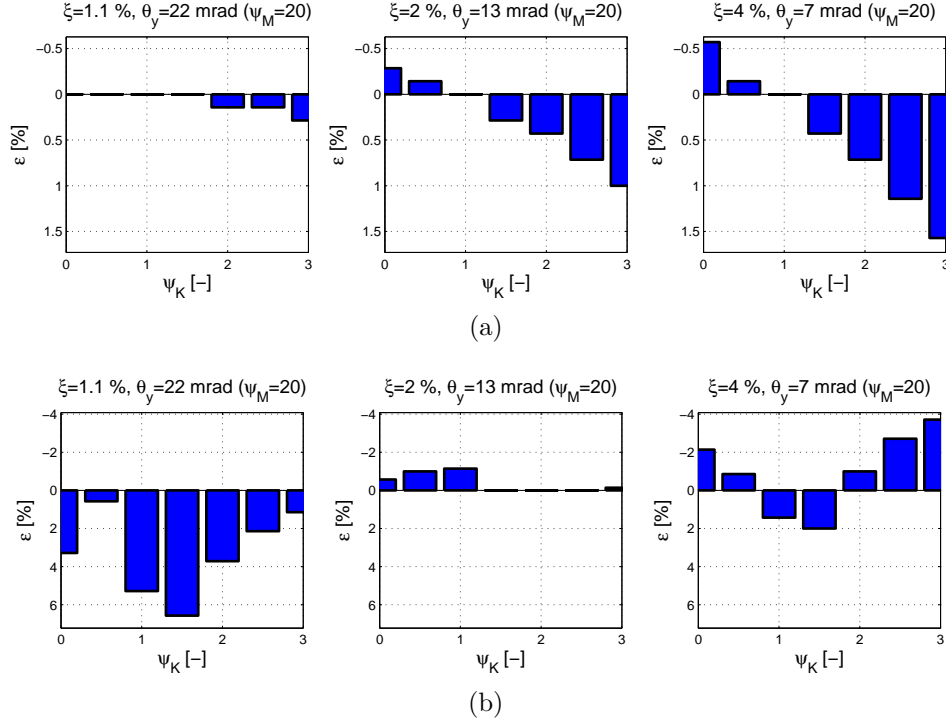
Figure II.11: Relative error in the assessment of the impulsive asymptotic solution for variable dimensionless parameters ($\alpha = 2$, $\beta = 1$, $\gamma = 1$) (a) for first ($\mu = 10$) and (b) second category of protection ($\mu = 20$).

Regarding the quasi-static solution (see Equ. (II.41)), the assessment of the relative error is performed similarly to the impulsive solution and the values of variables are maintained. The relative error of this approximation is defined as the following ratio $\left(\overline{p}_{act} - \overline{p}_{app} \right) / \overline{p}_{app}$ where $\overline{p}_{act}$ and $\overline{p}_{app}$ are respectively the actual and approximated quasi-static asymptotes.

For the first category of protection, the maximum relative error stands at $0.3\,\%$ (Figure II.12-a). However, for the second category of protection, the relative error tops out at $4\,\%$ (figure II.12-b) instead of $8\,\%$ without the correction coefficient S for $10 \leq \psi_M \leq 20$. Due to the softening-hardening structural behavior (for $2\ell/h = 10$ or $\xi = 4\,\%$) mentioned previously in Section II.2.4.2, the substructure may not be stable for $\mu = 10$ and $\psi_K \in [2.5; 3]$ as well as for $\mu = 20$ and $\psi_K \in [1; 2]$. If the parameter ψ_M is lower than or equal to 10, the maximum relative error drops to $2\,\%$. For $\alpha = 1$, the relative error is below $4\,\%$ for $\psi_M \in [0; 20]$.
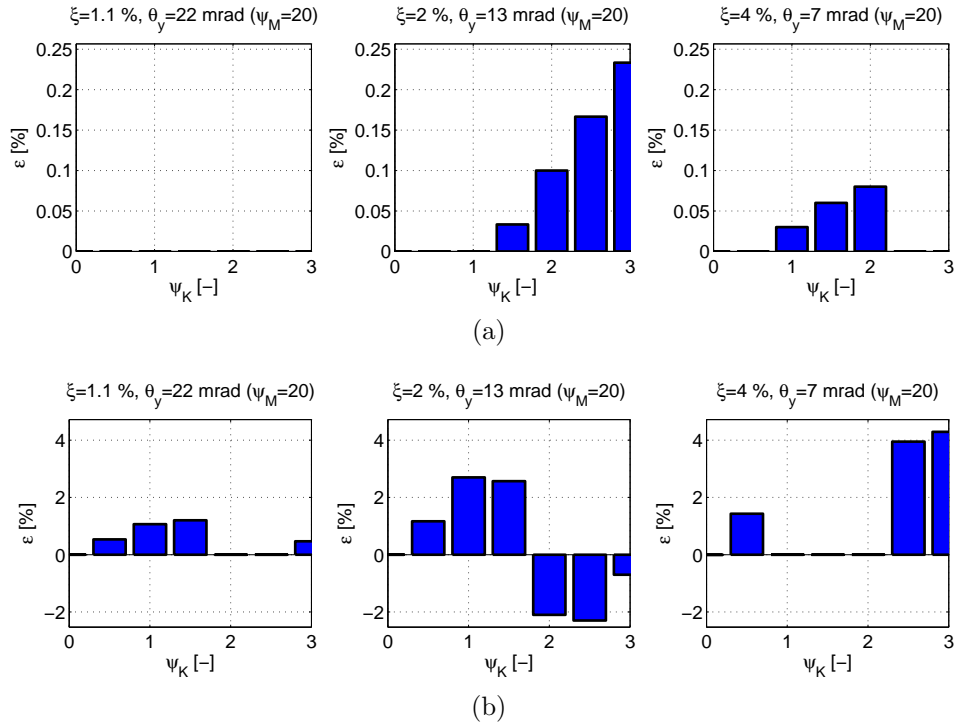
Figure II.12: Maximum relative error in the assessment of the quasi-static asymptotic solution for various values of ξ and θ_y ($\alpha = 2$, $\beta = 1$, $\gamma = 1$) (a) for first ($\mu = 10$) and (b) second ($\mu = 20$) category of protection.

II.2.4.4 Influence of parameters ξ and θ_y

The effect of parameters ξ and θ_y on the p-I diagram is illustrated in Figure II.13, for $\psi_K = 1$ and $\psi_M = 10$. The two parameters are not varied independently, but well along the hyperbola of high correlation disclosed in Fig. II.5. If the beam span-to-depth ratio is increased ($\xi \downarrow$ and $\theta_y \uparrow$), the energy dissipated in the plastic hinges is reduced. As a result, the lateral mass and restraint should contribute more to the dissipation of the energy generated by the blast loading. Therefore, the required ductility decreases, see Figure II.13-a, as the lateral force, which is a cubic function of the displacement, increases rapidly provided the lateral restraint remains elastic.

Same conclusions hold if the bending properties are constant and the beam axial plastic resistance is decreased ($\xi \uparrow$ and θ_y constant).
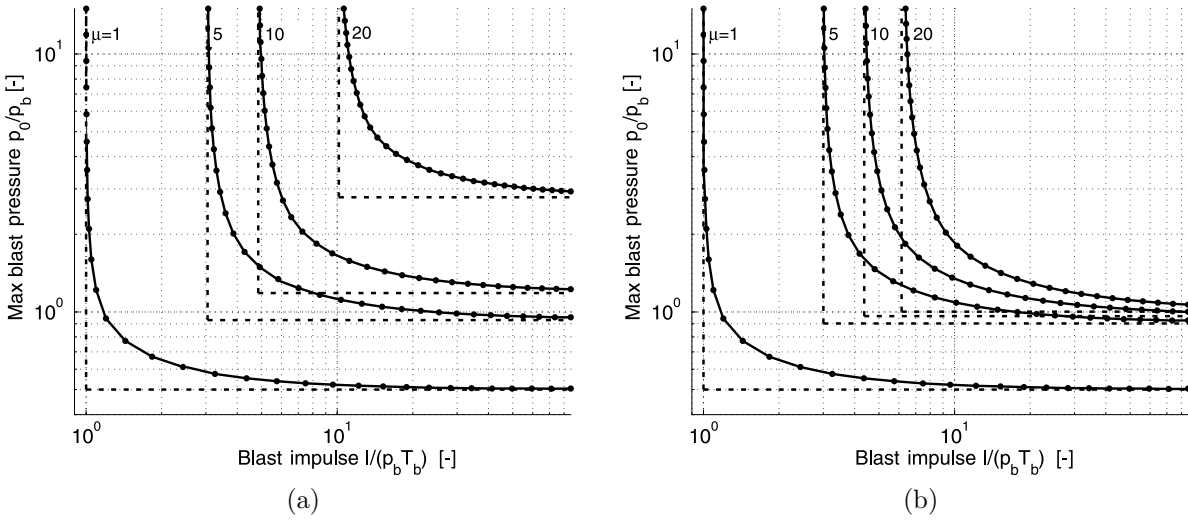
Figure II.13: Normalized p-I diagrams in logarithmic axes for $\psi_K = 1$, $\psi_M = 10$ (a) $\xi = 1.1\%$, $\theta_y = 22\,\mathrm{mrad}$ and (b) $\xi = 4\%$, $\theta_y = 7\,\mathrm{mrad}$.

II.2.4.5 Influence of the parameter ψ_M

With the help of numerical step-by-step simulations, it is found that the participating mass $M^\star$ does not affect significantly the response. In the impulsive regime, these numerical simulations reveal that parameter ψ_M does not affect significantly the response for ductility ratios lower than 10, see Figure II.14, but well for required ductility ratios of about 20, where an influence of up to 8% might be observed. Upon varying the values of other parameters in their practical range of interest, the maximum relative error in the impulsive and quasi-static regimes might reach respectively 12% and 8% for $\psi_M = 20$.
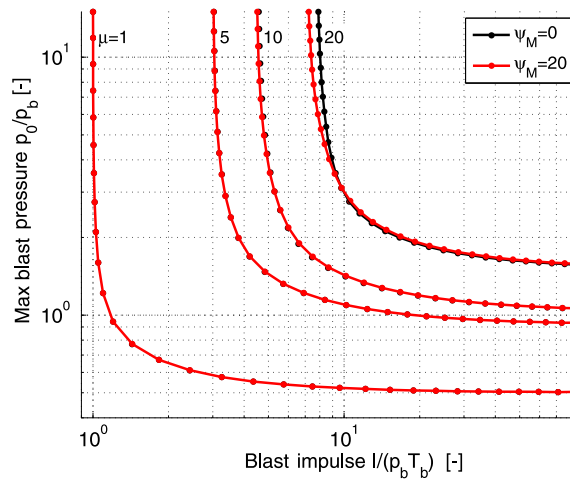
Figure II.14: Comparison of normalized p-I diagrams in logarithmic axes for $\psi_K = 1$, $\xi = 2\%$, $\theta_y = 13\,\mathrm{mrad}$, $\psi_M = 0$ and $\psi_M = 20$.

II.2.5   Conclusions

The problem treated in this Section is that of a frame beam subjected to blast loading considering the interaction with the indirectly affected part (IAP) of the structure, and assuming a linear elastic behavior of the IAP and stable adjacent columns. The purpose is to establish the p-I diagram for a beam extracted from an arbitrary structure (such as a steel, concrete or composite structure) taking into account the nonlinear membrane force, the M-N plastic interaction and the lateral inertia and restraint provided by the rest of the structure. One of the major limitations of the model is the inability to predict the shear failure or to capture the motion of plastic hinges for high peak overpressures. The material law of the beam is elastic-perfectly plastic, and does not account for strain hardening nor strain rate effects. In addition, the beam-to-column joints are perfectly rigid, the axial deformation is neglected and the rotation of the elastic elements connected to the beam is assumed to be negligible in comparison to the maximum plastic rotation of the beam ends.

   After carrying out some numerical simulations, the response of the beam obtained with the low-dimensional model shows good agreement with those of the global model.

   As a result of the dimensional analysis, four main dimensionless structural parameters affecting the required ductility of the frame beam are identified. Two parameters ψ_K and ψ_M are related to the behavior of the indirectly affected part (the lateral restraint and mass). Another one ξ is related to the mechanical properties of the investigated beam (i.e. its bending and axial resistances). The last parameter θ_y is related to the geometry of the problem (i.e. the yield rotation of the beam at its extremities). Another parameter λ_r corresponding to the rotational inertia effect is shown to be negligible for steel beams that exhibit a span-to-depth ratio between 10 and 30.

   Concerning the quasi-static asymptote of the P-I diagram, an empirical coefficient adjusts the quasi-static solution to include the effect of the parameter ψ_M. In the impulsive regime, the velocity at mid-span of the beam is assumed to decrease linearly according to the deflection in order to derive an analytical solution. Discrepancies between the numerical and analytical results are respectively found to be equal to 6 % and 4 % for quasi-static and impulsive asymptotic solutions. These relative errors are estimated in the following region of the parameter space: $\psi_K \in [0; 3]$, $\psi_M \in [0; 20]$, $2\ell/h \in [10; 30]$, $\beta = \gamma = 1$, $\mu \in [0; 20]$ and $\alpha = 1$ or 2. For the first level of protection, the magnitude of the blast loading can be respectively increased to 17 % and 7 % for quasi-static and impulsive regimes. For the second level of protection, it can be increased to 150 % and 50 %, respectively, although actually, these results are undoubtedly overestimated because of the assumption of the linear elastic behavior of the lateral restraint and the disregard of the plastic hinge elongations.

   In the quasi-static regime, the softening-hardening behavior of the beam for low span-to-depth ratios results in the coexistence of several stable solutions for a given peak overpressure. The dynamic analysis demonstrates that the substructure can not be stable after the first peak of the quasi-static solution until the pressure exceeds it.

   The effect of the four dimensionless parameters on the p-I diagram was also investigated. Parameter ψ_K outlines the favorable effect of the elastic indirectly affected part of the structure to limit the required ductility of the frame beam. If the beam span-to-depth ratio is increased ($\xi \downarrow$ and $\theta_y \uparrow$), the energy dissipated in the plastic hinges is reduced. Thus, the

lateral mass and restraint should contribute more to absorb the energy generated by the blast loading and reduce the demand of ductility. Parameter ψ_M influences the p-I diagrams for the second category of protection. The relative error made if this parameter is not taken into account can reach up to 12 %.

In Section II.3, the influence of the axial elongation of the beam on the ductility demand of the beam is investigated through comparisons between the SDOF and 2-DOF models.

II.3 Two-degree-of-freedom model

The kinematics of the 2-DOF model is first introduced in Section II.3.1.1. The normality rule is described in Section II.3.1.2. The energy conservation considerations are invoked in Section II.3.1.3 to derive the nonlinear governing equation of motion of the substructure, which is presented in Section II.3.1.4. A scaling of the equation of motion is carried out in Section II.3.1.5. Some numerical simulations of frame beams subjected to a given blast loading are presented in Section II.3.2; finally a comparison between the SDOF and 2-DOF models is realized and discussed, to come to by the conclusions of the present Section.

II.3.1 Problem reformulation

II.3.1.1 Description of the problem

In Refs [67, 84], the plastic axial elongation of the beam is shown to affect substantially the dynamic response of the beam in the plastic range when the membrane force becomes significant. A new degree-of-freedom, referring to the axial elongation of the beam $2\Delta_N$ (see Fig. II.15-a), is therefore introduced in the analytical model described previously in Section II.2.1.1.
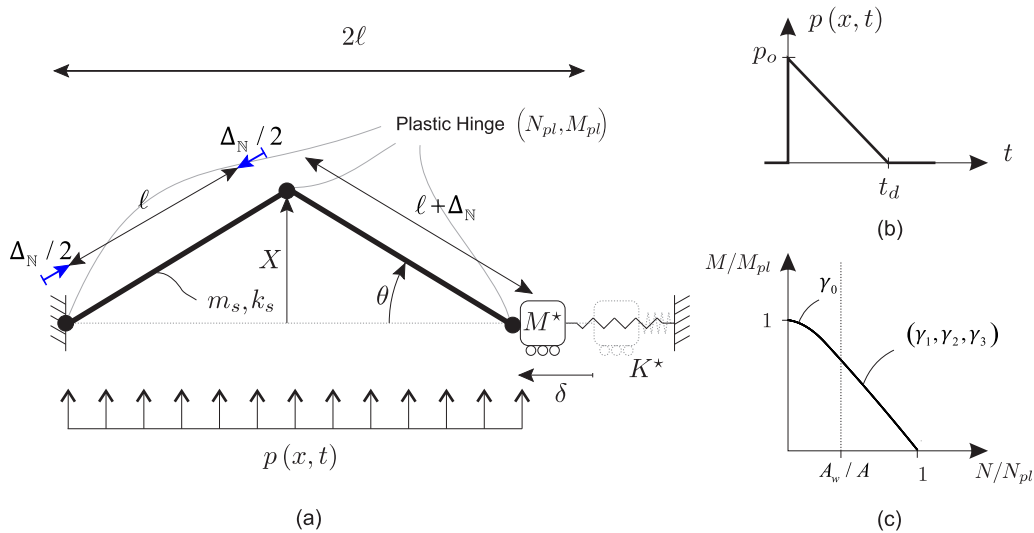
Figure II.15: (a) Sketch of the considered problem, (b) Idealized blast loading, (c) Axial force-bending moment interaction law of a I-shaped beam.

The M-N plastic interaction for I-shaped steel beam (see Fig. II.15-c) reads

$$\left(\frac{M}{M_{pl}}\right) = \begin{cases} 1 - \gamma_0 \left|\frac{N}{N_{pl}}\right|^2 & \text{for } 0 \leq \left|\frac{N}{N_{pl}}\right| \leq \frac{A_w}{A}, \\ 1 - \gamma_1 - \gamma_2 \left|\frac{N}{N_{pl}}\right| - \gamma_3 \left|\frac{N}{N_{pl}}\right|^2 & \text{for } \frac{A_w}{A} \leq \left|\frac{N}{N_{pl}}\right| \leq 1 \end{cases} \quad \text{(II.57)}$$

where coefficients γ_0, γ_1, γ_2 and γ_3 are given by Equ. (I.51).

The elongation of the lateral restraint is modified as follows

$$\delta = \frac{X^2}{\ell} - 2\Delta_N \quad \text{(II.58)}$$

Using an overhead dot to indicate differentiation with respect to time t, the shortening velocity and acceleration of the chord thus read

$$\dot{\delta} = \frac{2}{\ell}X\dot{X} - 2\dot{\Delta}_N \quad ; \quad \ddot{\delta} = \frac{2}{\ell}\left(\dot{X}^2 + X\ddot{X}\right) - 2\ddot{\Delta}_N \quad \text{(II.59)}$$

When the beam is in the plastic regime, the axial deformation of a half beam Δ_N is mainly localized in the plastic hinges as illustrated in Fig. II.15.

II.3.1.2   Normality flow rule

The bending moment-axial force (M-N) plastic interaction of I-shaped steel beam is illustrated in Fig. II.16 and their associated generalized strain rates $\dot{\kappa}$ and $\dot{\epsilon}$ are usually plotted along the corresponding axes of the generalized stresses M and N. These strain rates correspond to the time derivative of the curvature $\dot{\kappa}$ and axial deformation $\dot{\epsilon}$ of the cross-section in which yielding occurs. A consequence of Drucker's stability postulate is that the generalized strain rate vector, which is associated with plastic flow, must be normal to the corresponding generalized stress point on the yielding surface [37]. Indeed, if the plastic flow occurs at point A of Fig. II.16, the strain rate vector is normal to the two-dimensional plastic interaction curve of the generalized stresses M and N. Accordingly, the normality flow rule reads

$$\frac{dM}{dN} = -\frac{\dot{\epsilon}}{\dot{\kappa}} \quad \text{(II.60)}$$

and provides the direction of the generalized strain rate vector only (not its magnitude).
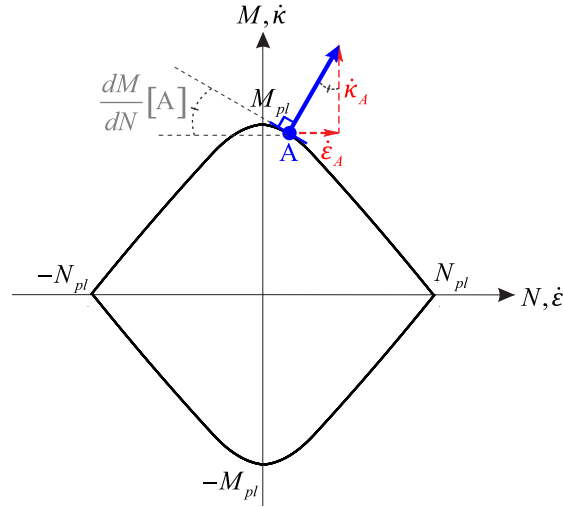
Figure II.16: Yield surface with normality rule.

Assuming that the length of the plastic hinges ℓ_h is constant, that the cross sections remain plane during the deformation (Bernoulli assumption) and the shear deformation is neglected, the generalized strain rates at the ends of a beam half can be expressed as follows

$$\dot{\epsilon} = \frac{\dot{\Delta}_N/2}{\ell_h} \quad ; \quad \dot{\kappa} = \frac{\dot{\theta}}{\ell_h} = \frac{\dot{X}}{\ell_h \ell}. \tag{II.61}$$

Substituting (II.61) into (II.60) provides

$$\frac{dM}{dN} = -\frac{\dot{\Delta}_N \ell}{2\dot{X}} \tag{II.62}$$

which allows to derive the expression of the axial force in the plastic regime as follows

$$\frac{N}{N_{pl}} = \begin{cases} \frac{1}{2\gamma_0}\left(\frac{N_{pl}}{M_{pl}}\frac{\dot{\Delta}_N \ell}{2\dot{X}}\right) & \text{for } 0 \le \frac{N}{N_{pl}} \le \frac{A_w}{A}, \\ \frac{1}{2\gamma_3}\left(\frac{N_{pl}}{M_{pl}}\frac{\dot{\Delta}_N \ell}{2\dot{X}} - \gamma_2\right) & \text{for } \frac{A_w}{A} \le \frac{N}{N_{pl}} \le 1. \end{cases} \tag{II.63}$$

Notice that, in the elastic regime, the axial force reads

$$N = 2k_{EA}\Delta_N \tag{II.64}$$

where $k_{EA} = \frac{EA}{2\ell}$ corresponds to the elastic axial stiffness of the beam.

II.3.1.3   Governing equations

The expression of the elastic and plastic energy U_1 and U_2 stored in the beam and the work W_p done by the blast loading does not change from those described in Section II.2.1.4. However, the strain energy stored in the lateral restraint becomes

$$U_3 = \frac{1}{2}K^\star \delta^2 = \frac{1}{2}K^\star \left(\frac{X^2}{\ell} - 2\Delta_N\right)^2. \tag{II.65}$$

The energy dissipated, axially, in plastic hinges or stored axially in the beam in the elastic regime is given by

$$U_4 = 2N\Delta_N. \tag{II.66}$$

Finally, the total kinetic energy can be written as follows

$$K = \frac{1}{2}M_s\dot{X}^2 + \frac{1}{2}M^\star \dot{\delta}^2 = \frac{1}{2}M_s\dot{X}^2 + \frac{1}{2}M^\star \left(\frac{2}{\ell}X\dot{X} - 2\dot{\Delta}_N\right)^2. \tag{II.67}$$

The dissipation of energy D due to damping is neglected ($D = 0$).

II.3.1.4   Equations of motion

The Lagrange's equations [85] read

$$\begin{cases} -\frac{d}{dt}\left(\frac{\partial K}{\partial \dot{X}}\right) + \left(\frac{\partial K}{\partial X}\right) - \sum\left(\frac{\partial U_i}{\partial X}\right) - \left(\frac{\partial D}{\partial \dot{X}}\right) + \frac{\partial W_p}{\partial X} = 0, \\ -\frac{d}{dt}\left(\frac{\partial K}{\partial \dot{\Delta}_N}\right) + \left(\frac{\partial K}{\partial \Delta_N}\right) - \sum\left(\frac{\partial U_i}{\partial \Delta_N}\right) - \left(\frac{\partial D}{\partial \dot{\Delta}_N}\right) + \frac{\partial W_p}{\partial \Delta_N} = 0 \end{cases} \tag{II.68}$$

which provide the following equations of motion

$$\begin{cases} \left(M_s + 4M^\star\frac{X^2}{\ell^2}\right)\ddot{X} + 4M^\star\frac{X\dot{X}^2}{\ell^2} - 4M^\star\frac{X}{\ell}\ddot{\Delta}_N + F_{int,b} + 2K^\star\frac{X^3}{\ell^2} - 4K^\star\frac{X}{\ell}\Delta_N = p\ell, \\ N = M^\star\left[\frac{2}{\ell}\left(\dot{X}^2 + X\ddot{X}\right) - 2\ddot{\Delta}_N\right] + K^\star\left[\frac{X^2}{\ell} - 2\Delta_N\right], \end{cases} \tag{II.69}$$

with $F_{int,b} = \begin{cases} k_s X & \text{for } X \leq X_y, \\ \frac{4}{\ell}M\left(N\right) & \text{for } X > X_y \text{ and } \dot{X} \geq 0. \end{cases}$

II.3.1.5   Dimensionless formulation

The dimensionless equations of motion read

$$\begin{cases} \left(1 + \psi_M\theta_y^2\overline{X}^2\right)\overline{X}'' + \psi_M\theta_y^2\overline{X}\left(\overline{X}'^2 - \frac{1}{\theta_y^2}\overline{\Delta}_N''\right) + \overline{F}_{int,b} + 2\psi_K\theta_y^2\overline{X}\left(\overline{X}^2 - \frac{2}{\theta_y^2}\overline{\Delta}_N\right) = \overline{p}\left(1 - \frac{\tau}{\tau_d}\right) \\ n = 8\xi\theta_y\psi_K\left(\overline{X}^2 - \frac{2}{\theta_y^2}\overline{\Delta}_N\right) + 4\psi_M\xi\theta_y\left(\overline{X}'^2 + \overline{X}\overline{X}'' - \frac{1}{\theta_y^2}\overline{\Delta}_N''\right) \end{cases} \tag{II.70}$$

with the equivalent internal force in the beam and the M-N plastic interaction respectively given by

$$\overline{F}_{int,b} = \begin{cases} \overline{X} & \text{for } \overline{X} \leq 1, \\ m\left(n\right) & \text{for } \overline{X} > 1 \text{ and } \overline{X}' \geq 0, \end{cases} \tag{II.71}$$

and

$$
m = \begin{cases} 1 - \gamma_0 n^2 & \text{for } 0 \le n \le \frac{A_w}{A}, \\ 1 - \gamma_1 - \gamma_2 n - \gamma_3 n^2 & \text{for } \frac{A_w}{A} \le n \le 1, \end{cases} \tag{II.72}
$$

where $\overline{\Delta}_N = \frac{\Delta_N}{\ell}$ is the dimensionless axial elongation of a half beam.

In the elastic regime, the axial force in the beam is given by

$$
n = 16 \psi_{KEA} \frac{\xi}{\theta_y} \overline{\Delta}_N \tag{II.73}
$$

where $\psi_{KEA} = k_{EA}/k_s$ is the ratio of the axial stiffness of the beam to the flexural stiffness of the beam.

In the plastic regime, the axial force in the beam is provided by the normality rule as follows

$$
n = A_n \left(\frac{\overline{\Delta}_N'}{\overline{X}'} \right) + B_n \tag{II.74}
$$

where the coefficients A_n and B_n are respectively given by

$$
A_n = \begin{cases} \frac{1}{8\xi\theta_y\gamma_0} & \text{for } 0 \le n \le \frac{A_w}{A}, \\ \frac{1}{8\xi\theta_y\gamma_3} & \text{for } \frac{A_w}{A} \le n \le 1, \end{cases} \tag{II.75}
$$

and

$$
B_n = \begin{cases} 0 & \text{for } 0 \le n \le \frac{A_w}{A}, \\ \frac{-\gamma_2}{2\gamma_3} & \text{for } \frac{A_w}{A} \le n \le 1. \end{cases} \tag{II.76}
$$

II.3.2   Numerical solutions

II.3.2.1   Description of the numerical method

The equations of motion (II.70) are rearranged to isolate the accelerations $\overline{X}''$ and $\overline{\Delta}_N''$ in order to use an existing numerical integration scheme, and expressed in a matrix form as follows

$$
\underbrace{\begin{bmatrix} 1 + \psi_M \theta_y^2 \overline{X}^2 & -\psi_M \overline{X} \\ 4\psi_M \xi \theta_y \overline{X} & -\frac{4\psi_M \xi}{\theta_y} \end{bmatrix}}_{=\mathbf{M}(\overline{X})} \begin{bmatrix} \overline{X}'' \\ \overline{\Delta}_N'' \end{bmatrix} = \left[\begin{array}{c} \overline{p}\left(1 - \frac{\tau}{\tau_d}\right) - \psi_M \theta_y^2 \overline{X} \overline{X}'^2 \\ n\left(\overline{\Delta}_N, \overline{\Delta}_N', \overline{X}'\right) - 8\xi\theta_y\psi_K\left(\overline{X}^2 - \frac{2}{\theta_y^2}\overline{\Delta}_N\right) \end{array} \right.
$$
$$
\left. \begin{array}{c} -\overline{F}_{int,b}\left(\overline{X}, m\left(n\left(\overline{\Delta}_N', \overline{X}'\right)\right)\right) - 2\psi_K \theta_y^2 \overline{X}\left(\overline{X}^2 - \frac{2}{\theta_y^2}\overline{\Delta}_N\right) \\ -4\psi_M \xi \theta_y \overline{X}'^2 \end{array} \right]. \tag{II.77}
$$

where $\mathbf{M}\left(\overline{X}\right)$ is the mass matrix of the beam extracted from the frame structure which depends on the transverse deflection.

Non negligible lateral mass $\psi_M \neq 0$

If the lateral mass is non negligible, the mass matrix $\mathbf{M}\left(\overline{X}\right)$ is invertible and the equations of motion can be rewritten as

$$
\begin{bmatrix} \overline{X}'' \\ \overline{\Delta}_N'' \end{bmatrix} = \begin{bmatrix} 1 + \psi_M \theta_y^2 \overline{X}^2 & -\psi_M \overline{X} \\ 4\psi_M \xi \theta_y \overline{X} & -\frac{4\psi_M \xi}{\theta_y} \end{bmatrix}^{-1} \left[\begin{array}{c} \overline{p}\left(1 - \frac{\tau}{\tau_d}\right) - \psi_M \theta_y^2 \overline{X}\overline{X}'^2 \\ n\left(\overline{\Delta}_N, \overline{\Delta}_N', \overline{X}'\right) - 8\xi\theta_y\psi_K\left(\overline{X}^2 - \frac{2}{\theta_y^2}\overline{\Delta}_N\right) \end{array} \right.
$$
$$
\left. \begin{array}{c} -\overline{F}_{int,b}\left(\overline{X}, m\left(n\left(\overline{\Delta}_N', \overline{X}'\right)\right)\right) - 2\psi_K\theta_y^2\overline{X}\left(\overline{X}^2 - \frac{2}{\theta_y^2}\overline{\Delta}_N\right) \\ -4\psi_M\xi\theta_y\overline{X}'^2 \end{array} \right] \tag{II.78}
$$

$$
\begin{bmatrix} \overline{X}'' \\ \overline{\Delta}_N'' \end{bmatrix} = \mathbf{f}\left(\overline{X}, \overline{X}', \overline{\Delta}_N, \overline{\Delta}_N'\right) \tag{II.79}
$$

However, in the vicinity of the maximum deflection, at time τ_{max}, the transverse and axial velocities $\overline{X}'$ and $\overline{\Delta}_N'$ tend to zero leading to an indetermination form "0/0" in the expression of the axial force (see Equ. (II.74)). L'Hospital's rule [86] is required to deal with this indetermination form

$$
\lim_{\tau \to \tau_{max}} \frac{\overline{\Delta}_N'(\tau)}{\overline{X}'(\tau)} \overset{\text{H.R.}}{=} \left(\frac{\overline{\Delta}_N''}{\overline{X}''}\right)_{\tau=\tau_{max}}, \tag{II.80}
$$

resulting in the following expression of the axial force in the vicinity of the maximum deflection

$$
\lim_{\tau \to \tau_{max}} n(\tau) \overset{\text{H.R.}}{=} A_n \left(\frac{\overline{\Delta}_N''}{\overline{X}''}\right)_{\tau=\tau_{max}} + B_n. \tag{II.81}
$$

Thus, the solution requires the use of an implicit numerical integration scheme to handle the indetermination

$$
\begin{bmatrix} \overline{X}'' \\ \overline{\Delta}_N'' \end{bmatrix} = \mathbf{f}\left(\overline{X}, \overline{X}', \overline{X}'', \overline{\Delta}_N, \overline{\Delta}_N', \overline{\Delta}_N''\right). \tag{II.82}
$$

Negligible lateral mass $\psi_M \simeq 0$

If the lateral mass is negligible, the mass matrix $\mathbf{M}\left(\overline{X}\right)$ is not invertible and the equations of motion are rearranged to isolate the acceleration $\overline{X}''$ and velocity $\overline{\Delta}_N'$ (the axial acceleration $\overline{\Delta}_N''$ does not appear in the equations any longer) in the plastic regime as follows

$$
\begin{bmatrix} 1 & 0 \\ 0 & \frac{A_n}{\overline{X}} \end{bmatrix} \begin{bmatrix} \overline{X}'' \\ \overline{\Delta}'_N \end{bmatrix} = \begin{bmatrix} \overline{p}\left(1 - \frac{\tau}{\tau_d}\right) - m\left(n\left(\overline{\Delta}'_N, \overline{X}'\right)\right) - 2\psi_K\theta_y^2\overline{X}\left(\overline{X}^2 - \frac{2}{\theta_y^2}\overline{\Delta}_N\right) \\ B_n - 8\xi\theta_y\psi_K\left(\overline{X}^2 - \frac{2}{\theta_y^2}\overline{\Delta}_N\right) \end{bmatrix},
$$
(II.83)

which can also be written as

$$
\begin{bmatrix} \overline{X}'' \\ \overline{\Delta}'_N \end{bmatrix} = \begin{bmatrix} f_1\left(\overline{X}, \overline{X}', \overline{\Delta}_N, \overline{\Delta}'_N\right) \\ f_2\left(\overline{X}, \overline{X}', \overline{\Delta}_N\right) \end{bmatrix},
$$
(II.84)

which is a mixed-order set of differential equations.

In the elastic regime, the equations of motion become

$$
\begin{bmatrix} 1 & -4\psi_K\overline{X} \\ 0 & 8\frac{\xi}{\theta_y}\left(2\psi_{KEA} + \psi_K\right) \end{bmatrix} \begin{bmatrix} \overline{X}'' \\ \overline{\Delta}_N \end{bmatrix} = \begin{bmatrix} \overline{p}\left(1 - \frac{\tau}{\tau_d}\right) - \overline{X} - 2\psi_K\theta_y^2\overline{X}^3 \\ 8\xi\theta_y\psi_K\overline{X}^2 \end{bmatrix},
$$
(II.85)

which can be simplified as

$$
\begin{bmatrix} \overline{X}'' \\ \overline{\Delta}_N \end{bmatrix} = \begin{bmatrix} f_1\left(\overline{X}\right) \\ f_2\left(\overline{X}\right) \end{bmatrix}.
$$
(II.86)

In case of a negligible lateral mass, the equation of motion (II.86) in the elastic regime shows that the model only depends on the transverse displacement at mid-span of the beam $\overline{X}$. The model can be solved for $\overline{X}$. Then the elongation $\overline{\Delta}_N$ is determined in a post-processing phase.

II.3.2.2 Comparison of SDOF and 2-DOF models

Figures II.17-a (or -c) and -b (or -d) respectively illustrate the time-history of the mid-span displacement of the beam and the M-N plastic interaction curve at plastic hinges predicted by the SDOF and 2-DOF analytical models for $\psi_K = 1$ and $\psi_M = 0$ (or $\psi_M = 20$). The other parameters are: $\xi = 2\%$; $\theta_y = 13\,\mathrm{mrad}$; $\overline{p} = 10$; $\tau_d = 1.5$; $\overline{I} = 7.5$. Four points labeled A, B, C and D describe the different stages of the response of the beam as previously done in Section II.2.3.2.

Firstly, let us consider the absence of lateral mass ($\psi_M = 0$) but taking into account the presence of lateral restraint ($\psi_K = 1$) in order to study its influence on the the axial elongation and transverse displacement of the beam (see Figs. II.17-a and -b). At point A, the plastic mechanism of the beam has just formed, meaning that $\overline{X} = 1$ (see Fig. II.17-a). The plastic bending moment is not affected by the small membrane action (see Fig. II.17-b). Between points A and B, the deflection increases to reach a value of 19 and 19.8 respectively for the SDOF and 2-DOF models while their corresponding membrane force $n = N/N_{pl}$ tops out to 0.71 and 0.51 (at point B). Due to the application of the normality rule in the plastic stage for 2-DOF model, the effect of the lateral restraint is mitigated by the axial

deformability of the plastic hinges, leading to a lower maximum axial force in comparison to the SDOF model.

After reaching the maximum displacement, the beam experiences an elastic unloading in the opposite direction. Indeed, the lateral restraint returns a part of its elastically stored energy to the beam. At point C, the plastic mechanism is developed in the opposite direction. Finally, at point D, the beam starts vibrating indefinitely elastically. The displacement predicted by the SDOF model substantially drops from point B to D as the energy stored in the lateral restraint is overestimated in comparison to the 2-DOF model, due to the neglected energy dissipated axially in plastic hinges.

For the second case ($\psi_K = 1$ and $\psi_M = 20$, see Figures II.17-c and -d), the membrane force is largely overestimated by the SDOF model leading to a reduction of $18\,\%$ of the plastic bending resistance when the plastic mechanism is formed at point A (see Fig. II.17-d). The membrane force continues to increase faster and even reaches the axial plastic resistance due to the inaccurate assessment of the acceleration of the lateral mass $\ddot{\delta}$. Indeed, the SDOF model neglects the positive contribution of the axial acceleration $\ddot{\Delta}_N$ on the membrane force $M^\star \ddot{\delta}$ (see Equ. (II.59)). As a result, the bending plastic resistance is underestimated through the application of the M-N plastic interaction, leading to the overestimation of the maximum deflection predicted by the SDOF model (Fig. II.17-c). Subsequent to the reaching of the axial plastic resistance, the membrane force starts decreasing due to the deceleration of the lateral mass until reaching point B, corresponding to the beginning of the unloading regime.

The unloading part of the curves predicted by the SDOF and 2-DOF models are different for the same reasons as mentioned previously for $\psi_K = 1$ and $\psi_M = 0$ (Fig. II.17-c). The prediction of the unloading regime of the beam is also essential for the study of the dynamic buckling of the neighbor columns under blast loading since the inertial forces along the beam will generate further compression in the column, additional to dead and live loads from upper stories, during this stage of motion; this aspect will be more deeply addressed in Chapter IV.

The permanent deflection at point D (Fig. II.17-c) seems to be equal to 0 for SDOF model, as if the beam has recovered its initial position without any damage. That approach is on the unsafe side since the beam is severely damaged after the blast event as it actually exhibits a permanent deflection of 15.6 at point D (see curve for 2-DOF model).
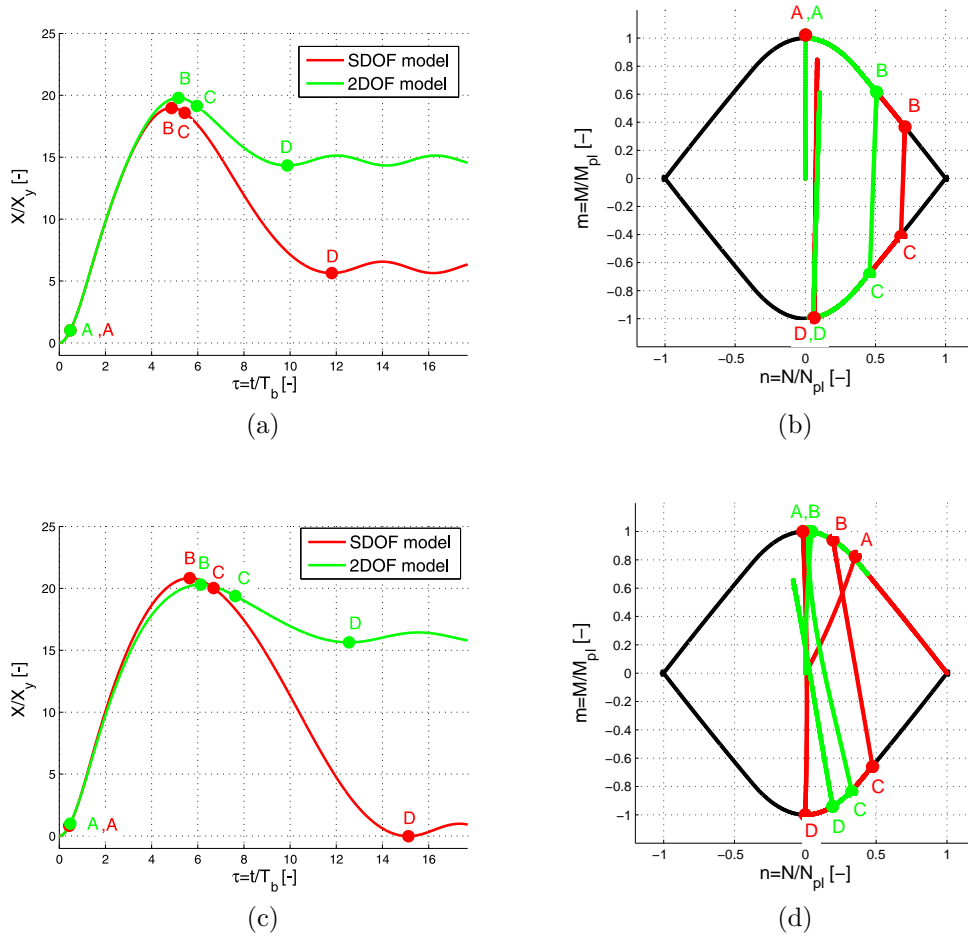
Figure II.17: Comparison of SDOF and 2-DOF models - influence of the parameters ψ_K and ψ_M. (a) Displacement versus time and (b) M-N plastic interaction for $\psi_K = 1$; $\psi_M = 0$. (c) Displacement versus time and (d) M-N plastic interaction for $\psi_K = 1$; $\psi_M = 20$. The other parameters are as follows: $\xi = 2\%$; $\theta_y = 13\,\text{mrad}$; $\overline{p} = 10$; $\tau_d = 1.5$; $\overline{I} = 7.5$.

Figures II.18-a and -b respectively illustrate the pressure-impulse diagram of a beam for the lateral mass to the beam mass ratio ψ_M of 0 and 20, and a lateral restraint stiffness to beam flexural stiffness ratio ψ_K that varies from 0 to 3. The iso-damage curves are derived for a target ductility ratio μ of 20, corresponding to threshold value of the second level of protection to the beam (see Table I.5), as it allows to better understand the effect of axial elongation on the dynamic behavior of the beam in large displacements and to compare the analytical models. Figures II.18-c and -d illustrate the corresponding maximum axial force $n = N/N_{pl}$ respectively predicted by the 2-DOF and SDOF models, for $\psi_K \in [0;3]$ and $\psi_M = 0$. The other parameters are $\xi = 2\%$ and $\theta_y = 13\,\text{mrad}$.

Relative errors on the impulsive and quasi-static asymptotes ϵ_I and ϵ_p by the SDOF model in comparison to the 2-DOF model are defined by

$$\epsilon_I = \frac{\overline{I}_{\infty,SDOF} - \overline{I}_{\infty,2DOF}}{\overline{I}_{\infty,2DOF}} \quad ; \quad \epsilon_p = \frac{\overline{p}_{\infty,SDOF} - \overline{p}_{\infty,2DOF}}{\overline{p}_{\infty,2DOF}} \tag{II.87}$$

where $\overline{I}_{\infty,SDOF}$ and $\overline{I}_{\infty,2DOF}$ are respectively the impulsive asymptotes predicted by the SDOF and 2-DOF models, while $\overline{p}_{\infty,SDOF}$ and $\overline{p}_{\infty,2DOF}$ are respectively the corresponding quasi-static asymptotes.

In the absence of lateral mass (see Fig. II.18-a), the SDOF model is on the unsafe side as it neglects the axial deformation of the beam as stated earlier. For $\psi_K \leq 1$, the iso-damage curves seem to be very close, meaning that the SDOF model is convenient to be applied in this range because the membrane force is rather small whereas it is not valid beyond this range. The relative errors ϵ_I and ϵ_p are limited for $\psi_K \leq 1$, since they respectively reach 5.8 % and 2.8 % (see Table II.4). However, beyond this range, they respectively surge to 21.3 % and 46 % for $\psi_K = 3$.

As illustrated in Figs. II.18-c and -d, the positive contribution of the lateral restraint on the dynamic response of the beam is overestimated by the SDOF model. For instance, the curve corresponding to $\psi_K = 1$ presents an average of the maximum axial forces n that is equal to 0.52 for the 2-DOF model while it is equal to 0.81 for the SDOF model while it is equal. As explained earlier, the axial deformability of the plastic hinges attenuates the membrane force associated with the presence of the elastic lateral restraint. The normal force predicted by the SDOF model (Fig. II.18-d) is steady along an iso-damage curve since it only depends on the stiffness of the lateral restraint and the demand of ductility in the absence of lateral mass (see Equ. (II.30)).

If the lateral mass is considered (see Fig. II.18-b), the impulsive region of the p-I diagram is not well assessed by the SDOF model, with a relative error on the impulsive asymptote ϵ_I of 10.7 % for $\psi_K = 0$ and $\psi_M = 20$ while it was equal to 0 for $\psi_K = 0$ and $\psi_M = 0$ (see Table II.4) as membrane forces are developing in such a configuration. As explained earlier, the acceleration of the lateral mass and thus, the membrane force are overestimated by the SDOF model, resulting in an underestimation of the plastic resistance of the beam. That involves a smaller impulse delivered to the beam to reach a given ductility in comparison to that predicted by the 2-DOF model. However, the effect of the lateral mass ψ_M is counterbalanced by the effect of the lateral restraint ψ_K in the impulsive regime, involving an increase of the impulse asymptotic value when ψ_K varies from 0 to 3 (see Table II.4) leading to a reduction of the error ϵ_I in terms of absolute value (see Table II.4).

Figures II.19-a and -c respectively illustrate the pressure-impulse diagram of a beam for ψ_K equal to 0 and 1, and ψ_M varying from 0 to 30. Figures II.19-b and -d show a zoom of the impulsive area of the p-I diagrams illustrated in Figs. II.19-a and -c. The iso-damage curves are derived for a target ductility ratio μ of 20 and the other parameters are $\xi = 2 \%$ and $\theta_y = 13$ mrad.

In the absence of lateral restraint (Figs. II.19-a and -b), the curves of the p-I diagram predicted by the 2-DOF model are very close to each other in contrast with these predicted by the SDOF model. As observed, the lateral mass has a positive role on the dynamic behavior of the beam as it globally increases the inertia of the substructure and reduces therefore the impulse to reach a given target ductility for the 2-DOF model. However, as discussed earlier,

the SDOF model overestimates the membrane force when a lateral mass is considered, which results in a reduction of the impulse to get a target ductility.

Irrespective of the lateral mass to the beam mass ratio ψ_M, the error in the quasi-static area of the p-I diagram made by the SDOF model is equal to 0 as shown in Table II.5. This is due to the slow dynamics of the system which annihilates the effect of the lateral mass. However, in the impulsive regime, the error grows with the ratio ψ_M and reaches a maximum value of 18.3 % for $\psi_M = 30$.

When the lateral restraint is taken into account (Figs. II.19-c and -d), the curves predicted by the SDOF and 2-DOF models get closer to each other than previously, meaning that the effect of the parameter ψ_M is significantly reduced with the increase of the parameter ψ_K. In the quasi-static regime, the relative error ϵ_p resulting from the SDOF model is different from 0 only due to the presence of the lateral restraint (Table II.5). Indeed, the lateral mass does not participate to the dynamic behaviour of the substructure in the quasi-static regime. In the impulsive regime, the lateral restraint compensates for the effect of the lateral mass, involving a smaller relative error in the impulsive asymptotic solutions although it reaches 8.2 %.

It can be shown that the effect of the lateral mass can be neglected if $\psi_M \leq 5$, since the maximum relative error between the curves $\psi_M = 0$ and $\psi_M = 5$ is equal to 1 % with other parameters varying in their practical ranges of interest.

	$\psi_M = 0$			
	$\psi_K = 0$	$\psi_K = 1$	$\psi_K = 2$	$\psi_K = 3$
ϵ_I [%]	0	2.8	10.9	21.3
ϵ_p [%]	0	5.8	22.1	46
	$\psi_M = 20$			
	$\psi_K = 0$	$\psi_K = 1$	$\psi_K = 2$	$\psi_K = 3$
ϵ_I [%]	−10.7	−5.9	−1.1	14.6
ϵ_p [%]	0	8.6	14.1	37.2

Table II.4: Relative error on the impulsive and quasi-static asymptotic solutions for ψ_K ($\psi_K \in [0; 3]$) and ψ_M ($\psi_M \in \{0, 20\}$). The other parameters are $\xi = 2\,\% \, ; \, \theta_y = 13\,mrad$.
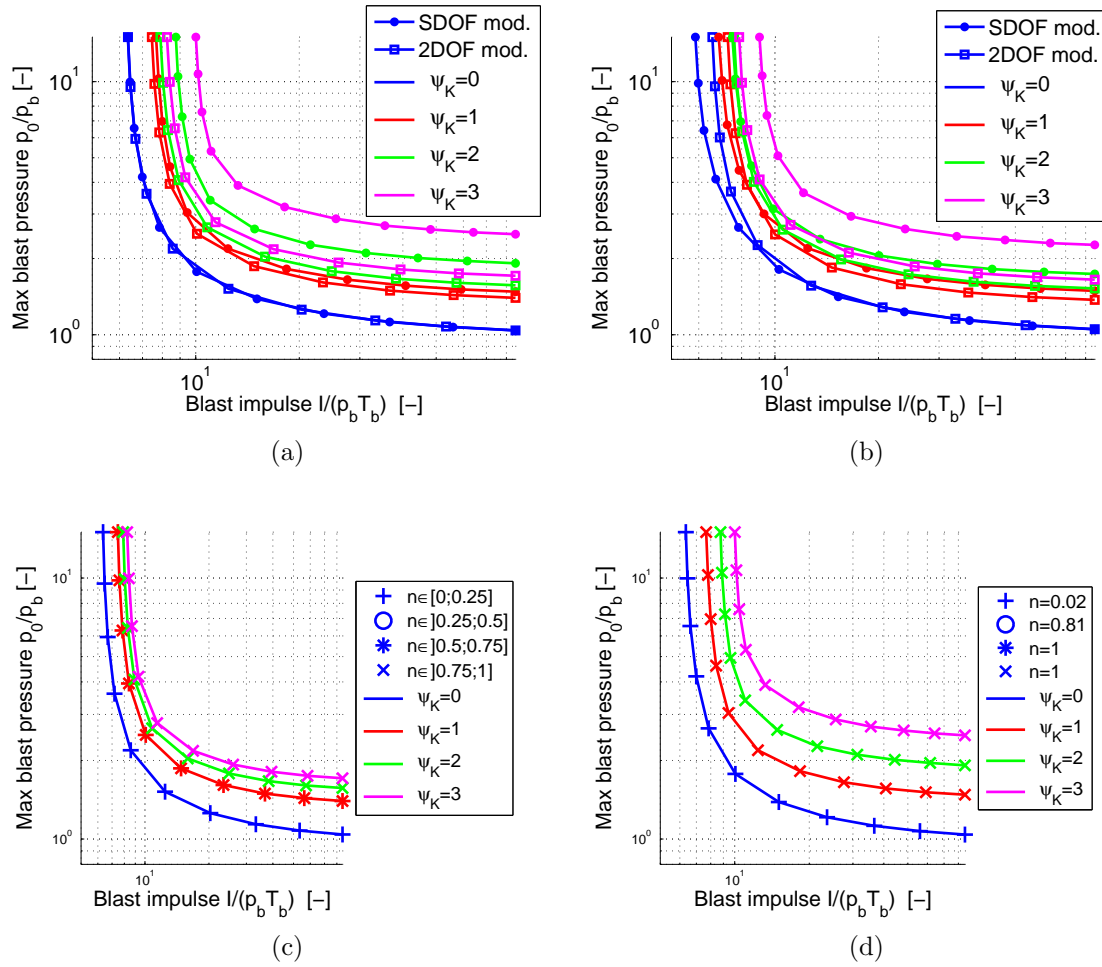
Figure II.18: Comparison of normalized p-I diagrams in logarithmic axes between SDOF and 2-DOF models for parameter ψ_K varying from 0 to 3 to reach a ductility $\mu = 20$. (a) $\psi_M = 0$, (b) $\psi_M = 20$. Corresponding maximum axial force of Fig. II.18-a predicted by (c) the 2-DOF model, and (d) SDOF model. The other parameters are $\xi = 2\,\%$; $\theta_y = 13\,\mathrm{mrad}$.

	$\psi_K = 0$			
	$\psi_M = 0$	$\psi_M = 10$	$\psi_M = 20$	$\psi_M = 30$
ϵ_I [%]	0	-3.6	-10.8	-18.3
ϵ_p [%]	0	0	0	0
	$\psi_K = 1$			
	$\psi_M = 0$	$\psi_M = 10$	$\psi_M = 20$	$\psi_M = 30$
ϵ_I [%]	2.9	2.6	-5.8	-8.2
ϵ_p [%]	5.8	8	8.6	8.3

Table II.5: Relative error on the impulsive and quasi-static asymptotic solutions for ψ_M ($\psi_M \in [0; 30]$) and ψ_K ($\psi_K \in \{0; 1\}$). The other parameters are $\xi = 2\,\%$; $\theta_y = 13\,\mathrm{mrad}$.
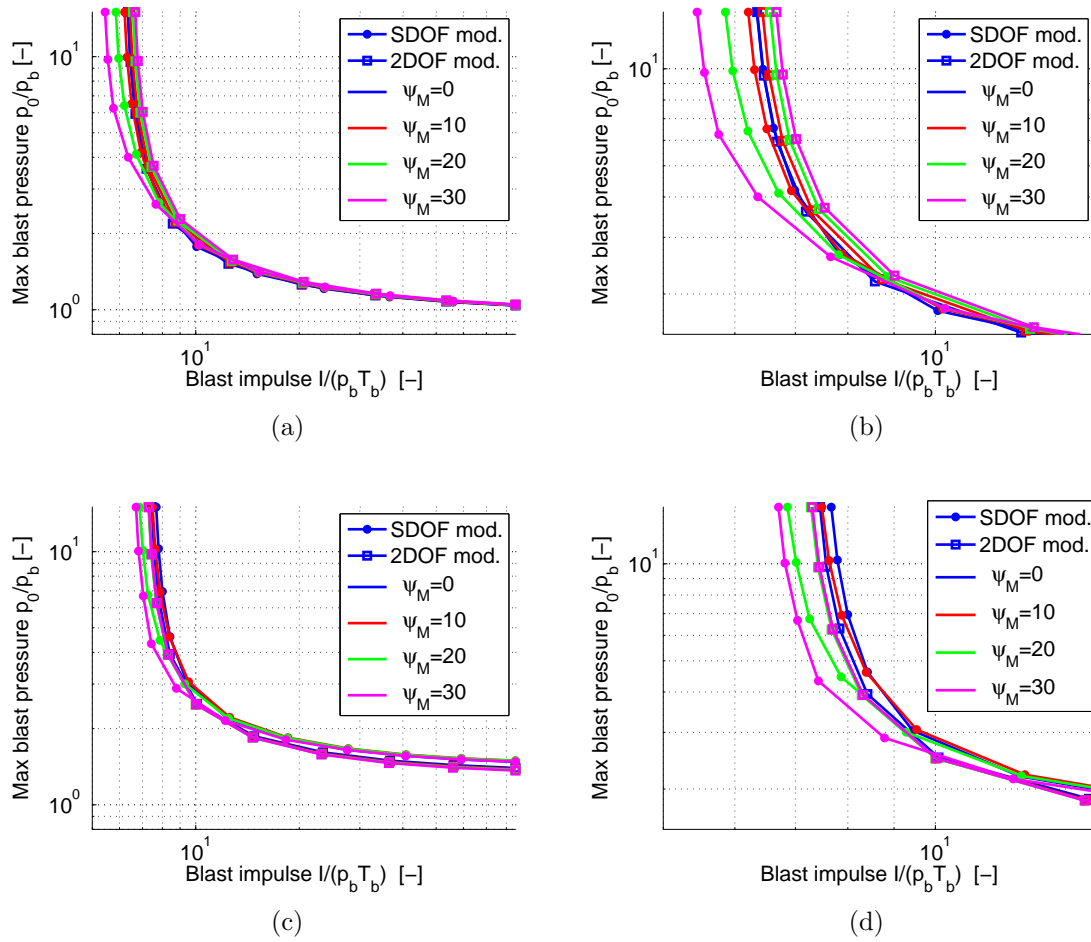
Figure II.19: Comparison of normalized p-I diagrams in logarithmic axes between SDOF and 2-DOF models for parameter ψ_M varying from 0 to 30 to reach a ductility $\mu = 20$. (a)-(b) $\psi_K = 0$, (c)-(d) $\psi_K = 1$. The other parameters are $\xi = 2\,\%$; $\theta_y = 13\,\mathrm{mrad}$.

II.3.3   Conclusions

A new degree-of-freedom, defined as the axial elongation of the beam, is introduced in the model of a frame beam extracted from a whole structure and subjected to internal blast loading. The purpose is to study the effect of this new DOF on the dynamic behaviour of the beam, taking account the non-linear membrane force, the lateral restraint and mass provided by the IAP of the structure, the M-N plastic interaction and the corresponding normality rule. The shear deformation and failure are still neglected in the analytical 2-DOF model. In order to use the normality rule, the length of the plastic hinges ℓ_h is assumed constant and the cross sections are supposed to remain plane during the deformation (Bernoulli assumption).

The numerical scheme to solve all the equations depends on the value of the parameter ψ_M, which is considered as negligible if $\psi_M \leq 5$ since the corresponding error is smaller than $1\,\%$. Moreover, in the vicinity of the maximum transverse deflection, L'Hospital's rule is

used to handle the indetermination form appearing in the normality rule due to the ratio of transverse to axial velocities.

After carrying out the analysis of the model, the effect of the lateral restraint on the dynamic response of the beam is shown to be mitigated by the axial deformability of the plastic hinges, leading to a lower maximum axial force predicted by the 2-DOF model in comparison to SDOF model, the SDOF model is on the safe side regarding the membrane force that is applied to the IAP of the structure. However, as a result of neglecting the axial deformation of the beam, the maximum deflection predicted by the SDOF model is smaller than that predicted by the 2-DOF model, inducing that the SDOF model is on the unsafe side for the beam. The relative errors made by the SDOF model in comparison to 2-DOF model in the quasi-static and impulsive regimes respectively reach 46% and 21.3% for $\mu = 20$, $\psi_K = 3$ (great value), $\psi_M = 0$, $\xi = 2\%$ and $\theta_y = 13$ mrad although both analytical models still assume that the lateral restraint remains elastic.

Concerning the effect of the lateral mass on the dynamic behavior of the beam, it is shown that the membrane force is significantly overestimated by the SDOF model (on the safe side) as the axial acceleration of the beam is neglected. As a result of application of the M-N plastic interaction, the maximum deflection predicted by the SDOF model is greater than that predicted by the 2-DOF model, leading to a SDOF model that is on the safe side for the beam. The relative errors made by the SDOF model in comparison to 2-DOF model in the quasi-static and impulsive regimes are respectively equal to 0% and 18.3% for $\mu = 20$, $\psi_K = 0$, $\psi_M = 30$ (great value), $\xi = 2\%$ and $\theta_y = 13$ mrad although the set of parameters corresponds to an extreme case.

Thus, taking into account the axial deformation of the beam is really important since it could significantly affect the level of permanent damage of the beam and neglecting it will lead to an overestimation of the axial force that is applied to the IAP of the structure.

II.4 Numerical validation with FinelG

The assumptions on the FinelG modeling are firstly exposed in Section II.4.1, and the values of the dimensionless parameters used in the benchmark study are given in Section II.4.2. Then, a comparison of the results predicted through the FinelG models and the 2-DOF model is carried out in Section II.4.3, which includes some discussions on the limitations of the models. Finally, Section II.4.5 draws the conclusion of the present section.

II.4.1 Modelling assumptions

In order to evaluate the accuracy of the analytical 2-DOF model of the beam under blast loading (see Fig. II.15-a), their corresponding results are compared with those of the FinelG models. The beam is modeled using 2D Euler-Bernoulli beam elements available in FinelG software (element type 33 for plane frames) with a large number of finite elements (200) to capture well the higher modes of vibration as well as some specific phenomena such as the possible traveling of plastic hinges (Fig. II.20). However, the shear deformation is not considered in the definition of the finite element and the kinematic-plastic constitutive

material law does not account for the effect of shear on plastic resistance. The strain rate effect as well as the strain hardening are also disregarded. No initial geometric imperfection nor residual stresses are considered in the modeling as the behavior of the beam is mainly investigated in plastic and large displacement domains, which are not significantly affected by the initial imperfections.

The beam is subjected to a uniformly distributed transverse blast loading as illustrated in Fig. II.15-b. The initial displacement, velocity and acceleration of the beam-column are equal to 0. The dynamic analysis is carried out using the implicit time integration scheme of Newmark with constant acceleration parameters [87] and a very small time step of integration $\Delta t/T = 6/1000$ to provide accurate responses of the beam under impulsive regime. This model will be called later on "the FinelG model".

In parallel to the FinelG model, a "simplified FinelG model" is also performed in order to validate the analytical model by making similar assumptions:

○ the plasticity is localized in four finite elements located at mid-span and at the ends of the beam. Between these sections, the beam is assumed to be indefinitely elastic and the phenomenon of traveling plastic hinges is therefore prevented;

○ vertical inertia only plays a role in the dynamic behavior of the beam (horizontal and rotational inertial forces of the beam are neglected).

Concerning the numerical results (e.g. the internal forces), they are improved using an 8th-order lowpass digital Butterworth filter with normalized cutoff frequency[1] of 0.08 for bending moment, and of 0.04 for normal and shear forces.
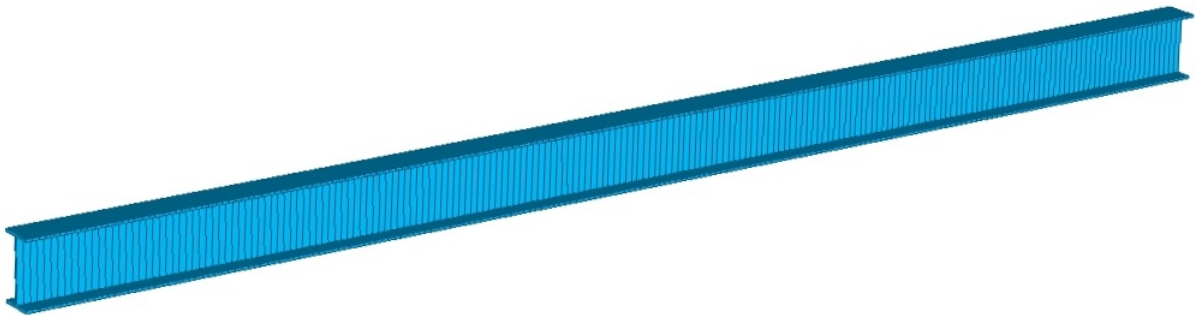

Figure II.20: Modelling of the beam extracted from the structure with element type 33 for plane frames.

II.4.2   Benchmark

A steel beam made of an IPE 270 profile with a S355 steel grade and an elastic modulus E of 210000 MPa is considered. The lineic mass of the reinforced concrete floor m_s and the

---

[1]Defined as the ratio of the cutoff frequency to Nyquist frequency.

length 2ℓ of the beam are respectively equal to $2500 \, \text{kg/m}$ and $5.4 \, \text{m}$. The plastic bending resistance M_{pl}, axial resistance N_{pl} and shear resistance V_{pl} of the beam are respectively equal to $163.5 \, \text{kN.m}$, $1562 \, \text{kN}$ and $453.8 \, \text{kN}$. According to Lescouar'ch's formula (see Equ. (II.57)), the coefficients γ_0, γ_1, γ_2 and γ_3 of M-N plastic interaction are respectively equal to 1.593, -0.212, 1.134 and 0.078 for strong axis bending. The ratio of the web area to the cross-section area A_w/A, corresponding to the axial force N/N_{pl} for which the plastic neutral axis moves from the web to a flange, is equal to 0.37. Concerning the mechanical properties of the IAP of the structure, the parameter $\psi_K = K^\star/k_s$ can be equal to 0 or 1 while the parameter $\psi_M = 6M^\star/m_s\ell$ to 0 or 20. The peak overpressure $\bar{p} = p_0/p_b$ and the positive phase duration $\tau_d = t_d/T_b$ of the blast loading generally take three couples of values $(1.5, 100)$, $(10, 1.5)$ and $(100, 0.15)$ corresponding to quasi-static, dynamic and impulsive blast loadings. The characteristic displacement, pressure and time are respectively

$$X_y = 0.034 \, \text{m} \quad ; \quad p_b = 89 \, \text{kN/m} \quad ; \quad T_b = 25 \, \text{ms}. \tag{II.88}$$

II.4.3 Comparison of FinelG and 2-DOF models

II.4.3.1 Case 1: $\psi_M = 0$ and $\psi_K = 1$

Quasi-static blast loading $(\bar{p}, \tau_d) = (1.5, 100)$

Figure II.21-a illustrate the time-history of mid-span deflection of the beam predicted by FinelG and 2-DOF models. Figure II.21-b depicts the M-N plastic interaction curves at mid-span and at the ends of the beam. A very good agreement is achieved between the FinelG results and analytical estimations since the error made by the 2-DOF model on the prediction of maximum deflection stands at $1.6 \, \%$ (Fig. II.21-a). A discrepancy is observed between the FinelG M-N interaction curves in Fig. II.21-b at mid-span cross-section because the simplified FinelG model assumes that the plasticity is localized in a confined central region of the beam, involving an abrupt change of curvature at mid-span of the beam which results in a yield propagation over the whole depth of the mid-span cross-section. On the contrary, the FinelG model enables yielding to extend all along the length of the member, resulting in a curvature at mid-span of the beam that is smaller than that predicted by the simplified FinelG model which leads to a part of the web that remains elastic even in large displacements. At the ends of the beam, the plasticity develops similarly for both numerical models explaining why the curves nearly coincide.
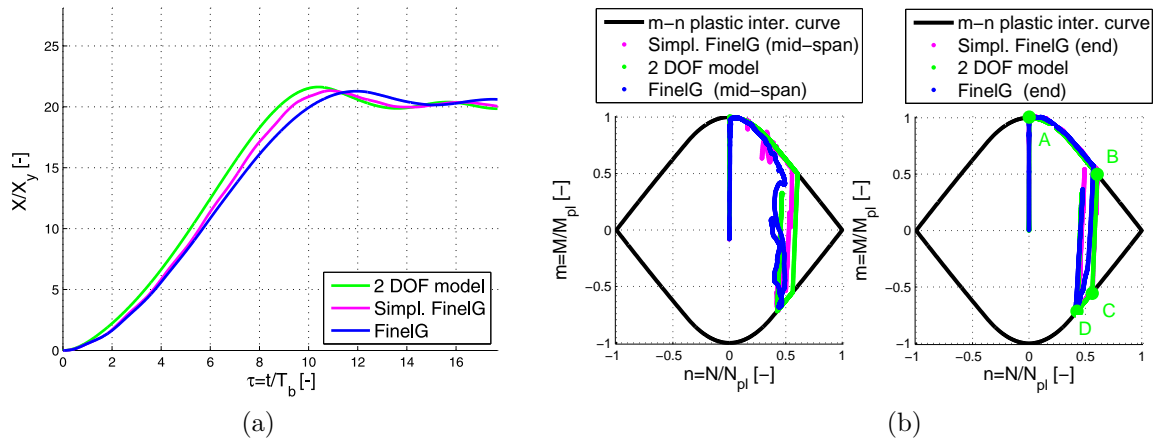
Figure II.21: Comparison of FinelG and analytical results. (a) Mid-span deflection versus time; (b) M-N plastic interaction considering the following set of parameters: $\psi_K = 1$; $\psi_M = 0$; $\xi = 2\,\%$; $\theta_y = 13\,\mathrm{mrad}$; $\overline{p} = 1.5$; $\tau_d = 100$; $\overline{I} = 75$.

Figures II.22-a and -b respectively illustrate the axial force vs. axial beam elongation graph and time-histories of elongations of the spring and the beam. As stated earlier, the points A, B, C and D enable to describe the transitions from elastic to plastic regimes, or the opposite, as illustrated in Fig. II.21-b. The axial force and the elongation are negligible when the plastic mechanism is formed (see Fig II.22-a). Subsequent to the reaching of point A, the axial force, derived from the normality rule (see Equ. (II.74)), increases until reaching the maximum transverse deflection corresponding to point B. Then, an elastic unloading regime is observed between the points B and C; the slope of line BC corresponds to the elastic axial stiffness of the beam. From C to D, the M-N plastic interaction is crossed in its negative part, and the normality rule is again used. At point D, the beam starts vibrating elastically indefinitely. Analytical estimations through Equs. (II.74) and (II.73) provide is very accurate in comparison to the numerical FinelG results. The maximum axial deformation at point B obtained with the FinelG model is greater than that captured by the 2-DOF model because of the propagation of plasticity along the beam which makes the beam more deformable. The analytical and simplified models assume that the length of the plastic hinges remain constant during the motion of the beam which is actually not the case.

Concerning the axial elongations of the beam $2\Delta_N/\ell$ and the lateral restraint δ/ℓ, it is shown that they reach the same order of magnitude (see Fig. II.21-b). The kinematic condition provided by Equ. (II.58) is satisfied by the simplified FinelG model, as the sum of the axial elongation of the beam and the lateral restraint $\delta_{tot}/\ell = \delta/\ell + 2\Delta_N/\ell$ is equal to X^2/ℓ^2. However, the FinelG model predicts a discrepancy between them due to deformed shape of the beam which is not bilinear as assumed in the models, see Fig. II.23-b. The deflected shape of the beam is shown to be different from a bilinear function corresponding to two straight parts connected by plastic hinges (Fig. II.23-a). Nevertheless, this non-linear geometrical aspect does not substantially affect the ductility of the beam (Fig. II.21-a).
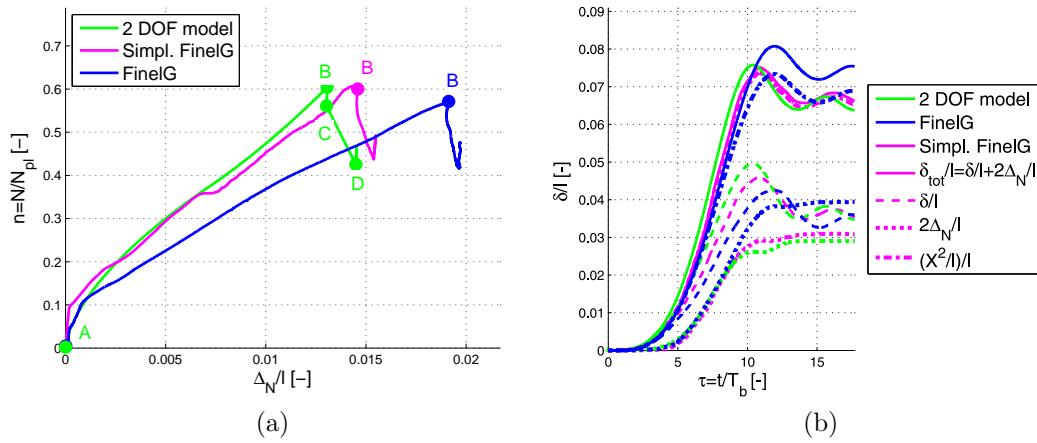
Figure II.22: Comparison of FinelG and analytical results. (a) End axial force vs. axial elongation of the beam; (b) time histories of elongations of the spring and the beam considering the following set of parameters: $\psi_K = 1$; $\psi_M = 0$; $\xi = 2\,\%$; $\theta_y = 13\,\mathrm{mrad}$; $\bar{p} = 1.5$; $\tau_d = 100$; $\bar{I} = 75$.
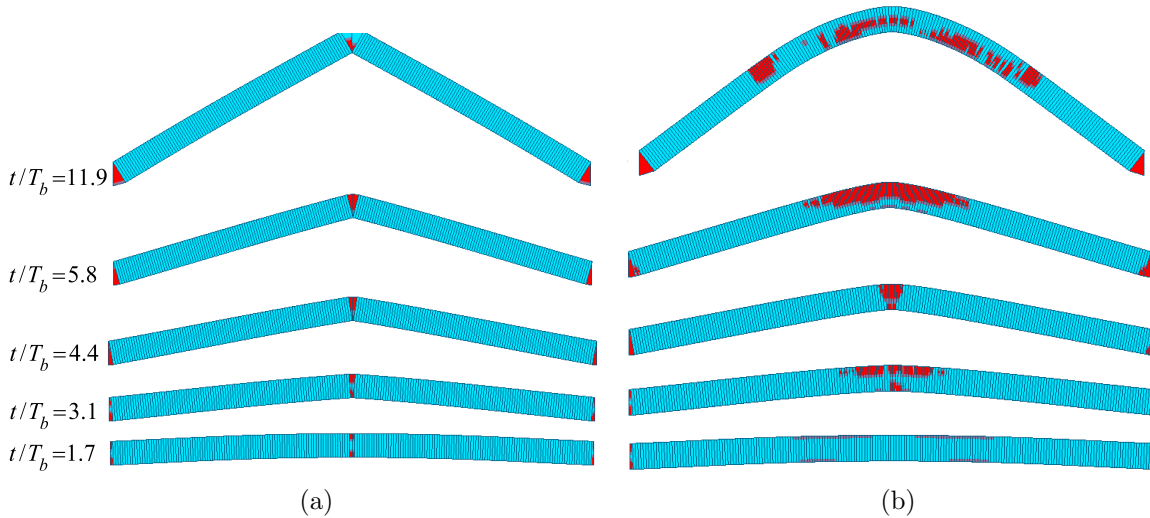
Figure II.23: Comparison of the two FinelG models. Yield zones predicted by (a) the simplified FinelG model and (b) FinelG model, considering the following set of parameters: $\psi_K = 1$; $\psi_M = 0$; $\xi = 2\,\%$; $\theta_y = 13\,\mathrm{mrad}$; $\bar{p} = 1.5$; $\tau_d = 100$; $\bar{I} = 75$.

Figure II.24 depicts the bending moment-shear force (M-V) interaction predicted by FinelG. M-V plastic interaction criteria is not defined in FinelG, although it should be considered since the shear force V/V_{pl} is greater than 0.5. As a consequence, a new degree-of-freedom defined as the shear angle should be introduced in the analytical and numerical models. The generalized strain rate vector is normal to the three-dimensional M-N-V plastic surface (see

Fig. I.22-b), thus providing two relationships expressing internal forces in terms of shear angle, axial elongation and rotation of the plastic hinges in plastic regime. This constitute a perspective to the proposed model.
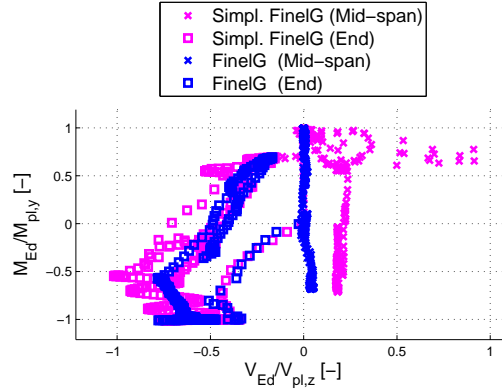
Figure II.24: Bending moment-shear force (M-V) interaction predicted by the FinelG software, considering the following set of parameters: $\psi_K = 1$; $\psi_M = 0$; $\xi = 2\%$; $\theta_y = 13\,\text{mrad}$; $\overline{p} = 1.5$; $\tau_d = 100$; $\overline{I} = 75$.

Impulsive blast loading $(\overline{p}, \tau_d) = (100, 0.15)$

Figures II.25-a and -b respectively illustrate the time-history of mid-span deflection and the M-N plastic interaction curves at mid-span and at the ends of the beam. The error made on the ductility by the simplified FinelG and analytical model in comparison to the FinelG one respectively stand at 9% and 7% on the safe side (see Fig. II.25-a) because the peak overpressure of the blast loading is so great that higher modes of vibration significantly contribute to the dynamic response of the beam at the beginning of the blast event [88, 89]. These higher modes generate plastic hinges that travel along the length of the member and coalesce at mid-span of the beam as illustrated in Fig. II.26 [67, 37]. This phenomenon dissipates more energy than assuming one plastic hinge localized and fixed in the central region during all the blast event, that accounts for the smaller deflection predicted by the FinelG model (Fig. II.25-a).

It should be noticed that only one plastic hinge appears in the middle of the beam for the quasi-static blast loading since the peak overpressure $\overline{p} = p_0/p_b = 1.5$ is smaller than 3 (see Fig. II.23-b). However, beyond this range $(\overline{p} > 3)$, the initial locations of the plastic hinges from the supports are given by a proportion $\sqrt{3/4\overline{p}}$ of the length of the beam 2ℓ [37]. In our case, the plastic hinges are located at a distance of 9% of the length of the beam from the supports of the beam (see Fig. II.26 for $t/T_b = 0.07$), as the peak overpressure $\overline{p}$ is equal to 100.

In addition, the simplified FinelG and analytical models disregard the rotational and horizontal inertial forces along the beam, which have a positive contribution to the dynamic

behaviour of the beam since they slow it down. In Fig. II.25-b, the axial force predicted by the FinelG model at mid-span of the beam seems to present a large discrepancy in comparison to that captured by the simplified model because of the horizontal inertia distribution along the beam. At the ends of the beam, the axial force is well captured by the analytical model because of the satisfaction of the boundary conditions related to presence of lateral mass and restraint.
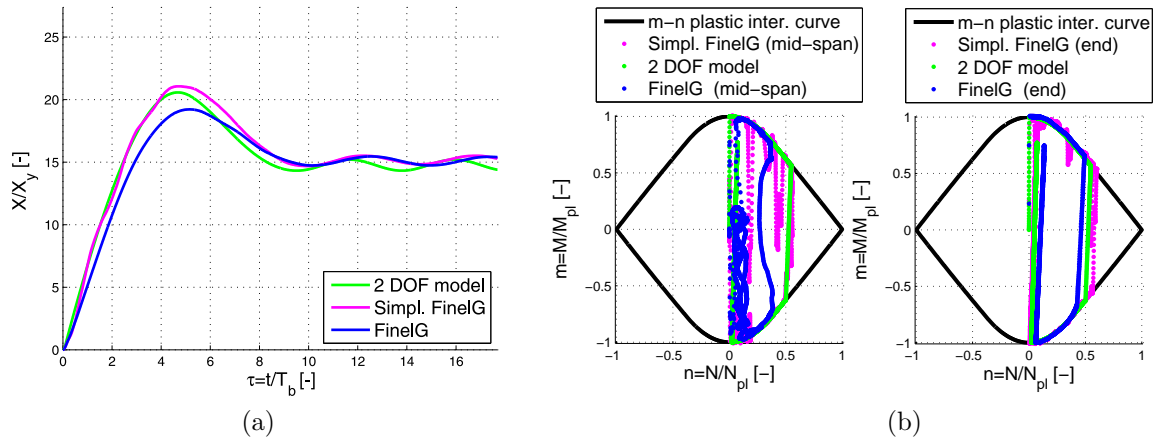
Figure II.25: Comparison of FinelG and analytical results. (a) Mid-span deflection versus time; (b) M-N plastic interaction considering the following set of parameters: $\psi_K = 1$; $\psi_M = 0$; $\xi = 2\%$; $\theta_y = 13\,\mathrm{mrad}$; $\bar{p} = 100$; $\tau_d = 0.15$; $\bar{I} = 7.5$.
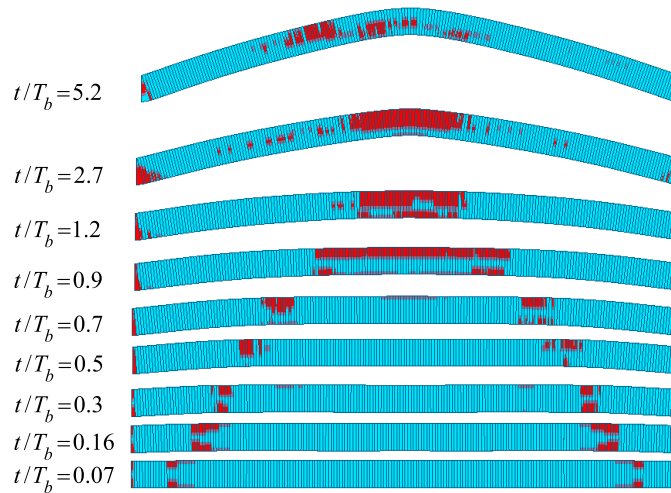
Figure II.26: Comparison of FinelG and analytical results. Yield zones considering the following set of parameters: $\psi_K = 1$; $\psi_M = 0$; $\xi = 2\%$; $\theta_y = 13\,\mathrm{mrad}$; $\bar{p} = 100$; $\tau_d = 0.15$; $\bar{I} = 7.5$.

Dynamic blast loading $(\bar{p}, \tau_d) = (10, 1.5)$

Figures II.27-a and -b respectively illustrate the time-history of mid-span displacement of the beam and the axial force vs. elongation. The analytical model predicts the deflection curve with full accuracy in comparison to the simplified model (see Fig. II.27-a), and the errors involved are within 6 %. The traveling plastic hinge phenomenon accounts for the errors on ductility although they remain smaller than those observed in the impulsive case because the peak overpressure is reduced. Initially, the central plastic hinges are at a distance of 27 % of the length of the beam from the supports and moves towards the centre where they merge. Concerning the prediction of the axial force, a very good agreement is again achieved between the results provided by numerical and analytical models (see Fig. II.27-b).
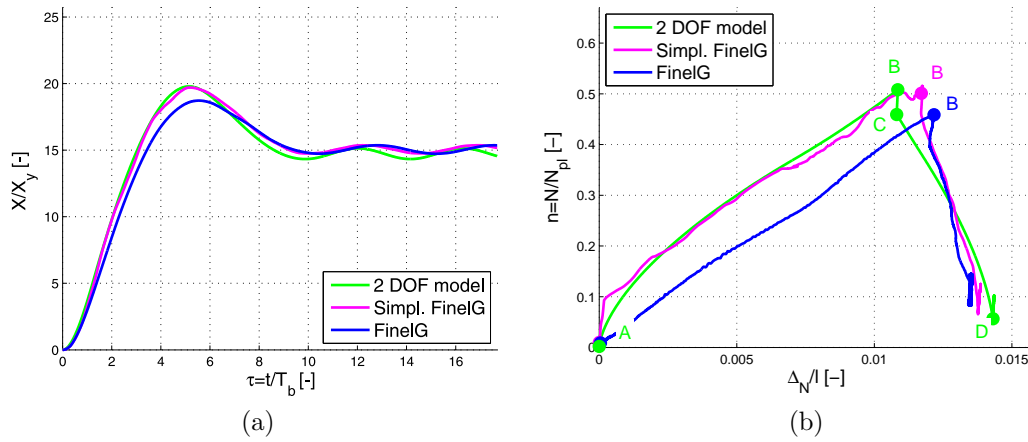
Figure II.27: Comparison of FinelG and analytical results. (a) Mid-span deflection versus time; (b) Axial force vs. axial elongation of the beam, considering the following set of parameters: $\psi_K = 1\,;\ \psi_M = 0\,;\ \xi = 2\,\%\,;\ \theta_y = 13\,mrad\,;\ \bar{p} = 10\,;\ \tau_d = 1.5\,;\ \bar{I} = 7.5$.

II.4.3.2 Case 2: $\psi_M = 0$ and $\psi_K = 0$

Figures II.28-a, -b and -c respectively show the time evolution of displacement of the beam under quasi-static, dynamic and impulsive blast loading. Some discrepancies between FinelG results are observed for dynamic and impulsive loadings due to the effect of traveling plastic hinges as explained earlier. Some discrepancies are also observed between the simplified FinelG and analytical models, although the plastic hinges are assumed to form in the middle and at the ends of the beam for both models.

Because of the absence of lateral mass and restraint, equation of motion (II.69) can be simplified as follows

$$M_s \ddot{X} + F_{int,b} = p\left(t\right)\ell \tag{II.89}$$

where $F_{int,b}$ is the equivalent internal force in the beam (see Fig. II.28-d) and is given by

$$F_{int,b} = \begin{cases} k_s X & \text{for } X \leq X_y, \\ \frac{4}{\ell} M_{pl} & \text{for } X > X_y \text{ and } \dot{X} \geq 0, \end{cases} \tag{II.90}$$

for the analytical model (membrane force $N = 0$). Multiplying Equ. (II.89) by the velocity $\dot{X}$ and integrating with respect to time t provides the energy conservation relationship

$$\frac{1}{2} M_s \dot{X}^2 + \int F_{int,b} dX = \int p(t) \ell \dot{X}(t) dt. \tag{II.91}$$

The right member of Equ. (II.91) reflects the way that the structure perceives the blast loading. Indeed, the blast-related energy is injected into the structure, respective to the magnitude of its velocity. However, the time evolutions of velocity predicted by the simplified FinelG and analytical models do not match well because of the assumptions made on the elastic range. For the analytical model, a secant stiffness k_s is supposed in the elastic range, assuming that all plastic hinges appear at the yield deflection X_y and the mass factor K_M is equal to $1/3$ irrespective of the regime. The internal force of the beam is actually bi-linear (see Fig. II.28-d) and the mass factor varies with respect to the regime (elastic, elastic-plastic or plastic regime). This difference of velocity at the end of the elastic regime is the source of the discrepancies of displacement in plastic regime as observed in Fig. II.28 although both models have exactly the same structural behavior in the plastic regime. In the example of Section II.4.3.1, the lateral restraint mitigates these discrepancies in the plastic regime as well as the lateral mass as highlighted in the next sections where good correlation is achieved between numerical and analytical results.
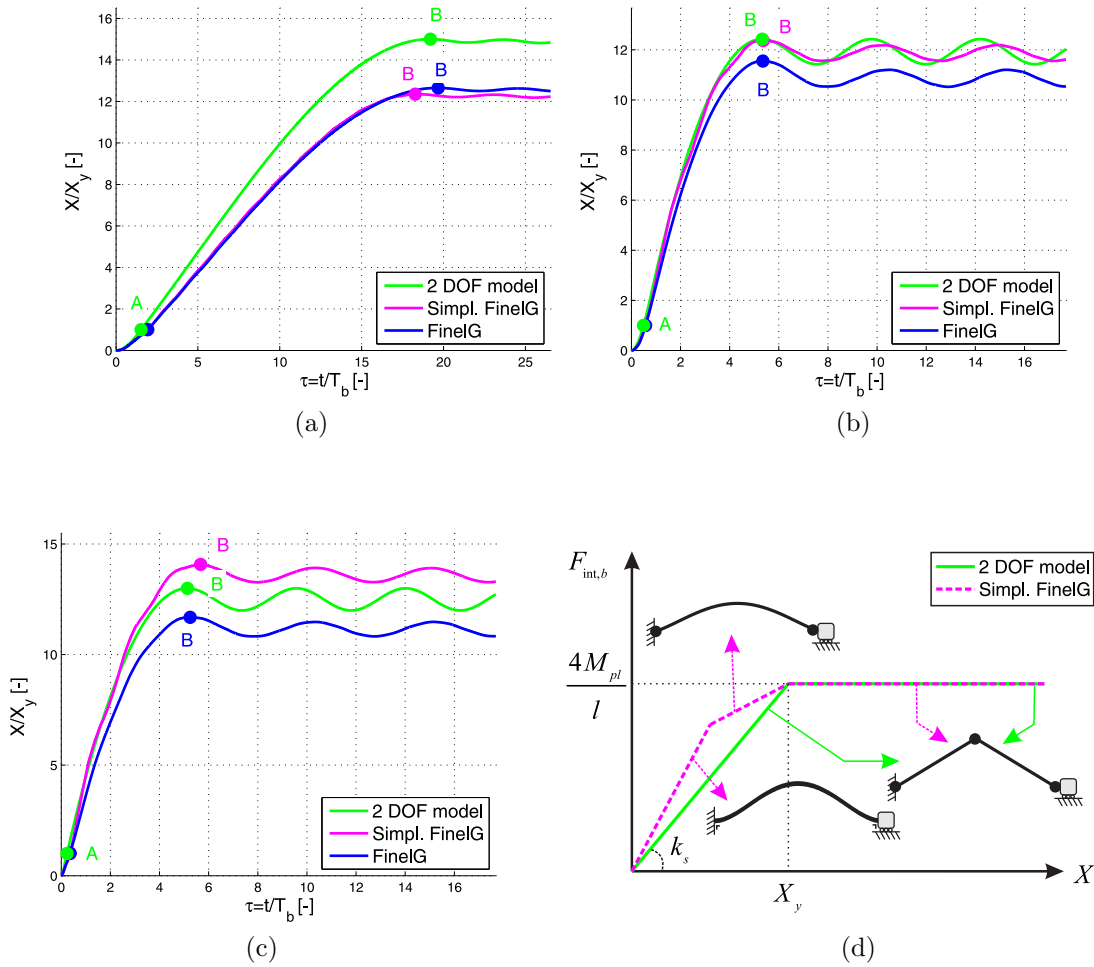
Figure II.28: Comparison of FinelG and analytical results. Mid-span deflection versus time for (a) $\overline{p} = 1.05$; $\tau_d = 100$; $\overline{I} = 52.5$; (b) $\overline{p} = 10$; $\tau_d = 1$; $\overline{I} = 5$ and (c) $\overline{p} = 100$; $\tau_d = 0.1$; $\overline{I} = 5$, considering the following set of parameters: $\psi_K = 0$; $\psi_M = 0$; $\xi = 2\,\%$; $\theta_y = 13\,\mathrm{mrad}$. (d) Schematic graph of the internal force $F_{int,b}$ versus mid-span displacement of the beam X.

II.4.3.3   Case 3: $\psi_M = 20$ and $\psi_K = 0$

Quasi-static blast loading $(\overline{p}, \tau_d) = (1, 100)$

Figures II.29-a and -b respectively depict the time-history of mid-span displacement and the M-N plastic interaction curves at mid-span and at the ends of the beam. Since the blast loading is featured by a small peak overpressure and long positive phase duration, the lateral mass does not contribute to the dynamic behaviour of the beam as highlighted in Fig. II.29-b where the membrane force is shown to be negligible. As a result, the discrepancies between the deflection can be justified as previously in Section II.4.3.2.
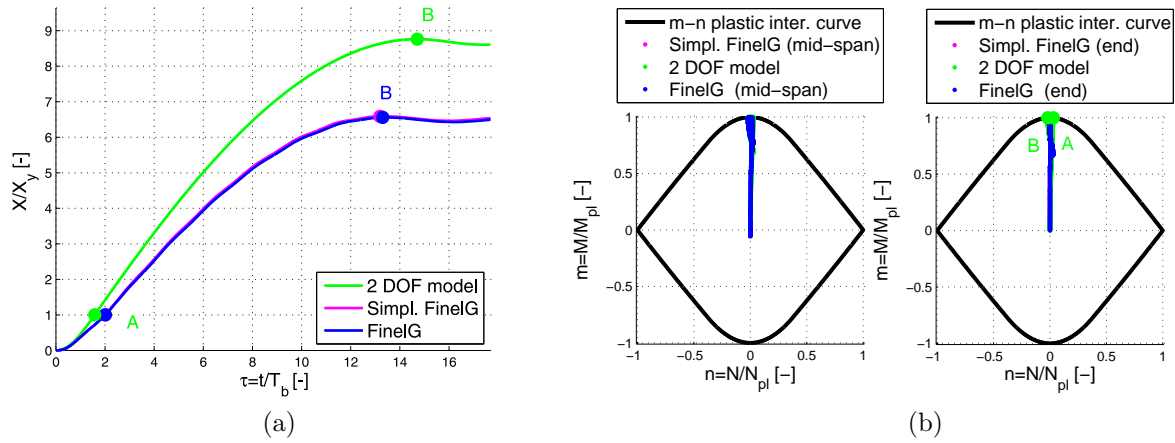
Figure II.29: Comparison of FinelG and analytical results. (a) Mid-span deflection versus time; (b) M-N plastic interaction considering the following set of parameters: $\psi_K = 0$; $\psi_M = 20$; $\xi = 2\,\%$; $\theta_y = 13\,\mathrm{mrad}$; $\overline{p} = 1$; $\tau_d = 100$; $\overline{I} = 50$.

Impulsive blast loading $(\overline{p}, \tau_d) = (100, 0.15)$

Figures II.30-a and -b respectively illustrate the time-history of mid-span deflection of the beam and the M-N plastic interaction curves at mid-span and at the ends of the beam. The error made on the ductility by the simplified FinelG and analytical model in comparison to the FinelG one respectively stand at 24 % and 14 % (see Fig. II.30-a) because of the effect of traveling plastic hinges. The large discrepancy between the maximum deflections predicted by the simplified FinelG and analytical models is due to a lack of accuracy of FinelG. Indeed, the axial force is largely overestimated, which results in a drop of the plastic bending resistance of the beam (see Fig. II.30-b) and therefore, an increase of the maximum mid-span deflection of the beam. But the analytical model remains on the safe side in comparison to the FinelG model.

As observed earlier, the axial force vs. elongation curve captured by the analytical model shows a good agreement with that predicted by the FinelG model (see Fig. II.31-a) thanks to the application of normality rule in the plastic regime (from points A and B). For an axial force $n = N/N_{pl}$ greater than $A_w/A = 0.37$, the plastic neutral axis moves from the web towards one flange and a discontinuity in the slope is observed for the 2-DOF and FinelG models in Figs. II.31-a and -b.
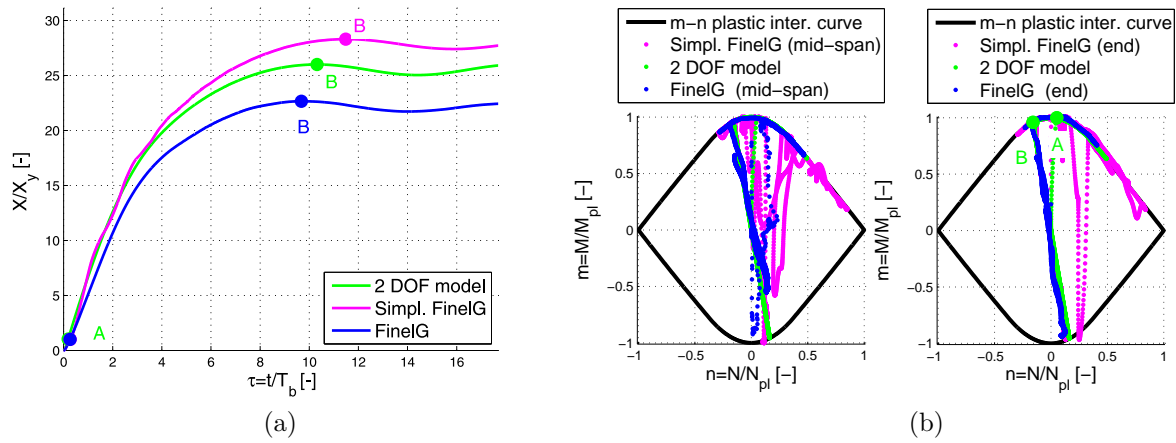
Figure II.30: Comparison of FinelG and analytical results. (a) Mid-span deflection versus time; (b) M-N plastic interaction considering the following set of parameters: $\psi_K = 0$; $\psi_M = 20$; $\xi = 2\,\%$; $\theta_y = 13\,\mathrm{mrad}$; $\overline{p} = 100$; $\tau_d = 0.15$; $\overline{I} = 7.5$.
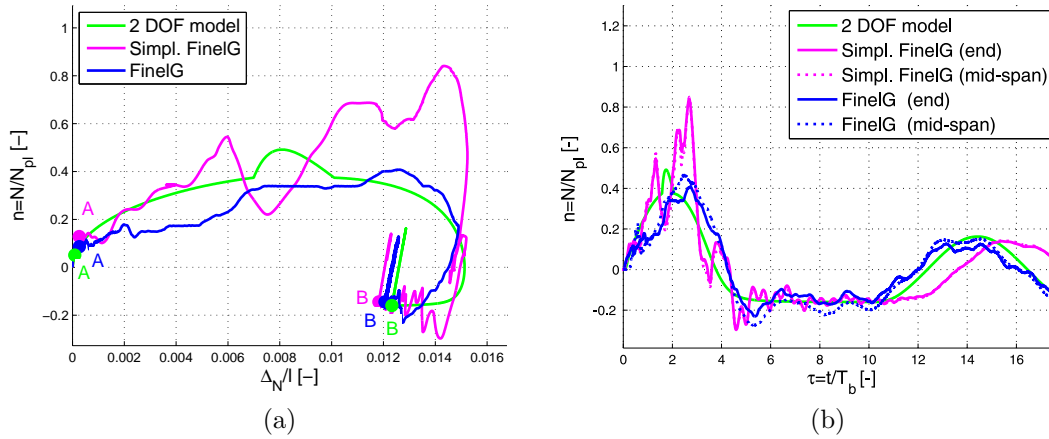
Figure II.31: Comparison of FinelG and analytical results. (a) End axial force vs. axial elongation of the beam; (b) time history of end axial force, considering the following set of parameters: $\psi_K = 0$; $\psi_M = 20$; $\xi = 2\,\%$; $\theta_y = 13\,\mathrm{mrad}$; $\overline{p} = 100$; $\tau_d = 0.15$; $\overline{I} = 7.5$.

Dynamic blast loading $(\overline{p}, \tau_d) = (10, 1)$

A perfect agreement is achieved between the mid-span deflection predicted by simplified and analytical models (see Fig. II.32-a). A discrepancy is observed between the curves predicted by the FinelG models because of the effect of traveling plastic hinges. The axial force vs. elongation graph shows also a good agreement between the analytical and numerical models (see Fig. II.32-b).
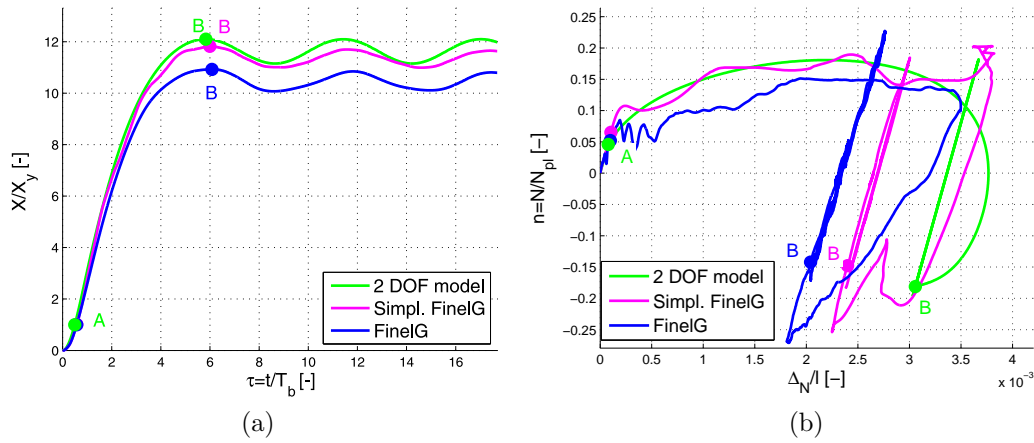
Figure II.32: Comparison of FinelG and analytical results. (a) Mid-span deflection versus time; (b) End axial force vs. axial elongation of the beam, considering the following set of parameters: $\psi_K = 0$; $\psi_M = 20$; $\xi = 2\,\%$; $\theta_y = 13\,\mathrm{mrad}$; $\bar{p} = 10$; $\tau_d = 1$; $\bar{I} = 5$.

II.4.3.4 Case 4: $\psi_M = 20$ and $\psi_K = 1$

Quasi-static blast loading $(\bar{p}, \tau_d) = (1.5, 100)$

A very good agreement is achieved between the mid-span deflection predicted by numerical and analytical models (see Fig. II.33-a). Figure II.33-b shows the axial force versus axial elongation of the beam. A very good match is also found between the numerical and analytical calculations.
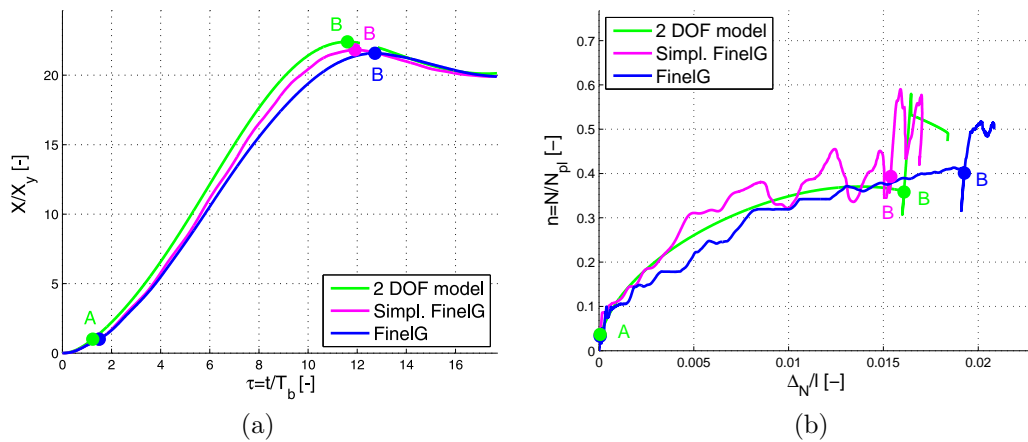
Figure II.33: Comparison of FinelG and analytical results. (a) Mid-span deflection versus time; (b) End axial force vs. axial elongation of the beam, considering the following set of parameters: $\psi_K = 1$; $\psi_M = 20$; $\xi = 2\,\%$; $\theta_y = 13\,\mathrm{mrad}$; $\bar{p} = 1.5$; $\tau_d = 100$; $\bar{I} = 75$.

Impulsive blast loading $(\overline{p}, \tau_d) = (100, 0.15)$

Simplified FinelG and analytical models agree well for the prediction of the ductility (see Fig. II.34-a). The error on ductility between the analytical and numerical predictions reach 10 % because of the effect of traveling plastic hinges. Figure II.34-b shows the axial force vs. axial elongation of the beam, the analytical and numerical predictions match rather well.
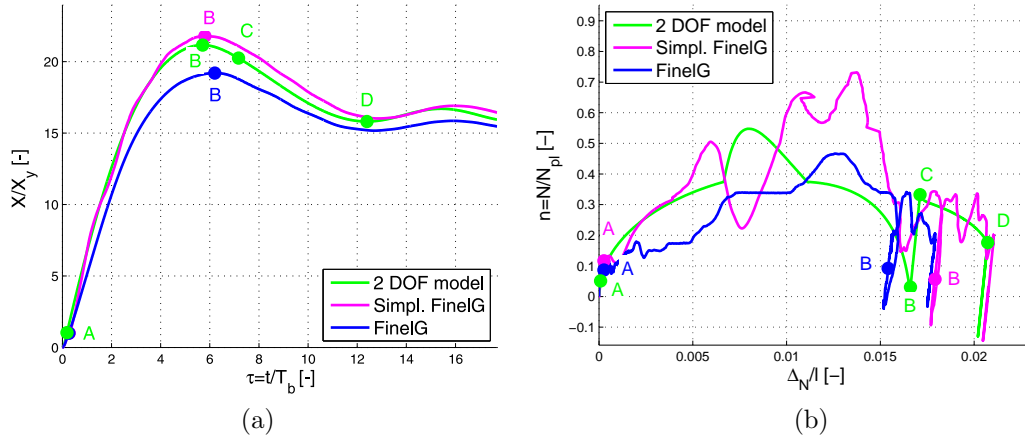
Figure II.34: Comparison of FinelG and analytical results. (a) Mid-span deflection versus time; (b) End axial force vs. axial elongation of the beam, considering the match rather well following set of parameters: $\psi_K = 1$; $\psi_M = 20$; $\xi = 2\%$; $\theta_y = 13\,\text{mrad}$; $\overline{p} = 100$; $\tau_d = 0.15$; $\overline{I} = 7.5$.

Dynamic blast loading $(\overline{p}, \tau_d) = (10, 1.5)$

A good correlation is found between deflection curves predicted by the simplified and analytical models (see Fig. II.35-a). The error on ductility of the analytical model reaches 8.8 % because of the effect of traveling plastic hinges. Concerning the prediction of the axial force, the analytical and numerical estimations agree well (see Fig. II.35-b).
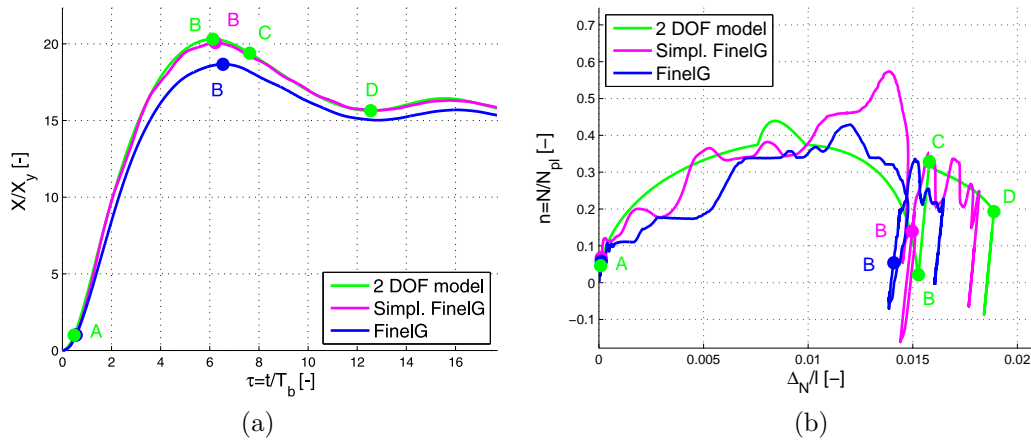
Figure II.35: Comparison of FinelG and analytical results. (a) Mid-span deflection versus time; (b) End axial force vs. axial elongation of the beam, considering the following set of parameters: $\psi_K = 1$; $\psi_M = 20$; $\xi = 2\,\%$; $\theta_y = 13\,\mathrm{mrad}$; $\bar{p} = 10$; $\tau_d = 1.5$; $\bar{I} = 7.5$.

II.4.4   Computational efficiency

Using computer with Intel® Core™ i5-2520M processors (CPU 2.5 GHz), it requires 20 seconds to get one point of the p-I diagram with the analytical model while it takes 2000 seconds with FinelG (assuming that 5 iterations are required to get one point of an iso-damage curve). Therefore, the analytical model enables to get the overall p-I diagram in 13 minutes while FinelG requires 22 hours.

II.4.5   Conclusions

To evaluate the level of accuracy of the results predicted by the analytical model, they are compared to those computed by the numerical models based on two-dimensional FEM simulation using FinelG. It accounts for large displacements and a kinematic-plastic constitutive material law, but it disregards any shear deformation and failure. Two numerical models are used; the first one does not make any assumptions in contrast with the second one (simplified model) which supposes that the plasticity is localized at the ends and in the middle of the beam and neglects horizontal and rotational inertial forces along the beam in order to validate the analytical model.

To perform the numerical validation, the parameters ψ_K and ψ_M are respectively varied from 0 to 1 and 0 to 20 while the blast loading is considered as quasi-static, dynamic or impulsive. It is shown that a good agreement is achieved between the results predicted by the analytical and simplified FinelG model. However, for high values of peak overpressure ($\bar{p} > 3$), the higher modes of vibration govern the response of the beam at the beginning of the blast event and even generates plastic hinges that travel along the length of the member and coalesce at mid-span of the beam. This phenomenon dissipates more energy

than assuming one plastic hinge localized in the central region during the blast event as done for the analytical model, that accounts for the smaller deflection predicted by the FinelG model in comparison to analytical model. Moreover, neglecting the rotational and horizontal masses along the beam is shown to be on the safe side for the analytical predictions since they slow down the motion of the beam. In the impulsive regime, the errors on ductility between the analytical and numerical estimations stand within 10 % on the safe side whereas it could even reach 20 % in the quasi-static regime for a specific case (no lateral mass and restraint) because the analytical model does not take into account the bi-linearity of the internal force in the elastic regime.

II.5   Conclusions

The considered problem was that of a frame beam subjected to blast loading considering the interaction with the indirectly affected part (IAP) of the structure, and assuming a linear elastic behavior of the IAP and stable adjacent columns. We have established p-I diagram of a beam extracted from an arbitrary structure taking into account the nonlinear membrane force, the M-N plastic interaction and the lateral inertia and restraint provided by the rest of the structure. The material law of the beam is elastic-perfectly plastic, and does not account for strain hardening nor strain rate effects.

Two analytical models are developed. The first model is based on a single-degree-of-freedom which is the transverse mid-span deflection and assumes that the axial elongation of the beam is negligible (SDOF model) by contrary to the second (2-DOF model). It is shown that disregarding the axial deformability of the beam could be unconservative when the stiffness of the lateral restraint is important since the non-linear rigidity provided by the structure to the beam is overestimated. Nevertheless, it could be conservative when the lateral mass and restraint respectively become significant and negligible.

As a result of the dimensional analysis, five main dimensionless structural parameters affecting the required ductility of the frame beam are identified. Two parameters ψ_K and ψ_M are related to the behavior of the indirectly affected part (the lateral restraint and mass). Another one ξ is related to the mechanical properties of the investigated beam (i.e. its bending and axial resistances). The last parameter θ_y is related to the geometry of the problem (i.e. the yield rotation of the beam at its extremities). Another parameter λ_r corresponding to the rotational inertia effect is shown to be negligible for steel beams that exhibit a span-to-depth ratio between 10 and 30. A comprehensive analysis and validation of the models was therefore performed with regard to ψ_K and ψ_M.

Parameters ψ_K and ψ_M represent the favorable effect of the elastic indirectly affected part of the structure to limit the required ductility of the frame beam. The effect of lateral mass is negligible in case of a ratio ψ_M smaller or equal to 5. If the beam span-to-depth ratio is increased ($\xi \downarrow$ and $\theta_y \uparrow$), the energy dissipated in the plastic hinges is reduced. Thus, the lateral mass and restraint contribute further to absorb the energy generated by the blast loading and as a result, they reduce the demand of ductility.

In order to carry out the validation of the analytical 2-DOF model, the results predicted by the analytical models are compared to those predicted by the two-dimensional FEM using FinelG. Parameters ψ_K and ψ_M are respectively varied from 0 to 1 and 0 to 20 while the blast loading is considered as quasi-static, dynamic or impulsive. It is shown that a very good agreement is achieved between the results predicted by the analytical and simplified FinelG models. However, for dynamic or impulsive blast loadings, the phenomenon of traveling plastic hinges and horizontal and rotational inertial forces significantly affect the behaviour of the blast-loaded beam (relative error of 14%). Neglecting them is however conservative.

Finally, the 2-DOF model is a simplified tool that enables to quickly assess the level of damage of a blast loaded beam extracted from a structure and to study the effect of structural parameters on blast resistant design. The tool is less time consuming than FinelG since it provides the overall p-I diagram in about 10 minutes while FinelG requires 100 times more time to establish it.

II.6 Perspectives

The goal of **Chapter II** was to accurately predict the behaviour of a blast-loaded beam which interacts with the elastic linear surrounding structure. The dynamic analysis is performed with large displacements, taking into account the development of membrane force and M-N plastic interaction, which results to the development of 2-DOF analytical model. An improvement could be provided to the analytical model by assuming that the behavior of the surrounding structure is elastic-perfectly plastic with a plastic resistance $R^\star$. The energy conservation relationship can be re-derived by writing the energy U_3 stored in the lateral restraint

$$U_3 = \begin{cases} \frac{1}{2}K^\star\delta^2 & \text{for } 0 \leq \delta \leq \delta_y, \\ \frac{1}{2}K^\star\delta_y^2 + R^\star\left(\delta - \delta_y\right) & \text{for } \delta_y < \delta \end{cases} \tag{II.92}$$

where $\delta = \frac{X^2}{\ell}$ is the elongation of the lateral restraint and $\delta_y = R^\star/K^\star$ corresponds to the elastic horizontal deflection of the lateral restraint. After some rearrangement, the equation of motion (II.69) becomes

$$\begin{cases} M_s\ddot{X} + F_{int,b} + 2N\frac{X}{\ell} = p\ell \\ N = M^\star\left[\frac{2}{\ell}\left(\dot{X}^2 + X\ddot{X}\right) - 2\ddot{\Delta}_N\right] + F_{int,K} \end{cases} \tag{II.93}$$

where the force in the lateral restraint is given by

$$F_{int,K} = \begin{cases} K^\star\delta & \text{for } 0 \leq \delta \leq \delta_y, \\ R^\star & \text{for } \delta_y < \delta, \end{cases} \tag{II.94}$$

this introduces one additional dimensionless number $\psi_R = R^\star/p_b\ell$ which corresponds to the ratio of the plastic resistance of the lateral restraint $R^\star$ to the characteristic force of the beam $p_b\ell = 4M_{pl}/\ell$.

Concerning the vertical restraints, new degrees-of-freedom defined as the elongations of these restraints could be added to the existing analytical model and Lagrange's approach should be applied again by taking into account these DOFs. For rotational restraints, the procedure is undoubtedly more complex as explained in [59] where the authors have recently proposed a closed-formed solution to predict the dynamic response of a beam with elastic semi-rigid restraints without any rotational inertia. The effect of these rotational restraints as well as the coupling between the horizontal, vertical and rotational restraints should be further investigated.

In reality, the behaviour of the indirectly affected part of the structure may be non linear; indeed, plastic hinges can appear progressively in the IAP of the structure, inducing a reduction of its stiffness. Some structural elements in the IAP of the structure may also buckle as well as their web or flange through local instability. The capacity of deformation of the IAP of the structure remains also unknown. Further investigations should be paid in the future to the characterization of the IAP of the structure.

The bi-linear internal force of the beam in the elastic regime could also be incorporated in the analytical model to accurately predict the dynamic response of the beam when the lateral mass and stiffness of the lateral restraint are negligible. Richer kinematic displacement fields for the beam, as described in Appendix VI.1 could be used to derive the equation of motion for each stage of motion of the beam. The minimum Δ_0 technique established by Symonds [90] should be applied to ensure the conservation of momentum at regime transitions.

In case of impulsive blast loading, the effects of traveling plastic hinges and horizontal and rotational inertial force distributions could be substantial. They can be considered in the model by defining new variables such as the location of the plastic hinges. However, the analytical developments become more complex and neglecting these effects on the beam is conservative in any circumstance.

The M-N plastic interaction equation (I.48) established by Lescouarc'h does not take into account the presence of fillet radius for I-shaped cross-section of a beam. One way to deal with this issue is to approximate the actual plastic interaction curve by an approximated function (II.6) where α is determined by minimizing the global error using the least mean square method and γ is equal to 1.

With the help of FinelG software, it is also shown that the shear force V/V_{pl} is much greater than 0.5, involving that an additional degree-of-freedom defined as the shear angle should be introduced in the analytical and numerical models. In the plastic regime, the generalized strain rate should be normal to a three-dimensional M-N-V plastic surface, thus providing two additional relationships (instead of one) expressing internal forces in terms of shear angle, axial elongation and rotation of the plastic hinges.

Chapter III

Analysis of a non-linear frame column

III.1 State-of-the-art on beam-column under blast loading

The blast design of beam-columns is important since their failure could affect the global stability of the damaged structure and potentially cause the progressive collapse of the building [5, 91, 92, 78, 93, 84]. Nowadays, developing some easy-to-apply tools to accurately predict the dynamic behavior of a beam-column under blast loading and axial load is a challenge. Axial load applied at the head of a beam-column, associated to dead and live loads from upper stories, becomes more eccentric relative to the deflected shape of the beam-column under transverse blast loading. This leads to a secondary bending moment additional to the primary one (due to blast loading) which eventually precipitates the buckling failure of the beam-column. This second order effect is commonly known as $P - \delta$ effect, and in the UFC design guide [4], it is accounted for using the so-called moment magnification factor (MMF). It firstly recommends to disregard the column axial load and to analyze it as a single beam which responds primarily in bending. Then, to ensure beam-column stability (due to axial compressive load) and plastic cross-section resistance, the UFC design guide proposes to check these following interaction formulas:

$$\frac{P}{P_u} + \frac{C_m M}{M_{pl} \left(1 - \frac{P}{P_{cr}} \right)} \leq 1 \tag{III.1}$$

$$\frac{P}{P_p} + \frac{M}{1.18 M_{pl}} \leq 1 \text{ for } \frac{P}{P_p} \geq 0.15 \tag{III.2}$$

$$\frac{M}{M_{pl}} \leq 1.0 \text{ for } \frac{P}{P_p} < 0.15 \tag{III.3}$$

where C_m, depends on the beam-column curvature caused by the applied moment ($C_m = 1.0$ for pinned beam-column under uniformly distributed load); P is the applied axial load; P_u is the ultimate compression capacity of beam-column (depending on the effective slenderness ratio of the member, the area of the member cross-section and the yield strength of the material); P_{cr} is the Euler elastic buckling of the beam-column; P_p is the cross-sectional axial compression capacity; M is the maximum applied bending moment; M_{pl} is the beam-column plastic moment capacity in the absence of axial load. Equ. (III.1) corresponds to the check of the column stability under blast loading, accounting for the $P - \delta$ effect through the moment magnification factor (MMF) :

$$MMF = \frac{C_m}{1 - \frac{P}{P_{cr}}}. \tag{III.4}$$

This factor multiplies the first-order bending moment M of the beam-column due to lateral blast loading to get its corresponding second-order response. The bending moment M in the elastic stage reads

$$M = -EI_c Y_m \left(\frac{\partial^2 \phi}{\partial z^2} \right)_{z=z_m} \tag{III.5}$$

where z_m represents the location of the maximum bending moment (in absolute value) and $\phi(z)$, the shape function of the beam-column in the elastic stage. The maximum displacement Y_m is obtained by solving the equation of motion of an elastic SDOF system (see section I.4.2.4) or using the dynamic load factor (DLF) curve as illustrated in Fig. I.15-b. The DLF is defined as the ratio of the maximum displacement of an indefinitely elastic system to its static deflection, and is function of the ratio of the blast loading positive phase duration t_d to the first natural period of the structure T.

Concerning the verification of the section strength, the bending moment-axial force plastic interaction at the critical cross-sections is described by Equs. (III.2) and (III.3). When the ratio P/P_p is smaller than 0.15, the axial load does not affect the plastic bending resistance.

The MMF incorporates the effect of reduction of the elastic stiffness of the column due to the presence of axial load. However, it disregards the elongation of the period of vibration T of the beam-column due to applied axial load P [94] as highlighted herein

$$T = \frac{T_0}{\sqrt{1 - \frac{P}{P_{cr}}}} \tag{III.6}$$

where $T_0 = 2\pi\sqrt{K_{LM}M_s/k_s}$ is the period of vibration of the column in the absence of axial load (M_s, k_s and K_{LM} respectively refer to the mass, the stiffness of the column and the load-mass factor). The subscript "0" means that no axial load is applied to the beam-column ($P = 0\,kN$). As a result, this period elongation decreases the maximum deflection of a beam-column under axial load and blast loading in comparison to a similar configuration without axial load. Indeed, Fig. I.15 reveals that increasing the period of vibration of a structure decreases the DLF value.

Therefore, Nassr *et al.* [79] proposes to bring a correction to the moment magnification factor as

$$MMF_{corr} = MMF\frac{DLF}{DLF_0} \tag{III.7}$$

where DLF and DLF_0 correspond to the dynamic load factor in the presence or absence of axial load, respectively considering the period of vibration T calculated according to Equ. (III.6) and T_0. Hence, the stability criteria reads

$$\frac{P}{P_u} + \frac{C_m M}{M_{pl}\left(1 - \frac{P}{P_{cr}}\right)}\frac{DLF}{DLF_0} \leq 1. \tag{III.8}$$

Beyond the elastic limit, the UFC approach assumes that the stiffness of the column remains constant even after yielding has occurred in the column, which leads to an underestimation of the maximum displacement. In any case, the stability equation (III.8) can not be satisfied after the occurrence of yielding. Accordingly, the design rule for beam-column stability is only valid for ductility ratios μ smaller than one as suggested in [79] although, in reality, the beam-column could experience permanent plastic deformation and remain stable.

Based on the concept of equivalent lateral load (ELL) [95], a new elastic-plastic SDOF model for a simply supported beam-column under blast loading and axial compressive load

is proposed in [96]. This model, which accounts for the effect of the axial load on the column strength and stability, is improved including accurately the influence of the strain rate on the column dynamic response in [79, 97]. Indeed, the cross-section is divided into a number of layers in which a strain rate stress-strain relationship is applied to capture the nonlinear stress distribution over its depth. The analytical approach has been validated by comparing their corresponding results with those of experimental results from blast tests on full scale steel columns and with the results of the finite element software LS-DYNA. This model has also been recently used to predict the buckling behavior of multi-layered glass structural element under blast loading and compressive load [98] and compared to numerical results provided by the software ABAQUS. A good agreement is achieved between these models and a simplified design approach, based on the use of a linear interaction curve, is proposed for the dynamic buckling check of simply supported glass columns under combined axial load and lateral blast loading. A large parametric study of this SDOF model has been performed in [80] (disregarding the effect of strain rate) and a general procedure to derive the analytical expressions of the asymptotes of the P-I curves is proposed.

A modified approach of the SDOF model of axially loaded steel columns under blast loading is provided in [99, 100], where a new resistance function of the column based on quasi-static approximation is derived. The validation has been made in [100] on steel columns with two different boundary conditions (rolled-pinned and rolled-fixed supports) by comparing the results of the analytical model with the experimental tests of Nassr [79] and numerical software LS-DYNA. A very good agreement is observed between the obtained results.

Another rapid assessment tool known as Dynamic Structural Analysis Suite (DSAS) is also used in [83, 101, 102] to predict the dynamic behavior of reinforced concrete columns subjected to axial and blast-induced transverse loads. DSAS is also based on an SDOF analysis, and utilizes a multilayer model to capture the moment-curvature relationship in critical sections of the structural member. This tool uses a static non linear FE analysis, based on an arc-length method, to obtain the resistance function, the equivalent load and mass.

A closed-form analytical model of beam-column under axial load and transverse load proposed by L. Chernin *et al.* [103] involves the resolution of the equation of motion in modal basis. This model deals with various spatial load distributions and pressure time-histories, it enables to predict quite accurately the impulsive response of the column governed by several modes of vibration but it is not able to capture the dynamic behaviour of the column in the plastic regime.

More advanced nonlinear finite element analysis [104, 53, 105, 106, 107, 108, 109, 110], accounting for geometric and material non-linearities, can also be performed to predict the dynamic behavior of a beam-column under combined axial load and lateral blast loading. Shi *et al.* [53, 106] show that the damage criterion used in P-I diagram, usually defined in terms of ductility, may not be suitable for structural elements under impulsive blast loading since the member could experience a brittle shear failure. A new damage criterion for reinforced concrete (RC) column is defined based on the ratio of the residual axial load-carrying capacity to the initial axial resistance (before blast event). A numerical parametric study is performed

to investigate the effects of column dimensions, material properties or reinforcement ratio on the P-I diagram. Based on the numerical results provided by the LS-DYNA software, analytical formulae to establish the iso-damage curves of the P-I diagram for RC beam-column are derived. In [111], the authors also propose an analytical formula based on a fitting of numerical results to derive the residual strength of blast damaged RC columns. Based on the same definition of damage criterion, Y. Ding *et al.* [112] propose to incorporate the effect of fire exposure time on analytical formula for predicting the P-I diagram of a steel tubular column subjected to explosion and post-explosion fire action.

In [113], an artificial neural network (ANN) has been used in conjunction with FE model to develop a fast running model to predict the residual capacity of blast loaded steel columns. The input parameters of the ANN consist of the scaled distance of the explosive charge (depending on the mass and the standoff distance of the vehicle bomb), the depth of the column cross-section, the web slenderness, the web to flange thickness ratio and the length of the column. The output parameter corresponds to the residual column capacity. The extreme and nominal values of the parameters are combined to generate 51 samples of data, which are introduced in the FE model to get the residual column capacity. Then, by using some sophisticated algorithm to minimize the error, the weights required for ANN are computed on the basis of these numerical results. This tool provides the results with a high level of accuracy in comparison to FE results (error $< 10\,\%$) and runs quickly, enabling to get a result in a few seconds.

All the aforementioned rapid assessment tools assume that the beam-columns present simple boundary conditions and disregard any interaction with the surrounding structure, whereas sophisticated software enable to predict the dynamic behaviour of beam-columns integrated in a whole frame building. In this Chapter, an intermediate solution is proposed by establishing an analytical model to capture the dynamic response of the beam-column under an axial compressive load and blast loading, which interacts with the surrounding structure. The model accounts for large displacement ($P - \delta$ effect), bending moment-axial force (M-N) plastic interaction as well as its interaction with the indirectly affected part (IAP) of the structure. The IAP of the structure is reduced to an elastic lateral spring $K^\star$ and mass $M^\star$ which are connected at the top of the beam-column, eventually authorizing a lateral movement at its head. Based on the decomposition of the field of displacement into shape functions amplified by generalized displacements and Lagrange's equation, the analytical model includes two degrees-of-freedom specific to each stage of motion of the beam-column. Four stages (or regimes) are identified, depending on the eventual development of plastic hinge(s) at the bottom or/and at mid-height of the column. Full dynamic non-linear simulations of 2D beam FE-model of the column under same loading and boundary conditions than the analytical model are performed with the software FinelG, accounting for large displacement and a plastic kinematic constitutive model for M-N plastic interaction, disregarding any shear failure. A very good correlation is found between the results provided by the two models although some discrepancies are also observed because of the assumption, in our model, of a stationary plastic hinge (at mid-height of the column) for intermediate values of $K^\star$.

The kinematics of the proposed model is first described in Section III.2, the equations of motion are also established and scaled to underline the dimensionless parameters that govern the dynamic behaviour of the beam-column under combined axial and lateral blast loads. The minimum Δ_0 technique to ensure the conservation of momentum quantities at transition between two regimes is further detailed. In Section III.3, SDOF models for free-fixed and pinned-fixed beam-columns are proposed based on the governing equations described in Section III.2 and their corresponding asymptotic solutions are derived in Section III.4. The numerical results and analytical estimations are compared and discussed in Section III.5. The analysis of the rapid assessment tool is performed through parametric study on the pressure-impulse (p-I) diagram in Section III.6, which is followed by the conclusions in Section III.7 and the perspectives in Section III.8.

III.2 Problem formulation

III.2.1 Description of the problem

The problem consists in predicting the dynamic behavior of a frame column under blast loading $p(z,t)$ (see Fig. III.1-a). As described in Section I.4.5, the beam-column can be extracted from the structure by using some condensation techniques in order to reduce the surrounding structure into a lateral elastic spring $K^\star$ and a mass $M^\star$. The column has a height H, and is characterized by a flexural rigidity EI_c and a lineic mass m_c. This column is assumed to be fixed at its basis, to have a lateral mass and to be restraint at its top. Since the interaction between the blast loaded beam and columns is neglected, no bending moment is induced at the top of the column and the dynamic component of axial load due to blast pressure applied to the adjacent beam is neglected. As a result, the column only carries a constant axial load P due to dead and live loads at its top coming from upper stories and is also subjected to a uniformly distributed blast loading (see Fig. III.1-b) defined as a decreasing linear function of time as follows

$$p(z,t) = p_0 \left(1 - \frac{t}{t_d}\right) \tag{III.9}$$

where t represents time variable, p_0 is the peak overpressure of the blast loading and t_d is the positive phase duration. The associated impulse I is given by

$$I = \frac{p_0 t_d}{2}. \tag{III.10}$$

The blast loading is supposed to act according to one of the principal axes of inertia of the column and the out-of-plane displacement of the column is assumed to be prevented. Thus, the out-of-plane axial buckling as well as the lateral torsional buckling are disregarded in the analysis of the beam-column. The analysis of the column is performed by accounting for large in-plane displacements and assuming an elastic-perfectly plastic material. The reduced plastic bending resistance (see Fig. III.1-c) for I-shaped steel beam-column can be obtained as follows
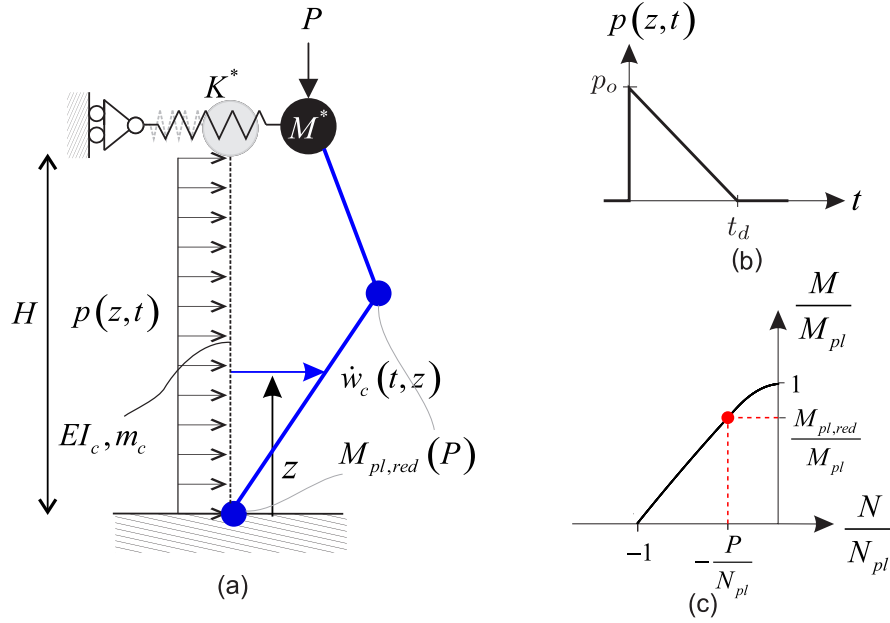
Figure III.1: (a) Sketch of the considered problem, (b) Idealized blast loading, (c) Axial force-bending moment interaction law.

$$M_{pl,red}(P) = M_{pl} \begin{cases} 1 - \gamma_0 \left(\frac{P}{N_{pl}}\right)^2 & \text{for } 0 \le \frac{P}{N_{pl}} \le \frac{A_w}{A}, \\ 1 - \gamma_1 - \gamma_2 \left(\frac{P}{N_{pl}}\right) - \gamma_3 \left(\frac{P}{N_{pl}}\right)^2 & \text{for } \frac{A_w}{A} \le \frac{P}{N_{pl}} \le 1, \end{cases} \qquad \text{(III.11)}$$

where coefficients γ_0, γ_1, γ_2 and γ_3 are given by Equ. (I.51).

The effect of the strain rate as well as the strain hardening on column strength and stability are neglected. Under a high impulsive blast loading, the beam-column could be significantly damaged by shear forces [66, 114, 53], but this effect is disregarded in the studied problem. It is further assumed that the plastic hinges do not travel along the column even though they could in some cases.

The transverse displacement w_c and velocity $\dot{w}_c$ of the beam-column read

$$w_c(\bar{z}, t) = \sum_{i=1}^{n} q_i(t)\,\phi_i(\bar{z}) \quad ; \quad \dot{w}_c(\bar{z}, t) = \sum_{i=1}^{n} \dot{q}_i(t)\,\phi_i(\bar{z}), \qquad \text{(III.12)}$$

where $q_i(t)$, $\dot{q}_i(t)$, $\phi_i(\bar{z})$ and $\bar{z} = z/H$ respectively represent the generalized displacements and velocities, the shape functions (see Fig. III.2) and dimensionless ordinates defined as the ratio of the ordinate z to the height of the column H. The shape functions fully describe the kinematics of the column, enabling to capture the transverse velocity of the column for the four following regimes:

○ Regime I: elastic behavior of the column;

○ Regime II: one plastic hinge at the fixed support of the column;

○ Regime III: full plastic mechanism;

○ Regime IV: one plastic hinge at "mid-height" of the column (at a distance z_m from the basis of the beam-column).

For each regime, two shape functions are used to represent the motion of the column, those with an odd subscript prevent any lateral displacement at head column while the others permit it (Figure III.2). The shape functions correspond to the static deflected shapes of the column under a uniformly distributed column, depending on the possible apparition of some plastic hinge(s) as well as the freedom of the column to move transversely at its head. For instance, the shape functions ϕ_2 and ϕ_3 respectively refer to the deflected shape of a free-fixed column and a simply supported column under a uniformly distributed static load. The shape functions ϕ_i and their corresponding boundary conditions (B.C.), shear force V_i and bending moment M_i are respectively given in Table III.1. The total bending moment M and shear force V of the column can be expressed as a sum of contributions associated to each shape function:

$$M\left(t, \bar{z}\right) = \sum_{i=1}^{n} M_i\left(t, \bar{z}\right) \tag{III.13}$$

$$V\left(t, \bar{z}\right) = \frac{1}{H}\frac{\partial M\left(t, \bar{z}\right)}{\partial \bar{z}} = \sum_{i=1}^{n} V_i\left(t, \bar{z}\right) \tag{III.14}$$

where $V_i\left(t, \bar{z}\right) = \frac{1}{H}\frac{\partial M_i(t,\bar{z})}{\partial \bar{z}}$.

III.2.2 Regime transitions

The regime transitions of the beam-column (see Fig. III.1-a) are fully described by the flow chart as illustrated in Figure III.3. The end of a regime corresponds to the possible apparition of one (or two) additional plastic hinge(s) or to the sign change of angular velocity in one (or two) plastic hinge(s). Indeed, the regime I ends with the development of a plastic hinge at its base (transition to regime II) or at mid-height of the column (transition to regime IV) while the regime III ends after the angular velocity in at least one of the two plastic hinges changes sign. The end of regime II could be that the angular velocity of the plastic hinge at its base changes sign (transition to regime I) or the development of an additional plastic hinge at its mid-height (transition to regime III). Finally, the regime IV is achieved by the change of sign of the angular velocity in the mid-height plastic hinge (transition to regime I) or the development of the full plastic mechanism (transition to regime III).

(a) Regime I

(b) Regime II

(c) Regime III
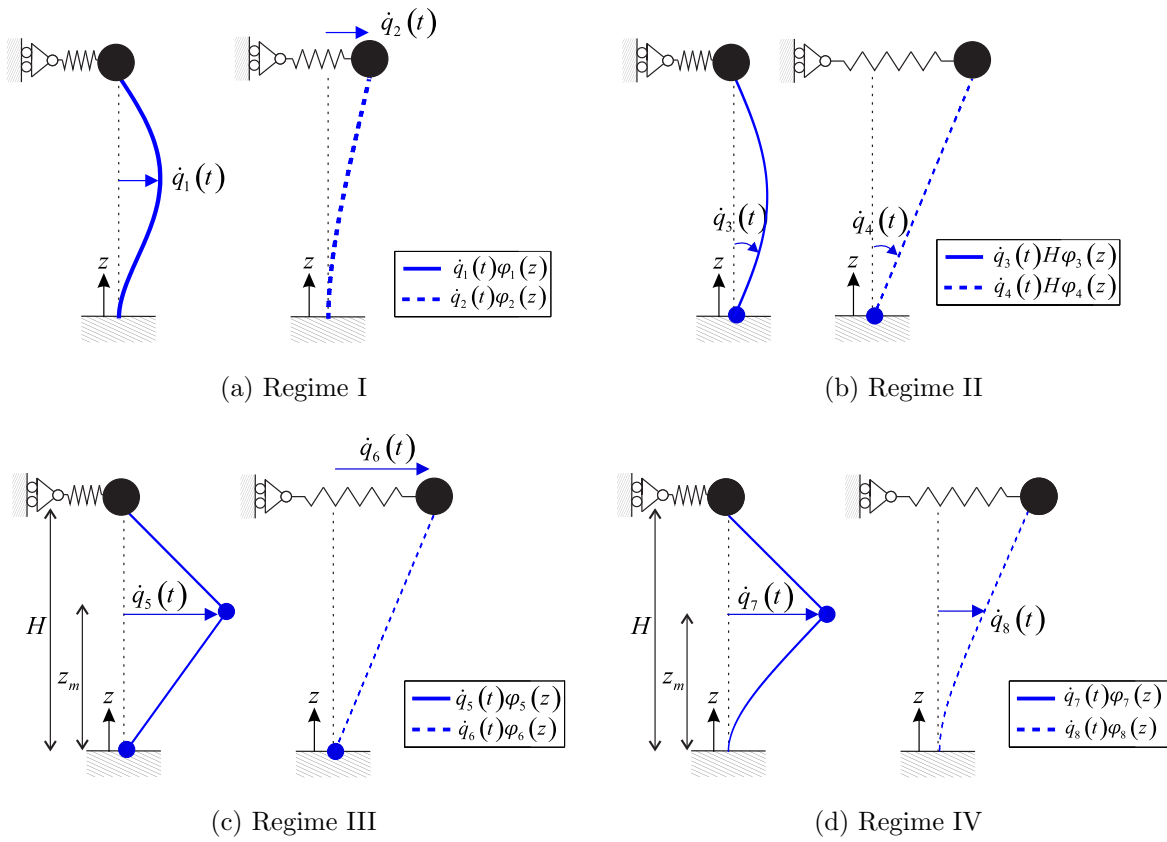
(d) Regime IV

Figure III.2: Schematic representations of shape functions during (a) Regime I: elastic behavior of the column; (b) Regime II: development of one plastic hinge at the fixed support of the column; (c) Regime III: development of full plastic mechanism and (d) Regime IV: development of one plastic hinge at "mid-height" of the column.

Regime I

i	1	2
$\phi_i(\bar{z})$	$\frac{185}{48}\left(2\bar{z}^4 - 5\bar{z}^3 + 3\bar{z}^2\right)$	$\frac{1}{3}\left(\bar{z}^4 - 4\bar{z}^3 + 6\bar{z}^2\right)$
$\frac{\partial \phi_i}{\partial \bar{z}}(\bar{z})$	$\frac{185}{48}\left(8\bar{z}^3 - 15\bar{z}^2 + 6\bar{z}\right)$	$\frac{1}{3}\left(4\bar{z}^3 - 12\bar{z}^2 + 12\bar{z}\right)$
$M_i(\bar{z})$	$\frac{185}{48}\frac{EI_c}{H^2}q_1\left(-24\bar{z}^2 + 30\bar{z} - 6\right)$	$\frac{1}{3}\frac{EI_c}{H^2}q_2\left(-12\bar{z}^2 + 24\bar{z} - 12\right)$
$V_i(\bar{z})$	$\frac{185}{48}\frac{EI_c}{H^2}q_1\left(-48\bar{z} + 30\right)$	$\frac{1}{3}\frac{EI_c}{H^2}q_2\left(-24\bar{z} + 24\right)$
B.C.	$\phi_1(1) = \phi_1(0) = \frac{\partial \phi_1}{\partial \bar{z}}(0) = 0,\ \max(\phi_1) = 1$ and $M_1(1) = 0$	$\phi_2(0) = \frac{\partial \phi_2}{\partial \bar{z}}(0) = 0,\ \phi_2(1) = 1$ and $T_2(1) = M_2(1) = 0$

Regime II

i	3	4
$\phi_i(\bar{z})$	$\left(\bar{z}^4 - 2\bar{z}^3 + \bar{z}\right)$	$\bar{z}$
$\frac{\partial \phi_i}{\partial \bar{z}}(\bar{z})$	$\left(4\bar{z}^3 - 6\bar{z}^2 + 1\right)$	1
$M_i(t,\bar{z})$	$\frac{EI_c}{H}q_3\left(-12\bar{z}^2 + 12\bar{z}\right)$	0
$V_i(t,\bar{z})$	$\frac{EI_c}{H}q_3\left(-24\bar{z} + 12\right)$	0
B.C.	$\phi_3(1) = \phi_3(0) = 0,\ \frac{\partial \phi_3}{\partial \bar{z}}(0) = 1,\ \frac{\partial \phi_3}{\partial \bar{z}}(1) = -1$ and $M_3(0) = M_3(1) = 0$	$\phi_4(0) = 0,\ \frac{\partial \phi_4}{\partial \bar{z}}(0) = 1$

Regime III

i	5	6
$\phi_i(\bar{z})$	$\begin{cases} \bar{z}/\bar{z}_m & \text{for } 0 \le \bar{z} \le \bar{z}_m \\ 1 - (\bar{z} - \bar{z}_m)/(1 - \bar{z}_m) & \text{for } \bar{z}_m < \bar{z} \le 1 \end{cases}$	$\bar{z}$
$\frac{\partial \phi_i}{\partial \bar{z}}(\bar{z})$	$\begin{cases} 1/\bar{z}_m & \text{for } 0 \le \bar{z} \le \bar{z}_m \\ -1/(1 - \bar{z}_m) & \text{for } \bar{z}_m < \bar{z} \le 1 \end{cases}$	1
$M_i(t,\bar{z})$	0	0
$V_i(t,\bar{z})$	0	0
B.C.	$\phi_5(1) = \phi_5(0) = 0,\ \phi_5(\bar{z}_m) = 1$	$\phi_6(0) = 0,\ \phi_6(1) = 1$

Table III.1: Shape functions, corresponding rotation, bending moment, shear force distributions and boundary conditions (B.C.).

(End of Table III.1: Shape functions, corresponding rotation, bending moment, shear force distributions and boundary conditions (BC).)

	Regime IV	
i	**7**	**8**
$\phi_i(\bar{z})$	$\begin{cases} \frac{1}{3}\left((\bar{z}/\bar{z}_m)^4 - 4(\bar{z}/\bar{z}_m)^3 + 6(\bar{z}/\bar{z}_m)^2\right) & \text{for } 0 \leq \bar{z} \leq \bar{z}_m \\ 1 - (\bar{z} - \bar{z}_m)/(1 - \bar{z}_m) & \text{for } \bar{z}_m < \bar{z} \leq 1 \end{cases}$	$\begin{cases} \frac{1}{3}\left((\bar{z}/\bar{z}_m)^4 - 4(\bar{z}/\bar{z}_m)^3 + 6(\bar{z}/\bar{z}_m)^2\right) & \text{for } 0 \leq \bar{z} \leq \bar{z}_m \\ 1 + 4(\bar{z} - \bar{z}_m)/(3\bar{z}_m) & \text{for } \bar{z}_m < \bar{z} \leq 1 \end{cases}$
$\frac{\partial \phi_i}{\partial \bar{z}}(\bar{z})$	$\begin{cases} \frac{1}{3\bar{z}_m}\left(4(\bar{z}/\bar{z}_m)^3 - 12(\bar{z}/\bar{z}_m)^2 + 12(\bar{z}/\bar{z}_m)\right) & \text{for } 0 \leq \bar{z} \leq \bar{z}_m \\ -1/(1-\bar{z}_m) & \text{for } \bar{z}_m < \bar{z} \leq 1 \end{cases}$	$\begin{cases} \frac{1}{3\bar{z}_m}\left(4(\bar{z}/\bar{z}_m)^3 - 12(\bar{z}/\bar{z}_m)^2 + 12(\bar{z}/\bar{z}_m)\right) & \text{for } 0 \leq \bar{z} \leq \bar{z}_m \\ 4/(3\bar{z}_m) & \text{for } \bar{z}_m < \bar{z} \leq 1 \end{cases}$
$M_i(t,\bar{z})$	$\begin{cases} -\frac{EI_c q_7}{3\bar{z}_m^2 H^2}\left(12(\bar{z}/\bar{z}_m)^2 - 24(\bar{z}/\bar{z}_m) + 12\right) & \text{for } 0 \leq \bar{z} \leq \bar{z}_m \\ 0 & \text{for } \bar{z}_m < \bar{z} \leq 1 \end{cases}$	$\begin{cases} -\frac{EI_c q_8}{3\bar{z}_m^2 H^2}\left(12(\bar{z}/\bar{z}_m)^2 - 24(\bar{z}/\bar{z}_m) + 12\right) & \text{for } 0 \leq \bar{z} \leq \bar{z}_m \\ 0 & \text{for } \bar{z}_m < \bar{z} \leq 1 \end{cases}$
$V_i(t,\bar{z})$	$\begin{cases} -\frac{EI_c q_7}{3\bar{z}_m^3 H^2}\left(24(\bar{z}/\bar{z}_m) - 24\right) & \text{for } 0 \leq \bar{z} \leq \bar{z}_m \\ 0 & \text{for } \bar{z}_m < \bar{z} \leq 1 \end{cases}$	$\begin{cases} -\frac{EI_c q_8}{3\bar{z}_m^3 H^2}\left(24(\bar{z}/\bar{z}_m) - 24\right) & \text{for } 0 \leq \bar{z} \leq \bar{z}_m \\ 0 & \text{for } \bar{z}_m < \bar{z} \leq 1 \end{cases}$
B.C.	$\phi_7(0) = \phi_7(1) = \frac{\partial \phi_7}{\partial \bar{z}}(0) = 0, \phi_7(\bar{z}_m) = 1$ and $M_7(\bar{z}_m) = T_7(\bar{z}_m) = 0$	$\phi_8(0) = \frac{\partial \phi_8}{\partial \bar{z}}(0) = 0, \phi_8(\bar{z}_m) = 1, \frac{\partial \phi_8}{\partial \bar{z}}(\bar{z}_m^-) = \frac{\partial \phi_8}{\partial \bar{z}}(\bar{z}_m^+) = 0$ and $M_8(\bar{z}_m) = T_8(\bar{z}_m) = 0$
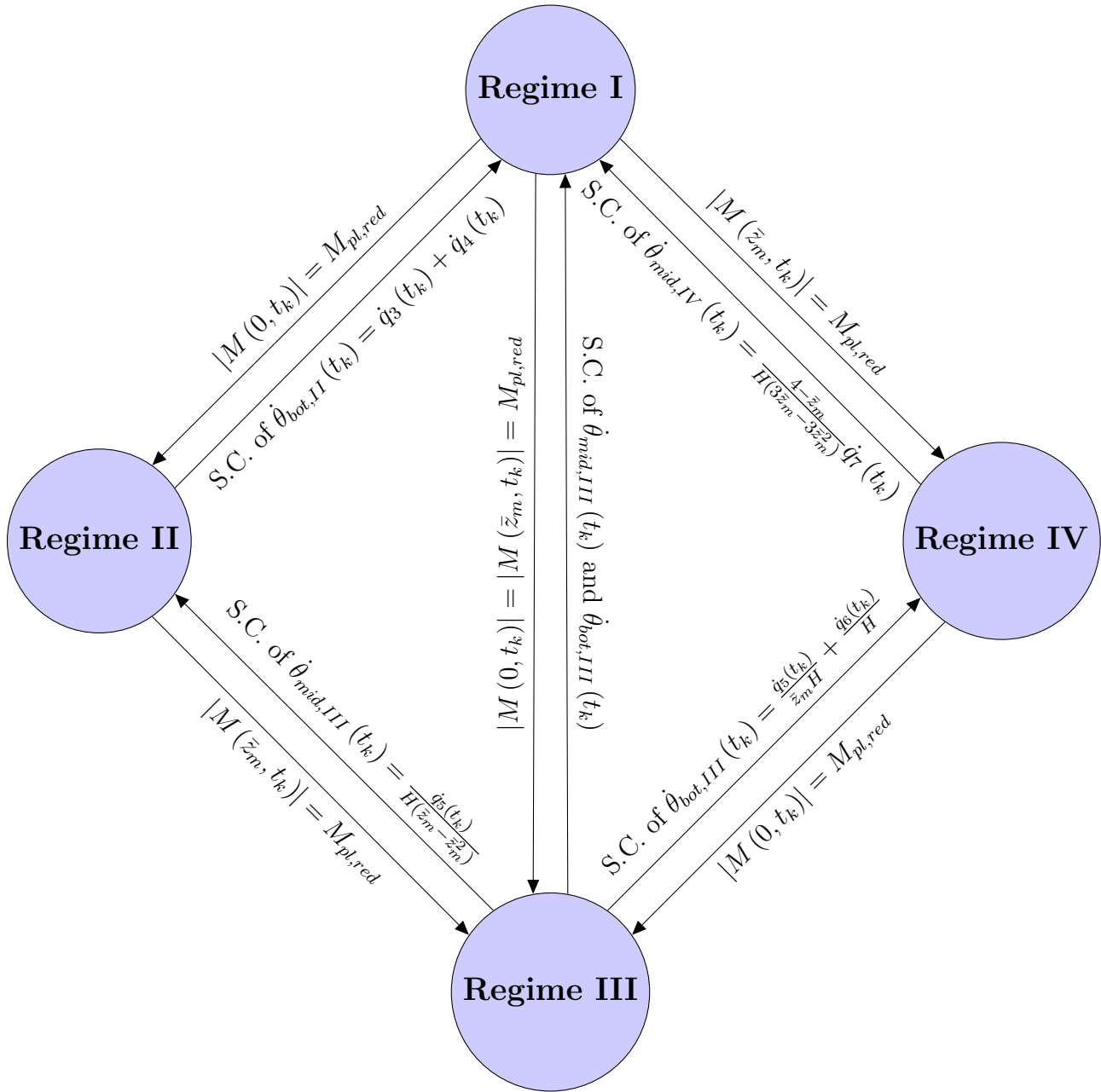
Figure III.3: Flow chart describing the transition between regimes (S.C. = sign change).

III.2.3 Governing equations

The elastic strain energy stored in the column is given by

$$U_1 = \frac{1}{2} \int_0^H EI_c \left(\frac{\partial^2 w_c}{\partial z^2} \right)^2 dz = \frac{EI_c}{2H^3} \int_0^1 \left(\frac{\partial^2 w_c}{\partial \bar{z}^2} \right)^2 d\bar{z} \qquad \text{(III.15)}$$

Taking into account the reduction of plastic bending moment due to the presence of axial load P, the energy dissipated in the plastic hinges can be expressed as

$$U_2 = M_{pl,red}\left(P\right)\left(\theta_{bot} + \theta_{mid}\right) \tag{III.16}$$

where $\theta_{bot} = \frac{1}{H}\frac{\partial w_c}{\partial \bar{z}}\big|_{\bar{z}=0^+}$ and $\theta_{mid} = \frac{1}{H}\left(\frac{\partial w_c}{\partial \bar{z}}\big|_{\bar{z}=\bar{z}_m^-} - \frac{\partial w_c}{\partial \bar{z}}\big|_{\bar{z}=\bar{z}_m^+}\right)$ respectively correspond to the variation of rotation angles at the plastic hinge locations.

The energy stored in the lateral restraint reads

$$U_3 = \frac{1}{2}K^\star w_c^2\big|_{\bar{z}=1}. \tag{III.17}$$

Damping does not affect significantly the dynamic behavior of the beam-column under blast waves before the first maximum displacement. Therefore the dissipation of energy D of the system is neglected.

The total kinetic energy can expressed as the sum of the kinetic contributions of the column and the lateral mass

$$K = \frac{1}{2}\int_0^H m_c \dot{w}_c^2 dz + \frac{1}{2}M^\star \dot{w}_c^2\big|_{\bar{z}=1} = \frac{m_c H}{2}\int_0^1 \dot{w}_c^2 d\bar{z} + \frac{1}{2}M^\star \dot{w}_c^2\big|_{\bar{z}=1}. \tag{III.18}$$

The work done by the axial load is

$$W_P = P\delta_c \tag{III.19}$$

where δ_c is the vertical displacement at the column head which can be calculated as follows

$$\delta_c = \int_0^H \frac{1}{2}\left(\frac{\partial w_c}{\partial z}\right)^2 dz = \frac{1}{2H}\int_0^1\left(\frac{\partial w_c}{\partial \bar{z}}\right)^2 d\bar{z}. \tag{III.20}$$

The external work done by the blast loading is given by

$$W_p = \int_0^H p w_c dz = pH\int_0^1 w_c d\bar{z}. \tag{III.21}$$

Finally, the Lagrange's Equation [85] reads

$$-\frac{d}{dt}\left(\frac{\partial K}{\partial \dot{q}_i}\right) + \left(\frac{\partial K}{\partial q_i}\right) - \sum_{j=1}^3\left(\frac{\partial U_j}{\partial q_i}\right) - \left(\frac{\partial D}{\partial \dot{q}_i}\right) + \frac{\partial\left(W_p + W_P\right)}{\partial q_i} = 0 \tag{III.22}$$

and provides the following generic equation of motion

$$\mathbf{M}_{\Gamma_i}\ddot{\mathbf{q}}_{\Gamma_i} + \mathbf{r}_{\Gamma_i} + \left(\mathbf{K}_{\Gamma_i} - \mathbf{K}_{P,\Gamma_i}\right)\mathbf{q}_{\Gamma_i} = \mathbf{p}_{\Gamma_i} - \left(\frac{EI_c}{H^3}\mathcal{H}_{A,\Gamma_i} - \frac{P}{H}\mathcal{H}_{B,\Gamma_i}\right)\mathbf{q}\left(t_{k-1}\right) \tag{III.23}$$

where Γ_i is the regime of the beam-column ($\Gamma_1 = $ I, $\Gamma_2 = $ II, $\Gamma_3 = $ III and $\Gamma_4 = $ IV). For regimes I, III and IV, the vector of the generalized displacements is given by

$$\mathbf{q}_{\Gamma_i} = \left[\begin{array}{c} q_{2i-1} \\ q_{2i} \end{array} \right] \tag{III.24}$$

while for regime II, it reads

$$\mathbf{q}_{II} = H \left[\begin{array}{c} q_3 \\ q_4 \end{array} \right]. \tag{III.25}$$

Symbols $\mathbf{M}_{\Gamma_i}$, $\mathbf{K}_{\mathbf{\Gamma_i}}$, $\mathbf{K}_{P,\Gamma_i}$, $\mathbf{r}_{\Gamma_i}$ and $\mathbf{p}_{\Gamma_i}$ are respectively the mass, linear stiffness and geometric matrices, the plastic resistance and the blast loading vectors of the substructure in regime Γ_i. Two dimensionless parameters χ_K and χ_M appear in the matrix expressions in Tables III.2 and III.3, respectively corresponding to the ratio of the lateral restraint stiffness $K^\star$ to rigidity EI_c/H^3 and the ratio of the lateral mass $M^\star$ to the beam-column mass $m_c H$. The matrices $\mathcal{H}_{A,\Gamma_i}$ and $\mathcal{H}_{B,\Gamma_i}$ include numerical values and the following vector $\mathbf{q}(t_{k-1})$ which contains the history of generalized displacements at the former regime transition time t_{k-1}:

$$\mathbf{q}^T (t_{k-1}) = \left[\begin{array}{cccc} \mathbf{q}_I (t_{k-1})^T & \mathbf{q}_{II} (t_{k-1})^T & \mathbf{q}_{III} (t_{k-1})^T & \mathbf{q}_{IV} (t_{k-1})^T \end{array} \right]. \tag{III.26}$$

Matrices provided in Tables III.2 and III.3 are given for a location of plastic hinge at "mid-height" of the beam-column $\overline{z}_m$ that is equal to 0.58. In appendix VI.3, Tables VI.1 and VI.2 include all these matrices, expressed in the general form as function of $\overline{z}_m$.

III.2.4   Description of the numerical method

The equation of motion (III.23) can be rearranged as

$$\mathbf{M}_{\Gamma_i} \ddot{\mathbf{q}}_{\Gamma_i} + \left(\mathbf{K}_{\Gamma_i} - \mathbf{K}_{P,\Gamma_i} \right) \mathbf{q}_{\Gamma_i} = \mathbf{p}_{\text{eq},\Gamma_i} (t) \tag{III.27}$$

where $\mathbf{p}_{\text{eq},\Gamma_i} (t) = \mathbf{p}_{\Gamma_i} (t) - \left(\frac{EI_c}{H^3} \mathcal{H}_{A,\Gamma_i} - \frac{P}{H} \mathcal{H}_{B,\Gamma_i} \right) \mathbf{q}(t_{k-1}) - \mathbf{r}_{\Gamma_i}$ is an equivalent load that includes the external blast loading and other terms that are time-independent. To solve this equation (III.27), we can use the Newmark's algorithm [87] for linear systems considering the constant acceleration parameters.

Table III.2

Regime	I	II	III	IV
$\mathbf{M}_{\Gamma_i}$	$m_c H \begin{bmatrix} \frac{130555}{290304} & \frac{2627}{10368} \\ \frac{2627}{10368} & \frac{104}{405} + \chi_M \end{bmatrix}$	$m_c H \begin{bmatrix} \frac{31}{630} & \frac{1}{10} \\ \frac{1}{10} & \frac{1}{3} + \chi_M \end{bmatrix}$	$m_c H \begin{bmatrix} 0.33 & 0.26 \\ 0.26 & 0.33 + \chi_M \end{bmatrix}$	$m_c H \begin{bmatrix} 0.29 & 0.43 \\ 0.43 & 1.11 + 3.89\chi_M \end{bmatrix}$
$\mathbf{K}_{\Gamma_i}$	$\frac{EI_c}{H^3} \begin{bmatrix} \frac{6845}{8} & \frac{64}{37} \\ \frac{64}{37} & \frac{16}{5} + \chi_K \end{bmatrix}$	$\frac{EI_c}{H^3} \begin{bmatrix} \frac{48}{10} & 0 \\ 0 & \chi_K \end{bmatrix}$	$\frac{EI_c}{H^3} \begin{bmatrix} 0 & 0 \\ 0 & \chi_K \end{bmatrix}$	$\frac{EI_c}{H^3} \begin{bmatrix} 16.53 & 16.53 \\ 16.53 & 16.53 + 3.89\chi_K \end{bmatrix}$
$\mathbf{K}_{P,\Gamma_i}$	$\frac{P}{H} \begin{bmatrix} \frac{6845}{1344} & \frac{185}{336} \\ -\frac{185}{336} & \frac{38}{7} \end{bmatrix}$	$\frac{P}{H} \begin{bmatrix} \frac{34}{70} & 0 \\ 0 & 1 \end{bmatrix}$	$\frac{P}{H} \begin{bmatrix} 4.1 & 0 \\ 0 & 1 \end{bmatrix}$	$\frac{P}{H} \begin{bmatrix} 4.35 & -0.33 \\ -0.33 & 4.21 \end{bmatrix}$
$\mathbf{p}_{\Gamma_i}$	$pH \begin{bmatrix} \frac{37}{64} \\ \frac{2}{5} \end{bmatrix}$	$pH \begin{bmatrix} \frac{1}{5} \\ \frac{1}{2} \end{bmatrix}$	$pH \begin{bmatrix} \frac{1}{2} \\ \frac{1}{2} \end{bmatrix}$	$pH \begin{bmatrix} 0.44 \\ 0.86 \end{bmatrix}$

Table III.2: Mass matrix, linear stiffness and geometric matrices and blast loading vectors of the structure for different regimes.

Table III.3

Regime	I	II
$\mathbf{r}_{\Gamma_i}$	$\begin{bmatrix} 0 \\ 0 \end{bmatrix}$	$\text{sign}\left(\dot{\theta}_{bot,II}\right) \frac{M_{pl,red}}{H} \begin{bmatrix} 1 \\ 1 \end{bmatrix}$
$\mathcal{H}_{A,\Gamma_i}$	$\begin{bmatrix} 0 & 0 & 13.88 & 0 & 0 & 0 & 21.9 & 21.9 \\ 0 & 0 & -2.4 & \chi_K & 0 & \chi_K & 6.86 & 6.86+1.97\chi_K \end{bmatrix}$	$\begin{bmatrix} 13.8 & -2.4 & 0 & 0 & 0 & 0 & -3.07 & -3.07 \\ 0 & \chi_K & 0 & 0 & \chi_K & 0 & 0 & 1.97\chi_K \end{bmatrix}$
$\mathcal{H}_{B,\Gamma_i}$	$\begin{bmatrix} 0 & 0 & 1.43 & 0 & 4.11 & 0 & 4.17 & -0.52 \\ 0 & 0 & -0.23 & 1 & -0.53 & 1 & -0.40 & 2.18 \end{bmatrix}$	$\begin{bmatrix} 1.43 & -0.24 & 0 & 0 & 1.24 & 0 & 1.12 & -0.30 \\ 0 & 1 & 0 & 0 & 1 & 0 & 1 & 1.97 \end{bmatrix}$

Regime	III	IV
$\mathbf{r}_{\Gamma_i}$	$\frac{M_{pl,red}}{H} \left\{ \text{sign}\left(\dot{\theta}_{bot,III}\right) \begin{bmatrix} 1.73 \\ 1 \end{bmatrix} + \text{sign}\left(\dot{\theta}_{mid,III}\right) \begin{bmatrix} 4.10 \\ 0 \end{bmatrix} \right\}$	$\text{sign}\left(\dot{\theta}_{mid,IV}\right) \frac{M_{pl,red}}{H} \begin{bmatrix} 4.68 \\ 0 \end{bmatrix}$
$\mathcal{H}_{A,\Gamma_i}$	$\begin{bmatrix} 0 & 0 & 0 & 0 & 0 & 0 & 0 & 0 \\ 0 & \chi_K & 0 & \chi_K & 0 & 0 & 0 & 1.97\chi_K \end{bmatrix}$	$\begin{bmatrix} 21.89 & 6.86 & 0 & 0 & 0 & 0 & 0 & 0 \\ 21.89 & 6.86+1.97\chi_K & -3.07 & -3.07 & 1.97\chi_K & 0 & 1.97\chi_K & 0 \end{bmatrix}$
$\mathcal{H}_{B,\Gamma_i}$	$\begin{bmatrix} 4.11 & -0.53 & 1.24 & 0 & 0 & 0 & 4.10 & -0.58 \\ 0 & 1 & 0 & 1 & 0 & 0 & 0 & 1.97 \end{bmatrix}$	$\begin{bmatrix} 4.17 & -0.40 & 1.12 & 0 & 4.10 & 0 & 0 & 0 \\ -0.52 & 2.18 & -0.30 & 1.97 & -0.58 & 1.97 & 1.97 & 0 \end{bmatrix}$

Table III.3: Plastic resistance vector and matrices $\mathcal{H}_{A,\Gamma_i}$ and $\mathcal{H}_{B,\Gamma_i}$ for different regimes.

III.2.5   Minimum Δ_0 technique

The minimum Δ_0 technique [115, 90, 116] allows to minimize the error in the unbalanced momentum quantities at the transition of two successive regimes. Using least mean square method, the cost function

$$\Delta_0 \left(v_1,\, v_2, \ldots, v_n \right) = \frac{1}{2} \int_0^1 m_c H \left(\dot{w}_{c,\Gamma_m} \left(\bar{z}, t_k \right) - \dot{w}_{c,\Gamma_n} \left(\bar{z}, t_k \right) \right)^2 d\bar{z} \qquad \text{(III.28)}$$

is minimized. In (III.28), where $\dot{w}_{c,\Gamma_n} \left(\bar{z}, t_k \right) = \sum\limits_{i=1}^{n} v_i \left(t_k \right) \phi_i \left(\bar{z} \right)$ and $\dot{w}_{c,\Gamma_m} \left(\bar{z}, t_k \right)$ respectively correspond to the velocity field of the current regime Γ_n and previous regime Γ_m, and $v_i \left(t_k \right)$ represents the generalized velocities in the beginning of the current regime.

Finding the minimum of a multivariate error $\Delta_0 \left(v_1,\, v_2, \ldots, v_n \right)$ involves that the gradient of Δ_0 with respect to these variables $v_1,\, v_2, \ldots, v_n$ is equal to zero

$$\nabla \left(\Delta_0 \right) = \begin{bmatrix} \frac{\partial \Delta_0}{\partial v_1} \\ \frac{\partial \Delta_0}{\partial v_2} \\ \vdots \\ \frac{\partial \Delta_0}{\partial v_n} \end{bmatrix} = \mathbf{0} \qquad \text{(III.29)}$$

which leads to a system of equations that should be solved as follows

$$m_c H \underbrace{\begin{bmatrix} \int_0^1 \phi_1 \left(\bar{z} \right)^2 d\bar{z} & \int_0^1 \phi_1 \left(\bar{z} \right) \phi_2 \left(\bar{z} \right) d\bar{z} & \cdots & \int_0^1 \phi_1 \left(\bar{z} \right) \phi_n \left(\bar{z} \right) d\bar{z} \\ \int_0^1 \phi_2 \left(\bar{z} \right) \phi_1 \left(\bar{z} \right) d\bar{z} & \int_0^1 \phi_2 \left(\bar{z} \right)^2 d\bar{z} & \cdots & \int_0^1 \phi_2 \left(\bar{z} \right) \phi_n \left(\bar{z} \right) d\bar{z} \\ \vdots & \vdots & \ddots & \vdots \\ \int_0^1 \phi_n \left(\bar{z} \right) \phi_1 \left(\bar{z} \right) d\bar{z} & \int_0^1 \phi_n \left(\bar{z} \right) \phi_2 \left(\bar{z} \right) d\bar{z} & \cdots & \int_0^1 \phi_n \left(\bar{z} \right)^2 d\bar{z} \end{bmatrix}}_{\mathbf{E}} \underbrace{\begin{bmatrix} v_1 \\ v_2 \\ \vdots \\ v_n \end{bmatrix}}_{\mathbf{v}}$$

$$= m_c H \underbrace{\begin{bmatrix} \int_0^1 \dot{w}_{c,\Gamma_m} \left(\bar{z}, t_k \right) \phi_1 \left(\bar{z} \right) d\bar{z} \\ \int_0^1 \dot{w}_{c,\Gamma_m} \left(\bar{z}, t_k \right) \phi_2 \left(\bar{z} \right) d\bar{z} \\ \vdots \\ \int_0^1 \dot{w}_{c,\Gamma_m} \left(\bar{z}, t_k \right) \phi_n \left(\bar{z} \right) d\bar{z} \end{bmatrix}}_{\mathbf{f}} \qquad \text{(III.30)}$$

$$\Rightarrow \mathbf{v} = \mathbf{E}^{-1} \mathbf{f}. \qquad \text{(III.31)}$$

In order to ensure that $\mathbf{v}$ corresponds to the minimum of the function Δ_0, the differential of Δ_0 should be computed in the vicinity of $\mathbf{v}$ as follows

$$\Delta_0 \left(v_1 + dv_1, \, v_2 + dv_2, \ldots, \, v_n + dv_n\right) - \Delta_0 \left(v_1, \, v_2, \ldots, v_n\right) = \begin{bmatrix} dv_1 & dv_2 & \cdots & dv_n \end{bmatrix} \underbrace{\begin{bmatrix} \frac{\partial \Delta_0}{\partial v_1} \\ \frac{\partial \Delta_0}{\partial v_2} \\ \vdots \\ \frac{\partial \Delta_0}{\partial v_n} \end{bmatrix}}_{=0}$$

$$+ \frac{1}{2} \underbrace{\begin{bmatrix} dv_1 & dv_2 & \cdots & dv_n \end{bmatrix}}_{\mathbf{dv}^T} \underbrace{\begin{bmatrix} \frac{\partial^2 \Delta_0}{\partial v_1^2} & \frac{\partial^2 \Delta_0}{\partial v_1 \partial v_2} & \cdots & \frac{\partial^2 \Delta_0}{\partial v_1 \partial v_n} \\ \frac{\partial^2 \Delta_0}{\partial v_2 \partial v_1} & \frac{\partial^2 \Delta_0}{\partial v_2^2} & \cdots & \frac{\partial^2 \Delta_0}{\partial v_2 \partial v_n} \\ \vdots & \vdots & \ddots & \vdots \\ \frac{\partial^2 \Delta_0}{\partial v_n \partial v_1} & \frac{\partial^2 \Delta_0}{\partial v_n \partial v_2} & \cdots & \frac{\partial^2 \Delta_0}{\partial v_n^2} \end{bmatrix}}_{\mathbf{H}} \underbrace{\begin{bmatrix} dv_1 \\ dv_2 \\ \vdots \\ dv_n \end{bmatrix}}_{\mathbf{dv}}$$

$$\tag{III.32}$$

which can be simplified as

$$\Delta_0 \left(v_1 + dv_1, \, v_2 + dv_2, \ldots, \, v_n + dv_n\right) - \Delta_0 \left(v_1, \, v_2, \ldots, v_n\right) = \frac{1}{2} \mathbf{dv}^T \mathbf{H} \mathbf{dv} > 0. \tag{III.33}$$

Thus, to get a local minimum at $\mathbf{v}$, the Hessian matrix $\mathbf{H}$ $(= \mathbf{E})$ should be positive-definite. In other words, the eigen values of the matrix $\mathbf{E}$ should be positive. For a 2-DOF model, the eigen values are positive; if the two following simple criteria are satisfied :

$$\mathrm{Det}\left(\mathbf{E}\right) > 0 \text{ and } \mathrm{Tr}\left(\mathbf{E}\right) > 0 \tag{III.34}$$

In our context, the analytical model includes two degrees of freedom. Therefore, the velocity fields at the beginning of the current regime Γ_n and at the end of the previous regime Γ_m can be respectively written as

$$\dot{w}_{c,\Gamma_m}\left(\bar{z}, t_k\right) = \sum_{r=2m-1}^{2m} v_r\left(t_k\right) \phi_r\left(\bar{z}\right) \tag{III.35}$$

and,

$$\dot{w}_{c,\Gamma_n}\left(\bar{z}, t_k\right) = \sum_{r=2n-1}^{2n} v_r\left(t_k\right) \phi_r\left(\bar{z}\right). \tag{III.36}$$

The generalized velocities of the current regime Γ_n can be expressed as a function of those of the previous regime Γ_m

$$\mathbf{v}_{\Gamma_n} = \mathbf{E}_{\Gamma_n, \Gamma_n}^{-1} \mathbf{f}\left(\mathbf{v}_{\Gamma_m}\right) \tag{III.37}$$

where $\mathbf{v}_{\Gamma_m} = \begin{bmatrix} v_{2m-1}\left(t_k\right) & v_{2m}\left(t_k\right) \end{bmatrix}^T$ and $\mathbf{v}_{\Gamma_n} = \begin{bmatrix} v_{2n-1}\left(t_k\right) & v_{2n}\left(t_k\right) \end{bmatrix}^T$. The matrix $\mathbf{E}_{\Gamma_n, \Gamma_n}^{-1}$ and vector $\mathbf{f}$ are respectively given by

$$\mathbf{E}_{\Gamma_n, \Gamma_n} = m_c H \begin{bmatrix} e_{2n-1,2n-1} & e_{2n-1,2n} \\ e_{2n,2n-1} & e_{2n,2n} \end{bmatrix}$$

and,

$$\mathbf{f} = m_c H \left[\begin{array}{c} \int_0^1 \dot{w}_{c,\Gamma_m} (\bar{z}, t_k) \, \phi_{2n-1} (\bar{z}) \, d\bar{z} + \chi_M \dot{w}_{c,\Gamma_m} (1, t_k) \, \phi_{2n-1} (1) \\ \int_0^1 \dot{w}_{c,\Gamma_m} (\bar{z}, t_k) \, \phi_{2n} (\bar{z}) \, d\bar{z} + \chi_M \dot{w}_{c,\Gamma_m} (1, t_k) \, \phi_{2n} (1) \end{array} \right]$$

where

$$e_{i,j} = \int_0^1 \phi_i (\bar{z}) \, \phi_j (\bar{z}) \, d\bar{z} + \chi_M \phi_i (1) \, \phi_j (1) = e_{j,i}. \tag{III.38}$$

It can be demonstrated that the matrix $\mathbf{E}_{\Gamma_n,\Gamma_n}$ corresponds to the mass matrix of the current regime $\mathbf{M}_{\Gamma_n}$. The vector $\mathbf{f}$ can be decomposed as follows

$$\begin{aligned} \mathbf{f} &= m_c H \left[\begin{array}{c} \int_0^1 \left(\sum_{r=2m-1}^{2m} v_r (t_k) \, \phi_r (\bar{z}) \right) \phi_{2n-1} (\bar{z}) \, d\bar{z} + \chi_M \left(\sum_{r=2m-1}^{2m} v_r (t_k) \, \phi_r (1) \right) \phi_{2n-1} (1) \\ \int_0^1 \left(\sum_{r=2m-1}^{2m} v_r (t_k) \, \phi_r (\bar{z}) \right) \phi_{2n} (\bar{z}) \, d\bar{z} + \chi_M \left(\sum_{r=2m-1}^{2m} v_r (t_k) \, \phi_r (1) \right) \phi_{2n} (1) \end{array} \right] \\ &= \mathbf{E}_{\Gamma_m,\Gamma_n} \mathbf{v}_{\Gamma_m} \end{aligned} \tag{III.39}$$

where

$$\mathbf{E}_{\Gamma_m,\Gamma_n} = m_c H \left[\begin{array}{cc} e_{2n-1,2m-1} & e_{2n-1,2m} \\ e_{2n,2m-1} & e_{2n,2m} \end{array} \right]. \tag{III.40}$$

Finally, the generalized velocities of the current regime Γ_n can be obtained

$$\mathbf{v}_{\Gamma_n} = \mathbf{M}_{\Gamma_n}^{-1} \mathbf{E}_{\Gamma_m,\Gamma_n} \mathbf{v}_{\Gamma_m} = \mathbf{G}_v \mathbf{v}_{\Gamma_m} \tag{III.41}$$

where $\mathbf{G}_v = \mathbf{M}_{\Gamma_n}^{-1} \mathbf{E}_{\Gamma_m,\Gamma_n}$ is given in Table III.4. It should be noted that $\mathbf{v}_{\Gamma_i} = \left[\begin{array}{cc} \dot{q}_{2i-1} (t_k) & \dot{q}_{2i} (t_k) \end{array} \right]^T$ for $\Gamma_i = $ I, II or IV whereas $\mathbf{v}_{II} = H \left[\begin{array}{cc} \dot{q}_3 (t_k) & \dot{q}_4 (t_k) \end{array} \right]^T$ for $\Gamma_i = $ II.

To \ From	Regime I	Regime II
Regime I	/	$\begin{bmatrix} \frac{32(709+5700\chi_M)}{925(69+608\chi_M)} & \frac{32(28(13+95\chi_M))}{925(69+608\chi_M)} \\ \frac{-19}{5(69+608\chi_M)} & \frac{(2(163+1520\chi_M))}{5(69+608\chi_M)} \end{bmatrix}$
Regime II	$\begin{bmatrix} \frac{925(32+285\chi_M)}{96(121+930\chi_M)} & \frac{-224(29+195\chi_M)}{96(121+930\chi_M)} \\ \frac{4625}{192(121+930\chi_M)} & \frac{32(751+5580\chi_M)}{192(121+930\chi_M)} \end{bmatrix}$	/
Regime III	$\begin{bmatrix} \frac{1.035+9.15\chi_M}{1+7.96\chi_M} & \frac{-0.198-1.433\chi_M}{1+7.96\chi_M} \\ \frac{0.147}{1+7.96\chi_M} & \frac{1.02+7.96\chi_M}{1+7.96\chi_M} \end{bmatrix}$	$\begin{bmatrix} \left(\frac{0.377+3.016\chi_M}{1+7.96\chi_M}\right) & 0 \\ \left(\frac{2.13\,10^{-3}}{1+7.96\chi_M}\right) & 1 \end{bmatrix}$
Regime IV	$\begin{bmatrix} \frac{1.157+9.995\chi_M}{1+8.1\chi_M} & \frac{-0.076-0.596\chi_M}{1+8.1\chi_M} \\ \frac{0.052}{1+8.1\chi_M} & \frac{0.509+4.11\chi_M}{1+8.1\chi_M} \end{bmatrix}$	/

To \ From	Regime III	Regime IV
Regime I	$\begin{bmatrix} \frac{0.925+7.54\chi_M}{1+8.81\chi_M} & \frac{0.182-1.334\chi_M}{1+8.81\chi_M} \\ \frac{-0.122}{1+8.81\chi_M} & \frac{0.945+8.81\chi_M}{1+8.81\chi_M} \end{bmatrix}$	$\begin{bmatrix} \frac{57+484\chi_M}{69+608\chi_M} & \frac{9.02+71.7\chi_M}{69+608\chi_M} \\ \frac{-3.69}{69+608\chi_M} & \frac{134.5+1198.7\chi_M}{69+608\chi_M} \end{bmatrix}$
Regime II	$\begin{bmatrix} \frac{2.47+19.74\chi_M}{1+7.69\chi_M} & 0 \\ \frac{0.048}{1+7.69\chi_M} & 1 \end{bmatrix}$	/
Regime III	/	$\begin{bmatrix} \frac{0.889+7.342\chi_M}{1+7.96\chi_M} & \frac{-0.25-1.73\chi_M}{1+7.96\chi_M} \\ \frac{0.043}{1+7.96\chi_M} & \frac{2.02+15.68\chi_M}{1+7.96\chi_M} \end{bmatrix}$
Regime IV	$\begin{bmatrix} \frac{1.092+8.622\chi_M}{1+8.10197\chi_M} & \frac{0.124+0.878\chi_M}{1+8.10197\chi_M} \\ \frac{-0.0185}{1+8.10197\chi_M} & \frac{0.497+4.11\chi_M}{1+8.10197\chi_M} \end{bmatrix}$	/

Table III.4: Matrix $\mathbf{G}_v$ according to the transition between two regimes.

III.2.6 Linear buckling analysis

To check the validity of the UFC approach described in Section III.1 and to establish the dimensionless formulation of the Equ. of motion (III.23) in the next Section III.2.7, the Euler critical axial load P_{cr} should be computed by performing a linear perturbation analysis. The linear buckling load is obtained by solving the following eigenvalue problem [117]

$$\left(\mathbf{K}_I - \lambda\mathbf{K}_{P,I}\right)\mathbf{q}_I = 0 \tag{III.42}$$

where λ is the load factor.

Non trivial solution involves that

$$\mathbf{q}_I \neq 0 \Rightarrow \mathrm{Det}\left(\mathbf{K}_I - \lambda\mathbf{K}_{P,I}\right) = 0. \tag{III.43}$$

The smallest eigenvalue of Equ. (III.43) corresponds to the critical load factor λ_{cr}. Hence, the critical axial load P_{cr} can be obtained as follows

$$P_{cr} = \lambda_{cr} P = \frac{\pi^2 EI_c}{(K_{cr}H)^2} \Rightarrow K_{cr} = \sqrt{\frac{\pi^2 EI_c}{\lambda_{cr} P H^2}}. \tag{III.44}$$

Finally, the effective column length factor K_{cr} can be expressed as a function of χ_K

$$K_{cr} = \frac{10.34}{\sqrt{141 + 5\chi_K - \sqrt{13056 + \chi_K(-865 + 25\chi_K)}}} \tag{III.45}$$

which respectively takes a value of 0.686 for $\chi_K \to \infty$ corresponding the pinned-fixed beam-column and 2 for $\chi_K = 0$ corresponding to the cantilever beam-column (see Fig III.4-a). The corresponding modes of instability are illustrated in Fig. III.4-b.

(a) (b)
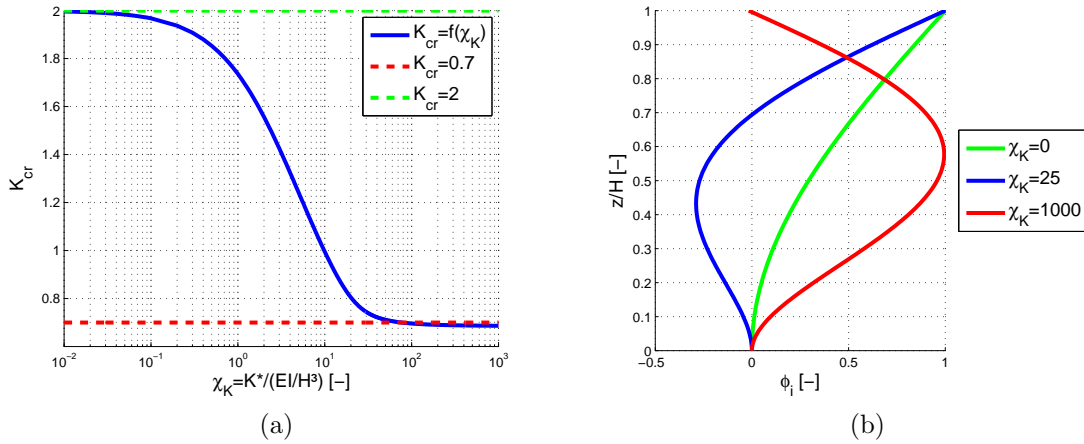
Figure III.4: (a) Effective length factor K_{cr} of the beam-column according to χ_K; (b) Modes of instability according to three values of χ_K.

III.2.7   Scaling and dimensionless formulation

A natural timescale of the problem is the following characteristic time T_c of the column

$$T_c = \sqrt{\frac{m_c H}{EI_c/H^3}}. \tag{III.46}$$

The characteristic pressure p_c and displacement Q_c are respectively given by

$$p_c = \frac{M_{pl}}{H^2} \quad ; \quad Q_c = \frac{p_c H}{EI_c/H^3}. \tag{III.47}$$

The equation of motion (III.23) can be written in a dimensionless form as follows

$$\tilde{\mathbf{M}}_{\Gamma_i} \tilde{\mathbf{q}}_{\Gamma_i}'' + m(n)\tilde{\mathbf{r}}_{\Gamma_i} + \left(\tilde{\mathbf{K}}_{\Gamma_i} - \frac{\pi^2 \alpha_{cr}}{K_{cr}^2} \tilde{\mathbf{K}}_{P,\Gamma_i} \right) \tilde{\mathbf{q}}_{\Gamma_i} = \tilde{\mathbf{p}}_{\Gamma_i} \tilde{p} \left(1 - \frac{\tilde{\tau}}{\tilde{\tau}_d} \right) - \left(\mathcal{H}_{A,\Gamma_i} - \frac{\pi^2 \alpha_{cr}}{K_{cr}^2} \mathcal{H}_{B,\Gamma_i} \right) \tilde{\mathbf{q}}(\tilde{\tau}_{k-1})$$
$$\tag{III.48}$$

where $\tilde{\mathbf{q}}_{\Gamma_i} = \mathbf{q}_{\Gamma_i}/Q_c$ and $\tilde{\mathbf{q}}\left(\tilde{\tau}_{k-1}\right) = \mathbf{q}\left(t_{k-1}\right)/Q_c$ are the vectors of dimensionless generalized displacements. $\tilde{\mathbf{M}}_{\Gamma_i} = \mathbf{M}_{\Gamma_i}/\left(m_cH\right)$, $\tilde{\mathbf{K}}_{\Gamma_i} = \mathbf{K}_{\Gamma_i}/\left(EI_c/H^3\right)$, $\tilde{\mathbf{K}}_{P,\Gamma_i} = \mathbf{K}_{P,\Gamma_i}/\left(P/H\right)$, $\tilde{\mathbf{r}}_{\Gamma_i} = \mathbf{r}_{\Gamma_i}/\left(M_{pl,red}/H\right)$ and $\tilde{\mathbf{p}}_{\Gamma_i} = \mathbf{p}_{\Gamma_i}/\left(pH\right)$ are respectively the dimensionless mass matrix, the linear stiffness and geometric matrices, the plastic resistance and the blast loading vectors of the substructure at the regime Γ_i. The prime symbol $'$ represents differentiation with respect to the dimensionless time $\tilde{\tau} = t/T_c$.

Other dimensionless parameters of the problem naturally appear as the ratio $\tilde{\tau}_d = t_d/T_c$ of the duration of blasting over the characteristic timescale, the ratio $\tilde{\tau}_{k-1} = t_{k-1}/T_c$ of the transition regime time over the characteristic timescale, the ratio $\chi_M = M^\star/m_cH$ of the lateral participating mass to the mass of the column, the ratio $\chi_K = K^\star/\left(EI_c/H^3\right)$ of the lateral restraint to the flexural rigidity of the column EI_c/H^3, the inverse of the critical load multiplier $\alpha_{cr} = P/P_{cr} = 1/\lambda_{cr}$ of the column defined as the ratio of the applied axial load P to the the Euler critical axial load P_{cr}, the dimensionless peak overpressure of the blast loading $\tilde{p} = p_0/p_c$. In addition, the bending moment-axial force plastic interaction reads

$$m\left(n\right) = \begin{cases} 1 - \gamma_0 n^2 & \text{for } 0 \leq n \leq \frac{A_w}{A}, \\ 1 - \gamma_1 - \gamma_2 n - \gamma_3 n^2 & \text{for } \frac{A_w}{A} \leq n \leq 1 \end{cases} \tag{III.49}$$

where $n = P/N_{pl}$ corresponds to the ratio of the axial load to the axial plastic resistance of the beam-column and γ_0, γ_1, γ_2 and γ_3 depend on the geometrical properties of the cross-section, see Equ. (I.51).

Therefore, the rapid assessment tool is ruled out by these dimensionless parameters n, α_{cr}, χ_M, χ_K, $\tilde{p}$ and $\tilde{\tau}_d$ (and also γ_0, γ_1, γ_2 and γ_3). Another choice of set of parameters could be $\bar{\lambda}$, α_{cr}, χ_M, χ_K, $\tilde{p}$ and $\tilde{\tau}_d$ where the reduced slenderness $\bar{\lambda}$ of the beam-column is given by

$$\bar{\lambda} = \sqrt{\frac{N_{pl}}{P_{cr}}} \tag{III.50}$$

and the axial force n could be expressed as a function of $\bar{\lambda}$ and α_{cr} as follows

$$n = \frac{\alpha_{cr}}{\bar{\lambda}^2}. \tag{III.51}$$

III.3 Particular cases

The 2-DOF model can be simplified into a SDOF model when the beam-column presents a pinned support ($K^\star \to +\infty$) or is free ($K^\star = 0$) at the top of the beam-column. This single degree of freedom respectively corresponds to the deflection at mid-height (for $K^\star \to +\infty$) or at the top of the beam-column (for $K^\star = 0$). They will be studied in the following sections.

III.3.1 Free-fixed beam-column

The equation of motion of the free-fixed beam-column under blast loading is given by

$$M_c\ddot{Y}\left(t\right) + R_r\left(Y\left(t\right)\right) = pH \tag{III.52}$$

where $Y(t)$ is the deflection at the top of the beam-column and the generalized mass M_c and the reduced resistance R_r of the beam-column respectively read

$$M_c = \begin{cases} \left(\frac{52}{81} + \frac{5}{2}\chi_M\right) m_c H & \text{for } Y(t) \leq Y_{el}, \\ 2\left(\frac{1}{3} + \chi_M\right) m_c H & \text{for } Y_{el} < Y(t), \end{cases} \tag{III.53}$$

$$R_r(Y(t)) = \begin{cases} k_{c,1}Y(t) - \frac{20}{7}\frac{P}{H}Y(t) & \text{for } Y(t) \leq Y_{el}, \\ R_u - 2\frac{P}{H}Y(t) & \text{for } Y_{el} < Y(t). \end{cases} \tag{III.54}$$

Other parameters $k_{c,1} = 8\frac{EI_c}{H^3}$, $R_u = 2\frac{M_{pl,red}}{H}$ and $Y_{el} = Y(t_1) = \frac{R_u}{k_{c,1}}$ respectively correspond to the bending elastic stiffness, the plastic resistance and the elastic deflection of the beam-column (subsequent to the development of a plastic hinge at time t_1). Equation (III.52) can be obtained from (III.23), by imposing that all the generalized displacements with an odd subscript are equal to zero.

Applying the Δ_0 minimum technique allows to express the velocity of the beam-column at the beginning of the plastic stage $\dot{Y}(t_1^+)$ as a function of the velocity at the end of the previous (elastic) stage $\dot{Y}(t_1^-)$

$$\dot{Y}(t_1^+) = \frac{\frac{13}{45} + \chi_M}{\frac{1}{3} + \chi_M} \dot{Y}(t_1^-). \tag{III.55}$$

Concerning the linear buckling analysis, the inertia and blast loading terms in Equ. (III.52) are disregarded to get the following condition

$$R_r(Y < Y_{el}) = 0 \tag{III.56}$$

which leads to the determination of the elastic critical axial load $P_{cr,SDOF}$ associated to this SDOF model

$$P_{cr,SDOF} = \pi^2 \frac{EI_c}{(1.88H)^2} > P_{cr} = \pi^2 \frac{EI_c}{(2H)^2}, \tag{III.57}$$

where $2H$ corresponds to the actual buckling length of a free-fixed beam-column. Equation (III.57) reveals that the critical axial load is overestimated for the SDOF model, as a result of the definition of shape functions.

The reduced resistance can also be rewritten as

$$R_r(Y(t)) = \begin{cases} \left[k_{c,1}\left(1 - \frac{P}{P_{cr,SDOF}}\right)\right]Y(t) & \text{for } Y(t) \leq Y_{el}, \\ R_u - 2\frac{P}{H}Y(t) & \text{for } Y_{el} < Y(t) \end{cases} \tag{III.58}$$

which highlights that the axial load P reduces the flexural elastic stiffness of the beam-column.

The periods of vibration of the elastic free-fixed beam-column in the absence or presence of axial load are respectively given by

$$T_0 = 2\pi \sqrt{\frac{\left(\frac{52}{81} + \frac{5}{2}\chi_M\right) m_c H}{k_{c,1}}} \tag{III.59}$$

and

$$T = 2\pi \sqrt{\frac{\left(\frac{52}{81} + \frac{5}{2}\chi_M\right) m_c H}{k_{c,1}\left(1 - \frac{P}{P_{cr,SDOF}}\right)}} = \frac{T_0}{\sqrt{1 - \frac{P}{P_{cr,SDOF}}}}. \tag{III.60}$$

III.3.2 Pinned-fixed beam-column

The equation of motion of the pinned-fixed beam-column

$$M_c \ddot{Y}(t) + R_r(Y(t)) = pH \tag{III.61}$$

where $Y(t)$ is the deflection at mid-height (at a distance z_m from the basis) of the beam-column and the generalized mass M_c and the reduced resistance R_r of the beam-column respectively read

$$M_c = \begin{cases} \frac{3515}{4536} m_c H & \text{for } Y(t) \le Y_{el,1}, \\ \frac{248}{315} m_c H & \text{for } Y_{el,1} < Y(t) \le Y_{el}, \\ \frac{2}{3} m_c H & \text{for } Y_{el} < Y(t), \end{cases} \tag{III.62}$$

and,

$$R_r(Y(t)) = \begin{cases} \left(k_{c,1} - \frac{185}{21}\frac{P}{H}\right) Y(t) & \text{for } Y(t) \le Y_{el,1}, \\ R_y + \left(k_{c,2} - \frac{272}{35}\frac{P}{H}\right)(Y(t) - Y_{el,1}) - \frac{2405}{336}\frac{P}{H}Y_{el,1} & \text{for } Y_{el,1} < Y(t) \le Y_{el}, \\ R_u - 8.2\frac{P}{H}Y(t) - 0.258\frac{P}{H}Y_{el,1} + 0.242\frac{P}{H}Y_{el} & \text{for } Y_{el} < Y(t). \end{cases}$$
$$\tag{III.63}$$

Other parameters $k_{c,1} = 185\frac{EI_c}{H^3}$, $k_{c,2} = \frac{384}{5}\frac{EI_c}{H^3}$, $R_y = 8\frac{M_{pl,red}}{H}$ and $R_u = 11.66\frac{M_{pl,red}}{H}$ respectively correspond the elastic bending stiffness of a pinned-fixed and simply supported beam-column, the plastic resistance associated to the development of the first plastic hinge (at time t_1) and the second plastic hinge (at time t_2). The elastic deflection, corresponding to the development of the full plastic mechanism, is described by

$$Y_{el} = Y(t_2) = Y_{el,1} + (R_u - R_y)/k_{c,2} \tag{III.64}$$

where $Y_{el,1} = Y(t_1) = R_y/k_{c,1}$ represents the deflection of the beam-column when the first plastic hinge appears.

Equation (III.61) can be obtained from (III.23), by imposing that all generalized displacements with an even subscript are equal to zero.

Regarding the velocities at regime transitions, they can be obtained by using again the Δ_0 minimum technique

$$\dot{Y}(t_1^+) = 0.923\dot{Y}(t_1^-) \quad , \quad \dot{Y}(t_2^+) = 1.213\dot{Y}(t_2^-). \tag{III.65}$$

A linear buckling analysis of the SDOF model enables to get the corresponding elastic critical load

$$R_r\left(Y < Y_{el,1}\right) = 0 \tag{III.66}$$

$$\Rightarrow P_{cr,SDOF} = \pi^2 \frac{EI_c}{\left(0.686H\right)^2} > P_{cr} = \pi^2 \frac{EI_c}{\left(0.7H\right)^2} \tag{III.67}$$

which indicates a slightly higher value than the real one. It should be mentioned that $0.7H$ corresponds to the buckling length of a pinned-fixed beam-column.

Therefore, the reduced resistance can be reformulated as

$$R_r\left(Y\left(t\right)\right) = \begin{cases} \left[k_{c,1}\left(1 - \frac{P}{P_{cr,SDOF}}\right)\right]Y\left(t\right) & \text{for } Y\left(t\right) \leq Y_{el,1}, \\ R_y + \left(k_{c,2} - \frac{272}{35}\frac{P}{H}\right)\left(Y\left(t\right) - Y_{el,1}\right) - \frac{2405}{336}\frac{P}{H}Y_{el,1} & \text{for } Y_{el,1} < Y\left(t\right) \leq Y_{el}, \\ R_u - 8.2\frac{P}{H}Y\left(t\right) - 0.258\frac{P}{H}Y_{el,1} + 0.242\frac{P}{H}Y_{el} & \text{for } Y_{el} < Y\left(t\right). \end{cases} \tag{III.68}$$

Finally, the periods of vibration of the elastic pinned-fixed beam-column in the absence or presence of axial load are respectively given by

$$T_0 = 2\pi\sqrt{\frac{\frac{3515}{4536}m_cH}{k_{c,1}}} \tag{III.69}$$

and

$$T = 2\pi\sqrt{\frac{\frac{3515}{4536}m_cH}{k_{c,1}\left(1 - \frac{P}{P_{cr,SDOF}}\right)}} = \frac{T_0}{\sqrt{1 - \frac{P}{P_{cr,SDOF}}}}. \tag{III.70}$$

III.4 Asymptotic solutions

Dragos *et al.* [73] propose to derive the analytical expressions of the asymptotic solutions of the P-I diagram for steel columns under lateral blast loading and axial constant load. These analytical asymptotic solutions are established for SDOF models and can be therefore applied in two specific configurations: for free-fixed or pinned-fixed beam-columns.

III.4.1 Free-fixed beam-column

To get the quasi-static asymptotic solution $(t_d/T \gg 1)$, the work done W_p by the blast loading is balanced with the strain energy E_r stored in the structure at maximum displacement Y_m $(\geq Y_{el})$

$$W_p = p_\infty H Y_m = E_r\left(Y_m\right) \tag{III.71}$$

where the strain energy reduced by the presence of axial load is given by

$$
\begin{aligned}
E_r\left(Y_m\right) &= \int_0^{Y_m} R_r dY \\
&= -\frac{3H^3 M_{pl,red}^2 P}{112\left(EI_c\right)^2} - \frac{H M_{pl,red}^2}{4EI_c} + \frac{2M_{pl,red} Y_m}{H} - \frac{PY_m^2}{H}.
\end{aligned}
\tag{III.72}
$$

The quasi-static asymptotic solution p_∞ can be expressed as a function of the maximum displacement

$$
p_\infty = \frac{2M_{pl,red}}{H^2} - \frac{M_{pl,red}^2\left(28EI_c + 3H^2 P\right)}{112\left(EI_c\right)^2 Y_m} - \frac{PY_m}{H^2}.
\tag{III.73}
$$

Differentiating Equ. (III.71) with respect to Y_m yields the maximum value of p_∞ before the beam-column becomes unstable

$$
\frac{dp_\infty}{dY_m} = 0
\tag{III.74}
$$

where the corresponding maximum displacement $Y_{b,p}$ satisfying Equ. (III.74) is given by

$$
Y_{b,p} = \frac{0.094 H M_{pl,red}\sqrt{28EI_c + 3H^2 P}}{EI_c\sqrt{P}}.
\tag{III.75}
$$

The impulsive asymptotic solution $(t_d/T \ll 1)$ is derived by equating the initial kinetic energy of the system and the strain energy at maximum displacement

$$
K = \frac{1}{2}M_c\left(Y > Y_{el}\right)\dot{Y}_0^2 = \frac{1}{2}\frac{I_\infty^2 H^2}{M_c\left(Y > Y_{el}\right)} = E_r\left(Y_{b,i}\right)
\tag{III.76}
$$

where $M_c\left(Y > Y_{el}\right) = 2\left(\frac{1}{3} + \chi_M\right)m_c H$ is the generalized mass of the beam-column in the plastic regime. The initial velocity of the beam-column is obtained by writing the momentum conservation as follows

$$
\begin{aligned}
M_c\left(Y > Y_{el}\right)\dot{Y}_0 &= I_\infty H \\
\Rightarrow \dot{Y}_0 &= \frac{I_\infty H}{M_c\left(Y > Y_{el}\right)}.
\end{aligned}
\tag{III.77}
$$

Therefore, Equ. (III.76) provides the expression of the impulsive asymptotic solution

$$
\begin{aligned}
I_\infty &= \frac{0.077\sqrt{2Hm_c + 6M^\star}}{EI_c H^{3/2}}\left(-28EI_c H^2 M_{pl,red}^2 - 3H^4 M_{pl,red}^2 P + 224\left(EI_c\right)^2 M_{pl,red}Y_{b,i}\right. \\
&\quad \left. -112\left(EI_c\right)^2 PY_{b,i}^2\right)^{1/2}
\end{aligned}
\tag{III.78}
$$

where the maximum displacement $Y_{b,i}$ before the column buckles is obtained by satisfying this relationship

$$\begin{aligned} R_r\left(Y_{b,i} > Y_{el}\right) &= 0 \\ \Rightarrow Y_{b,i} &= \frac{M_{pl,red}}{P}. \end{aligned} \tag{III.79}$$

Equation (III.79) expresses that the $P-\delta$ effect is so important that it annihilates the flexural resistance of the column. As a result, the inertial forces are no longer counterbalanced by the reduced internal resistance R_r (see Equ. (III.52)), leading to the instability of beam-column beyond displacement $Y_{b,i}$.

It should be noted that the subscript b relates to *buckling* while the subscripts p and i respectively refer to *quasi-static* and *impulsive* blast loading.

III.4.2 Pinned-fixed beam-column

The procedure to derive the asymptotic solutions is similar to the one described in Section III.4.1. Thus, the asymptotic solutions of pinned-fixed beam-column are summarized in this Section.

The quasi-static asymptotic solution for pinned-fixed beam-column can also be obtained from Equ. (III.71)

$$p_\infty = \frac{1.1\,10^{-3}H^2 M_{pl,red}^2 P}{(EI_c)^2 Y_{b,p}} - \frac{0.418 M_{pl,red}^2}{EI_c Y_{b,p}} + \frac{0.0108 M_{pl,red} P}{EI_c} + \frac{11.66 M_{pl,red}}{H^2} - \frac{4.10 P Y_{b,p}}{H^2} \tag{III.80}$$

where the corresponding maximum displacement $Y_{b,p}$ before buckling is described by

$$Y_{b,p} = \frac{4.008\sqrt{6.35\,10^{-3}EI_c H^2 M_{pl,red}^2 - 1.655\,10^{-5}H^4 M_{pl,red}^2 P}}{EI_c\sqrt{P}}. \tag{III.81}$$

The impulsive asymptotic solution for pinned-fixed beam-column can be obtained from Equ. (III.76)

$$\begin{aligned} I_\infty &= \frac{6.855\sqrt{m_c}}{EI_c H}\Big(0.331\left(EI_c\right)^2 M_{pl,red} Y_{b,i} - 0.116\left(EI_c\right)^2 P Y_{b,i}^2 - 1.187\,10^{-2}EI_c H^2 M_{pl,red}^2 \\ &\quad + 3.07\,10^{-4}EI_c H^2 M_{pl,red} P Y_{b,i} + 3.095\,10^{-5}H^4 M_{pl,red}^2 P\Big)^{1/2} \end{aligned} \tag{III.82}$$

where the corresponding maximum displacement $Y_{b,i}$ before buckling is defined by

$$Y_{b,i} = \frac{1.32\,10^{-3}\,H^2 M_{pl,red}}{EI_c} + \frac{1.422 M_{pl,red}}{P}. \tag{III.83}$$

III.5   FinelG numerical validation

III.5.1   Benchmark study

Consider a steel beam-column made of a W150x24 profile with a yield strength f_y of 470 MPa and an elastic modulus E of 180000 MPa as in [79, 80]. The lineic mass m_c and height H of the beam-column are respectively equal to 23.7 kg/m and 4 m. The plastic bending resistance M_{pl}, axial resistance N_{pl} and shear resistance V_{pl} are respectively equal to 89 kN.m, 1420 kN and 268 kN. According to Lescouar'ch formula (see Equ. (III.11)), the coefficients γ_0, γ_1, γ_2 and γ_3 of M-N plastic interaction are respectively equal to 1.826, -0.158, 1.040 and 0.118 for strong axis bending. The lateral mass $M^\star$, the stiffness of the lateral restraint $K^\star$, the blast loading p and the vertical axial load P will be varied in order to study their influence on the dynamic stability of the column. The characteristic pressure, time and displacement are respectively given by

$$p_c = 5.562 \, \text{kN/m} \quad ; \quad T_c = 50.4 \, \text{ms} \quad ; \quad Q_c = 0.596 \, \text{m}. \tag{III.84}$$

They scale the results shown in Section III.5.3, except for the displacement which is scaled according to the yield displacement Y_{el} in the presence of axial load (or $Y_{el,0}$ in the absence of it).

III.5.2   Assumptions on the modeling

In order to evaluate the accuracy of the analytical models (SDOF, 2-DOF models and UFC approach) of the beam-column under blast loading (see Fig. III.1-a), their corresponding results are compared with those of the FinelG model and their limitations are also discussed in Section III.5.3. The beam-column is modeled using the 2D Euler-Bernoulli beam elements incorporated in FinelG software (element type of 33 for plane frames) with a large number of finite elements (120) to capture well the higher modes of vibration as well as some specific phenomena such as the possible traveling of plastic hinge(s).

The axial gravity load is firstly applied at the top of the beam-column, then the beam-column is subjected to a uniformly distributed transverse blast loading as illustrated in Fig. III.1-b. The initial displacement, velocity and acceleration of the beam-column are equal to 0. The dynamic analysis is carried out using the implicit time integration scheme of Newmark with constant acceleration parameters [87] and a very small time step of integration $\Delta t = 3 \, 10^{-2} \, \text{ms}$ ($\Delta t / T_c = 6 \, 10^{-4}$) to provide accurate responses of the dynamic buckling of the beam-column under impulsive regime.

III.5.3   Comparison of FinelG model and 2-DOF model

The numerical simulations are performed in two steps, firstly by assuming that the material law is indefinitely linear elastic and secondly, by considering it as elastic-perfectly-plastic. The assumptions made on the analytical models are discussed, and the limitations of the analytical models are eventually highlighted. The influence of the parameters χ_K and χ_M are studied through several case studies.

III.5.3.1 Indefinitely elastic material

Pinned-fixed beam-column

The pinned-fixed beam-column has a buckling length of $0.7H$ leading to an axial critical load of $P_{cr} = 3138\,\text{kN}$. Due to the simple support at the top of the beam-column, the parameters χ_K and χ_M tend to infinity. For this first study case, the column is subjected to a blast loading, featured by a peak overpressure $\tilde{p} = p_0/p_c$ of 80 and positive phase duration $\tilde{\tau}_d = t_d/T_c$ of 0.1. The axial load P applied at the top of the column is equal to $1000\,\text{kN}$, leading to the following inverse of critical multiplier $\alpha_{cr} = 0.319$.

Figure III.5 shows the time-history of mid-height and top displacement of the beam-column predicted by the SDOF, 2-DOF and FinelG models. A perfect agreement is achieved between the analytical and numerical results. The first natural dimensionless periods of vibration T/T_c and T_0/T_c, respectively associated to the presence and absence of axial load, are equal to 0.49 and 0.41. They are obtained from the modal analysis of 2-DOF model and they correspond to the elapsed time between two successive positive peaks of displacement. As observed in Fig. III.5-a, for a same duration, the number of peaks is smaller when the axial load P is applied than in the absence of it, confirming the discrepancy in the periods of vibration. Moreover, the maximum displacement is slightly amplified when the axial load P is applied to the beam-column due to the reduction of flexural stiffness related to the presence of a compressive force.

The time-history of the bending moment predicted by the analytical models are calculated on the basis of the curvatures of shape functions and generalized displacements in the elastic regime (see Equ.(III.13)). Figure III.5-b illustrates the time evolution of the bending moment at the bottom and at mid-height of the beam-column (at a distance z_m from the basis), the analytical models provide very accurate results in comparison to numerical model.

Table III.5 collects all the values of the amplification factors obtained from the UFC approach, the 2-DOF and FinelG models. The results highlight a very good correlation between the different approaches for this first case study. It should be noted that the periods of vibration T and T_0 accounted in the computation of the dynamic load factors (DLF and DLF_0) for the UFC approach are based on the modal analysis of 2-DOF model. For this case study, they are identical to those computed for the SDOF model (see (III.70) and (III.69)) as the beam-column responds primarily in the first mode of vibration, but this is not always the case.
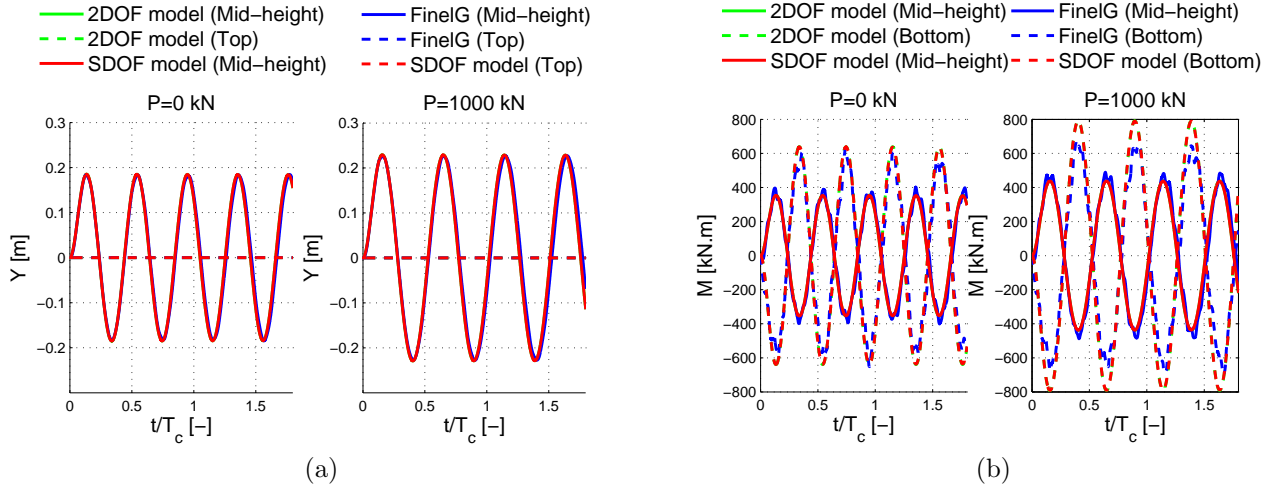
Figure III.5: Comparison of analytical and FinelG results for pinned-fixed beam-column ($\chi_K \to \infty$ and $\chi_M \to \infty$) with indefinitely elastic material, under blast loading ($\tilde{p} = 80$ and $\tilde{\tau}_d = 0.1$). Time-histories of (a) mid-height and top displacements and (b) bending moment at the bottom and at mid-height of the beam-column for $P = 0\,\text{kN}$ and $P = 1000\,\text{kN}$.

Free-fixed beam-column

The free-fixed beam-column has a buckling length of $2H$ leading to an axial critical load of $P_{cr} = 368\,\text{kN}$. Due to the free-end condition, the parameter χ_K is equal to 0. For this second case study, the column is subjected to a blast loading, characterized by a peak overpressure $\tilde{p} = p_0/p_c$ of 12 and positive phase duration $\tilde{\tau}_d = t_d/T_c$ of 0.1. The axial load P applied at the top of the column is equal to $300\,\text{kN}$, leading to the following inverse of critical multiplier $\alpha_{cr} = 0.814$. The lateral mass of the structure is neglected ($\chi_M = 0$). The first natural periods of vibration T/T_c and T_0/T_c obtained from the modal analysis of 2-DOF model are respectively equal to 4.14 and 1.79.

Comparative analytical estimations of the 2-DOF model and FinelG calculations results in a perfect agreement for the deflections at mid-height and top of the beam-column as illustrated in Figure III.6-a. However, a discrepancy between the results of the FinelG and SDOF models is found since the critical axial load of the SDOF model $P_{cr,SDOF}$ is overestimated (see Equ. (III.57)), leading to a mitigation of the $P - \delta$ effect. Indeed, this overestimation of critical axial load accounts for the shortening of the period of vibration and the underestimation of the maximum displacement predicted by the SDOF model. It can be also observed that some very small oscillations of displacement at high frequencies are well captured by the 2-DOF model because it incorporates the contribution of the second mode of vibration (see Fig. III.6-b) although it is observed, after performing the dynamic analysis in modal basis, that the second mode does not affect the value of the maximum deflections. The large value of $\alpha_{cr} = P/P_{cr}$ leads to a large value of MMF as shown in Table III.5; a good correlation is found between the different approaches.
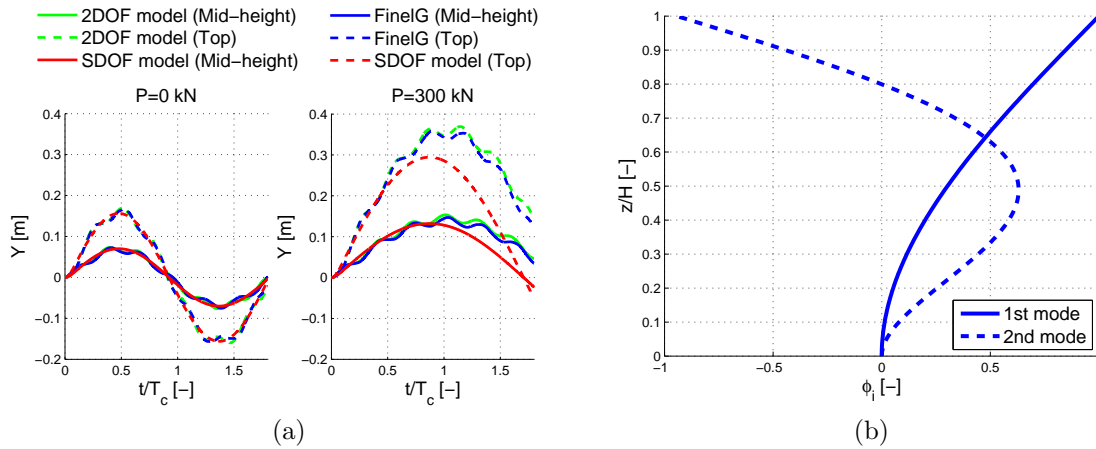
Figure III.6: Comparison of analytical and FinelG numerical results for free-fixed beam-column ($\chi_K = 0$ and $\chi_M = 0$) under blast loading ($\tilde{p} = 12$ and $\tilde{\tau}_d = 0.1$), with indefinitely elastic material. (a) Displacement at the mid-height and at the top of the beam-column vs. time for $P = 0\,\text{kN}$ and $P = 300\,\text{kN}$; (b) Modes of vibration of the beam-column obtained by performing a modal analysis of the 2-DOF analytical model ($\chi_K = \chi_M = 0$).

Figure III.7 illustrates the bending moment diagrams provided by the analytical and FinelG models at different times (from $t/T_c = 0.13$ to 0.51). The bending moment predicted by the SDOF model has a same negative sign along its entire height as its motion is only governed by the first mode of vibration which is only curved in one direction (see Fig. III.6-b), while the 2-DOF model implicitly consists of the two modes of vibrations, enabling to capture the sign change of curvature along the length of the member at high frequencies of vibration. Thus, even though the second mode of vibration has a negligible effect on the deflections, it could significantly affect the bending moment distribution due to high curvature of the corresponding mode shape.
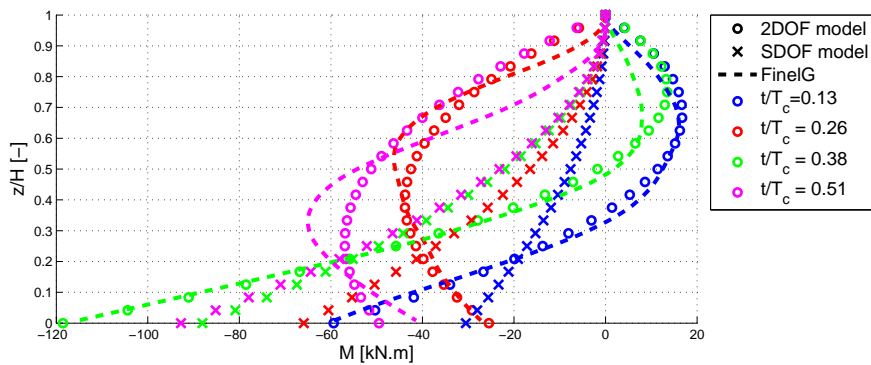

Figure III.7: Comparison of analytical and FinelG models: bending moment diagram vs. time for free-fixed beam-column ($\chi_K = 0$ and $\chi_M = 0$) with indefinitely elastic material, under blast loading ($\tilde{p} = 12$ and $\tilde{\tau}_d = 0.1$) and without any axial load ($P = 0\,\text{kN}$).

For the third case study, the column is subjected to a blast loading, characterized by a higher peak overpressure ($\tilde{p} = 80$) and a same positive phase duration ($\tilde{\tau}_d = 0.1$) than the second case study. The axial load P applied at the top of the column is maintained ($\alpha_{cr} = 0.814$) but the parameter χ_M is increased to a value of 10. Due to the increase of the lateral mass, the periods of vibration T/T_c and T_0/T_c obtained from the modal analysis of the 2-DOF model have been significantly risen to 26.9 and 11.6 in comparison to the second case study (4.14 and 1.79).

The time evolution of displacement at the mid-height and at the top of the beam-column shows the limitation of the SDOF model (see Fig. III.8-a). Although the time-history of the top displacement is quite well estimated by the SDOF model, the rapid assessment tool is not able to predict accurately the time-history of the mid-height displacement at high frequencies since the second mode of vibration is disregarded. The maximum displacement does not occur at the top but at mid-height of the beam-column in the absence of axial load (see Figure III.8-b), raising the following question: "On which basis should one of the transverse displacements of the beam-column be selected as the reference one to characterize the dynamic behavior of the beam-column ?" Concerning the predictions of the 2-DOF model, a high level of accuracy is achieved in comparison to those provided by the numerical model.

Continuing the reasoning to a very large mass ($\chi_M \to +\infty$), the SDOF model is bound to provide a negligible displacement along the entire height of the beam-column since the transverse displacement field is proportional to the top displacement which is annihilated by the inertia effect of the lateral mass. However, the 2-DOF model exhibits a non-negligible mid-height displacement of the beam-column because it includes the contribution of the second mode in opposition with what is done in the SDOF model. Thus, the influence of the second mode on the beam-column dynamic response becomes more important when the lateral mass is increased. These observations highlight another limitation of the UFC approach: it assumes that the response of the beam-column can accurately be derived with one single mode of vibration which is not always the case.

As expected, Table III.5 shows that the UFC approach badly assesses the amplification factor because the dynamic load factors (DLF and DLF_0) are computed by using the first natural periods of vibration T and T_0. It should be noted that the calculations of the amplification factors is based on a reference displacement selected as the mid-height one since it exhibits the maximum value over the height of the beam-column (Fig. III.8-b).
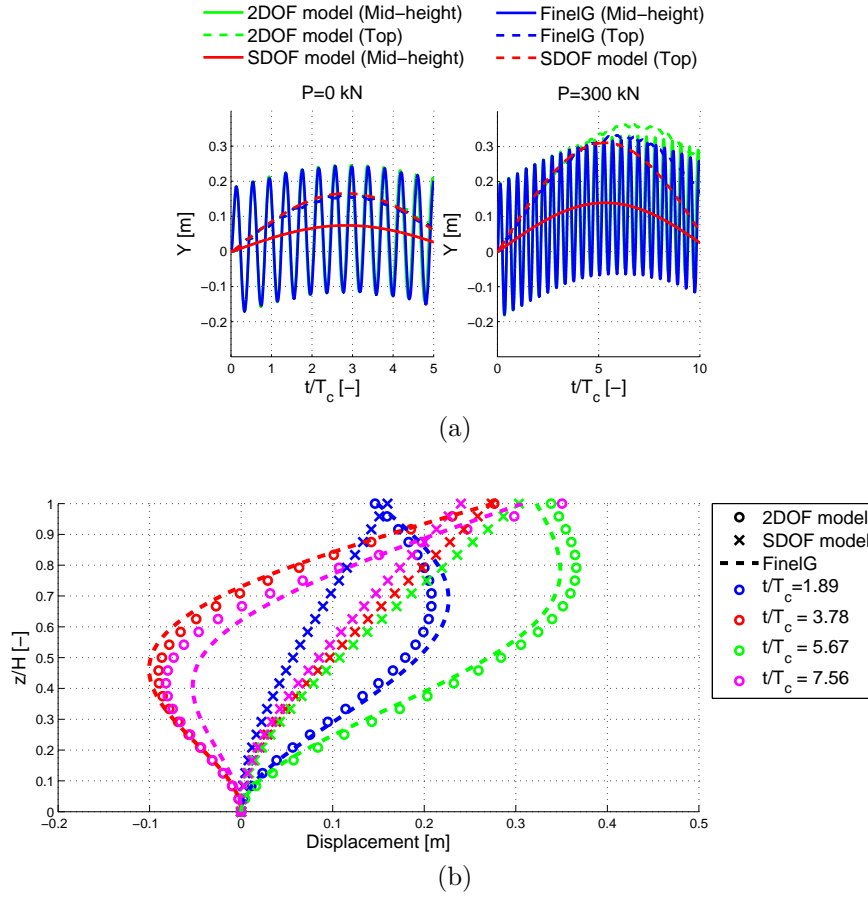
Figure III.8: Comparison of analytical and FinelG numerical results for free-fixed beam-column ($\chi_K = 0$ and $\chi_M = 10$) under blast loading ($\tilde{p} = 80$ and $\tilde{\tau}_d = 0.1$), with indefinitely elastic material. (a) Displacement at the mid-height and at the top of the beam-column vs. time for $P = 0\,\text{kN}$ and $P = 300\,\text{kN}$; (b) Field of displacement vs. time for $P = 300\,\text{kN}$.

Variable lateral restraint and mass at the top of the beam-column

For the fourth case study, the parameters χ_K and χ_M are respectively equal to 5 and 0, leading to a buckling length of $1.25H$ and a corresponding axial critical load $P_{cr} = 956\,\text{kN}$. The beam-column is subjected to a blast loading, characterized by a peak overpressure $\tilde{p} = p_0/p_c$ of 40 and positive phase duration $\tilde{\tau}_d = t_d/T_c$ of 0.1. The axial load P applied at the top of the column is equal to $800\,\text{kN}$, leading to the following inverse of critical multiplier $\alpha_{cr} = 0.837$. The first natural periods of vibration T/T_c and T_0/T_c obtained from the modal analysis with the 2-DOF model are respectively given by 2.50 and 1.11. Comparative analytical and numerical calculations result in a very good agreement between the predicted displacements (Fig. III.9-a) as well as bending moments (Fig. III.9-b).
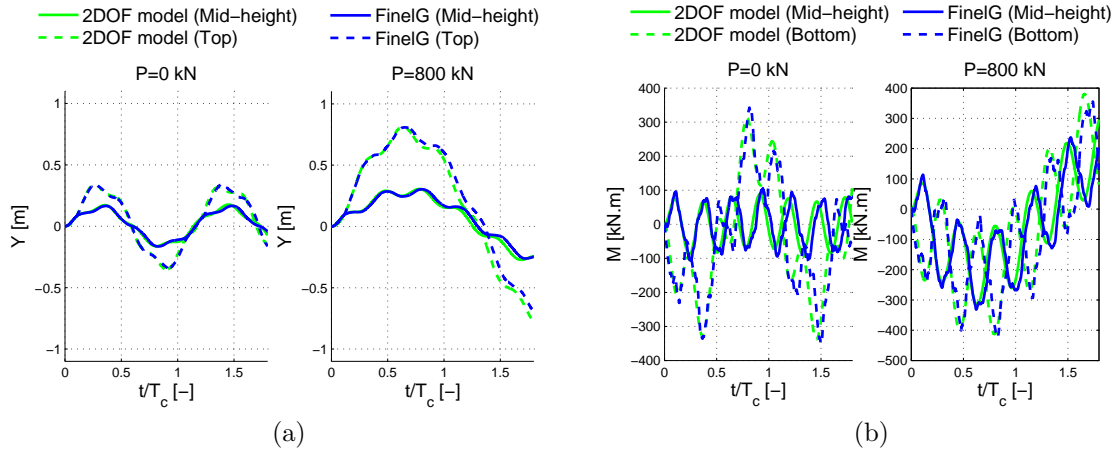
Figure III.9: Comparison of analytical and FinelG numerical results for beam-column with lateral restraint ($\chi_K = 5$) and mass ($\chi_M = 0$) under blast loading ($\tilde{p} = 40$ and $\tilde{\tau}_d = 0.1$), assuming an indefinitely elastic material. (a) Displacement and (b) bending moment at the bottom of the beam-column versus time for $P = 0\,\text{kN}$ and $P = 800\,\text{kN}$.

For the last case study, the parameters χ_K and χ_M are respectively equal to 26.8 and 5, leading to a buckling length of $0.76H$ and a corresponding axial critical load of $P_{cr} = 2570\,\text{kN}$. The beam-column is subjected to a blast loading, characterized by a peak overpressure $\tilde{p} = p_0/p_c$ of 120 and positive phase duration $\tilde{\tau}_d = t_d/T_c$ of 0.1. The axial load P applied at the top of the column is equal to $2000\,\text{kN}$, leading to the following inverse of critical multiplier $\alpha_{cr} = 0.78$. The first natural periods of vibration T/T_c and T_0/T_c obtained from the modal analysis of 2-DOF model are respectively equal to 4.3 and 2.6. The results obtained with the analytical model are corroborated with the FinelG model (see Figs. III.10-a and -b). Due to lateral mass, the mid-height displacement is greater than the top displacement because of the excitation of the second mode which is more significant in comparison to the fourth case study, leading to the inaccurate assessment of the amplification factor predicted by the UFC approach (see Table III.5).
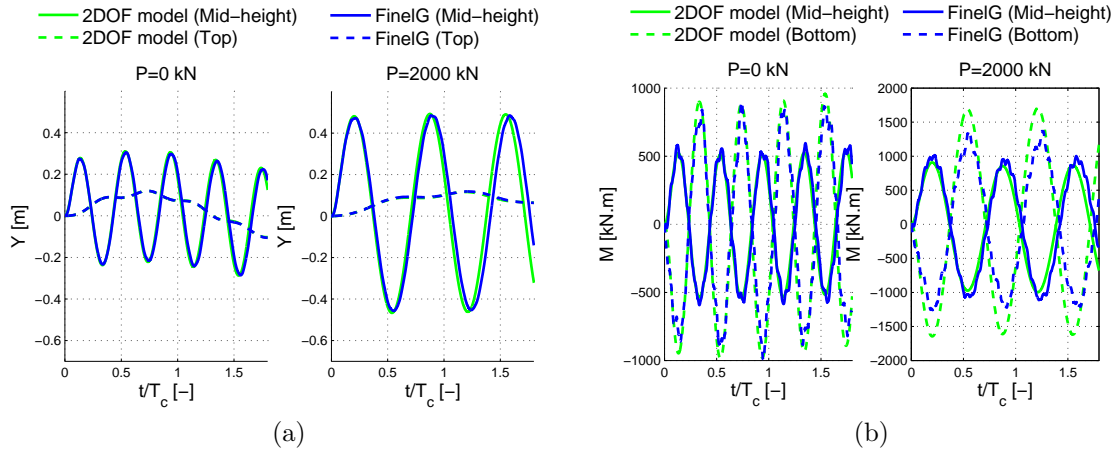
Figure III.10: Comparison of analytical and FinelG numerical results for beam-column with lateral restraint ($\chi_K = 26.8$ and $\chi_M = 5$) under blast loading ($\tilde{p} = 120$ and $\tilde{\tau}_d = 0.1$), assuming an indefinitely elastic material. Time-histories of (a) mid-height and top displacements and (b) bending moment at the bottom and mid-height of the beam-column for $P = 0\,\text{kN}$ and $P = 2000\,\text{kN}$.

Case study	χ_K [$-$]	χ_M [$-$]		$P = 0\,\text{kN}$	$P \neq 0\,\text{kN}$	Amplification factor [-]
1	$+\infty$	$+\infty$	2-DOF model	0.184 m	0.227 m	1.238
			FinelG	0.185 m	0.229 m	1.233
			UFC approach: $\frac{C_m}{1-P/P_{cr}}\frac{DLF}{DLF_0}$			1.238
2	0	0	2-DOF model	0.169 m	0.370 m	2.182
			FinelG	0.166 m	0.359 m	2.168
			UFC approach: $\frac{C_m}{1-P/P_{cr}}\frac{DLF}{DLF_0}$			2.322
3	0	10	2-DOF model	0.251 m	0.374 m	1.488
			FinelG	0.243 m	0.332 m	1.366
			UFC approach: $\frac{C_m}{1-P/P_{cr}}\frac{DLF}{DLF_0}$			2.316
4	5	0	2-DOF model	0.339 m	0.814 m	2.403
			FinelG	0.341 m	0.808 m	2.373
			UFC approach: $\frac{C_m}{1-P/P_{cr}}\frac{DLF}{DLF_0}$			2.493
5	26.8	5	2-DOF model	0.315 m	0.493 m	1.566
			FinelG	0.305 m	0.485 m	1.590
			UFC approach: $\frac{C_m}{1-P/P_{cr}}\frac{DLF}{DLF_0}$			2.124

Table III.5: Comparison of the amplification factors between the 2-DOF and FinelG models, and the UFC approach (modified by Nassr *et al.* [79]) for the case studies.

III.5.3.2   Elastic-perfectly plastic material

Pinned-fixed beam-column

Due to the simple support at the top of the beam-column, the parameters χ_K and χ_M tend to infinity. For this first case study, the column is subjected to a blast loading, featured by a peak overpressure $\tilde{p} = p_0/p_c$ of 44 and a positive phase duration $\tilde{\tau}_d = t_d/T_c$ of 0.1. The pinned-fixed beam-column has a buckling length of $0.7H$ resulting in an axial critical load of $P_{cr} = 3138\,\text{kN}$ and a reduced slenderness $\bar{\lambda} = \sqrt{N_{pl}/P_{cr}}$ of 0.67. The axial load P applied at the top of the column is equal to $300\,\text{kN}$, leading to the following inverse of critical multiplier $\alpha_{cr} = P/P_{cr} = 0.10$ (axial force $n = P/N_{pl} = \alpha_{cr}/\bar{\lambda}^2 = 0.21$). The elastic displacements $Y_{el,0} = 5\,\text{cm}$ and $Y_{el} = 5.3\,\text{cm}$ respectively scale the results shown in Fig. III.11 for $P = 0\,kN$ and $P = 300\,\text{kN}$. The first natural periods of vibration T/T_c and T_0/T_c, associated with the presence and absence of axial load, are both equal to 1.25 since the ratio P/P_{cr} is very small.

Figure III.11-a shows the time-histories of mid-span and top displacements of the beam-column predicted by the SDOF, 2-DOF and FinelG models. A very good agreement is achieved between the analytical and numerical results. As previously observed for the indefinitely elastic material, the period of vibration of the beam-column and the ductility, defined as the ratio of the maximum displacement to the elastic displacement, are increased when the axial load is applied to the beam-column.

Figure III.11-b illustrates the time evolution of the regime, the end of regime I corresponds to the apparition of a plastic hinge at the bottom of the beam-column while the regime II is achieved with the development of the full plastic mechanism (see flow chart in Fig. III.3). During the regime III, the beam-column dissipates blast-related energy through the plastic hinges, involving a decrease of velocity to 0 corresponding to the beginning of the elastic unloading stage (regime I).
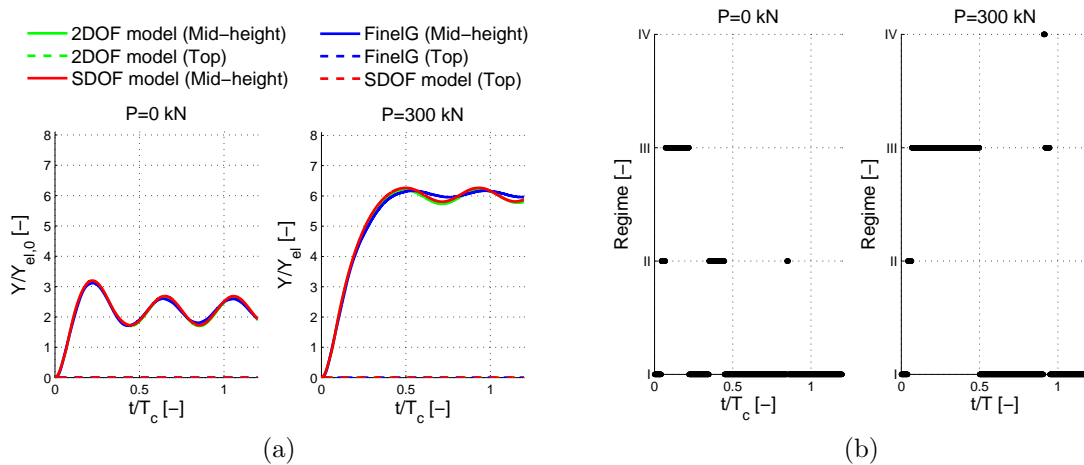

Figure III.11: Comparison of analytical and FinelG results for pinned-fixed beam-column ($\chi_K \to \infty$ and $\chi_M \to \infty$) under blast loading ($\tilde{p} = 44$ and $\tilde{\tau}_d = 0.1$), assuming an elastic-perfectly plastic material. (a) Time-histories of mid-span and top displacements of the beam-column; (b) Regime vs. time for $P = 0\,\text{kN}$ and $P = 300\,\text{kN}$.

Figures III.12-a and -b respectively illustrate the time-histories of the bending moment and the shear force at the bottom and mid-height of the beam-column. Concerning the prediction of the bending moment, analytical calculations given by Equ. (III.13) provide a high level of accuracy in comparison to corresponding numerical results. A difference of amplitude variations in the unloading regime is observed between analytical and numerical models for $P = 300$ kN in Fig. III.12-a, due to the limited number of modes captured by the analytical model and sensibility of the structure to numerical perturbation [118, 71].

However, a large discrepancy between the analytical estimations and numerical results for the prediction of the shear force is highlighted in Fig. III.12-b. Derived from Equ. (III.14), the shear force can be expressed as the derivative of the bending moment according to ordinate z or as a sum of contributions of shear forces associated to each shape function. The bending moment distribution (or bending curvature) does not change during regime III, since the full plastic mechanism is fully described by two straight elastic parts connected by some plastic hinges (see shape function ϕ_5 in Fig. III.2-c). As a result, the shear force predicted by the analytical models remains constant during regime III although that is not actually the case as shown in Fig. III.12-b.

Moreover, the shape functions does not incorporate any specific boundary conditions about shear force which leads to wrong analytical estimations. At the beginning of regime II (illustrated by the black vertical broken line in Fig. III.12-b) related to the formation of a plastic hinge at the bottom of the beam-column, the ratio of shear force to its corresponding plastic resistance V/V_{pl} attains a maximum value of 0.6. Since this ratio is greater than 0.5, the reduction of the plastic bending resistance due to the shear force should be taken into account through Equ. (I.50) although it quickly falls below this threshold value.
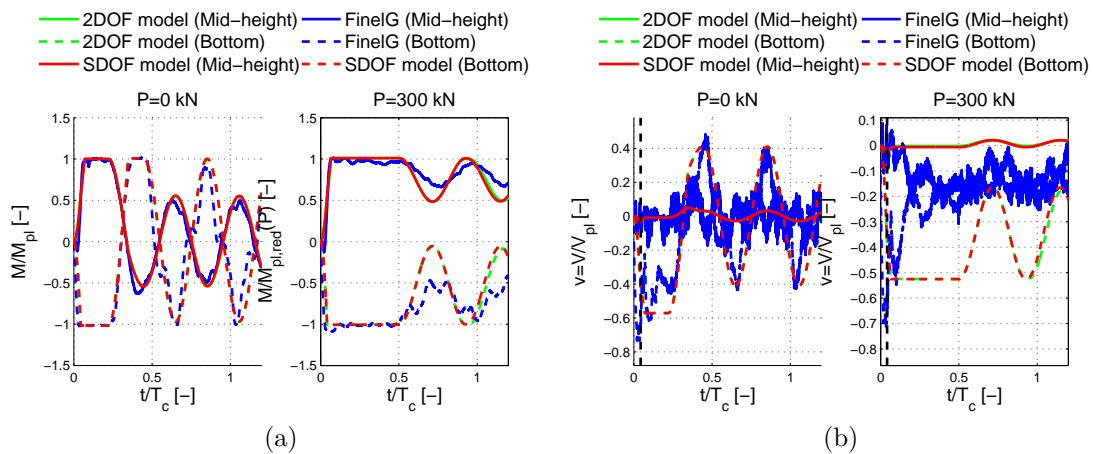
Figure III.12: Comparison of analytical and FinelG results for pinned-fixed beam-column ($\chi_K \to \infty$ and $\chi_M \to \infty$) under blast loading ($\tilde{p} = 44$ and $\tilde{\tau}_d = 0.1$), with elastic-perfectly plastic material. Time-histories of (a) bending moment and (b) shear force at the bottom and at mid-height of the beam-column for $P = 0$ kN and $P = 300$ kN.

Figure III.13-a illustrates the time evolution of momentum of the beam-column predicted

by the 2-DOF model according to four regimes. The momentum of the beam-column can be obtained as follows

$$\int_0^1 m_c H \dot{w}_c \left(\overline{z}, t \right) d\overline{z}. \tag{III.85}$$

The minimum Δ_0 technique is adopted to ensure the conservation of momentum at the transition of two regimes (see Section III.2.5). Despite using this technique of error minimization, the momentum rises by $2.6\,\%$ at the transition from regimes I to II while it decreases by $5.2\,\%$ from II to III (for both cases $P = 0\,\text{kN}$ and $P = 300\,\text{kN}$).

Figure III.13: Momentum of the pinned-fixed beam-column vs. time predicted by 2-DOF model for $P = 0\,\text{kN}$ and $P = 300\,\text{kN}$ and under the following blast loading $\tilde{p} = 44$ and $\tilde{\tau}_d = 0.1$.
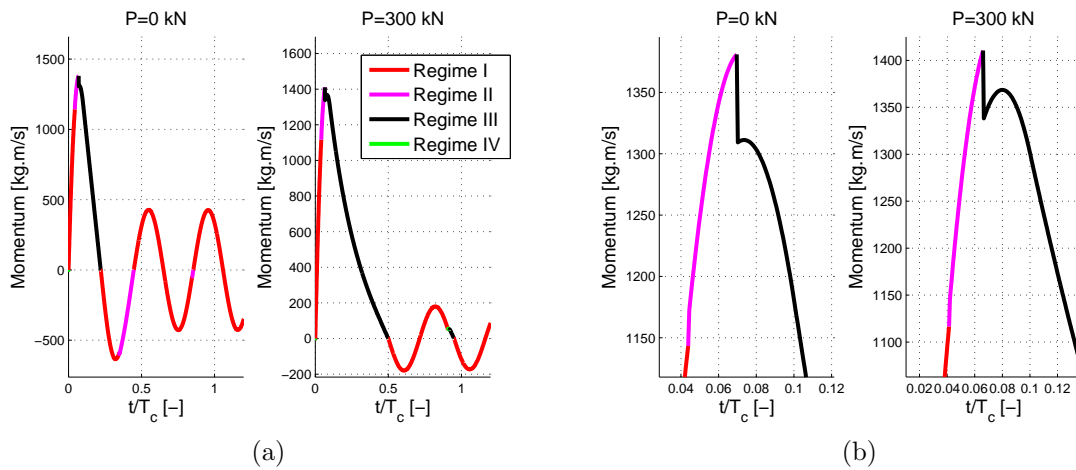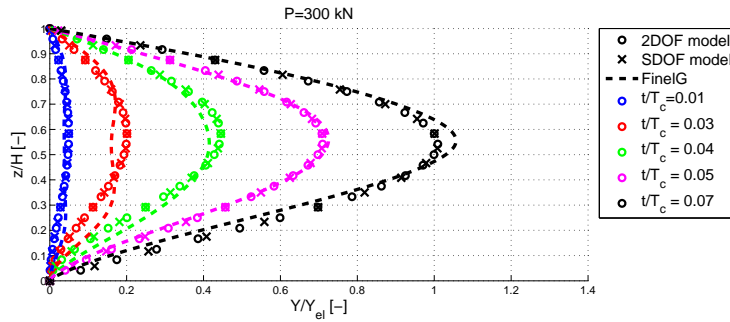
Figures III.14-a and -b respectively show the field of displacement of the beam-column for a ductility ratio Y/Y_{el} smaller and greater than 1 while Figs. III.14-c and -d illustrate their corresponding bending moment distribution (for $P = 300\,\text{kN}$). Results predicted by the SDOF and 2-DOF analytical models perfectly coincide, meaning that SDOF model is appropriate to describe the dynamic behavior of the pinned-fixed beam-column.

During regime I ($t/T_c \leq 0.03$), the rotation is prevented at the fixed support ($\overline{z} = 0$) whereas it is free at the regime II ($t/T_c > 0.03$) after the formation of plastic hinge at the bottom of the beam-column (see Fig. III.14-a). Some significant discrepancies between the analytical and numerical models are observed in the central region of the beam-column between deflection (see Fig. III.14-a) and bending moment (see Fig. III.14-c) because the higher modes of vibration can not be captured by the analytical models. However, the effect of higher modes quickly tails off before the apparition of any plastic hinge in the central region. For a same impulse, if the pressure is increased significantly (or the positive phase duration is decreased significantly), two plastic hinges could appear in the central region of the beam-column. These two plastic hinges are likely to travel towards each other along the height of the member until their coalescence at mid-height of the beam-column. This
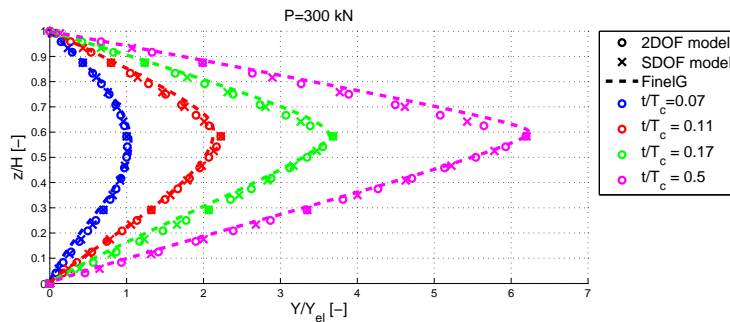
phenomenon [63, 66], despite being disregarded by the analytical models, may affect the dissipation of energy in the plastic hinges and the kinetic energy based on the deflected shape of the beam-column and thus, the dynamic response of the beam-column.

At time $t/T_c = 0.07$, the full plastic mechanism is developed with two plastic hinges at the bottom and at mid-height of the beam-column as illustrated in Fig. III.14-c. As expressed by Equ. (III.12), the field of displacement can be expressed as a combination of shape functions amplified by generalized displacements. For pinned-fixed beam-column, the generalized displacement with even subscript are equal to zero because of the pinned support at the top of the beam-column. During regime III ($t/T_c \in [0.07; 0.5]$), the contribution $q_5\phi_5$ becomes more and more significant in comparison to other contributions $q_1\phi_1$ and $q_3H\phi_3$ (see shape functions in Fig. III.2), leading to a displacement field that gets closer and closer to a bi-linear function corresponding to the deflected shape of the beam-column deforming as a plastic mechanism. The corresponding bending moment does not change during regime III since the curvature of $q_5\phi_5$ is equal to zero although actually, the bending moment decreases due to the progressive reduction of inertial forces between plastic hinges of the beam-column.

Let us consider that all the parameters do not change except for the peak overpressure $\tilde{p} = p_0/p_c$ which is risen from 44 to 46 for the second case study to highlight the ability of the analytical model to predict the dynamic buckling of the beam-column. As observed in Fig. III.15-a, the beam-column buckles for $P = 300\,\text{kN}$ as the transverse deflection becomes too large to find a stable configuration under axial load and blast loading. No unloading stage (= regime I) is observed in Fig. III.15-b for $P = 300\,\text{kN}$ after the plastic mechanism of the beam-column (= regime III) has formed. This confirms the instability of the beam-column. A very good agreement is thus achieved between the analytical and numerical models for pinned-fixed beam-column under axial load and lateral blast load.
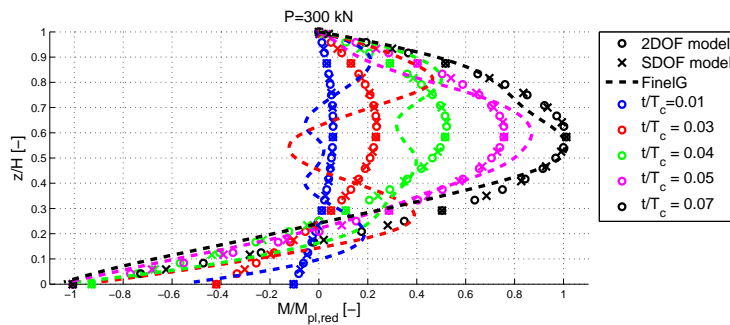
Figure III.14: Comparison of analytical and FinelG results for pinned-fixed beam-column ($\chi_K \to \infty$ and $\chi_M \to \infty$) under blast loading ($\tilde{p} = 44$ and $\tilde{\tau}_d = 0.1$) and axial load $P = 300\,\mathrm{kN}$, with elastic-perfectly plastic material. Field of displacement vs. time for (a) $Y/Y_{el} \leq 1$; (b) $Y/Y_{el} \geq 1$. Bending moment distribution vs. time for (c) $Y/Y_{el} \leq 1$; (d) $Y/Y_{el} \geq 1$.

Figure III.15: Comparison of analytical and FinelG results for pinned-fixed beam-column ($\chi_K \to \infty$ and $\chi_M \to \infty$) under blast loading ($\tilde{p} = 46$ and $\tilde{\tau}_d = 0.1$), assuming an elastic-perfectly plastic material. Time-histories of (a) mid-height and top displacements of the beam-column and (b) regime for $P = 0\,\text{kN}$ and $P = 300\,\text{kN}$.

Free-fixed beam-column
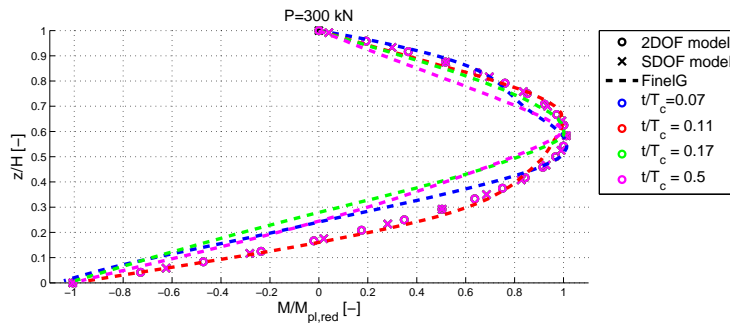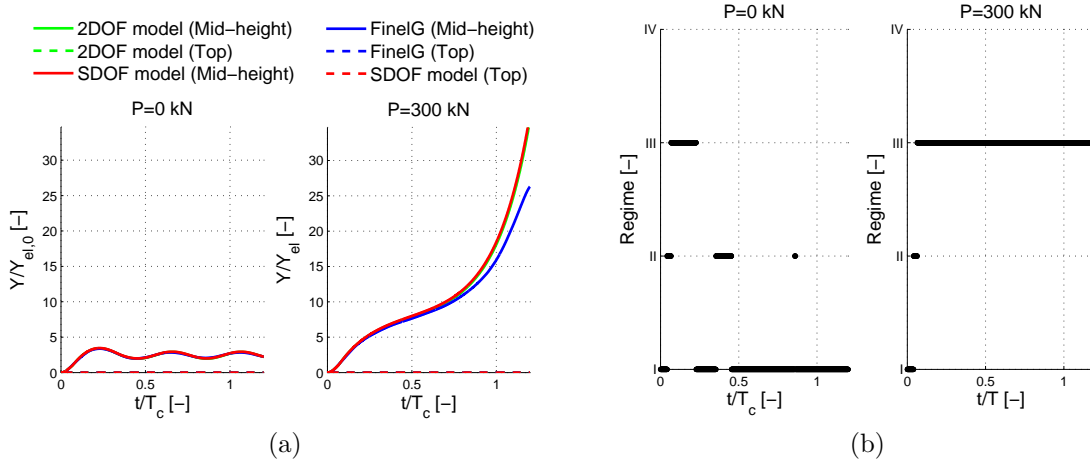
Due to the free-end condition at the top of the beam-column, the parameter χ_K is equal to 0. For this third case study, the column does not have any lateral mass ($\chi_M = 0$) and it is subjected to a blast loading, characterized by a peak overpressure $\tilde{p} = p_0/p_c$ of 12 and positive phase duration $\tilde{\tau}_d = t_d/T_c$ of 0.1. The free-fixed beam-column has a buckling length of $2H$ leading to an axial critical load of $P_{cr} = 368\,\text{kN}$ and a reduced slenderness $\bar{\lambda} = \sqrt{N_{pl}/P_{cr}}$ of 1.96. The axial load P applied at the top of the column is equal to $200\,\text{kN}$, leading to the following inverse of critical multiplier $\alpha_{cr} = P/P_{cr} = 0.54$ (axial force $n = P/N_{pl} = \alpha_{cr}/\bar{\lambda}^2 = 0.14$). The elastic displacements $Y_{el,0} = 13.1\,cm$ and $Y_{el} = 15.3\,cm$ respectively scale the results shown in Fig. III.16 for $P = 0\,\text{kN}$ and $P = 200\,\text{kN}$. The first natural periods of vibration T/T_c and T_0/T_c obtained from the modal analysis of 2-DOF model are respectively given by 2.59 and 1.79.

Figure III.16-a illustrates the time-histories of the mid-height and top displacements of the beam-column predicted by the SDOF, 2-DOF and FinelG models. A very good agreement is achieved between the 2-DOF analytical and numerical models. However, a large discrepancy between the deflections predicted by SDOF and FinelG models is observed for $P = 200\,\text{kN}$ because the SDOF model overestimates the Euler buckling axial load in the elastic stage (regime I) as stated earlier (see Equ. (III.57)) and disregards the contribution of the second mode (Figure III.16-b).

The field of velocity for the axially loaded case ($P = 200\,\text{kN}$) is illustrated in Fig. III.16-c, corroborating the results predicted by the 2-DOF analytical model with those of the FinelG model. At time $t/T_c = 0.49$, the angular velocity at the bottom of the beam-column is

negative involving an unloading of the plastic hinge while the transverse velocity at the top of the beam-column is positive (see Fig. III.16-c), which emphasizes the role played by the second mode in the dynamic behaviour of the beam-column. Indeed, it is possible to observe an unloading in the plastic hinge while the beam-column head continues to move in the opposite direction. Due to this effect, the bending moment at the bottom of the beam-column presents some unloading stages during range of time $t/T_c \in [0.4; 1.1]$ in the axially loaded case (see Fig. III.16-d), which could affect the dissipation of energy in the plastic hinges and thus, the prediction of the maximum deflection. This effect can not be captured by the SDOF model which assumes a linear shape function ϕ_4 in the plastic regime (see Fig. III.2-b).

Concerning the prediction of the shear force (see Fig. III.2-e), the results predicted by the 2-DOF model, contrary to the SDOF model, agrees quite well with those predicted by the FinelG model. When the plastic hinge is formed at the bottom of the beam-column (see black interrupted vertical line), the parabolic bending moment distribution estimated by the SDOF model at the end of the elastic regime (I) is frozen during plastic regime (II), leading to a linear shear force distribution that is time-independent during regime II. That accounts for the horizontal plateau predicted by SDOF model at range time $t/T_c \in [0.3; 0.7]$ for the axially loaded case, whereas the 2-DOF model is able to capture the oscillations at high frequencies because of the contribution of the second mode. Since the ratio V/V_{pl} is smaller than 0.5, the shear force has no effect on the plastic bending reduced resistance.

Figure III.16: Comparison of analytical and FinelG results for free-fixed beam-column ($\chi_K = \chi_M = 0$) under blast loading ($\tilde{p} = 12$ and $\tilde{\tau}_d = 0.1$), assuming an elastic-perfectly plastic material. (a) Time-histories of mid-height and top displacements of the beam-column; (b) Mode shapes for $P = 200\,\text{kN}$; (c) Field of velocity vs. time for $P = 200\,\text{kN}$. Time-histories of (d) the bending moment and (e) the shear force at the bottom and mid-height of the beam-column.

For the fourth case study, consider a peak overpressure $\tilde{p}$ that is slightly increased to 14.4 while other parameters of the third case study are conserved (see Fig. III.17-a). A perfect correlation is achieved between the 2-DOF analytical and numerical results; the dynamic buckling of the beam-column is well captured by the 2-DOF model while the SDOF model provides unsafe results. Indeed, the peak overpressure should be increased up to 16.4 to predict an instability of the free-fixed beam-column with the SDOF model, resulting in an underestimation by 14 % of the real impulsive blast loading.

For the fifth case study, let us consider a quasi-static blast loading characterized by a peak overpressure $\tilde{p}$ of 0.65 and positive phase duration $\tilde{\tau}_d$ of 100 while other parameters do not change. The contribution of the second mode is negligible in this case, but the overestimation of the Euler elastic buckling axial load $P_{cr,SDOF}$ in elastic stage again accounts for the large discrepancy between SDOF and FinelG models (see Fig. III.17-b).
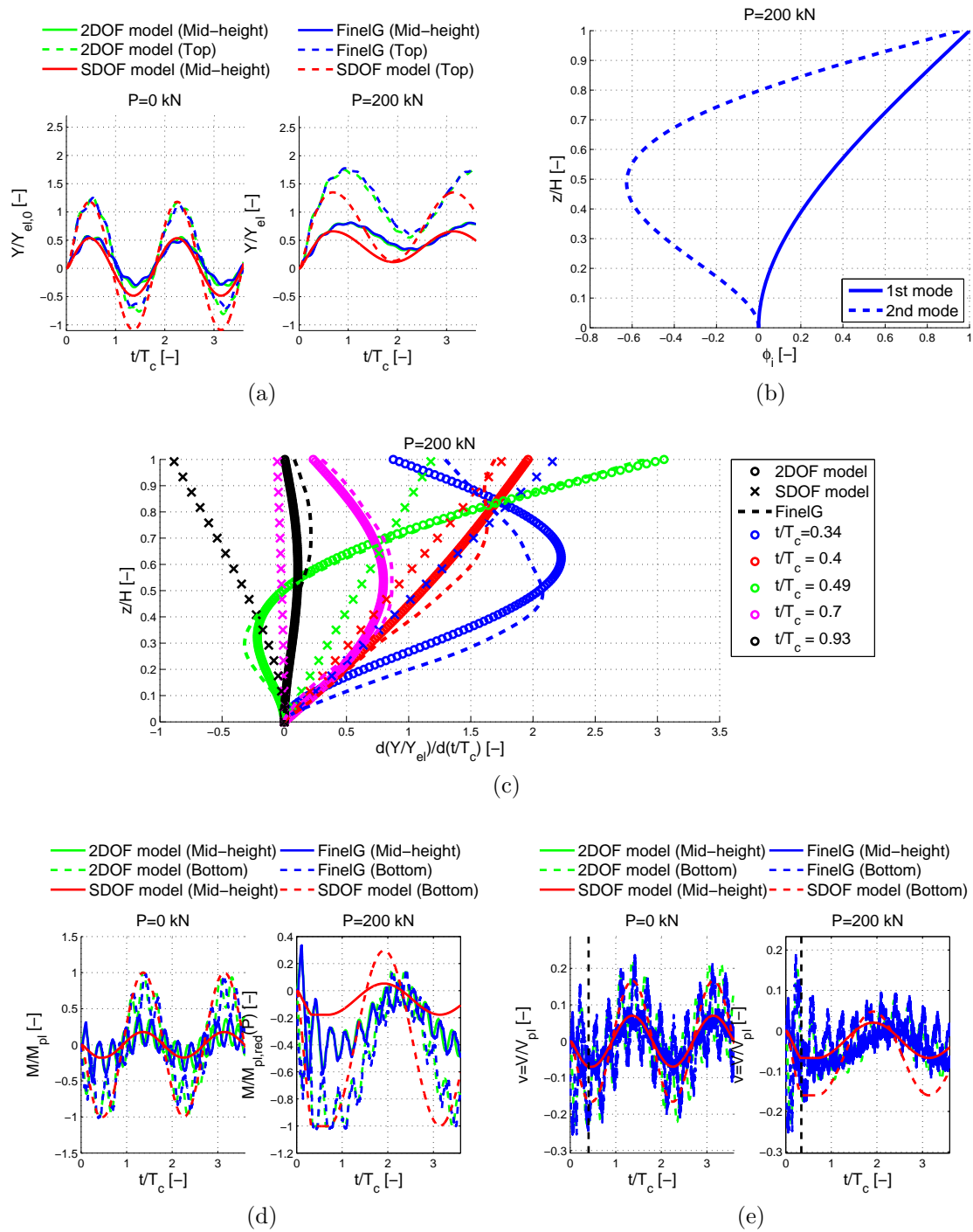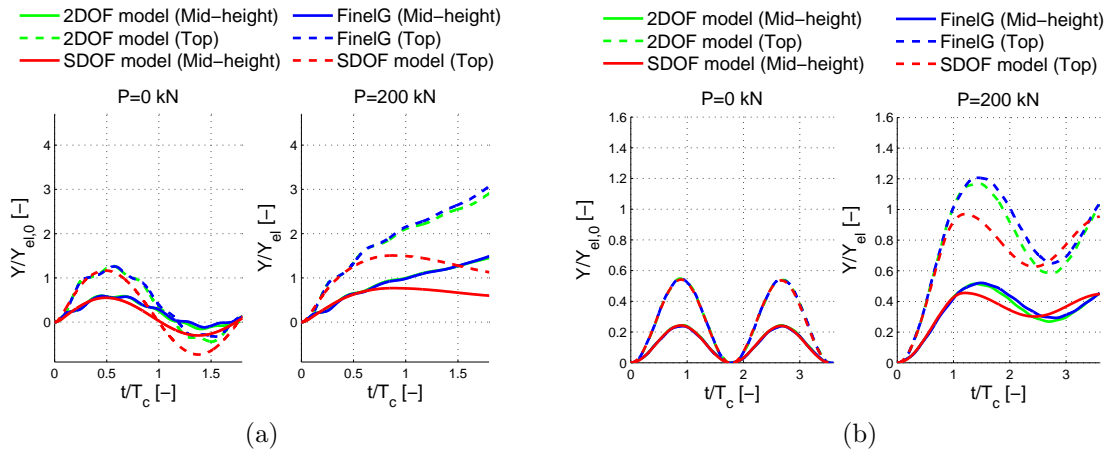

Figure III.17: Comparison of analytical and FinelG results for free-fixed beam-column ($\chi_K = \chi_M = 0$), assuming an elastic-perfectly plastic material. Time-histories of mid-height and top displacements of the beam-column for $P = 0\,\text{kN}$ and $P = 200\,\text{kN}$ and the following blast loading (a) $\tilde{p} = 14.4$ and $\tilde{\tau}_d = 0.1$; (b) $\tilde{p} = 0.65$ and $\tilde{\tau}_d = 100$.

For the sixth case study, the parameters are the same as those of the third case study ($\tilde{p} = 12$, $\tilde{\tau}_d = 0.1$, $P = 200\,\text{kN}$ and $\chi_K = 0$) except for the lateral mass χ_M at the top of the beam-column which is increased from 0 to 5.

Figures III.18-a and -b respectively illustrate the time-histories of the transverse deflection and bending moment and Figures III.18-c and -d show their corresponding zooming in the vicinity of the maximum deflection. Irrespective of the axial load P, the maximum displacement at the top of the beam-column is overestimated (Figs. III.18-a and -c) because of the application of the minimum Δ_0 technique which introduces some artificial increment of momentum quantity inside the system at each regime transition artificial increment which is accumulated through the large number of regime transitions. Indeed, a large number of regime transitions is observed due to the successive loading and unloading phases of the bottom plastic hinge (Figs. III.18-b and -d). For the axially loaded case, 34 regime transitions

occur whereas for $P = 0\,\text{kN}$, we observe only 16 regime transitions, explaining why the error on displacement is smaller for $P = 0\,\text{kN}$ than that associated to $P = 200\,\text{kN}$.

As explained earlier in Section III.5.3.1, the SDOF model does not predict well the response of the beam-column because of neglecting the second mode of vibration. In case of very large mass ($\chi_M \to +\infty$), the SDOF model is bound to provide a negligible displacement along the entire height of the beam-column since the transverse displacement field is proportional to the top displacement which is annihilated by the inertia effect of the lateral mass.
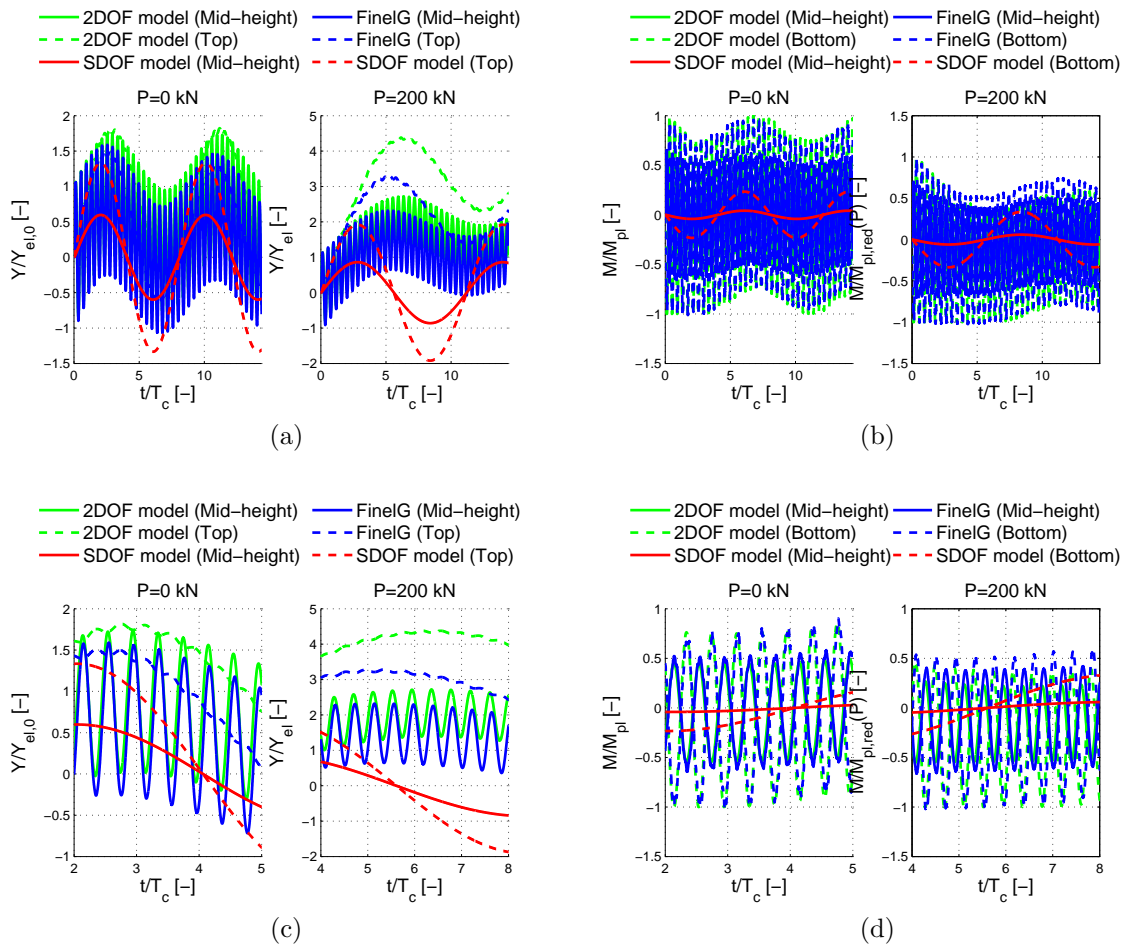
Figure III.18: Comparison of analytical and FinelG results for free-fixed beam-column ($\chi_K = 0$ and $\chi_M = 5$) under blast loading ($\tilde{p} = 12$ and $\tilde{\tau}_d = 0.1$) and axial compressive load $P = 200\,\text{kN}$, assuming an elastic-perfectly plastic material. (a)-(c) Time-histories of mid-height and top displacements of the beam-column and (b)-(d) Time-histories of the bending moment at the bottom and mid-height of the beam-column.

Variable lateral restraint at the top of the beam-column

For the seventh case study, the parameters χ_K and χ_M are respectively equal to 26.8 ($K^\star = 1000\,\text{kN/m}$) and 0, leading to a buckling length of $0.76H$ and a corresponding axial critical load of $P_{cr} = 2570\,\text{kN}$. The reduced slenderness $\bar{\lambda} = \sqrt{N_{pl}/P_{cr}}$ of the beam-column is equal to 0.74. The beam-column is subjected to a blast loading, characterized by a peak overpressure $\tilde{p} = p_0/p_c$ of 64 and positive phase duration $\tilde{\tau}_d = t_d/T_c$ of 0.1. The axial load P applied at the top of the column is equal to $130\,\text{kN}$ ($160\,\text{kN}$), leading to the following inverse of critical multiplier $\alpha_{cr} = 0.05$ ($\alpha_{cr} = 0.06$) and axial force $n = P/N_{pl} = 0.09$ ($n = 0.11$). The elastic displacements $Y_{el,0} = 10.6\,\text{cm}$ and $Y_{el} = 10.2\,\text{cm}$ respectively scale the results shown in Fig. III.16 for $P = 0\,\text{kN}$ and $P = 130\,\text{kN}$ ($160\,\text{kN}$). The first natural periods of vibration T/T_c and T_0/T_c obtained from the modal analysis of 2-DOF model are respectively given by 0.66 and 0.65.

Figure III.19 illustrates the time-histories of mid-height and top deflections of the beam-column considering an axial load that varies from 0 to $160\,\text{kN}$. The simplified FinelG model assumes that the plasticity is localized at the bottom and at mid-height ($\bar{z}_m = 0.58$) of the beam-column, preventing any traveling of plastic hinge along the height of the member. A perfect agreement is observed between the analytical and numerical results for $P = 0\,\text{kN}$. However, a discrepancy between the simplified and FinelG models is observed for $P = 130\,\text{kN}$ because the plastic hinge at mid-height of the beam-column moves upwards as illustrated in Fig. III.20-a. This motion of plastic hinge affects the dissipation of energy as well as the inertial force distribution in the beam-column. As observed in Figs. III.20-b and -c, the field of displacement predicted by the simplified FinelG model is close to that of the 2-DOF analytical model, validating the rapid assessment tool and highlighting that the assumption of stationary central plastic hinge is on the safe side. The beam-column buckles for an axial load equal to $160\,\text{kN}$ as observed in Fig. III.19.
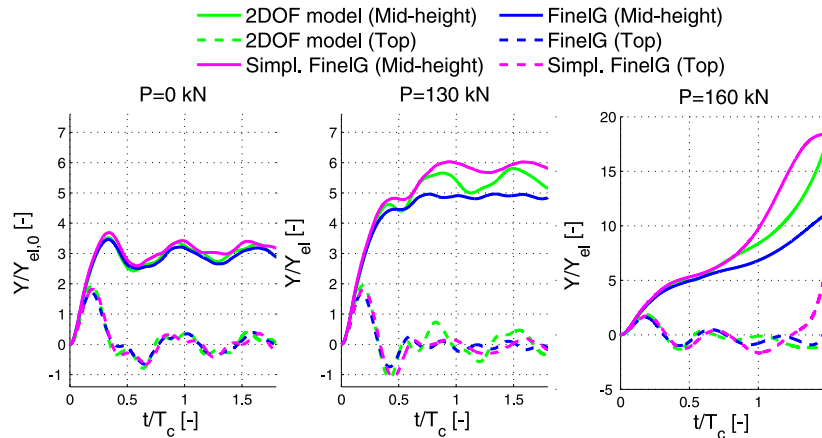
Figure III.19: Comparison of analytical and FinelG numerical results for beam-column with lateral restraint ($\chi_K = 26.8$) and mass ($\chi_M = 0$) under blast loading ($\tilde{p} = 64$ and $\tilde{\tau}_d = 0.1$), assuming an elastic-perfectly plastic material. Time-histories of mid-height and top displacements of the beam-column for $P = 0\,\text{kN}$, $P = 130\,\text{kN}$ and $P = 160\,\text{kN}$.

(a)

(b)

(c)
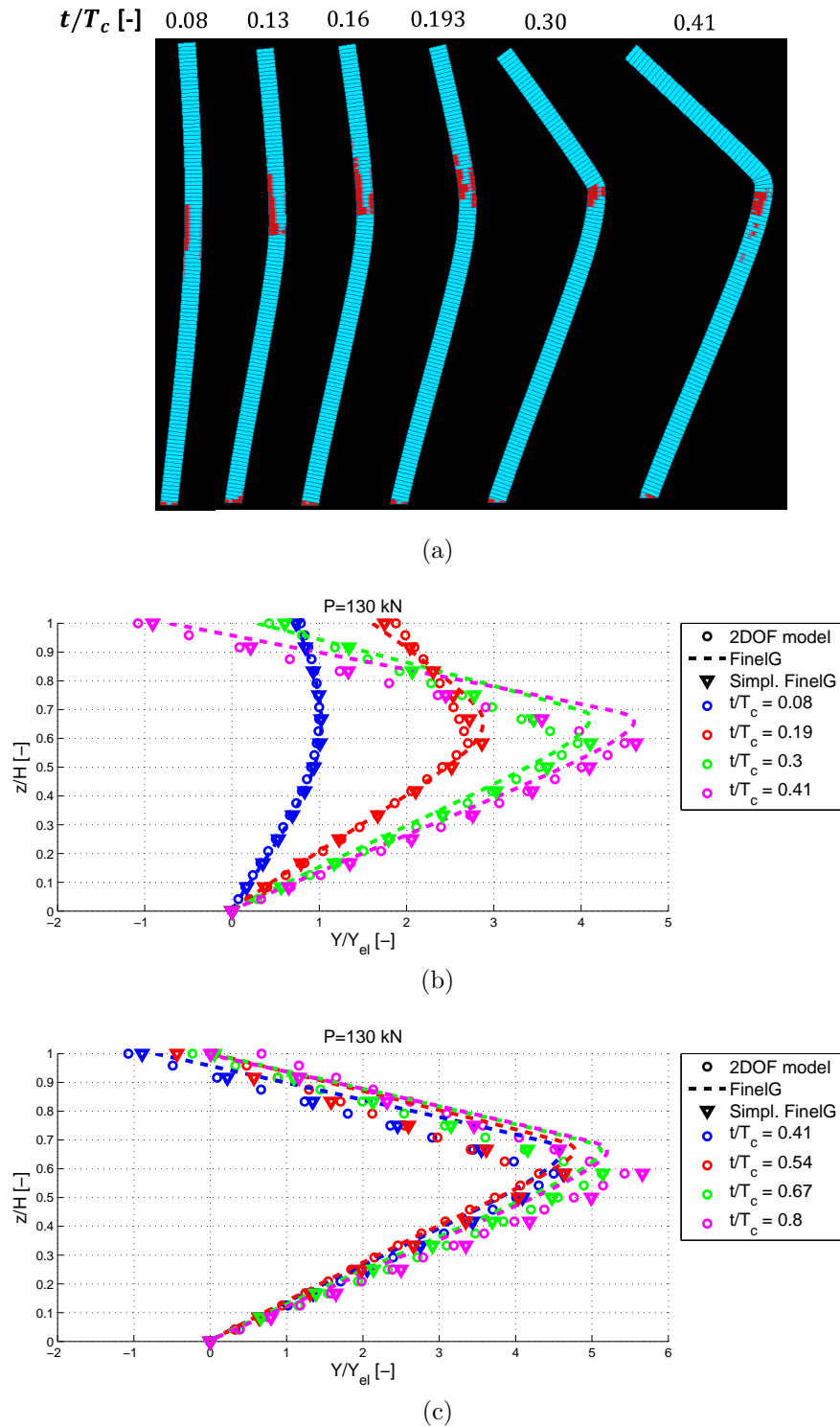
Figure III.20: Beam-column with lateral restraint ($\chi_K = 26.3$) and mass ($\chi_M = 0$) under blast loading ($\tilde{p} = 64$ and $\tilde{\tau}_d = 0.1$) and axial load $P = 130\,\text{kN}$, assuming an elastic-perfectly plastic material. (a) Captures of the traveling of the mid-height plastic hinge predicted by FinelG software during the period $t/T_c \in [0.08; 0.41]$. Comparison of the field of displacement vs. time between the analytical and numerical models (b) for $t/T_c \in [0.08; 0.41]$; (c) $t/T_c \in [0.41; 0.8]$.

For the eighth case study, the parameters χ_K and χ_M are respectively equal to 5 and 0, leading to a buckling length of $1.24H$ and a corresponding axial critical load of $P_{cr} = 956\,\text{kN}$. The reduced slenderness $\bar{\lambda} = \sqrt{N_{pl}/P_{cr}}$ of the beam-column is equal to 1.22. The beam-column is subjected to a blast loading, characterized by a peak overpressure $\tilde{p} = p_0/p_c$ of 40 and positive phase duration $\tilde{\tau}_d = t_d/T_c$ of 0.1. The axial load P applied at the top of the column is varying as shown in Table III.6, which gives the inverse of critical multiplier, the normal force, the yield displacement and the first natural period of vibration according to the axial load P.

Figure III.21-a illustrates the time-histories of the displacements at mid-height and at top of the beam-column. For $P = 420\,\text{kN}$, a perfect agreement is achieved between results predicted by the analytical and simplified FinelG models, the effect of the axial load on the maximum deflection and period of vibration is significant as compared to $P = 0\,\text{kN}$. However, the analytical model predicts the buckling of the beam-column for $P = 425\,\text{kN}$ whereas the simplified FinelG model estimates the axial buckling load as equal to $470\,\text{kN}$. The FinelG model assesses that the buckling axial load of the beam-column under blast loading is equal to $525\,\text{kN}$, highlighting that the analytical approach is on the safe side.

Figure III.21-b shows that a good match is observed between the time-histories of bending moment predicted by the analytical and simplified FinelG models for $P \leq 420\,\text{kN}$ (and even a perfect match for $P \leq 400\,\text{kN}$). However, some problems of convergence are observed in the results captured by the FinelG simplified model for $P = 470\,\text{kN}$, confirming the dynamic instability of the beam-column.

These results highlight that some improvements should be provided to the analytical model since the relative error between the predictions of the maximum displacement of the analytical and simplified FinelG models stands at $10\,\%$ on the safe side despite being based both on the same assumptions.

	$P = 0\,\text{kN}$	$P = 420\,\text{kN}$	$P = 425\,\text{kN}$	$P = 470\,\text{kN}$
$\alpha_{cr}\ [-]$	0	0.44	0.44	0.49
$n\ [-]$	0	0.30	0.30	0.33
$Y_{el,0}$ or Y_{el} [cm]	3.28	2.74	2.68	2.56
T_0/T_c or $T/T_c\ [-]$	1.12	1.43	1.43	1.49

Table III.6: Inverse of critical multiplier, normal force, yield displacement and first natural period of vibration of the beam-column for various axial compressive load P.

For the nineth one, the parameter χ_M is increased to 5 while other parameters are maintained ($\chi_K = 5$, $\bar{\lambda} = 1.22$, $\tilde{p} = 40$ and $\tilde{\tau}_d = 0.1$). The axial load P applied at the top of the column is equal to $420\,\text{kN}$. The elastic displacements $Y_{el,0} = 5.4\,\text{cm}$ and $Y_{el} = 4.57\,\text{cm}$ respectively scale the deflection curves shown in Fig. III.21 for $P = 0\,\text{kN}$ and $P = 420\,\text{kN}$.

For $P = 0\,\text{kN}$, when the lateral mass is increased, the top deflection becomes smaller than the mid-height deflection as can be observed in Fig. III.22 as compared to Fig. III.21-a. For

$P = 420\,\mathrm{kN}$, the top deflection of the beam-column is close to 0 due to lateral mass while the mid-height deflection tends to infinity as the beam-column buckles (Fig. III.21).
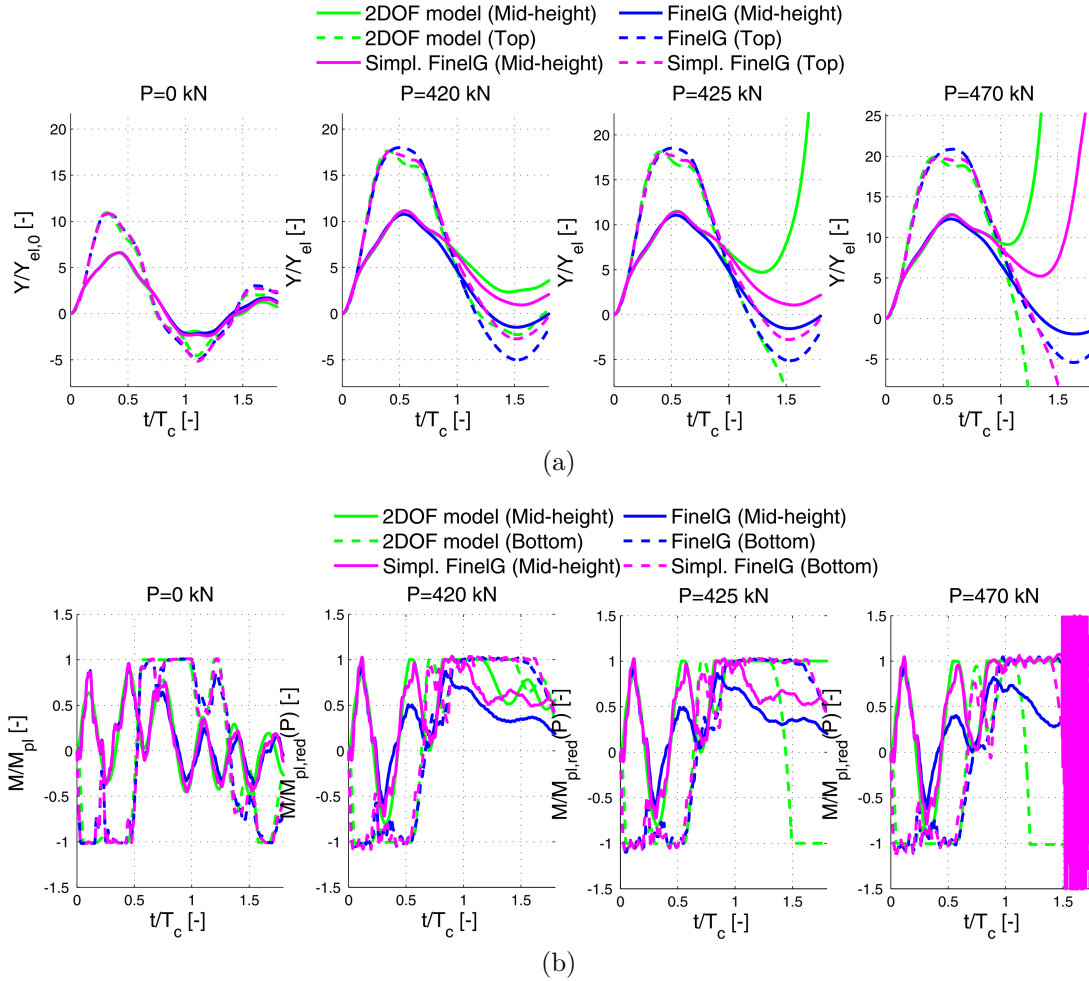
Figure III.21: Comparison of analytical and FinelG numerical results for beam-column under blast loading ($\tilde{p} = 40$ and $\tilde{\tau}_d = 0.1$) and various axial compressive load $P \in \{0\,\mathrm{kN}; 420\,\mathrm{kN}; 425\,\mathrm{kN}; 450\,\mathrm{kN}\}$, assuming an elastic-perfectly plastic material, a lateral restraint $\chi_K = 5$ and mass $\chi_M = 0$. Time-histories of (a) mid-height and top deflections and (b) bending moments at bottom and mid-height of the beam-column.
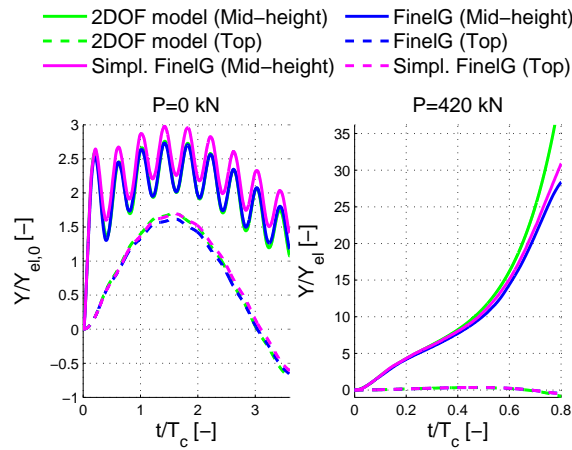
Figure III.22: Comparison of time-histories of mid-height and top deflections predicted by analytical and FinelG models for beam-column under blast loading ($\tilde{p} = 40$ and $\tilde{\tau}_d = 0.1$) and axial load $P = 420$ kN, assuming an elastic-perfectly plastic material, a lateral restraint $\chi_K = 5$ and mass $\chi_M = 5$.

III.6   Analysis of the model

This section consists in investigating the effect of the lateral restraint $K^\star$, the lateral mass $M^\star$ and the axial load P on the stability of the beam-column under lateral blast loading. The parametric study is performed by establishing the pressure-impulse (p-I) diagram of the beam-column which indicates, with a simple reading, the eventual buckling of that structural member according to a damage criterion.

The damage criterion commonly used in literature [53, 112, 113] is generally function of the ratio of the residual axial capacity of the damaged column to the design axial capacity. Four degrees of damage are established in [53]: low, medium, high damages and collapse if the residual axial capacity is smaller than 20 % of the initial design capacity. However, this damage ratio requires to perform a non-linear static analysis of the beam-column in the initial and deformed (after carrying out a blast analysis) configurations, considering an incremental increase of the axial load until reaching the buckling of the beam-column. The advantage of that approach is that it incorporates all the damage failures (local buckling of web/flanges, shear failure at the support, axial instability of the structural element,...), and eventually includes the strain rate effect or the strain hardening on the dynamic behavior of the beam-column although the main drawback is the need of a non-linear static analysis software for each point of the pressure impulse diagram. That explains why the authors [53, 112, 113] propose to interpolate and fit the numerical results in order to derive general analytical expressions of iso-damage curves of p-I diagram, which are expressed as function of the main structural parameters of the beam-column.

In [79], the ratio of the axial load to the critical elastic axial load $\alpha_{cr} = P/P_{cr}$ and the

demand of ductility Y_b/Y_{el} are preferred since they respectively allow to check the stability of the column and to compare the required ductility to the deformation limits proposed in literature (see Section I.4.4.3). However, using the ratio α_{cr} may be definitely inappropriate for beam-columns characterized by a small value of the reduced slenderness $\bar{\lambda} = \sqrt{N_{pl}/P_{cr}}$, since the yielding of the cross-section governs the axial resistance of the beam-column rather than buckling of the beam-column. Another choice of damage parameter could be the inverse of the ultimate multiplier α_u of the beam-column defined as follows

$$\alpha_u = \frac{P}{N_{b,Rd}} \qquad \text{(III.86)}$$

where the design axial buckling resistance $N_{b,Rd}$ is as defined in Eurocode 3 part 1-1 [36]. The advantage of that last parameter is that it includes both types of failures (cross-section axial yielding and buckling of the beam-column) and is therefore selected as the damage criterion in this thesis. It should be noted that the critical axial load P_{cr} is obtained from the linear buckling analysis of the 2-DOF model (see Fig III.4-a).

Concerning the deformation limits, a structural primary frame member with significant compression should present a ductility limit of 3 and without significant compression a value of 6 for high level of damage (see Table I.6 extracted from the ASCE design guide). The axial load is significant when it is greater than 20 % of the dynamic axial capacity of the member, which is equal to the static one in this thesis since we neglect the strain rate effect on the plastic resistance. The high level of damage corresponds to a situation in which a component suffers from significant deflecting (but is not failed yet), causing it to be unrepairable.

Six case studies are considered with the parameters χ_K and χ_M which are varied from 0 to $+\infty$, the corresponding reduced slenderness and design axial buckling resistance are given in Table III.7. The last parameter α_u is used to draw the iso-damage curves of the p-I diagrams and is assumed to have four values: 0.1, 0.3, 0.5 and 0.7. The pressure-impulse diagrams are established by using Blasko's procedure based on a polar coordinate system and the bisection method [83].

Case study	$\chi_K = \frac{K^\star}{EI_c/H^3}$ [−]	$\chi_M = \frac{M^\star}{m_c H}$ [−]	$\bar{\lambda} = \sqrt{\frac{N_{pl}}{P_{cr}}}$ [−]	$N_{b,Rd}$ [kN]
1	$+\infty$	$+\infty$	0.67	1220
2	0	0	1.96	328
3	26.3	0	0.74	1173
4	5	0	1.22	736
5	0	5	1.96	328
6	5	5	1.22	736

Table III.7: Case studies for parametric study through pressure-impulse diagram. Values of the corresponding lateral mass χ_M, restraint χ_K, reduced slenderness $\bar{\lambda}$ and corresponding design axial buckling resistance $N_{b,Rd}$ of the beam-column.

Figures III.23-a, b and c respectively illustrate the p-I diagrams of the pinned-fixed beam-column, the corresponding ductility, defined as the ratio of the deflection before buckling Y_b

to the elastic deflection Y_{el}, and the dimensionless shear force at the bottom of the beam-column, defined as the ratio of the maximum shear force V_m to its associated plastic resistance $V_{pl,Rd}$.

A perfect agreement is achieved between the p-I diagrams predicted by the SDOF and 2-DOF analytical models (Fig. III.23-a). Let us consider a ratio of α_u equal to 30 %, the triangle labeled A corresponds to a couple of pressure and impulse $\left(\tilde{p}, \tilde{I}\right) = (5, 15)$ for which the beam-column buckles since the triangle is above the red iso-damage curve whereas the triangle labeled B representing the couple of coordinates $\left(\tilde{p}, \tilde{I}\right) = (2, 10)$ is below the iso-damage curve, meaning that the column remains stable after blast event. The larger the axial load P (or the ratio α_u) is, the smaller the pressure and the impulse that the beam-column can bear without buckling is. The quasi-static and impulsive asymptotes represented by interrupted lines are computed on the basis of Equs. (III.80) and (III.82), and are validated by the curves predicted by the analytical models.

As demonstrated in [80], the ductility Y_b/Y_{el} before global instability occurs is greater in the impulsive region than in the quasi-static region of the p-I diagram (see Fig. III.23-b). As expected, the ductility decreases when the ratio α_u increases, and could even tend to infinity for a particular case corresponding to a beam-column not being subjected to any compression load. The iso-damage curve corresponding to $\alpha_u = 70$ % respects the deformation limit proposed in ASCE design guide while these limits are not satisfied for other iso-damage curves in the dynamic and impulsive areas.

The ratio of the shear force to its associated plastic resistance at the bottom of the beam-column becomes significant for ratio $\alpha_u \leq 30$ % (see Fig. III.23-c) since it is greater than 0.5, corresponding to the limit at which the shear force affects the bending plastic resistance (see Section I.4.3). However, as discussed previously, the shape functions (see Table III.1) are not defined to incorporate the boundary conditions on the shear force, which results to an inaccurate estimation of the shear force at the bottom of the beam-column. Indeed, it was shown earlier that the shear is assumed to remain constant with time during regime III which is not the case (see Fig. III.12). The shear force at mid-height of the beam-column is not represented because it is negligible and thus, does not affect the dissipation of energy in the mid-height plastic hinge.

Figures III.23-d, e and f respectively illustrate the pressure-impulse diagram of the free-fixed beam-column, the corresponding ductility and the shear force at the bottom of the beam-column. As observed in Fig. III.23-d, a discrepancy between the p-I diagrams predicted by the SDOF and 2-DOF analytical models is found since the SDOF model overestimates the critical elastic axial load $P_{cr,SDOF}$ (see Equ. (III.57)) leading to a fictive attenuation of the $P - \delta$ effect in the elastic regime which results in some unsafe stability curves of the p-I diagram. The relative error made at each point of the p-I diagram increases with the ratio α_u. For instance, the relative errors in the assessment of the impulsive asymptote between the SDOF and 2-DOF models are respectively 16 % and 25 %, for $\alpha_u = 10$ % and $\alpha_u = 70$ %. The iso-damage curves predicted by the SDOF model also validate the asymptotic solutions.

The deformation limits are satisfied for curves corresponding to ratios α_u equal to 50 % and 70 % whereas they are not respected for other curves in the dynamic and impulsive

regimes (see Fig. III.23-e). These results highlight that the formation of a plastic hinge at the bottom of a free-fixed beam-column, corresponding to a ductility ratio of 1, does not involve an axial instability of the structural member in contrast with a static analysis.

Figure III.23-f illustrates the maximum shear force at the bottom of a free-fixed beam-column. The shear force is well predicted by the 2-DOF model as shown in Section III.5.3.2 (in Part "Free-fixed beam-column") and is smaller than 0.5, involving no reduction on the plastic bending resistance.

Figures III.24-a, -b, -c and -d illustrate the pressure-diagrams for intermediate values of the stiffness of the lateral restraint and the lateral mass (see the case studies 3-6 in Table III.7). The fourth case study ($\chi_K = 5$ and $\chi_M = 0$) is characterized by a reduced slenderness $\bar{\lambda} = 1.22$ which is intermediate between that of the free-fixed beam-column ($\bar{\lambda} = 1.96$) and the pinned-fixed beam-column ($\bar{\lambda} = 0.67$). The dynamic region of the p-I diagram (Fig. III.24-b) seems to be complex for $\alpha_u = 50\%$ and $\alpha_u = 70\%$; some improvement should be provided to the analytical model as reported in Section III.5.3.2 (see Fig. III.21). However, when the parameter χ_K is increased to 26.8 (and $\chi_M = 0$), that anomalous behaviour in the dynamic region disappears (Fig. III.24-a). Indeed, for this set of parameters, a perfect agreement was observed previously for the assessment of the axial buckling load under a given blast loading as reported in Section III.5.3.2 (see Fig. III.19).

The fifth case study corresponds to a free-fixed beam-column with a lateral mass at its top ($\chi_K = 0$ and $\chi_M = 5$). The iso-damage curves predicted by the SDOF model again validate the asymptotic solutions (Fig. III.24-c). The curves established with the 2-DOF model match well with the SDOF model in the quasi-static region of the p-I diagram for $\alpha_u \leq 50\%$ because the contribution of the second mode of vibration is less significant in this part of the p-I diagram. However, for $\alpha_u = 70\%$, the quasi-static asymptotic solution predicted by the 2-DOF model is smaller than that of the SDOF model because the SDOF model mitigates the $P - \delta$ effect through the overestimation of the critical axial load. Further investigations should focus on understanding and eventually correcting the 2-DOF model in the dynamic and impulsive areas of the p-I diagram.

Finally, for the last case study ($\chi_K = 5$ and $\chi_M = 5$), it was shown in Section III.5.3.2 that the 2-DOF model was able to predict accurately the dynamic buckling of the beam-column under an impulsive blast loading (see Fig. III.22). The asymptotes of the p-I diagram naturally appear for this case study (Fig. III.24-d), and no anomalies are identified in this p-I diagram.
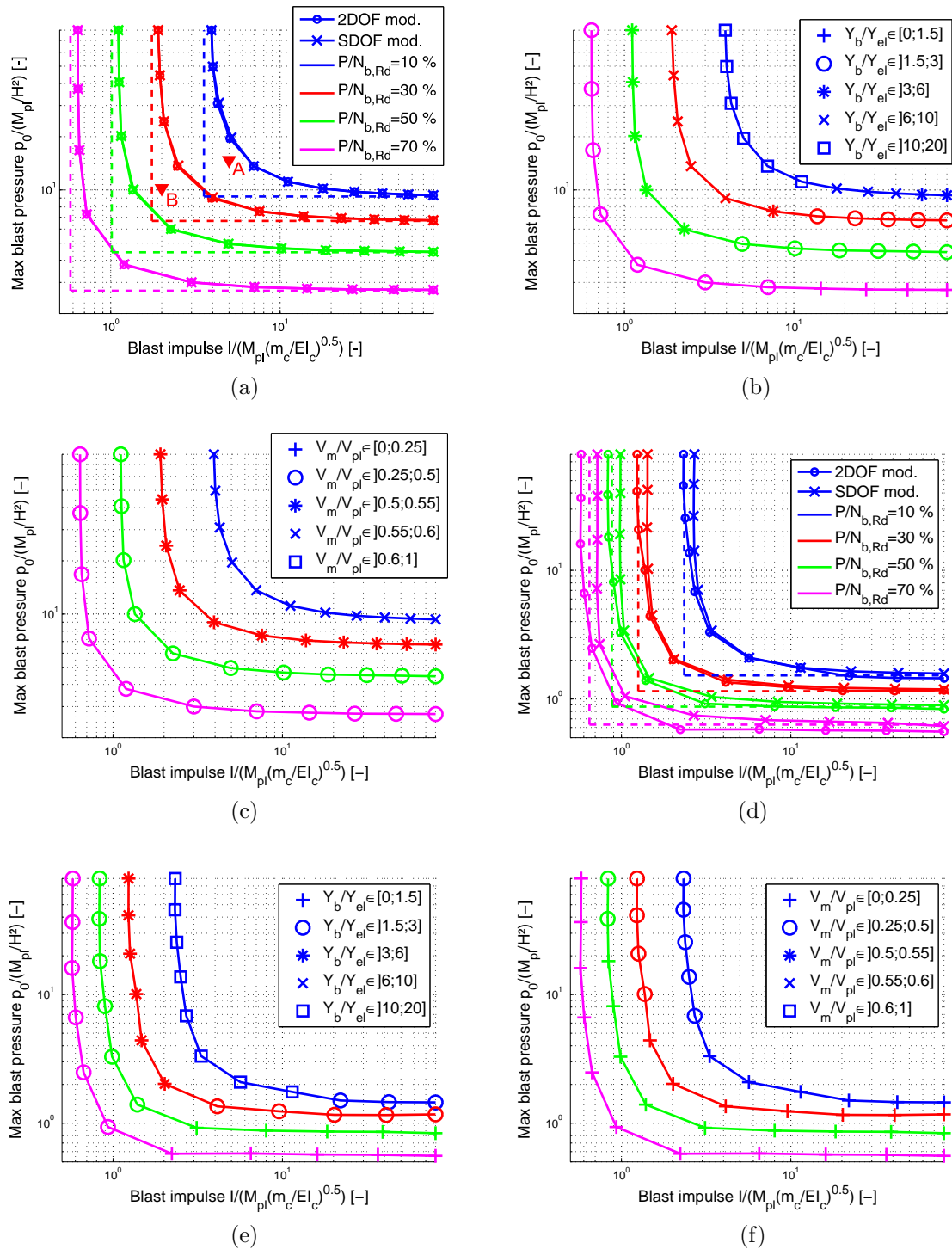
Figure III.23: (a) Pressure-impulse diagram of a pinned-fixed beam-column - Comparison of SDOF and 2-DOF analytical models; (b) Corresponding ductility and (c) maximum dimensionless shear force at the bottom of the beam-column predicted by the 2-DOF model. (d) Pressure-impulse diagram of a free-fixed beam-column - Comparison of SDOF and 2-DOF analytical models; (e) Corresponding ductility and (f) maximum dimensionless shear force at the bottom of the beam-column predicted by the 2-DOF model.
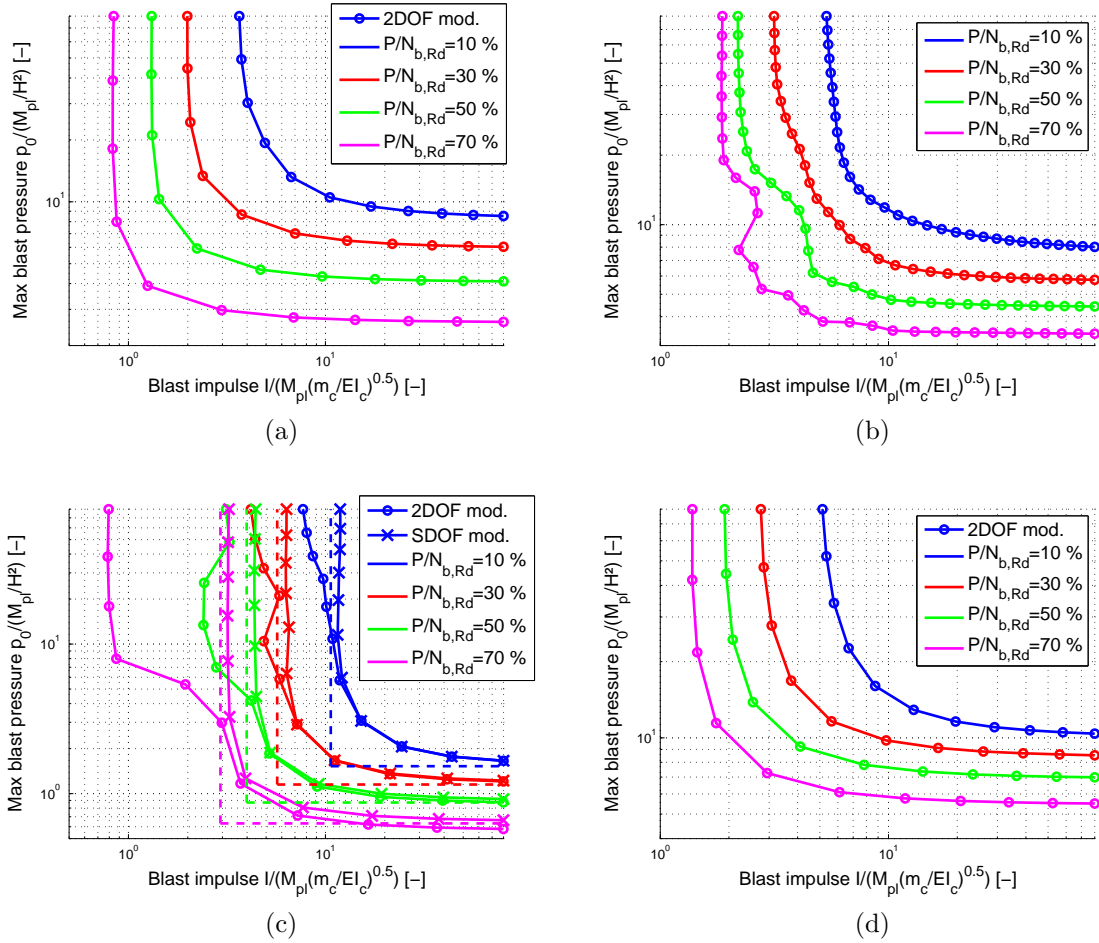
Figure III.24: Pressure-impulse diagram of a beam-column with intermediate values of the stiffness of the lateral restraint and the lateral mass. (a) $\chi_K = 26.8$ and $\chi_M = 0$; (b) $\chi_K = 5$ and $\chi_M = 0$; (c) $\chi_K = 0$ and $\chi_M = 5$ and (d) $\chi_K = 5$ and $\chi_M = 5$.

III.7 Conclusions

The purpose of this chapter was to develop an analytical model to capture the dynamic response of beam-columns under axial compressive load and blast loading, which interacts with the surrounding structure. The model accounts for large displacement ($P - \delta$ effect), bending moment-axial force (M-N) plastic interaction as well as its interaction with the indirectly affected part (IAP) of the structure. The IAP of the structure is simplified into an elastic lateral spring $K^\star$ and mass $M^\star$ which are connected at the top of the beam-column, eventually authorizing a lateral motion at its head.

Based on the decomposition of the field of displacement into shape functions amplified by generalized displacements and Lagrange's equation, the analytical model includes two

degrees-of-freedom (2 DOFs) specific to each stage of motion of the beam-column. Four stages (or regimes) were identified, depending on the eventual development of plastic hinge(s) at the bottom or/and mid-height of the column. The minimum Δ_0 technique is also adopted to minimize the error in momentum quantities at the regime transitions according to the least mean square method.

In addition to the development of the 2-DOF model, two SDOF models were also derived for particular cases (for free-fixed and pinned-fixed beam-columns) as well as their asymptotic impulsive and quasi-static solutions.

The dimensional analysis of the problem reveals that, under the considered assumptions, four dimensionless parameters mainly influence the dynamic stability of the beam-column. Two of them are related to the behavior of the indirectly affected part (the lateral restraint χ_K and mass χ_M). Another one is related to the critical load multiplier α_{cr} (i.e. the ratio of the axial compressive load to Euler elastic buckling resistance). The last parameter is the reduced slenderness $\bar{\lambda}$ of the beam-column.

Full non-linear dynamic simulations of 2D FEM models of columns under same loading and boundary conditions as for the analytical model were performed with FinelG, accounting for large displacement and a plastic kinematic constitutive model to capture the M-N plastic interaction, disregarding any shear failure since the FEM formulation is based on Euler-Bernoulli assumption. The strain rate effect as well as the strain hardening were disregarded. No initial geometric imperfection and residual stresses were considered in the modelling. The numerical simulations were performed in two steps, firstly by assuming that the material law is indefinitely linear elastic and then, by considering it as elastic-perfectly-plastic. The influence of the parameters χ_K and χ_M were studied through out several case studies.

When the material is assumed to be indefinitely elastic, a very good correlation is achieved between the results predicted by the SDOF, 2-DOF and FinelG models for pinned-fixed beam-column. For free-fixed beam-column, comparative analytical estimations of 2-DOF model and FinelG calculations also results in a perfect agreement. However, some discrepancies are observed between the results predicted by the FinelG and SDOF models mainly for two reasons: the Euler elastic buckling axial load $P_{cr,SDOF}$ is overestimated (see Equ. (III.57)) by the SDOF model leading to a mitigation of the $P - \delta$ effect and this simplified model does not account for the second mode of vibration which governs the dynamic response of the beam-column when the lateral mass at its top is non-negligible. For intermediate values of stiffness of the lateral restraint and the lateral mass, a very good match is found between the estimations of the 2-DOF and FinelG models.

The modified UFC approach (by Nassr *et al.* [79]), only valid in the elastic regime, provided an accurate estimation of the moment magnification factor (MMF) except for the case studies where the second mode of vibration significantly affects the response of the beam-column. Indeed, it is implicitly assumed that the MMF can be well predicted with one single mode of vibration through the use of the dynamic load factor (DLF) graph (see Fig. I.15) although it is not always valid as shown earlier.

When the material is elastic-perfectly plastic, both analytical SDOF and 2-DOF models were able to predict accurately the response of the pinned-fixed beam-column and to capture

its potential dynamic buckling. Despite using the minimum Δ_0 technique, the maximum relative error in the momentum quantity at the regime transitions reached about $5 - 6\%$.

For the free-fixed beam-column, a perfect agreement was also achieved between the predictions of the 2-DOF and FinelG models except for the case studies which present a significant lateral mass. Indeed, when the lateral mass is significant, the top of the beam-column moves slowly because of the inertia of the lateral mass while the central region of the beam-column vibrates more quickly at a higher frequency than its top due to the second mode of vibration. Those high frequency oscillations cause a series of loading/unloading phases at the bottom plastic hinge which results in a large number of regime transitions. Moreover, at each regime transition, the application of the minimum Δ_0 technique introduced some artificial increment of momentum quantity in the system. The large number of regime transitions and the application of the Δ_0 technique account both for the overestimation of the maximum displacement. Concerning the predictions of SDOF model, a substantial discrepancy was found between them and those of the FinelG model because the analytical model overestimates the Euler buckling axial load in the elastic stage as stated earlier and disregards the contribution of the second mode of vibration.

For $\chi_K = 26.8$ and $\chi_M = 0$, a very good match was again found between the estimations of the 2-DOF and simplified FinelG models irrespective of the axial load. The simplified FinelG model assumes that the plasticity is localized at the bottom and at mid-height ($\overline{z}_m = 0.58$) of the beam-column, preventing any traveling of plastic hinge along the height of the member. Concerning the prediction of the deflection by the FinelG model, it does not correspond perfectly to that of the simplified FinelG model because the central plastic hinge moves upwards at a maximum distance of 7% of the height of the beam-column. Neglecting the traveling of the central plastic hinge is however on the safe side.

For $\chi_K = 5$ and $\chi_M = 0$, a relative error of 10% (resp. 20%) on the safe side was observed between the axial buckling load of the beam-column under a given blast loading predicted by the analytical and simplified FinelG model (resp. FinelG model). Those results highlighted that some improvements should be provided to the analytical model.

For $\chi_K = 5$ and $\chi_M = 5$, a perfect agreement was achieved between the analytical and numerical predictions for an impulsive blast loading.

Concerning the prediction of the shear force, a bad correlation was found between the analytical and numerical calculations except for the free-fixed beam-column. Indeed, the shape functions were not defined to include any specific boundary conditions on the shear force, leading to wrong analytical estimations of its response. In some cases, the shear force predicted with FinelG was greater than the half of the plastic shear resistance of the beam-column, implying that a reduction should be provided to the plastic bending resistance although the shear force quickly falls under the threshold value during the blast event.

The effects of the lateral restraint $K^\star$, the lateral mass $M^\star$ and the axial load P on the stability of the beam-column under lateral blast loading were studied. The parametric study was performed by establishing the pressure-impulse (p-I) diagram of the beam-column which indicates, with a simple reading, the eventual buckling of that structural member according to a damage criterion. The inverse of the ultimate multiplier α_u was chosen as the damage parameter since it enables to includes both types of axial failures: cross-section axial yielding

and elastic axial buckling of the beam-column. As expected, the higher the axial load applied at the top of the beam-column (or the parameter α_u) was, the smaller the pressure and the impulse to provoke the dynamic buckling of the beam-column were.

For pinned-fixed beam-column, a perfect agreement was observed between the iso-damage curves predicted by the SDOF and 2-DOF models, and the asymptotic solutions were validated by the predictions of the SDOF model. Moreover, only the curve corresponding to $\alpha_u = 70\%$ and the quasi-static regions of the other curves exhibited some ductility ratios that were smaller than the deformation limit suggested in the ASCE design guide.

For free-fixed beam-column, the SDOF model was shown to be unsafe for the prediction of the curve of the p-I diagram as compared to the 2-DOF models because it mitigates the $P - \delta$ effect in the elastic regime as explained earlier. The maximum relative error in the assessment of the impulsive asymptotic solution between the two analytical models can even reach 25 % for $\alpha_u = 70\%$, $\chi_K = 0$ and $\chi_M = 0$. When the lateral mass is significant ($\chi_M = 5$ and $\chi_K = 0$), the curves established with the 2-DOF model match well with the SDOF model in the quasi-static region of the p-I diagram but some improvements should be provided to the 2-DOF model in other regions of the p-I diagram.

For $\chi_K = 5$ and $\chi_M = 0$, the dynamic region of the p-I diagram (Fig. III.24-b) seems to be complex for $\alpha_u = 50\%$ and $\alpha_u = 70\%$ and further investigations should be paid to this part of the graph. For $\chi_K = 26.8$ and $\chi_M = 0$ as well as $\chi_K = 5$ and $\chi_M = 5$, no anomalies were found in the drawing of the p-I diagrams.

III.8   Perspectives

The first perspective consists in improving the analytical developments to better capture the dynamic behaviour of the beam-column for intermediate stiffness of the lateral restraint and mass. Then, the second perspective would be to better predict the stability of the beam-column under transverse blast loading (see Fig. III.25-b), interacting with the rest of the structure as depicted in Fig. III.25-a. The IAP of the structure can be modeled with elastic-perfectly plastic springs and masses. The interaction between the blast loaded beam and the column is totally neglected.

The horizontal, vertical and rotational springs are assumed to be decoupled and characterized by the following stiffnesses $K_h^\star$, $K_v^\star$ and $K_\theta^\star$ which are obtained from the condensation techniques (see Section I.4.5). The plastic resistances $R_h^\star$, $R_v^\star$ and $R_\theta^\star$ (see Fig. III.25-c) can be provided by a non-linear pushover analysis of the IAP of the structure (assuming that no instability occurs in that part of the structure). For instance, in order to determine the plastic resistance $R_v^\star$ of the structure, two forces are applied at the top of the lost columns and are progressively risen until the complete formation of a plastic mechanism or the collapse of the upper part of the structure (see Fig. III.26), neglecting any coupling with other failure modes caused by the horizontal force or the bending moment at the top of the beam-column. The corresponding masses of the IAP of the structure are called $M_h^\star$, $M_v^\star$ and $M_\theta^\star$ and are also obtained by the condensation techniques and are decoupled. The bending moment-axial force plastic interaction of the beam-column is illustrated in Fig. III.25-d.
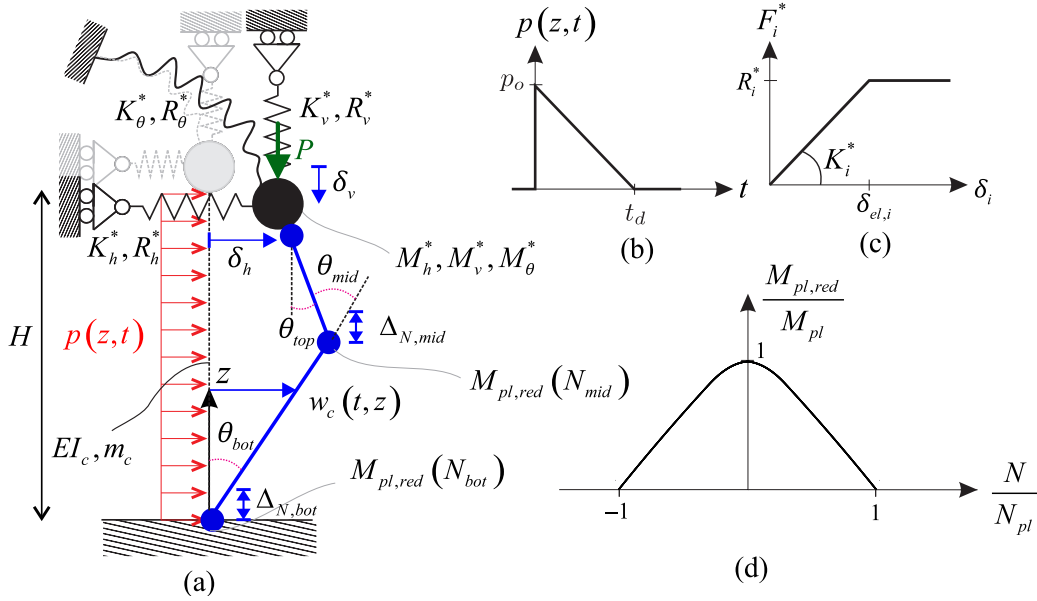
Figure III.25: (a) Sketch of the considered problem, (b) Idealized blast loading, (c) Elastic-perfectly plastic law of the spring, (d) Axial force-bending moment interaction law.

However, the first main challenge is to define a rapid assessment tool that satisfies these requirements at the top of the beam-column

$$M\left(t, \bar{z}=1\right) = -\frac{EI_c}{H^2}\frac{\partial^2 w_c\left(\bar{z},t\right)}{\partial \bar{z}^2}\Big|_{\bar{z}=1} = \begin{cases} K_\theta^\star \theta_{top} & \text{for } 0 \leq |\theta_{top}| \leq R_\theta^\star/K_\theta^\star \\ R_\theta^\star & \text{for } R_\theta^\star/K_\theta^\star < |\theta_{top}| \end{cases} + M_\theta^\star \ddot{\theta}_{top} \quad \text{(III.87)}$$

$$V\left(t, \bar{z}=1\right) = -\frac{EI_c}{H^3}\frac{\partial^3 w_c\left(\bar{z},t\right)}{\partial \bar{z}^3}\Big|_{\bar{z}=1} = \begin{cases} K_h^\star \delta_h & \text{for } 0 \leq |\delta_h| \leq R_h^\star/K_h^\star \\ R_h^\star & \text{for } R_h^\star/K_\theta^\star < |\delta_h| \end{cases} + M_h^\star \ddot{\delta}_h \quad \text{(III.88)}$$

where $\theta_{top} = \frac{1}{H}\frac{\partial w_c(\bar{z},t)}{\partial \bar{z}}\Big|_{\bar{z}=1}$ and $\ddot{\theta}_{top} = \frac{1}{H}\frac{\partial^3 w_c(\bar{z},t)}{\partial t^2 \partial \bar{z}}\Big|_{\bar{z}=1}$ respectively correspond to the rotation and angular acceleration at the top of the beam-column, $\delta_h = w_c|_{\bar{z}=1}$ and $\ddot{\delta}_h = \ddot{w}_c|_{\bar{z}=1}$ respectively refer to the elongation of the horizontal spring and acceleration of the horizontal mass. These boundary conditions (III.87) and (III.88) are difficult to impose since the shape functions are defined such that they are time-independent (principle of the separation of time and space variables).

Let consider the closest structural configuration of that studied in the present Chapter III by assuming that a pinned restraint is considered at the top of the beam-column ($K_\theta^\star = M_\theta^\star = R_\theta^\star = 0$). The shape functions described in Table III.1 can be used provided the force in the lateral restraint remains smaller than the plastic resistance $R_h^\star$. Two degrees-of-freedom $\Delta_{N,bot}$ and $\Delta_{N,mid}$ should be incorporated in the model to take into account the axial elongations of the two plastic hinges (see Fig. III.25-a) because of the vertical spring

and mass. We mainly focus on the effect of the horizontal and vertical springs and masses on the dynamic stability of the beam-column and tolerate an inaccuracy in the predictions of the shear force since Equ. (III.88) is disregarded in the definition of the shape functions.
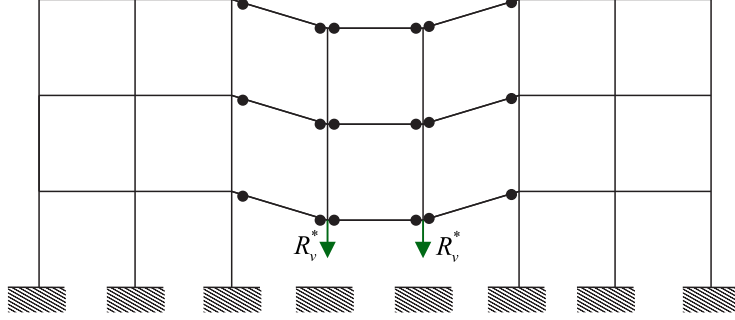

Figure III.26: Determination of the plastic resistance $R_v^\star$ of the indirectly affected part of the structure.

The elongation of the vertical spring and acceleration of the vertical mass are respectively given by

$$\delta_v = \delta_c - \Delta_N \quad ; \quad \ddot{\delta}_v = \ddot{\delta}_c - \ddot{\Delta}_N \tag{III.89}$$

where δ_c is the chord elongation of the beam-column given by Equ. (III.20) and Δ_N is the total axial elongation of the beam-column and is equal to $\Delta_{N,bot} + \Delta_{N,mid}$ in the plastic regime.

The elastic energy U_1 stored in the column is given by Equ. (III.15) while the energy dissipated in the plastic hinges U_2 becomes

$$U_2 = \int_0^{\theta_{bot}} M_{pl,red}\left(N_{bot}\right) d\theta + \int_0^{\theta_{mid}} M_{pl,red}\left(N_{mid}\right) d\theta \tag{III.90}$$

where $\theta_{bot} = \frac{1}{H}\frac{\partial w_c}{\partial \bar{z}}\big|_{\bar{z}=0^+}$ and $\theta_{mid} = \frac{1}{H}\left(\frac{\partial w_c}{\partial \bar{z}}\big|_{\bar{z}=\bar{z}_m^-} - \frac{\partial w_c}{\partial \bar{z}}\big|_{\bar{z}=\bar{z}_m^+}\right)$ respectively correspond to the variation of rotations at the plastic hinge locations, N_{bot} and N_{mid} are the axial forces at the bottom and at mid-height of the beam-column.

The energy stored in the lateral and vertical restraints reads

$$U_3 = \begin{cases} \frac{1}{2}K_h^\star\delta_h^2 & \text{for } 0 \leq \delta_h \leq \delta_{h,el} \\ \frac{1}{2}K_h^\star\delta_{h,el}^2 + R_h^\star\left(\delta_h - \delta_{h,el}\right) & \text{for } \delta_{h,el} < \delta_h \end{cases} + \begin{cases} \frac{1}{2}K_v^\star\delta_v^2 & \text{for } 0 \leq \delta_v \leq \delta_{v,el} \\ \frac{1}{2}K_v^\star\delta_{v,el}^2 + R_v^\star\left(\delta_v - \delta_{v,el}\right) & \text{for } \delta_{v,el} < \delta_v \end{cases},$$
$$\tag{III.91}$$

where $\delta_{h,el} = R_h^\star/K_h^\star$ and $\delta_{v,el} = R_v^\star/K_v^\star$ respectively correspond to the elastic horizontal and vertical deflections of the indirectly affected part of the structure.

The dissipation D of energy is neglected and the energy dissipated axially in plastic hinges is given by

$$U_4 = N_{bot}\Delta_{N,bot} + N_{mid}\Delta_{N,mid}. \tag{III.92}$$

The total kinetic energy can be expressed as the sum of the kinetic contributions of the column and the lateral and vertical masses

$$K = \frac{m_c H}{2} \int_0^1 \dot{w}_c^2 d\bar{z} + \frac{1}{2} M_h^\star \dot{\delta}_h^2 + \frac{1}{2} M_v^\star \dot{\delta}_v^2. \tag{III.93}$$

The work done by the axial load and the blast loading are respectively described by

$$W_P = P\delta_v = (M_v^\star g)\,\delta_v \tag{III.94}$$

and,

$$W = \int_0^H p w_c dz = pH \int_0^1 w_c d\bar{z} \tag{III.95}$$

where g is the gravity acceleration.

It can be shown that the axial force in the column is steady when the axial inertia of the beam-column is neglected

$$N_{mid} = N_{bot} = N. \tag{III.96}$$

In the elastic regime, the axial force in the column is given by

$$N = \frac{EA_c}{H}\Delta_N, \tag{III.97}$$

while in the plastic regime, the normality rule enables to derive the axial force

$$\frac{dM_{pl,red}}{dN} = f(N) = -\frac{\dot{\Delta}_{N,bot}}{\dot{\theta}_{bot}} = -\frac{\dot{\Delta}_{N,mid}}{\dot{\theta}_{mid}} \tag{III.98}$$

and provides the kinematic relationship between the axial deformations in the two plastic hinges

$$\dot{\Delta}_{N,mid} = \dot{\Delta}_{N,bot}\frac{\dot{\theta}_{mid}}{\dot{\theta}_{bot}}. \tag{III.99}$$

Finally, the Lagrange's Equations [85] reads

$$-\frac{d}{dt}\left(\frac{\partial K}{\partial \dot{r}_j}\right) + \left(\frac{\partial K}{\partial r_j}\right) - \sum_{k=1}^{4}\left(\frac{\partial U_k}{\partial r_j}\right) - \left(\frac{\partial D}{\partial \dot{r}_j}\right) + \frac{\partial (W + W_P)}{\partial r_j} = 0 \quad , j \in [1;3] \tag{III.100}$$

where the generalized coordinates $r_1 = q_{2i-1}$, $r_2 = q_{2i}$ and $r_3 = \Delta_N$ (where $i = 1$, 2, 3 and 4 is the subscript of the regime Γ_i). The unknowns that appear in the set of 6 equations (see Equs. (III.96), (III.97)/(III.98), (III.99) and (III.100)) are q_{2i-1}, q_{2i}, $\Delta_{N,bot}$, $\Delta_{N,mid}$, N_{bot} and N_{mid} which can be reduced to a 3-DOF analytical model (q_j, q_{j+1} and Δ_N).

For instance, assuming that no yielding occurs in the lateral restraint ($|K_h^\star \delta_h| < R_h^\star$) or in the beam-column ($|M(t, \bar{z})| < M_{pl,red}(N)$), the Lagrange's Equations for the regime I are given by

$$
m_c H \begin{bmatrix} \frac{130555}{290304} & \frac{2627}{10368} \\ \frac{2627}{10368} & \frac{104}{405} + \frac{M_h^\star}{m_c H} \end{bmatrix} \begin{bmatrix} \ddot{q}_1 \\ \ddot{q}_2 \end{bmatrix} + \left\{ \frac{EI_c}{H^3} \begin{bmatrix} \frac{6845}{64} & \frac{37}{8} \\ \frac{37}{8} & \frac{16}{5} + \frac{K_h^\star H^3}{EI_c} \end{bmatrix} + \frac{N}{H} \begin{bmatrix} \frac{6845}{1344} & -\frac{185}{336} \\ -\frac{185}{336} & \frac{8}{7} \end{bmatrix} \right\} \begin{bmatrix} q_1 \\ q_2 \end{bmatrix}
$$

$$
= pH \begin{bmatrix} \frac{37}{64} \\ \frac{2}{5} \end{bmatrix} \tag{III.101}
$$

$$
N = F_v(q_1, q_2, \Delta_N) + M_v^\star \ddot{\delta}_v\left(q_1, q_2, \dot{q}_1, \dot{q}_2, \ddot{q}_1, \ddot{q}_2, \ddot{\Delta}_N\right) - P \tag{III.102}
$$

where the force, the axial elongation of vertical restraint[1] and the acceleration of the vertical mass are respectively described by

$$
F_v = \begin{cases} K_v^\star \delta_v(q_1, q_2, \Delta_N) & \text{for } 0 \leq \delta_v \leq \delta_{v,el}, \\ R_v^\star & \text{for } \delta_{v,el} < \delta_v \end{cases} \tag{III.103}
$$

$$
\delta_v = \frac{1}{2H}\left(-\frac{185}{168}q_1 q_2 + \frac{6845}{1344}q_1^2 + \frac{8}{7}q_2^2\right) - \Delta_N \tag{III.104}
$$

and

$$
\ddot{\delta}_v = \frac{1}{2H}\left(-\frac{185}{168}q_2\ddot{q}_1 + \frac{6845}{672}q_1\ddot{q}_1 - \frac{185}{84}\dot{q}_1\dot{q}_2 + \frac{6845}{672}\dot{q}_1^2 - \frac{185}{168}q_1\ddot{q}_2 + \frac{16}{7}q_2\ddot{q}_2 + \frac{16}{7}\dot{q}_2^2\right) - \ddot{\Delta}_N. \tag{III.105}
$$

The set of equations (III.97), (III.101) and (III.102) is highly nonlinear since the membrane force N depends on the response of the beam-column (q_1, q_2, Δ_N and their time derivative). An iterative numerical scheme must be used to get the dynamic response of the column. Equation (III.101) presents the same generic form as the equation of motion (III.23) except that the membrane force in the column $-N$ appears in the expression of the matrix $\mathbf{K}_{P,I}$ instead of the constant axial load P. More generally, the matrices in Table

---

[1]The expression of the axial elongation of the vertical spring taking into account the history of motion of the beam-column is actually more complex:

$$
\begin{aligned}
\delta_v =\ & q_1(t)\left(-\frac{0.55}{H}q_2(t) - \frac{0.85}{H}q_7(t_{k-1}) - \frac{0.85}{H}q_8(t_{k-1}) + 1.43q_3(t_{k-1})\right) + \frac{2.55q_1(t)^2}{H} - 0.38q_3(t_{k-1})q_7(t_{k-1}) - 0.38q_3(t_{k-1})q_8(t_{k-1}) \\
& + q_2(t)\left(\frac{1.73}{H}q_5(t_{k-1}) + \frac{q_6(t_{k-1})}{H} + \frac{2.3q_7(t_{k-1})}{H} + \frac{2.3q_8(t_{k-1})}{H} - 0.24q_3(t_{k-1}) + q_4(t_{k-1})\right) + \frac{0.57q_2(t)^2}{H} + 0.24Hq_3(t_{k-1})^2 \\
& + 0.5Hq_4(t_{k-1})^2 + \frac{1.49}{H}q_5(t_{k-1})^2 + \frac{1.73}{H}q_5(t_{k-1})q_6(t_{k-1}) + \frac{3.57}{H}q_5(t_{k-1})q_7(t_{k-1}) + \frac{3.57}{H}q_5(t_{k-1})q_8(t_{k-1}) + \frac{0.5q_6(t_{k-1})^2}{H} \\
& + \frac{2.07q_6(t_{k-1})q_7(t_{k-1})}{H} + \frac{2.07q_6(t_{k-1})q_8(t_{k-1})}{H} + \frac{2.35q_7(t_{k-1})^2}{H} + \frac{4.7}{H}q_7(t_{k-1})q_8(t_{k-1}) + \frac{2.35q_8(t_{k-1})^2}{H} + 1.73q_4(t_{k-1})q_5(t_{k-1}) \\
& + q_4(t_{k-1})q_6(t_{k-1}) + 2.07q_4(t_{k-1})q_7(t_{k-1}) + 2.07q_4(t_{k-1})q_8(t_{k-1}) - \Delta_N(t)
\end{aligned}
$$

III.2 are still convenient except for the symbol P which must be replaced by $-N$ when the vertical restraint of the IAP is taken into account. It is interesting to notice that the plastic resistance $R_v^\star$ must be considered in the expression of the force in the vertical spring (see Equ. (III.103)), otherwise the beam-column will never experience a buckling instability. In addition, four additional regimes should be introduced in Table III.2 in case of the yielding of the lateral restraint. Each regime would be featured by one shape function that exhibits a lateral deflection at the top of the beam-column (with even subscripts as illustrated in Fig. III.2), involving a reduction of number of DOFs to 2 during these regimes.

In case of fixed-end restraint at the top of the beam-column ($K_\theta^\star$, $M_\theta^\star \to +\infty$ and $R_\theta^\star > M_{pl}$), new shape functions can be defined with the possible development of three plastic hinges along the beam-column instead of 2. The number of regimes should be increased to 8 (and even to 16 in case of yielding of the lateral restraint).

However, for intermediate values of $K_\theta^\star$, $M_\theta^\star$ and $R_\theta^\star$, it is difficult to find the shape functions that satisfy Equ. (III.87) and are time-independent. In [59], the authors have recently proposed a closed-formed solution to predict the dynamic response of a beam with elastic semi-rigid rotational restraints (neglecting any rotational mass), where the aforementioned boundary condition is checked. This intermediate case is more complex to deal with and must be also investigated further in the future.

To better assess the shear force at the supports of the beam-column, the bending moment-axial and shear force (M-N-V) plastic interaction must be considered and a new DOF should be incorporated to the kinematics of the simplified model (Fig. III.25-a), additional to the rotation θ and axial elongation Δ_N of the plastic hinge, which is the shear angle γ_v. As a consequence, new shape functions should be defined and the expressions derived from the normality law (see Equs. (III.98) and (III.99)) must be revisited since the generalized strain rate vector must be normal to a three-dimensional yield surface and not to an yield curve.

Concerning the traveling of mid-height plastic hinge, this phenomenon is complex to implement in a rapid assessment tool since it requires to consider the location of the plastic hinge z_m (see Figs. III.2-c and -d) as a time-dependent variable. The dynamic response of the beam-column is rather sensitive to this phenomenon although it is commonly and safely neglected in the literature.

Chapter IV

Simple frame structure under internal blast loading

IV.1 State-of-the-art on frame under blast loading

Recent researches have focused on the alternate load path (ALP) method to deal with frame building subjected to extreme loading (impact, explosion,...). That approach consists in studying the behaviour of the structure under a column loss independently of the threat [91, 119, 92, 93, 120, 84]. The purpose of that method is to avoid progressive collapse after the sudden column loss by conferring a second-order stable configuration to the structure through redistribution of the vertical load supported by this column to the surrounding structure.

In the context of an impact scenario involving a vehicle that damages one column of the structure and causes its failure, the ALP approach could be convenient to assess the level of robustness of the structure under this extreme loading ([121, 122]). However, when the structure is subjected to blast loading, several structural elements could be damaged and even failed as highlighted in Refs. [123, 124, 125, 126] where the ALP approach is shown to be unconservative in some cases. Indeed, the "member-removal" method neglects the damage and non-zero initial velocities of vulnerable load-carrying structural members induced by blast loads. A procedure was developed in [106] to tackle these drawbacks, it consists in determining the initial velocities of these structural elements using SDOF analysis (based on momentum conservation) and assessing the residual capacity of damaged RC columns by using their corresponding pressure-impulse diagrams (analytical formula to establish p-I diagram are developed in [53]). Then, introducing these input data into the modeling of the structure, the non-linear dynamic analysis of the RC frame can be performed. It is shown, in opposition with the "member-removal" approach, that the proposed method provides similar predictions of the frame collapse to those of the direct blast analysis. This new method requires less computational effort than the the direct numerical simulations, and is more accurate than the traditional ALP method.

In [108], the direct blast analysis of a ten-storey RC frame building (with four and five bays in the two orthogonal directions) subjected to a near-field external explosion is performed in two steps. The first step consists in carrying out a linear elastic analysis of the whole structure in order to locate the vulnerable area of the building, to identify the structural members that present internal forces that are greater than their associated capacity. Then, the second step is to perform a rigorous non-linear dynamic analysis (accounting for the strain rate effect) of the sub-frame including vulnerable structural elements by using LS-DYNA. The sub-frame is extracted from the whole structure and presents the same boundary conditions as the entire building at its basis although at its top, the columns are allowed to rotate and translate in all directions except for the translation in the blast direction. The technique used by Jayasooriya *et al.* [108] enables to assess the level of damage and residual capacity of the building by reducing as much as possible the size of the problem and thus, its corresponding computational time.

Izzudin *et al.* [127, 128] were first to propose an adaptive method for integrating fire and explosion on analysis of two-dimensional (2D) steel frames. Chen and Liew [43, 44] extended the work to three-dimensional frames in which the local and lateral torsional buckling as well

as shear yielding were incorporated into the model by using shell elements for the critical members directly exposed to internal blast loading. The indirectly affected part of the three-storey frame structure (non-critical members) were modeled using beam elements for a sake of computational efficiency. They show that the blast load may cause instabilities, shear failure and permanent deformations on load carrying members which will affect the stability and resistance of the frame when it is later exposed to fire.

However, the direct blast analysis of an entire frame always requires some sophisticated software such as LS-DYNA or ABAQUS which are time consuming, complex to use and expensive for a common design office. Some simplified assessment tools can be used to predict the level of damage of structural elements that are extracted and isolated from the frame under blast loading (as described in Sections II.1 and III.1) although they disregard any interaction with other structural elements. In this Chapter, some investigations have been paid to the dynamic behaviour of a very simple laterally braced frame under internal blast loading. Some SDOF models of the frame members are available in the literature and are combined in order to study the global stability of a frame.

The final aim of this research is to propose a predictive model able to assess the level of damage of a compartment of a structure under internal blast loading (Fig. I.2-c) using condensation techniques for its extraction and analytical models of structural elements such as those established in Chapters II and III.

IV.2 Problem formulation

IV.2.1 Description of the problem

Consider a laterally braced frame subjected to an internal blast loading, in which the structural elements are pinned at their ends as shown in Fig. IV.1-a. The variables X and Y respectively represent the mid-span deflection of the beam and the column. The beam and the beam-column respectively have a length L and H, and are characterized by an elastic flexural stiffness $k_b = 384 E_b I_b / 5 L^3$ and $k_c = 384 E_c I_c / 5 H^3$ (where E and I respectively denote the Young's modulus and the inertia of the structural element) and a lineic mass m_b and m_c. Two compressive loads P due to dead and live loads from upper stories are applied at the top of the columns.

Since the explosive charge is assumed to be equidistant to both beam-columns, the blast loading profile applied to the frame is symmetric. Blast overpressures applied to frame members are assumed to be uniformly distributed and present a triangular time-history shape with zero rise time (Fig. IV.1-b), as expressed in Equ. (IV.1)

$$p_{r,c}\left(z, t\right) = p_{0,c}\left(1 - \frac{t}{t_{d,c}}\right) \; ; \; p_{r,b}\left(x, t\right) = p_{0,b}\left(1 - \frac{t}{t_{d,b}}\right) \tag{IV.1}$$

where $p_{r,b}$, $p_{r,c}$ are respectively the reflected blast overpressure of the beam and the column, $p_{0,b}$, $p_{0,c}$ represent their peak overpressure and $t_{d,b}$, $t_{d,c}$ their positive phase duration, t corresponds to the time variable.

For the beam-column, the plastic bending resistance is initially reduced due to the application of compressive loads P, and it increases during the upward motion of the beam under blast loading and then diminishes during the unloading phase of the beam. According to [35], the M-N plastic interaction law for I steel profile (Fig. IV.1-c) is described by

$$M_{int,c} = M_{pl,c} \begin{cases} \left(1 - \gamma_0 \left(\frac{N_{int,c}}{N_{pl,c}}\right)^2\right) & \text{for } 0 \leq \frac{N_{int,c}}{N_{pl,c}} \leq \frac{A_{w,c}}{A_c}, \\ \left(1 - \gamma_1 - \gamma_2 \left(\frac{N_{int,c}}{N_{pl,c}}\right) - \gamma_3 \left(\frac{N_{int,c}}{N_{pl,c}}\right)^2\right) & \text{for } \frac{A_{w,c}}{A_c} \leq \frac{N_{int,c}}{N_{pl,c}} \leq 1, \end{cases} \tag{IV.2}$$

where $M_{pl,c}$ and $N_{pl,c}$ respectively represent the pure plastic bending and axial resistance of the beam-column, $A_{w,c}$ and A_c are respectively the area of the web and the total area of the column cross-section, and coefficients γ_0, γ_1, γ_2 and γ_3 are computed from Equ. (I.51) for the beam-column.

As the beam is axially constrained at its ends, the membrane force increases together with the transverse displacement X. Due to the M-N plastic interaction, the residual bending resistance $M_{int,b}$ drops as the membrane force $N_{int,b}$ consumes a growing part of the cross-section resistance (Fig. IV.1-c). However, Lescouarc'h's law will not be used since it assumes that all the cross-section is yielded which is not actually the case when the membrane force is very large for small curvature of the beam. Therefore, a multilayer representation of the cross-section is preferred as detailed in the next section IV.2.2.
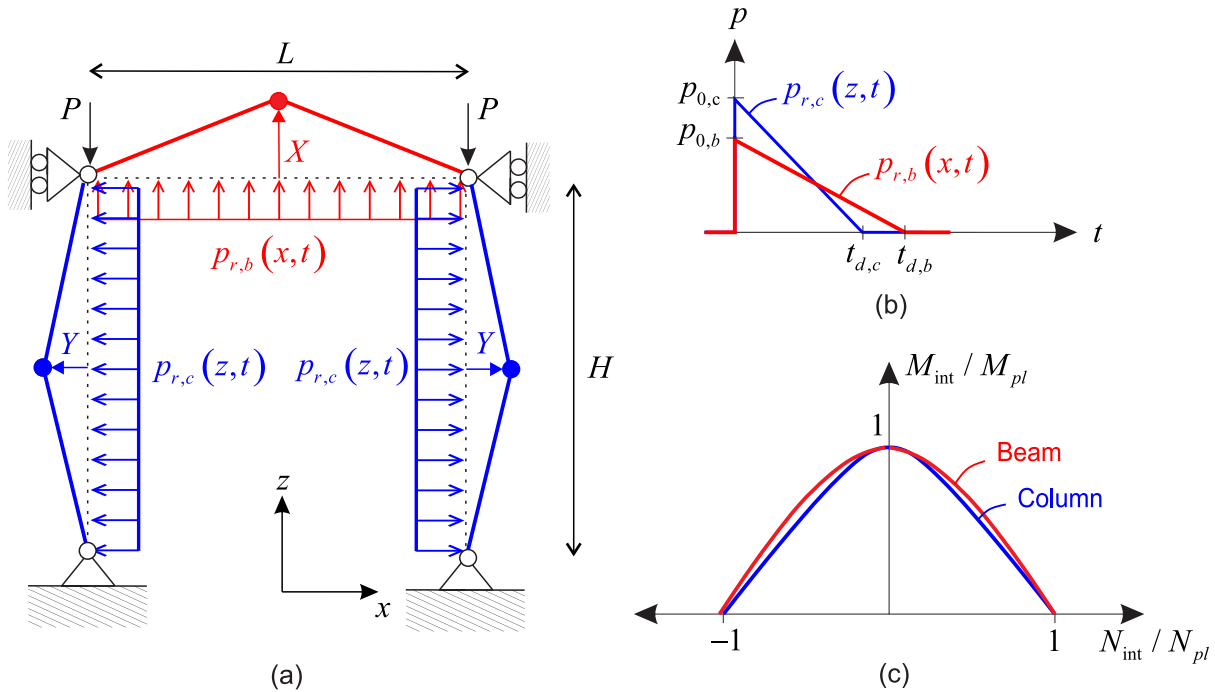

Figure IV.1: Sketch of a frame subjected to internal blast loading.

IV.2.2 Multi-layer model of the central hinge of the beam

IV.2.2.1 Resulting axial force and bending moment

The mid-span cross-section of the beam is divided into a number of layers (Fig. IV.2-a) and, based on Euler-Bernoulli beam theory, the strain variation over the depth of the cross-section is assumed linear [79, 80, 84]. The multilayer model developed in [84] is described in this section but the model is re-written in a general form to take into account the variable number of springs in the web and the flanges.

The material is assumed to be elastic-perfectly plastic, involving that the ith spring is characterized by an internal force $F_{int,i}$ (Fig. IV.2-b) given by

$$F_{int,i} = \begin{cases} k_i \delta_i & \text{for } 0 \leq |\delta_i| \leq \delta_{el,i}, \\ F_{pl,i} \text{sign}\left(\dot{\delta}_i\right) & \text{for } \delta_{el,i} \leq |\delta_i|, \end{cases} \tag{IV.3}$$

where $k_i = E_b A_i / (\ell_h / 2)$ is the elastic stiffness of the spring (A_i is the area of ith layer and ℓ_h is the length of the hinge), $F_{pl,i} = A_i f_y$ is the plastic axial resistance of the spring, δ_i and $\delta_{el,i} = F_{pl,i} / k_i$ are the axial elongation of the spring and is corresponding elastic elongation. The plastic axial resistance of the ith spring of an I-shaped cross-section reads

$$F_{pl,i} = \begin{cases} F_{pl,w} & \text{for } 0 \leq |h_i| \leq \frac{h_w}{2}, \\ F_{pl,f} & \text{for } \frac{h_w}{2} \leq |h_i|, \end{cases} \tag{IV.4}$$

with $F_{pl,f}$ and $F_{pl,w}$, referring to the plastic resistance of a layer located in the flange and the web of the beam, are respectively given by

$$F_{pl,f} = \frac{2}{n_f} \frac{M_{pl,b} - N_{pl,b} \frac{h_w}{4}}{h} \quad ; \quad F_{pl,w} = \frac{1}{n_w} \left(N_{pl,b} - 2n_f F_{pl,f}\right), \tag{IV.5}$$

where $M_{pl,b}$ and $N_{pl,b}$ respectively represent the pure plastic bending and axial resistance of the beam, n_f and n_w are respectively the number of layers in one flange and the web of the beam, h_w and h refer to the web depth and the depth of the section of the beam (Fig. IV.2-a). Relationships (IV.5) are obtained by writing these equilibrium equations

$$\sum_{i=1}^{n_w + 2n_f} F_{pl,i} = N_{pl,b} \quad ; \quad \sum_{i=1}^{n_w + 2n_f} F_{pl,i} |h_i| = M_{pl,b}. \tag{IV.6}$$

The stiffness of the ith spring of an I-shaped cross-section reads

$$k_i = \begin{cases} \frac{1}{n_w} \frac{E_b t_w h_w}{\ell_h / 2} & \text{for } 0 \leq |h_i| \leq \frac{h_w}{2}, \\ \frac{1}{n_f} \frac{E_b t_f b_f}{\ell_h / 2} & \text{for } \frac{h_w}{2} \leq |h_i|, \end{cases} \tag{IV.7}$$

where t_w, t_f and b_f are respectively the web and flange thicknesses and the width of the flange (Fig. IV.2-a).

The axial elongation of the ith spring is given by

$$\delta_i = \Delta_{N,h} + h_i \theta \tag{IV.8}$$

where $\theta = 2X/L$ is the rotation at the end of the beam, and $\Delta_{N,h}$ is the axial elongation of half part of the central hinge determined in section IV.2.3.

The axial force $N_{int,b}$ and bending moment $M_{int,b}$ in the hinge at mid-span of the beam

$$N_{int,b} = \sum_{i=1}^{n_w+2n_f} F_{int,i} \quad ; \quad M_{int,b} = \sum_{i=1}^{n_w+2n_f} F_{int,i} h_i. \tag{IV.9}$$
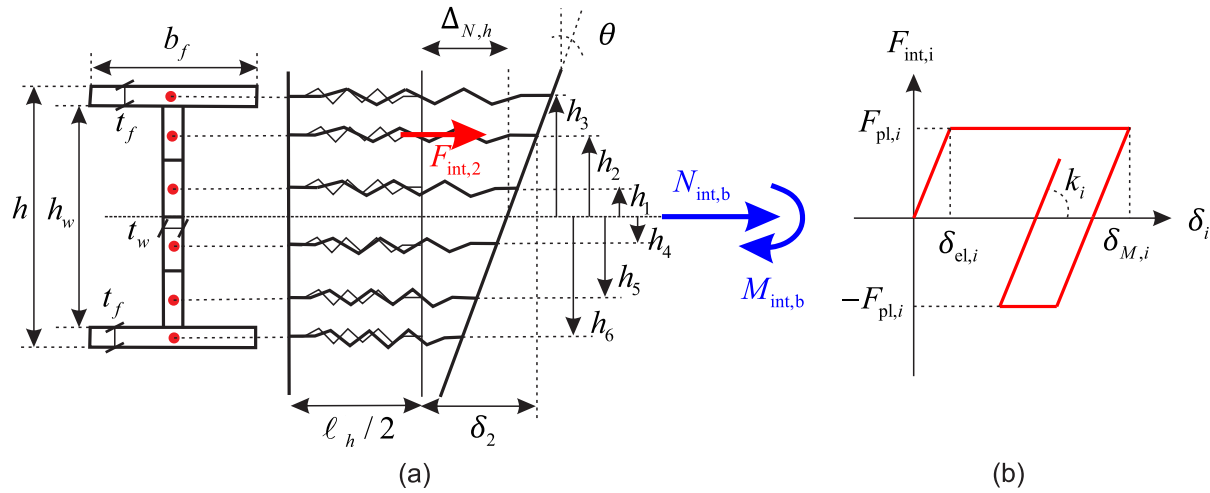
Figure IV.2: (a) Spring model for the cross-section at mid-span of the beam (sketch modified from [84]), (b) Elastic-perfectly plastic internal force in the ith spring.

IV.2.2.2 Length of the central hinge of the beam

In the elastic regime, the bending moment in the central hinge is given by

$$M_{int,b} = -E_b I_b \left. \frac{\partial^2 w_b}{\partial x^2} \right|_{x=L/2} = \frac{48}{5} \frac{E_b I_b}{L^2} X \tag{IV.10}$$

where the transverse displacement field of the beam reads

$$w_b(x,t) = \frac{16}{5} X(t) \left(\left(\frac{x}{L}\right)^4 - 2\left(\frac{x}{L}\right)^3 + \left(\frac{x}{L}\right) \right). \tag{IV.11}$$

Moreover, the bending moment can be written as follows

$$M_{int,b} = \sum_{i=1}^{n_w+2n_f} F_{int,i} h_i = \sum_{i=1}^{n_w+2n_f} k_i \delta_i h_i = 4 \frac{E_b I_{b,t}}{\ell_h L} X \tag{IV.12}$$

where $I_{b,t} = \sum_{i=1}^{n_w+2n_f} A_i h_i^2$ is the sum of transport inertia terms of all the layers and tends to inertia I_b when the number of layers in the web n_w is sufficiently large.

Equating and simplifying (IV.10) to (IV.12) gives the length of the hinge in the elastic regime

$$\ell_h = \frac{5}{12} \frac{I_{b,t}}{I_b} L \simeq \frac{5}{12} L. \tag{IV.13}$$

However, the length of the hinge varies during the plastic stage but for a sake of simplicity, it is assumed to remain constant irrespective of the regime of the beam.

IV.2.3   Compatibility equations for the beam

The small rotation/large displacement assumption allows to express the sum of the axial elongations of one half of the central hinge $\Delta_{N,h}$ and of the rest of the beam $\Delta_{N,EA}$ in terms of vertical deflection X

$$\Delta_{N,h} + \Delta_{N,EA} = \sqrt{\left(\frac{L}{2}\right)^2 + X^2} - \frac{L}{2} \simeq \frac{X^2}{L}. \tag{IV.14}$$

Due to equilibrium of axial forces along the beam, the axial force in the hinge is equal to that in the rest of the beam

$$N_{int,b} = \sum_{i=1}^{n_w+2n_f} F_{int,i}\left(\Delta_{N,h}, X\right) = k_{b,EA} \Delta_{N,EA} \tag{IV.15}$$

where $k_{b,EA} = \frac{E_b A_b}{(L-\ell_h)/2}$ is the axial stiffness of one half of the rest of the beam.

Equations (IV.14) and (IV.15) allow to express $\Delta_{N,h}$ and thus, the axial elongation of spring δ_i in terms of vertical deflection X..

IV.2.4   Equations of motion

Concerning the beam under explosion, some analytical models have been proposed in [67, 129] to capture the dynamic behavior of an axially constrained rectangular shape beam under blast loading, taking into account the bending moment-axial force (M-N) plastic interaction. After providing some slight modifications to their developments – accounting for the elastic state and a general M-N interaction – the equation of motion can be rewritten as follows

$$K_{LM,b} m_b L \ddot{X} + F_{int,b} + \frac{8 N_{int,b}}{L} X = p_{r,b} L b_b \tag{IV.16}$$

with the equivalent internal force in the beam given by:

$$F_{int,b} = \begin{cases} k_b X & \text{for } X \le X_{el}, \\ \frac{8 M_{int,b}}{L} & \text{for } X_{el} > X, \end{cases} \tag{IV.17}$$

where $K_{LM,b} = 2/3$ is the load-mass factor, b_b is the blast-loaded width of the concrete slab above the beam and $X_{el} = 8M_{pl,b}/k_bL$ is the yield deflection of the beam.

Taking into account the effect of axial load on column stability, the SDOF model validated in [79] is used, with slight modification as follows:

$$K_{LM,c}m_cH\ddot{Y} + F_{int,c} - \frac{8N_{int,c}\left(X, \ddot{X}\right)}{H}Y = p_{r,c}Hb_c \tag{IV.18}$$

with the equivalent internal force in the column given by :

$$F_{int,c} = \begin{cases} k_cY & \text{for } Y \leq Y_{el}, \\ \frac{8M_{int,c}(N_{int,c})}{H} & \text{for } Y_{el} > Y, \end{cases} \tag{IV.19}$$

and the load-mass factor by:

$$K_{LM,c} = \begin{cases} 0.78 & \text{for } Y \leq Y_{el}, \\ \frac{2}{3} & \text{for } Y_{el} > Y, \end{cases} \tag{IV.20}$$

where $Y_{el} = 8M_{pl,c}/k_cH$ is the elastic deflection of the beam-column and b_c is the blast-loaded width of the column corresponding to its flange width.

Concerning the beam-colum, its axial force $N_{int,c}$ reads

$$N_{int,c} = -P + R_b \tag{IV.21}$$

with the vertical reaction of the beam given by

$$R_b = \frac{1}{2}\left(p_{r,b}Lb_b - \int_0^L m_b\ddot{w}_b dx\right) + N_{int,b}\theta \tag{IV.22}$$

which can be rewritten as follows

$$R_b = \frac{1}{2}\left(p_{r,b}Lb_b - \chi m_b L\ddot{X}\right) + 2N_{int,b}\frac{X}{L} \tag{IV.23}$$

where $\chi = 1/2$ when the plastic hinge is in the centre of the beam (Fig. IV.3-a) but could reach 1 when the plastic hinges are close to the supports in case of a beam under very large impulsive blast loading (Fig. IV.3-b).

The coupling of the column and beam models is ensured through the axial force $N_{int,c}$ appearing in Equ. (IV.18). The influence of the inertial forces of the beam in Equ. (IV.23) on the stability of the beam-column will be studied in next section.
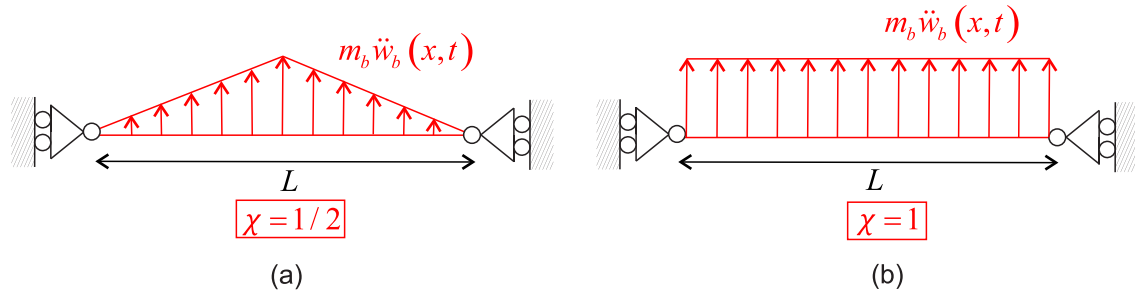
Figure IV.3: Inertial forces (a) when the plastic hinge is in the centre of the beam, (b) when the (traveling) plastic hinges are at the supports (for large impulsive blast loading).

IV.3   Analysis of the model

IV.3.1   Description of the two case studies

The beam and the columns of the frame illustrated in Fig. IV.1 are respectively made of IPE 270 and W150x24 profiles with a steel grade of 355 MPa and 470 MPa. The blast loaded width of the concrete slab b_b above the beam is equal to $3\,m$ while that of the column b_c is equal to $0.102\,m$. The other parameters are as follows $L = 5.4\,\mathrm{m}$, $H = 4\,\mathrm{m}$, $P = 500\,\mathrm{kN}$, $m_b = 2500\,\mathrm{kg/m}$ and $m_c = 24\,\mathrm{kg/m}$. The yield deflections X_{el} and Y_{el} of the beam and the column are respectively equal to $0.043\,\mathrm{m}$ and $0.062\,\mathrm{m}$.

Concerning the blast loading applied to the structural elements, the blast wave parameters depend on the scaled distance $Z = R/W^{1/3}$ where the variables R and W respectively refer to the distance from the centre of a spherical charge and the charge mass of equivalent TNT (see Section I.4.1.1). The range R is equal to H and $L/2$ for the beam and the column while the mass of the explosive charge is assumed to vary from 10 to 100 kg.

The peak reflected overpressures of the beam $p_{0,b}$ and the column $p_{0,c}$ are computed on the basis of Equ. (I.10). Assuming that the ratio of reflected to side-on impulse is equal to the ratio of their corresponding peak overpressures as in [130]

$$\frac{I_r}{I_s} \simeq \frac{p_{0,r}}{p_{0,s}} \tag{IV.24}$$

and that pressure-time histories are triangular, the positive phase duration of the reflected shock wave is equal to that of the incident shock wave:

$$t_{d,r} \simeq t_{d,s}. \tag{IV.25}$$

Thus, Equ. (I.8) can be used to determine the positive phase duration of the reflected blast loading although is only valid for side-on blast pressure.

By varying the mass of the explosive charge from 10 to 100 kg, the blast wave parameters of the beam-column can be expressed approximately in terms of those related to the beam as follows

$$p_{0,c} = 2.8p_{0,b} \quad ; \quad t_{d,c} = 0.4t_{d,b}. \tag{IV.26}$$

Two blast scenarii are detailed in Table IV.1. The dimensionless peak overpressures $\overline{p}$ is defined as the ratio of the peak overpressure to the static pressure that provokes the plastic mechanism of the structural member (without taking into account any axial load). Dimensionless positive phase duration is defined as the ratio of the positive phase duration to the characteristic period of the structural element (for the beam: $T_b = \sqrt{\frac{K_{LM,b}m_b L}{k_b}}$ and for the column $T_c = \sqrt{\frac{K_{LM,c}m_c H}{k_c}}$). The first case study corresponds to a quasi-static blast loading whereas the second case study refers to a dynamic blast loading.

	Beam		Column	
	$\overline{p}_b = \frac{p_{0,b}b_b L^2}{8M_{pl,b}}$	$\tau_{d,b} = \frac{t_{d,b}}{T_b}$	$\overline{p}_c = \frac{p_{0,c}b_c H^2}{8M_{pl,c}}$	$\tau_{d,c} = \frac{t_{d,c}}{T_c}$
Case study 1	1.5	100	0.15	240
Case study 2	10	1.5	0.98	3.6

Table IV.1: Case studies.

IV.3.2 Numerical results

In order to evaluate the accuracy of the analytical model of the frame under blast loading (Fig. IV.1), their corresponding results are compared with those of the FinelG model. The frame is modeled using the 2D Euler-Bernoulli beam elements incorporated in FinelG software (element type of 33 for plane frames) with a large number of finite elements (FE) (120 FE for the columns and 80 FE for the beam) to capture well the higher modes of vibration as well as some specific phenomena such as the eventual traveling of plastic hinge(s).

The axial gravity load is first applied at the top of the beam-columns; then the frame is subjected to a uniformly distributed transverse blast loading as illustrated in Figs. IV.1-a and -b. The initial displacement and velocity of the beam-columns and the beam are equal to 0. The dynamic analysis is carried out using the implicit time integration scheme of Newmark with constant acceleration parameters [87] and a small time step of integration $\Delta t = 0.15\,\text{ms}$ to provide accurate responses of the frame under dynamic regime.

IV.3.2.1 Case study 1

Figures IV.4-a and -b respectively illustrate the time histories of the mid-span deflection and bending moment-axial force interaction for the beam and the columns. A good agreement is achieved between the deflections predicted by the analytical and numerical models. The column remains in the elastic regime since its ductility is smaller than 1 while the beam experiences a ductility demand of 8. Bending moment-axial force (M-N) interaction curves

of the beam and column present good correlation between the numerical and analytical model although the multi-layer model of the beam overestimates the bending plastic resistance due to the approximation of the length of the central hinge in the plastic regime (see Section IV.2.2.2). Concerning the M-N interaction of the beam-column, the curves predicted by the analytical and numerical models remain inside the plastic interaction curve, confirming the absence of yielding in the column.
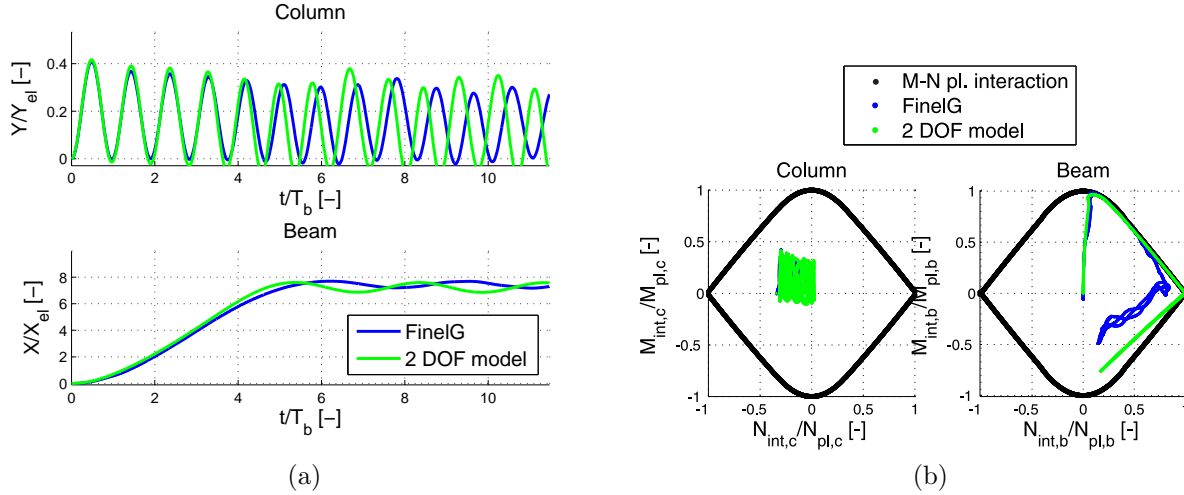
Figure IV.4: (a) Mid-span deflection vs. time, (b) bending moment-axial force interaction for the beam and the columns under quasi-static blast loading (case study 1).

Figure IV.5 depicts the values of ratios of internal force-to-plastic resistance of layers over the depth of the cross-section of the beam for different couples of axial force and bending moment. The web of the beam is divided into 10 layers (blue arrows) while the flanges into 4 layers (red arrows). The dashed black line indicates the ratio of the elongation of each spring to the maximum elongation of the spring (at the top of the cross-seciton) over the depth of the section.

At the beginning of the blast loading, the axial force in the beam is negligible ($N_{int,b}/N_{pl,b} \simeq 0.02$) and the bending moment is still below the plastic bending resistance $M_{pl,b}$. The distribution of internal forces in springs is linear, and no yield is observed in the cross-section. Then, the axial force increases to 0.1 while the bending moment approximately reaches the plastic bending resistance of the beam. A part of the cross-section is yielded while the central part remains elastic, which accounts for a bending moment that is slightly smaller than its associated plastic resistance ($M_{int,b}/M_{pl,b} = 0.97$). The axial force $N_{int,b}$ progressively rises while the mid-span deflection of the beam increases, involving a progressive diminution of the bending moment $M_{int,b}$ until the plastic axial resistance of the beam $N_{pl,b}$ is reached.
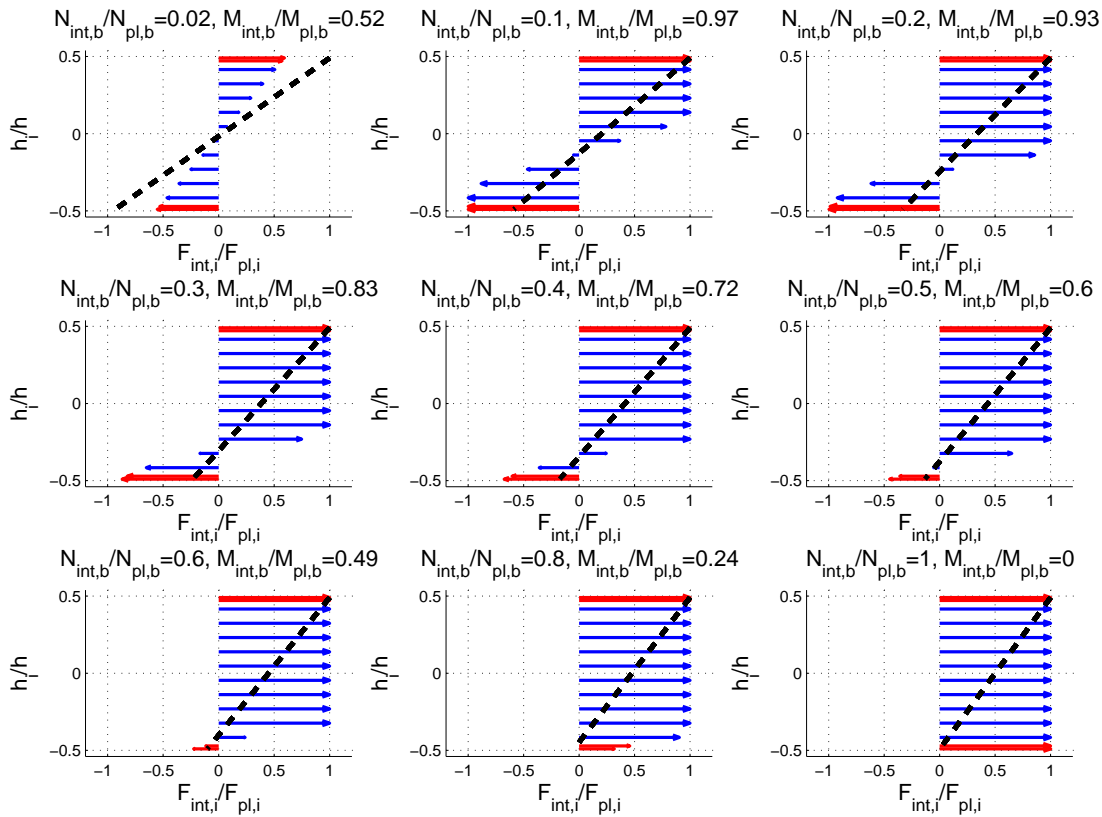
Figure IV.5: Ratios of internal force to plastic resistance of layers over the depth of the beam cross-section for different couples of axial force and bending moment (for case study 1).

Figures IV.6-a and b show the time evolution of the axial forces in the beam and the column. For the beam, a good correspondence is found between numerical and analytical curves although the axial force increases too quickly when the neutral axis get closer to the bottom flange and even reaches the plastic axial resistance (Fig. IV.6-a). It is likely due to the approximation made on the assessment of the length of hinge in the plastic regime.

Incorporating the output results predicted by the FinelG model into Equs. (IV.21) and (IV.22) and comparing them to the curve of axial force in the column predicted by numerical model results in a perfect agreement as illustrated in Fig. IV.6-b and serves as a validation of these equations. The difference between the curves of axial force predicted by the analytical and numerical models is related to the approximation of the resultant of inertial forces along the beam, as highlighted by the coefficient χ in Equ. (IV.23). For the analytical model, it is assumed that the deformed shape is bilinear since it corresponds to two straight rigid parts that are connected together with a plastic hinge in the central region, leading to a coefficient χ equal to $1/2$. However, this coefficient χ evolves during time depending on the distribution of inertial forces along the beam. It should be noticed that assuming a constant compressive load P is conservative for this case study.
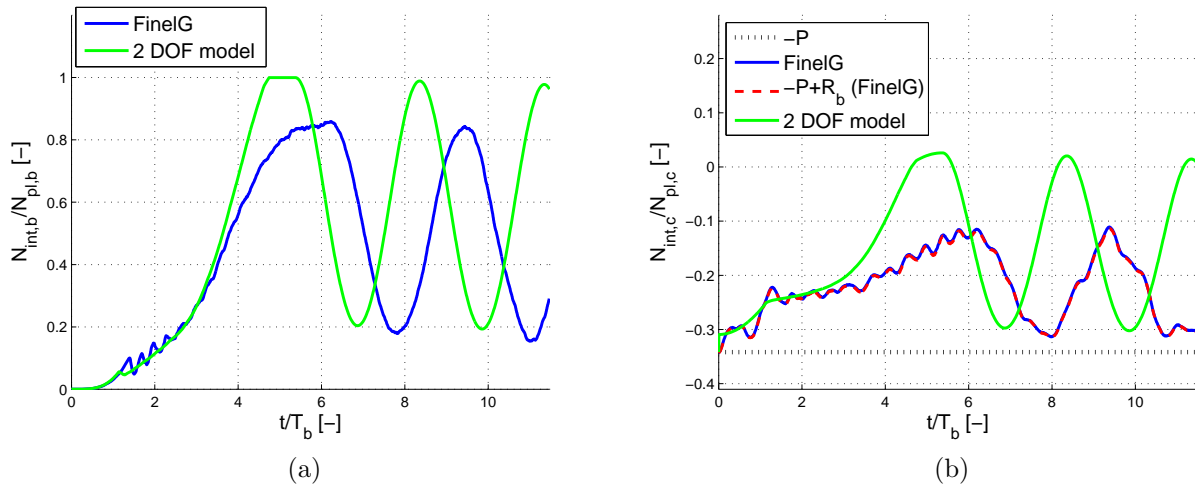
Figure IV.6: (a) Axial force in the beam vs. time, (b) Axial force in the column vs. time. (case study 1)

IV.3.2.2   Case study 2

Figures IV.7-a and -b illustrate the mid-span deflection and M-N plastic interaction of the beam and column. A good agreement is observed between the deflection curves of the beam predicted by the analytical and numerical models. The dynamic buckling of the beam-column, predicted by both analytical and numerical models, occurs after the end of blast loading because of the $P - \delta$ effect.

Figures IV.8-a and -b provide the axial force in the beam and the columns predicted by the 2-DOF analytical and FinelG models. As observed, a good correspondence is ensured between the time-histories of the axial force the beam predicted by the numerical and analytical models (Fig. IV.8-a). Equs. (IV.21) and (IV.22) are again validated in Fig. IV.8-b although the analytical model does not predict well the axial force in the column because of the approximation on the coefficient χ. The axial force in the column predicted by FinelG model goes beyond the initial compressive load P due to dead and live loads from upper stories (increase of compressive force of about 15 %). This latter observation emphasizes the importance to predict accurately the unloading phase of the beam or of the upper part of the structure since their corresponding inertial forces can compress further the columns. Further investigations should be paid to the prediction of the inertial forces around the blast-loaded compartment of the structure.

(a)   (b)
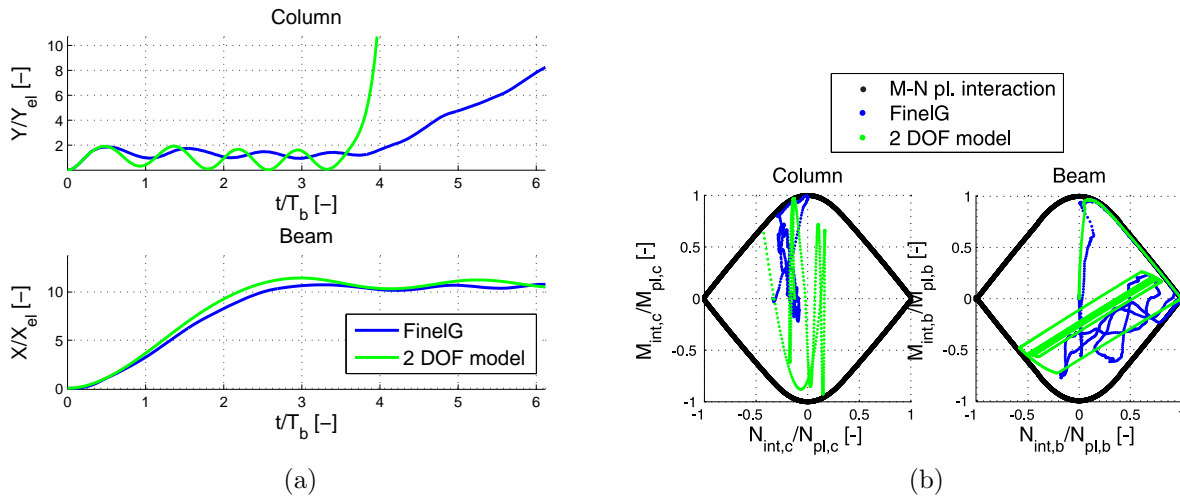
Figure IV.7: (a) Mid-span deflection vs. time, (b) bending moment-axial force interaction for the beam and the columns under quasi-static blast loading (case study 2).


(a)   (b)
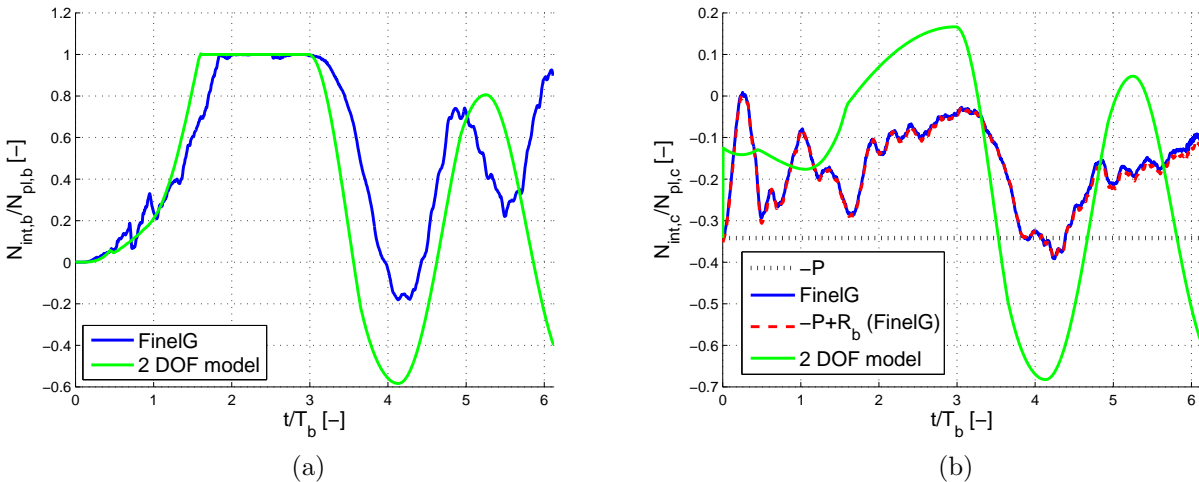
Figure IV.8: (a) Axial force in the beam vs. time, (b) Axial force in the column vs. time (case study 2).

IV.4   Conclusions and perspectives

The goal of this Chapter is to study the dynamic behaviour of a simple frame under blast loading using a 2-DOF model. A multi-layer model of the cross-section of the beam is used to derive the bending moment-axial force (M-N) plastic interaction instead of the Lescouarc'h formula and normality rule, because a significant part of the cross-section remains elastic when the membrane force and the curvature are respectively large and small. For the columns, the

Lescouarc'h formula for the M-N plastic interaction is applied. The coupling of the beam and the columns is ensured through the vertical reactions of the beam applied at the top of the columns. These reactions depend on the reflected blast overpressure applied to the beam, the vertical projection of the membrane force within the beam as well as the inertial force distribution of the beam. Two blast scenarii are involved in the studies, the first one corresponds to a quasi-static blast loading while the other refers to a dynamic blast loading. The reverberation effect due to re-reflections of shock waves inside the compartment and the gas pressure build up due to its eventual confinement are neglected for a sake of simplicity, but they can be easily introduced in the model for the future.

The first case study shows that a very good agreement is observed between the results predicted by the analytical and numerical models. In both models, the columns remain stable after the blast event while the beam experiences large deflection leading to the plastic axial resistance of the beam. However, a discrepancy is observed in the time-histories of axial force predicted by the analytical and numerical models because the inertial force distribution shape is not well captured by the analytical model. Indeed, the analytical model assumes that its shape is bi-linear while it is actually time-dependent.

The second case study illustrates that, in both models, the columns are predicted to fail by buckling due to the $P - \delta$ effect. Those column failures are caused by the acceleration of the beam in downward direction during the unloading regime, which further compresses the columns as compared to the initial compressive load (due dead and live loads from upper stories). According to numerical results, the axial force in the column can exceed by 15 % the initial compressive load. Nevertheless, the inertial force distribution shapes is again not well predicted by the analytical model, highlighting that a last improvement should be provided in that part of the analytical model.

Chapter V

Conclusions

V.1 General conclusions

V.1.1 Objective and assumptions

The purpose of this thesis was to develop analytical models to predict the dynamic behaviour of structures under internal blast loading but the proposed rapid assessment tools are readily applicable for moment resisting frames subjected to external blast loading. The type of the structure considered in the investigations was a skeleton frame made of beams and columns which did not include slabs nor walls. The blast-loaded compartment of the structure was extracted from the whole structure using some condensation techniques to simulate the influence of the indirectly affected part (IAP) of the structure (i.e. the part of the structure surrounding the loaded compartment) by equivalent elastic springs and masses. The out-of-plane instabilities of the structural elements were supposed to be prevented as well as local buckling and the effects of the strain rate and shear force on the plastic interaction curve were neglected in the developments.

Concerning the blast loading, it was assumed that the blast pressure is uniformly distributed along each structural member although actually, it depends on the distance from the explosion centre. The type of explosion could be a deflagration due to gas combustion or detonation due to chemical reaction throughout explosive charge such as TNT, which involves different shapes of pressure-time history. The models developed in this thesis can be applied for both types of explosion although they had been only formalized for the detonation without taking into account the level of confinement provided by the structure.

For the sake of simplicity in the analysis, the structural elements were firstly studied separately to highlight the effect of the lateral restraint of the surrounding structure on the dynamic behaviour of these elements (the vertical and rotational restraints were disregarded in this thesis). In a second step, the dynamic interaction between the beam and the adjacent columns was investigated through the study of the dynamic behavior of a simple braced frame under internal blast loading.

V.1.2 Conclusions for the beam under blast loading

The considered problem was that of a frame beam subjected to blast loading considering the interaction with the indirectly affected part (IAP) of the structure, and assuming a linear elastic behavior of the IAP and stable adjacent columns. We developed simple analytical tools able to predict the p-I diagram of a beam extracted from an arbitrary structure taking into account the nonlinear membrane force, the M-N plastic interaction and the lateral inertia and restraint provided by the rest of the structure. The material law of the beam was assumed elastic-perfectly plastic, and did not account for strain hardening nor strain rate effects.

Two analytical models were developed. The first model is based on a single-degree-of-freedom which is the transverse mid-span deflection and assumes that the axial elongation of the beam is negligible (SDOF model) in contrast with the second (2-DOF model). It was shown that disregarding the axial deformability of the beam could be unconservative when the stiffness of the lateral restraint is important since the non-linear rigidity provided by

the structure to the beam is overestimated. Nevertheless, it could be conservative when the lateral mass and restraint respectively become significant and negligible.

As a result of the dimensional analysis, five main dimensionless structural parameters affecting the required ductility of the frame beam were identified. Two parameters ψ_K and ψ_M are related to the behavior of the indirectly affected part (the lateral restraint and mass). Another one ξ is related to the mechanical properties of the investigated beam (i.e. its bending and axial resistances). Parameter θ_y is related to the geometry of the problem (i.e. the yield rotation of the beam at its extremities). At last, parameter λ_r corresponding to the rotational inertia effect is shown to be negligible for steel beams that exhibit a span-to-depth ratio between 10 and 30. A comprehensive analysis and validation of the models was therefore performed with regard to ψ_K and ψ_M.

Parameters ψ_K and ψ_M represent the favorable effect of the elastic indirectly affected part of the structure to limit the required ductility of the frame beam. The effect of lateral mass is negligible in case of a ratio ψ_M smaller or equal to 5. If the beam span-to-depth ratio is increased ($\xi \downarrow$ and $\theta_y \uparrow$), the energy dissipated in the plastic hinges is reduced. Thus, the lateral mass and restraint contribute further to absorb the energy generated by the blast loading and as a result, they reduce the demand of ductility.

In order to carry out the validation of the analytical 2-DOF model, the results predicted by the analytical models were compared to those predicted by FEM simulations using FinelG. Parameters ψ_K and ψ_M are respectively varied from 0 to 1 and 0 to 20 while the blast loading is considered as quasi-static, dynamic or impulsive. It is shown that a very good agreement is achieved between the results predicted by the analytical and simplified FinelG models. However, for dynamic or impulsive blast loadings, the phenomenon of traveling plastic hinges and horizontal and rotational inertial forces significantly affect the behaviour of the blast-loaded beam (maximum relative error of 14 %). Neglecting them is however conservative.

Finally, the proposed 2-DOF model is a simplified tool that enables to quickly assess the level of damage of a blast loaded beam extracted from a structure and to study the effect of structural parameters on blast resistant design. The tool is less time consuming than FinelG since it provides the overall p-I diagram in about 10 minutes while FinelG requires approximately 100 times more time to establish it.

V.1.3   Conclusions for the beam-column under blast loading

A 2-DOF model was developed to capture the dynamic response of the beam-column under axial compressive load and blast loading, which interacts with the surrounding structure. The model accounts for large displacement ($P - \delta$ effect), bending moment-axial force (M-N) plastic interaction as well as its interaction with the indirectly affected part (IAP) of the structure. The IAP of the structure is simplified into an elastic lateral spring $K^\star$ and a mass $M^\star$ which are connected at the top of the beam-column, while authorizing a possible lateral motion at its head.

In addition to the development of the 2-DOF model, two SDOF models were also derived for particular cases (for free-fixed and pinned-fixed beam-columns) as well as their asymptotic

impulsive and quasi-static solutions.

The dimensional analysis of the problem revealed that, under the considered assumptions, four dimensionless parameters mainly influence the dynamic stability of the beam-column. Two of them are related to the behavior of the indirectly affected part (the lateral restraint χ_K and mass χ_M). Another one is related to the critical load multiplier α_{cr} (i.e. the ratio of the axial compressive load to Euler elastic buckling resistance). The last parameter is the reduced slenderness $\bar{\lambda}$ of the beam-column.

To validate the analytical models, full non-linear dynamic simulations of 2D FEM model of columns were performed with FinelG, accounting for large displacement and a plastic kinematic constitutive model to capture the M-N plastic interaction.

Considering the constitutive material as indefinitely elastic, a very good agreement was achieved between the results predicted by the analytical and numerical models. However, some discrepancies were found between the results predicted by the FinelG and SDOF models of the free-fixed beam-column under blast loading mainly for two reasons: the Euler elastic buckling axial load is overestimated by the SDOF model leading to a mitigation of the $P - \delta$ effect and this simplified model does not account for the second mode of vibration which governs the dynamic response of the beam-column when the lateral mass at its top is non-negligible.

When the material is elastic-perfectly plastic, both the 1-DOF and 2-DOF analytical models were able to accurately predict the response of the pinned-fixed beam-column and to capture its potential dynamic buckling.

For the free-fixed beam-column, a perfect agreement was also achieved between the predictions of the 2-DOF and FinelG models when the lateral mass is negligible. However, when the lateral mass is significant, the maximum displacement might be overestimated because of the application of the Δ_0 technique a great number of times. Concerning the predictions of SDOF model, a substantial discrepancy was found between them and those of the FinelG model because of the two aforementioned reasons when the material is indefinitely elastic.

For intermediate values of the stiffness of the lateral restraint and the lateral mass, a very good match was found between the analytical and numerical results in some cases, but some improvements should be provided to the analytical model for other structural configurations.

The parametric study was performed by establishing the pressure-impulse (p-I) diagram of the beam-column which indicates, with a simple reading, the eventual buckling of that structural member according to a damage criterion. The inverse of the ultimate multiplier α_u was chosen as the damage parameter since it enables to includes both types of axial failures: cross-section axial yielding and elastic axial buckling of the beam-column. As expected, the higher the axial load applied at the top of the beam-column (or the parameter α_u) was, the smaller the pressure and the impulse to provoke the dynamic buckling of the beam-column were. As stated earlier, some improvements should be provided to the analytical model for $(\chi_K; \chi_M) = (5; 0)$ and $(\chi_K; \chi_M) = (0; 5)$.

V.1.4 Conclusions for the simple frame under blast loading

The dynamic behaviour of a simple frame under blast loading was studied with a 2-DOF model. A multi-layer model of the cross-section of the beam was used to derive the bending moment-axial force (M-N) plastic interaction. Coupling of the beam and of the columns is ensured through the vertical reactions of the beam applied at the top of the columns. These reactions depend on the reflected blast overpressure applied to the beam, the vertical projection of the membrane force within the beam as well as the inertial force distribution of the beam.

Two blast scenarios were involved in the studies, the first one corresponds to a quasi-static blast loading while the other refers to a dynamic blast loading. The analytical model predicted quite accurately the time evolution of the deflection curves of the structural elements, and even assessed the eventual buckling of the beam-columns as the FinelG model. For the second blast scenario, it was shown numerically that the axial force in the column could even exceed by 15 % the initial compressive load due to the unloading phase of the beam, highlighting the necessity to study the dynamic interaction between the structural members. However, the time history of the normal force in the column was not well captured by the analytical model because it is assumed that the inertial force distribution is time-independent. A last improvement should be provided to that part of the analytical model.

V.2 Perspectives

In view of improving the proposed simplified models, further investigations could be contemplated

- The IAP of the structure can be reduced to equivalent springs and masses using condensation techniques. However, the behaviour of the IAP of the structure may be non linear; indeed, plastic hinges can appear progressively in the IAP of the structure, inducing a reduction of its stiffness. Some structural elements in the IAP of the structure may also buckle as well as their web or flange through local instability. The capacity of deformation of the IAP of the structure remains also unknown. A first short-term step could be to consider an elastic-perfectly plastic behaviour of these springs but further effort should be dedicated to the characterization of the IAP in its actual non-linear state in a long-term perspective.

- The pulse shape of the blast loading was assumed to be triangular, neglecting any re-reflections of the shock waves inside the compartment as well as the build-up of quasi-static pressure due to gas expansion. However, the analytical developments remain valid for other pulse shapes (even an external blast loading applied to a moment resisting frame) and could be incorporated in the future.

- Concerning the beam under blast loading, the current analytical models can be improved as follows

- – Richer kinematic displacement fields for the beam should be used to derive a better prediction of the dynamic behaviour of the beam in the elastic regime. It is important to estimate accurately the response of the beam in this regime in case of negligible stiffness of the lateral restraint and the lateral mass.

- – In case of impulsive blast loading, the effects of traveling plastic hinges and horizontal and rotational inertial force distributions could be substantial. They can be considered in the model by defining new variables such as the location of the plastic hinges. However, the analytical developments become more complex and neglecting these effects on the beam is conservative in any circumstance (for the beam).

- – In this thesis, only the lateral restraint and mass were taken into account in the modelling of the beam under blast loading. However, the vertical and rotational elastic-perfectly plastic springs and masses of the IAP of the structure should be incorporated in the future in the analytical model.

○ Concerning the beam-column under blast loading, the current analytical models can be improved as follows

- – Some effort should be dedicated to understand and eventually correct the 2-DOF model for the results predicted for these couples of parameters: $(\chi_K; \chi_M) = (5; 0)$ and $(\chi_K; \chi_M) = (0; 5)$.

- – The horizontal, vertical and rotational elastic-perfectly plastic springs and masses of the IAP of the structure should be introduced in the analytical model. The procedure to take into account the horizontal and vertical restraints and masses has already been described in Section III.8.

○ Concerning the compartment under blast loading, the current analytical models can be improved as follows

- – The actual inertial force distribution shape of the beam which is time-dependent should be implemented in order to better assess the normal force in the beam-columns and to better predict the eventual dynamic buckling of those last ones under lateral blast loading.

- – The final aim of this research is to develop a rapid assessment tool which combines the dynamic behaviour of the beam-columns with the beam taking into account the condensed IAP of the structure. This easy-to-apply tool would be the lowest-order model to predict the partial damage or collapse of the frame structures in which one compartment is under blast loading.

○ The Lescouarc'h M-N plastic interaction equation (I.48) does not take into account the presence of fillet radius for I-shaped cross-section of a beam. One way to deal with this issue is to approximate the actual plastic interaction curve by an approximated function (II.6) where α is determined by minimizing the global error using the least mean square method.

○ Since the ratio of the shear to its associated plastic resistance may be greater than 0.5 for the beam and the column, the bending moment-axial and shear force (M-N-V) plastic interaction must be considered. Moreover, a new DOF should be incorporated to the kinematics of the simplified model, additional to the rotation θ and axial elongation Δ_N of the plastic hinge, which is the shear angle γ_v. As a consequence, new shape functions should be defined and the generalized strain rate vector must be expressed as normal to a three-dimensional yield surface and not to a yield curve anymore.

○ The effects of the strain rate on the yield strength and the ductility capacity of the structural elements were neglected in the developments but they should also be considered in the future.

V.3 Personal contributions

Our personal contributions to the present investigations are listed here below:

○ Development of a SDOF model to predict the dynamic behaviour of the beam under blast loading, assuming that the axial deformation of the beam is negligible and taking into account the presence of lateral restraint and mass of the IAP of the structure, the development of non-linear membrane force and the bending-tension (M-N) plastic interaction (see Section II.2). Procedure to substitute the IAP of the structure by an equivalent lateral mass and restraint at one end of the beam (Section II.2.1.2). Dimensionless analysis to identify the structural parameters that affect the response of the beam (Section II.2.1.6). Establishment of the asymptotic quasi-static and impulsive solutions of the non-linear SDOF model (Section II.2.2);

○ Development of a 2-DOF model to predict more accurately the behaviour of the beam under blast loading, accounting for another degree of freedom to the SDOF model which is the axial deformation of the beam (Section II.3.1.1). Dimensionless parametric study to assess the validity domain of the SDOF model (Sections II.3.2);

○ Numerical validation of the 2-DOF model of the beam through comparison with results predicted by FinelG, analyses and interpretations of the results. Numerical quantification of the effect of the traveling plastic hinges along the beam on the ductility demand of that structural member (Section II.4);

○ Development of a 2-DOF model to predict the stability of the beam-column under axial compressive load and blast loading, which interacts with the surrounding structure. The model accounts for large displacement ($P-\delta$ effect), bending moment-axial force (M-N) plastic interaction as well as its interaction with the indirectly affected part (IAP) of the structure (Section IV.2). Dimensionless analysis to identify the structural parameters that affect the stability of the beam-column under blast loading (Section III.2.7).

○ Establishment of an analytical formula to compute the effect of the column length for a beam-column with a lateral restraint at its top by performing a linear buckling analysis [117] (Section III.2.6);

○ Development of SDOF models for free-fixed and pinned-fixed beam-columns under compressive load and lateral blast loading (Section III.3). Development of the analytical asymptotic solutions for these specific beam-columns using the general approach recently developed in [73] (Section III.4);

○ Numerical validation of the analytical models of the beam-column through comparison with results predicted by FinelG, analyses and interpretations of the results (Section III.5);

○ Numerical validation of the UFC approach (modified by Nassr *et al.* [79]) through comparison with results predicted by FinelG and finding of another limitation of that method (Section III.5.3.1);

○ Definition of a new damage index to derive the p-I diagram for steel beam-columns under blast loading based on the buckling plastic resistance (Section III.6);

○ Procedure to develop a 3-DOF model for beam-column which presents additional vertical restraints and masses at its top as compared to the developed 2-DOF model (Section III.8);

○ Coupling of existing models of independent structural members to finally have a tool that enables to assess the level of damage of a simple frame under internal blast loading in which the members interact with each other (Section IV.2).

Chapter VI

Appendix

VI.1 Effect of the elastic contribution of the deflection on the strain energy stored in the lateral restraint

Figure VI.1: Scheme of transverse deflection shapes for 3 stages: elastic regime without plastic hinge (stage 1). plastic hinges at the end of the beam (stage 2) and full plastic mechanism (stage 3).

Neglecting the axial deformation of the beam, the elongation of the lateral restraint reads [61]:

$$\delta = \frac{1}{2} \int_0^{2l} \left(\frac{\partial w_b}{\partial x} \right)^2 dx \tag{VI.1}$$

where $w_b(x,t)$ is the transverse deflection of the beam and x is the abscissa along the beam (Figure VI.1).

By changing the variable x into $\overline{x} = x/2l$, the integral (VI.1) becomes

$$\delta = \frac{1}{4l} \int_0^1 \left(\frac{\partial w_b}{\partial \overline{x}} \right)^2 d\overline{x}. \tag{VI.2}$$

Consider the following transverse deflection field for the first stage, before the appearance of the first plastic hinges,

$$w_b(\overline{x}, t) = 16X \left(\overline{x}^2 (\overline{x} - 1)^2 \right) \tag{VI.3}$$

where $0 \leq \overline{x} \leq 1$ and $w_b(\overline{x} = 1/2) = X$.

Differentiating (VI.3) with respect to $\overline{x}$ gives

$$\frac{\partial w_b}{\partial \overline{x}} = 32X \left(\overline{x}(\overline{x} - 1)(2\overline{x} - 1) \right). \tag{VI.4}$$

The lateral displacement for the first stage is

$$\delta = \frac{1}{4l} \int_0^1 \left(\frac{\partial w_b}{\partial \overline{x}} \right)^2 d\overline{x} = 1.22 \frac{X^2}{l}. \tag{VI.5}$$

The second stage starts with the formation of plastic hinges at the ends of the beam, and completes when the plastic mechanism is fully developed $(X_e \leq X \leq X_y)$. The transverse deflection is described by

$$w_b(\overline{x}, t) = 16X_e\left(\overline{x}^2(\overline{x} - 1)^2\right) + \frac{16}{5}(X - X_e)\left(\overline{x}^4 - 2\overline{x}^3 + \overline{x}\right) \tag{VI.6}$$

which can also be written as

$$w_b(\overline{x}, t) = 6X_y\left(\overline{x}^2(\overline{x} - 1)^2\right) + \frac{16}{5}\left(X - \frac{3}{8}X_y\right)\left(\overline{x}^4 - 2\overline{x}^3 + \overline{x}\right) \tag{VI.7}$$

where $0 \leq \overline{x} \leq 1$ and $X_e = \frac{3}{8}X_y$ correspond to the mid-span deflection when the first two plastic hinges appear at the ends of the beam. Differentiating (VI.7) with respect to $\overline{x}$ gives

$$\frac{\partial w_b}{\partial \overline{x}} = 12X_y\left(\overline{x}(\overline{x} - 1)(2\overline{x} - 1)\right) + \frac{16}{5}\left(X - \frac{3}{8}X_y\right)\left(4\overline{x}^3 - 6\overline{x}^2 + 1\right). \tag{VI.8}$$

The lateral displacement for the second stage becomes

$$\delta = \frac{1}{4l}\int_0^1\left(\frac{\partial w_b}{\partial \overline{x}}\right)^2 d\overline{x} = \left(0.0377\frac{X_y^2}{X^2} - 0.1097\frac{X_y}{X} + 1.243\right)\frac{X^2}{l}. \tag{VI.9}$$

The third stage refers to the full formation of the plastic mechanism $(X \geq X_y)$, and the transverse deflection of the beam reads

$$w_b(\overline{x}, t) = 6X_y\left(\overline{x}^2(\overline{x} - 1)^2\right) + \frac{16}{5}\left(X_y - \frac{3}{8}X_y\right)\left(\overline{x}^4 - 2\overline{x}^3 + \overline{x}\right) + 2(X - X_y)\overline{x} \tag{VI.10}$$

where $0 \leq \overline{x} \leq 1/2$.

Differentiating (VI.7) with respect to $\overline{x}$ gives

$$\frac{\partial w_b}{\partial \overline{x}} = 12X_y\left(\overline{x}(\overline{x} - 1)(2\overline{x} - 1)\right) + 2X_y\left(4\overline{x}^3 - 6\overline{x}^2 + 1\right) + 2(X - X_y). \tag{VI.11}$$

The lateral displacement for the third stage is

$$\delta = \frac{1}{2l}\int_0^{1/2}\left(\frac{\partial w_b}{\partial \overline{x}}\right)^2 d\overline{x} = 0.171\frac{X_y^2}{l} + \frac{X^2}{l}. \tag{VI.12}$$

Substituting (VI.12) into (II.17) leads to

$$U_3 = \int_0^\delta K^\star\Delta\, d\Delta = \int_0^X K^\star\left(0.171\frac{X_y^2}{l} + \frac{\mathcal{X}^2}{l}\right)\frac{2\mathcal{X}}{\ell}\, d\mathcal{X} = 0.171K^\star\frac{X_y^2 X^2}{l^2} + \frac{1}{2}K^\star X^2\frac{X^2}{\ell^2}. \tag{VI.13}$$

where U_3 is the strain energy stored in the spring.

The dimensionless equation of motion becomes

$$\left(1 + \psi_M \theta_y^2 \overline{X}^2 + \lambda_r^2\right) \overline{X}'' + \psi_M \theta_y^2 \overline{XX}'^2 + \overline{F}_{int,b}\left(\overline{X}, \overline{X}', \overline{X}''\right) + 0.342\psi_K \theta_y^2 \overline{X} + 2\psi_K \theta_y^2 \overline{X}^3 = \overline{p}\left(1 - \frac{\tau}{\tau_d}\right)$$
(VI.14)

There is an additional term $0.342\psi_K \theta_y^2 \overline{X}$ in comparison with (II.27) that takes a maximum value of $1/100$ for $\overline{X} = 20$, $\psi_K = 3$ and $\theta_y = 22/1000$ rad, which is negligible since the order of magnitude of $\overline{p}$ and other terms is the unity.

VI.2 Effect of the elastic contribution of the deflection on the kinetic energies

The kinetic energy due to rotational motion of the beam is given by

$$K_R = \frac{1}{2} \int\limits_0^L I_{rot,b} \left(\frac{\partial^2 w_b}{\partial t \partial x}\right)^2 dx = \frac{I_r}{L} \int\limits_0^{1/2} \left(\frac{\partial^2 w_b}{\partial t \partial \overline{x}}\right)^2 d\overline{x}.$$
(VI.15)

For the three stages of motion, the angular velocity of the beam is described by

$$\frac{\partial^2 w_b}{\partial t \partial \overline{x}} = \begin{cases} 32\dot{X}\left(\overline{x}\left(\overline{x} - 1\right)\left(2\overline{x} - 1\right)\right), & 0 \leq X \leq X_e \\ \frac{16}{5}\dot{X}\left(4\overline{x}^3 - 6\overline{x}^2 + 1\right), & X_e < X \leq X_y \\ 2\dot{X}, & X_y < X. \end{cases}$$
(VI.16)

Therefore, the rotational kinetic energy at three different stages reads

$$K_R = \begin{cases} \frac{1}{2}\left(2.438\frac{I_{rot,b}}{l}\right)\dot{X}^2, & 0 \leq X \leq X_e \\ \frac{1}{2}\left(2.487\frac{I_{rot,b}}{l}\right)\dot{X}^2, & X_e < X \leq X_y \\ \frac{1}{2}\left(2\frac{I_{rot,b}}{l}\right)\dot{X}^2, & X_y < X. \end{cases}$$
(VI.17)

Moreover, the velocity of the lateral mass is given by:

$$\dot{\delta} = \begin{cases} 2.44\frac{X\dot{X}}{l}, & 0 \leq X \leq X_e \\ \left(-0.11X_y + 2.48X\right)\frac{\dot{X}}{l}, & X_e < X \leq X_y \\ 2\frac{X\dot{X}}{l}, & X_y < X. \end{cases}$$
(VI.18)

Thus, the kinetic energy of the lateral mass is given by :

$$K_{M^\star} = \begin{cases} \frac{1}{2}M^*\left(5.95\frac{X^2}{l^2}\right)\dot{X}^2, & 0 \leq X \leq X_e \\ \frac{1}{2}\left(0.012\frac{X_y^2}{l^2} - 0.546\frac{XX_y}{l^2} + 6.15\frac{X^2}{l^2}\right)\dot{X}^2, & X_e < X \leq X_y \\ \frac{1}{2}\left(4\frac{X^2}{l^2}\right)\dot{X}^2, & X_y < X. \end{cases}$$
(VI.19)

The velocity $\dot{X}$, at the beginning of each stage of motion, can be determined from the velocity field of the preceding phase, using the Symonds minimum Δ_0 technique [90].

VI.3 Mass, stiffness, resistance and loading matrices of the column, defined as a function of the plastic hinge location $\bar{z}_m$

Regime	I	II	III
$\mathbf{M}_{\Gamma_i}$	$m_c H \begin{bmatrix} \frac{130555}{290304} & \frac{2627}{10368} \\ \frac{2627}{10368} & \frac{104}{405}+\chi_M \end{bmatrix}$	$m_c H \begin{bmatrix} \frac{31}{630} & \frac{1}{10} \\ \frac{1}{10} & \frac{1}{3}+\chi_M \end{bmatrix}$	$m_c H \begin{bmatrix} \frac{1}{3} & \frac{(1+\bar{z}_m)}{6} \\ \frac{(1+\bar{z}_m)}{6} & \frac{1}{3}+\chi_M \end{bmatrix}$
$\mathbf{K}_{\Gamma_i}$	$\frac{EI_c}{H^3} \begin{bmatrix} \frac{6845}{64} & \frac{37}{8} \\ \frac{37}{8} & \frac{16}{5}+\chi_K \end{bmatrix}$	$\frac{EI_c}{H^3} \begin{bmatrix} \frac{48}{10} & 0 \\ 0 & \chi_K \end{bmatrix}$	$\frac{EI_c}{H^3} \begin{bmatrix} 0 & 0 \\ 0 & \chi_K \end{bmatrix}$
$\mathbf{K}_{P,\Gamma_i}$	$\frac{P}{H} \begin{bmatrix} \frac{6845}{1344} & -\frac{185}{336} \\ -\frac{185}{336} & \frac{8}{7} \end{bmatrix}$	$\frac{P}{H} \begin{bmatrix} \frac{34}{70} & 0 \\ 0 & 1 \end{bmatrix}$	$\frac{P}{H} \begin{bmatrix} (1-\bar{z}_m)\bar{z}_m & 0 \\ 0 & 1 \end{bmatrix}$
$\mathbf{pr}_i$	$pH \begin{bmatrix} \frac{37}{64} \\ \frac{2}{5} \end{bmatrix}$	$pH \begin{bmatrix} \frac{1}{5} \\ \frac{1}{2} \end{bmatrix}$	$pH \begin{bmatrix} \frac{1}{2} \\ \frac{1}{2} \end{bmatrix}$

Regime	IV
$\mathbf{M}_{\Gamma_i}$	$m_c H \begin{bmatrix} \frac{1}{405}\left(135-31\bar{z}_m\right) & \frac{180+(45-17\bar{z}_m)\bar{z}_m}{810\bar{z}_m} \\ \frac{180+(45-17\bar{z}_m)\bar{z}_m}{810\bar{z}_m} & \frac{-(-240+\bar{z}_m(180+(-45+\bar{z}_m)\bar{z}_m))}{405\bar{z}_m^2}+\chi_M\frac{(-4+\bar{z}_m)^2}{9\bar{z}_m^2} \end{bmatrix}$
$\mathbf{K}_{\Gamma_i}$	$\frac{EI}{H^3} \begin{bmatrix} \frac{16}{5\bar{z}_m^3} & \frac{16}{5\bar{z}_m^3} \\ \frac{16}{5\bar{z}_m^3} & \frac{16}{5\bar{z}_m^3}+\chi_K\left(1+4\frac{(1-\bar{z}_m)}{(3\bar{z}_m)}\right)^2 \end{bmatrix}$
$\mathbf{K}_{P,\Gamma_i}$	$\frac{P}{H} \begin{bmatrix} \frac{(-8+\bar{z}_m)}{(7(-1+\bar{z}_m)\bar{z}_m)} & -\frac{4}{21\bar{z}_m} \\ -\frac{4}{21\bar{z}_m} & \frac{-8(-14+5\bar{z}_m)}{63\bar{z}_m^2} \end{bmatrix}$
$\mathbf{pr}_i$	$pH \begin{bmatrix} \frac{1}{10}\left(5-\bar{z}_m\right) \\ \frac{10-5\bar{z}_m+\bar{z}_m^2}{15\bar{z}_m} \end{bmatrix}$

Table VI.1: Mass matrix, first- and second-order stiffness matrices and blast loading vectors of the structure for different regimes.

Regime I

$$\mathbf{r}_{\Gamma_i}=\begin{bmatrix}0\\0\end{bmatrix}$$

$$\mathcal{H}_{A,\Gamma_i}=\begin{bmatrix}0&0&\frac{111}{8}&0&0&0&\frac{37\left(20+\bar z_m(-25+8\bar z_m)\right)}{24\bar z_m}\\[4pt]0&0&-\frac{12}{5}&\chi_K&0&\chi_K&\frac{8\left(10+(-5+\bar z_m)\bar z_m\right)}{15\bar z_m}+\chi_K\left(\frac{4-\bar z_m}{3\bar z_m}\right)\end{bmatrix}$$

$$\mathcal{H}_{B,\Gamma_i}=\begin{bmatrix}0&0&\frac{481}{336}&0&185\left(\frac{\bar z_m}{16}-\frac{\bar z_m^2}{24}\right)&0&\frac{37\bar z_m\left(189+\bar z_m(-175+31\bar z_m)\right)}{504}&-\frac{37\bar z_m\left(42+\bar z_m(-35+8\bar z_m)\right)}{1008}\\[4pt]0&0&-\frac{5}{21}&1&-1+\bar z_m-\frac{\bar z_m^2}{3}&1&-\frac{\left(315+\bar z_m(-441-31(-7+\bar z_m)\bar z_m)\right)}{315}&-\frac{4\left(-105+\bar z_m^2(21+(-7+\bar z_m)\bar z_m)\right)}{315\bar z_m}\end{bmatrix}$$

Regime II

$$\mathbf{r}_{\Gamma_i}=\mathrm{sign}\left(\dot\theta_{end,II}\right)\frac{M_{pl,red}}{H}\begin{bmatrix}1\\1\end{bmatrix}$$

$$\mathcal{H}_{A,\Gamma_i}=\begin{bmatrix}\frac{11}{8}&-\frac{12}{5}&\frac{4}{5}\left(-5+2\bar z_m\right)&\frac{4}{5}\left(-5+2\bar z_m\right)\\[4pt]0&\chi_K&0&\left(\frac{4-\bar z_m}{3\bar z_m}\right)\chi_K\end{bmatrix}$$

$$\mathcal{H}_{B,\Gamma_i}=\begin{bmatrix}\frac{481}{336}&-\frac{5}{21}&\left(1+\bar z_m-\bar z_m^2\right)&\frac{1}{105}\left(105+\bar z_m(-161+31\bar z_m)\right)&-\frac{1}{105}\left(35-14\bar z_m^2+4\bar z_m^3\right)\frac{4-\bar z_m}{3\bar z_m}\\[4pt]0&1&0&0&0\end{bmatrix}$$

Regime III

$$\mathbf{r}_{\Gamma_i}=\frac{M_{pl,red}}{H}\left\{\mathrm{sign}\left(\dot\theta_{end,III}\right)\begin{bmatrix}\frac{1}{\bar z_m}\\1\end{bmatrix}+\mathrm{sign}\left(\dot\theta_{mid,III}\right)\begin{bmatrix}\bar z_m(1-\bar z_m)\\0\end{bmatrix}\right\}$$

$$\mathcal{H}_{A,\Gamma_i}=\begin{bmatrix}0&0&0&0&0\\0&0&0&0&0\\0&\chi_K&0&\chi_K&\frac{4-\bar z_m}{3\bar z_m}\chi_K\end{bmatrix}$$

$$\mathcal{H}_{B,\Gamma_i}=\begin{bmatrix}\frac{185}{48}\bar z_m(3-2\bar z_m)&\frac{1}{3}\left(-\bar z_m^2+3\bar z_m-3\right)&\left(-\bar z_m^2+3\bar z_m-3\right)&0&0&0&-\frac{1}{3\bar z_m}\\[4pt]0&-(-1+\bar z_m)\bar z_m&0&0&1&0&0\\0&1&0&&&&\frac{4-\bar z_m}{3\bar z_m}\end{bmatrix}$$

Regime IV

$$\mathbf{r}_{\Gamma_i}=\mathrm{sign}\left(\dot\theta_{mid,IV}\right)\frac{M_{pl,red}}{H}\begin{bmatrix}\frac{(4-\bar z_m)}{(3\bar z_m-3\bar z_m^2)}\\0\end{bmatrix}$$

$$\mathcal{H}_{A,\Gamma_i}=\begin{bmatrix}\frac{37\left(20+\bar z_m(-25+8\bar z_m)\right)}{24\bar z_m}&\frac{8\left(10+(-5+\bar z_m)\bar z_m\right)}{15\bar z_m}&\frac{4}{5}\left(-5+2\bar z_m\right)&0&0&0&0\\[4pt]\frac{37\left(20+\bar z_m(-25+8\bar z_m)\right)}{24\bar z_m}&\frac{8\left(10+(-5+\bar z_m)\bar z_m\right)}{15\bar z_m}+\chi_K\frac{(4-\bar z_m)}{3\bar z_m}&\frac{4}{5}\left(-5+2\bar z_m\right)&\chi_K\frac{(4-\bar z_m)}{3\bar z_m}&0&\chi_K\frac{(4-\bar z_m)}{3\bar z_m}&0\end{bmatrix}$$

$$\mathcal{H}_{B,\Gamma_i}=\begin{bmatrix}\frac{37}{504}\bar z_m\left(189+\bar z_m(-175+31\bar z_m)\right)&-\frac{\left(315+\bar z_m(-441-31(-7+\bar z_m)\bar z_m)\right)}{315}&1+\bar z_m-\frac{23\bar z_m^2}{15}+\frac{31\bar z_m^3}{105}&0&0&0\\[4pt]-\frac{37}{1008}\bar z_m\left(42+\bar z_m(-35+8\bar z_m)\right)&-\frac{4\left(-105+\bar z_m^2(21+(-7+\bar z_m)\bar z_m)\right)}{315\bar z_m}&-\frac{1}{105}\left(35+2\bar z_m^2\left(-7+2\bar z_m\right)\right)&0&\chi_K\frac{(4-\bar z_m)}{3\bar z_m}&0\\0&-\frac{1}{(-1+\bar z_m)\bar z_m}&1+\bar z_m-\frac{1}{105}\left(35+2\bar z_m^2(-7+2\bar z_m)\right)&&&\\&\frac{4-\bar z_m}{3\bar z_m}&&&&\end{bmatrix}$$

Table VI.2: Resistance vector and matrices $\mathcal{H}_{A,\Gamma_i}$ and $\mathcal{H}_{B,\Gamma_i}$ for different regimes.

Bibliography

[1] B. Longinow, A and Ellingwood, "The Impact of the Ronan Point collapse-25 Years after," in *Structural Engineering World Wide 1998*. Elsevier Science, 1998. Cited on page 2.

[2] C. Pearson and N. Delatte, "Ronan Point apartment tower collapse and its effect on building codes," *Journal of Performance of Constructed Facilities*, vol. 19, no. 2, pp. 172–177, 2005. Cited on page 2.

[3] B. H. S. Norville, N. Harvill, A. Member, E. J. Conrath, S. Shariat, and S. Mallonee, "Glass-related injuries in Oklahoma City bombing," in *Journal of Performance of Constructed Facilities*, vol. 13, no. 2. American Society of Civil Engineers, 1999, pp. 50–56. Cited on page 2.

[4] U.S. Department of Defense, *Unified Facilities Criteria (UFC) 3-340-02 - Structures to resist the effects of accidental explosions*, Washington, DC, 2008. Cited on pages 2, 3, 8, 9, 10, 11, 12, 13, 14, 15, 18, 19, 31, 32, 37, 38, 39, 40, 48, and 108.

[5] D. O. Dusenberry, *Handbook for blast resistant design of buildings*. Wiley Online Library, 2010. Cited on pages 2 and 108.

[6] P. D. Smith and T. A. Rose, "Blast wave propagation in city streets-an overview," *Progress in Structural Engineering and Materials*, vol. 8, no. 1, pp. 16–28, Jan. 2006. [Online]. Available: http://doi.wiley.com/10.1002/pse.209 Cited on page 2.

[7] A. M. Remennikov and T. A. Rose, "Modelling blast loads on buildings in complex city geometries," *Computers & Structures*, vol. 83, no. 27, pp. 2197–2205, Oct. 2005. [Online]. Available: http://linkinghub.elsevier.com/retrieve/pii/S0045794905002002 Cited on page 2.

[8] X. Wen, M. Yu, Z. Liu, and W. Sun, "Large eddy simulation of methane-air deflagration in an obstructed chamber using different combustion models," *Journal of Loss Prevention in the Process Industries*, vol. 25, no. 4, pp. 730–738, Jul. 2012. [Online]. Available: http://linkinghub.elsevier.com/retrieve/pii/S0950423012000617 Cited on page 2.

[9] B. Luccioni, R. Ambrosini, and R. Danesi, "Analysis of building collapse under blast loads," *Engineering Structures*, vol. 26, no. 1, pp. 63–71, Jan. 2004. [Online]. Available: http://linkinghub.elsevier.com/retrieve/pii/S0141029603002086 Cited on page 2.

[10] Y. Lu and Z. Wang, "Characterization of structural effects from above-ground explosion using coupled numerical simulation," *Computers & Structures*, vol. 84, no. 28, pp. 1729–1742, Nov. 2006. [Online]. Available: http://linkinghub.elsevier.com/retrieve/pii/S0045794906001866 Cited on page 2.

[11] C. Wu and H. Hao, "Numerical simulation of structural response and damage to simultaneous ground shock and airblast loads," *International Journal of Impact Engineering*, vol. 34, no. 3, pp. 556–572, Mar. 2007. [Online]. Available: http://linkinghub.elsevier.com/retrieve/pii/S0734743X05001521 Cited on page 2.

[12] D. Hyde, "ConWep, conventional weapons effects program," *US Army Engineer Waterways Experiment Station, USA*, 1991. Cited on page 2.

[13] U. Nyström and K. Gylltoft, "Numerical studies of the combined effects of blast and fragment loading," *International Journal of Impact Engineering*, vol. 36, no. 8, pp. 995–1005, Aug. 2009. [Online]. Available: http://linkinghub.elsevier.com/retrieve/pii/S0734743X09000529 Cited on page 3.

[14] J. M. Biggs, *Introduction to structural dynamics.* McGraw-Hill College, 1964. Cited on page 3.

[15] R. Bourgeois, "Structures subjected to explosion (in French)," Brussels, Tech. Rep., 1995. Cited on pages 7, 8, 9, 14, and 32.

[16] R. A. Strehlow and W. E. Baker, "The characterization and evaluation of accidental explosions," *Progress in Energy and Combustion Science*, vol. 2, no. 1, pp. 27–60, 1976. Cited on page 7.

[17] E. C. N., "Eurocode 1: Actions on Structures - Part 1-7 General Actions - Accidental Actions," *Brussels: European Standard EN*, 2004. Cited on page 7.

[18] G. C. Mays and P. D. Smith, *Blast effects on buildings: Design of buildings to optimize resistance to blast loading.* Thomas Telford, 1995. Cited on pages 8, 10, 12, 14, 16, 17, 20, 21, 28, 29, 31, 33, 35, 39, 48, and 56.

[19] B. Hopkinson, "British ordnance board minutes 13565," *The National Archives, Kew, UK*, 1915. Cited on page 11.

[20] C. Cranz, "Lehrbuch der Ballistik," *Springer*, 1926. Cited on page 11.

[21] P. Bulson, *Explosive Loading of Engineering Structures.* Chapman & Hall, London, Storbritannien, 1997. Cited on page 11.

[22] H. L. Brode, "Numerical Solutions of Spherical Blast Waves," *Journal of Applied Physics*, vol. 26, no. 6, p. 766, 1955. [Online]. Available: http://link.aip.org/link/JAPIAU/v26/i6/p766/s1&Agg=doi Cited on page 11.

[23] K. J. Kinney, Gilbert F and Graham, *Explosive shocks in air.* Springer Science & Business Media, 2013. Cited on page 11.

[24] J. Ngo, T and Mendis, P and Gupta, A and Ramsay, "Blast loading and blast effects on structures-an overview," *Electronic Journal of Structural Engineering*, vol. 7, pp. 76–91, 2007. Cited on page 12.

[25] H. W. Liepmann and A. Roshko, *Elements of gasdynamics.* Courier Corporation, 1957. Cited on page 12.

[26] R. G. Stoner and W. Bleakney, "The attenuation of spherical shock waves in air," *Journal of Applied Physics*, vol. 19, no. 7, pp. 670–678, 1948. Cited on page 12.

[27] H. E. Lindberg and R. D. Firth, "Simulation of transient surface loads by explosive blast waves," Air Force Weapons Lab, Kirtland, USA, Tech. Rep., 1967. Cited on page 12.

[28] W. E. Baker, P. A. Cox, J. J. Kulesz, R. A. Strehlow, and P. S. Westine, *Explosion hazards and evaluation.* Elsevier, 1983. Cited on pages 13, 14, 16, 17, 19, 25, 27, 28, and 48.

[29] W. J. M. Rankine, "On the thermodynamic theory of waves of finite longitudinal disturbance," *Philosophical Transactions of the Royal Society of London*, vol. 160, no. January, pp. 277–288, 1870. [Online]. Available: http://rstl.royalsocietypublishing.org/cgi/doi/10.1098/rstl.1870.0015 Cited on page 14.

[30] J. Hetherington and P. Smith, *Blast and ballistic loading of structures.* Oxford: Digital Press, 1994. Cited on pages 16, 20, 25, 26, 28, 48, 61, and 62.

[31] A. Zyskowski, I. Sochet, G. Mavrot, P. Bailly, and J. Renard, "Study of the explosion process in a small scale experiment-structural loading," *Journal of Loss Prevention in the Process Industries*, vol. 17, no. 4, pp. 291–299, 2004. [Online]. Available: http://linkinghub.elsevier.com/retrieve/pii/S0950423004000257 Cited on page 16.

[32] C. J. Gantes and N. G. Pnevmatikos, "Elastic-plastic response spectra for exponential blast loading," *International Journal of Impact Engineering*, vol. 30, no. 3, pp. 323–343, Mar. 2004. [Online]. Available: http://linkinghub.elsevier.com/retrieve/pii/S0734743X03000770 Cited on page 23.

[33] D. E. Jarrett, "Derivation of British explosives safety distances," *Annals of the New York Academy Of Sciences*, no. 152, pp. 18–35, 1968. Cited on page 25.

[34] N. Jones, *Structural Impact.* Cambridge: Cambridge University Press, 2011. [Online]. Available: http://ebooks.cambridge.org/ref/id/CBO9780511820625 Cited on page 29.

[35] Y. Lescouarch, "Capacité de résistance d'une section soumises à divers types de sollicitations," *Construction Métallique*, vol. 23, no. 2, pp. 50–54, 1977. Cited on pages 34 and 172.

[36] E. C. N., "Eurocode 3: Design of steel structures - Part 1-1: General rules and rules for buildings," *Brussels: European Standard EN*, 2005. Cited on pages 34, 52, and 156.

[37] N. Jones, *Structural Impact*. Cambridge: Cambridge University Press, 2011. Cited on pages 36, 48, 76, and 93.

[38] K. Marsh and J. Campbell, "The effect of strain rate on the post-yield flow of mild steel," *Journal of the Mechanics and Physics of Solids*, vol. 11, pp. 49–63, 1963. Cited on pages 36 and 37.

[39] J. Campbell and R. Cooper, "Yield and flow of low-carbon steel at medium strain rates," in *Proceeding Conference on the Physical Basis of Yield and Fracture*. London: Institute of Physics and Physical Society, 1966, pp. 77–87. Cited on page 36.

[40] P. S. GR Cowper, "Strain-hardening and strain-rate effects in the impact loading of cantilever beams," Tech. Rep., 1957. [Online]. Available: http://oai.dtic.mil/oai/oai?verb=getRecord&metadataPrefix=html&identifier=AD0144762 Cited on page 36.

[41] P. Symonds, "Survey of methods of analysis for plastic deformation of structures under dynamic loading," Tech. Rep., 1967. [Online]. Available: http://oai.dtic.mil/oai/oai?verb=getRecord&metadataPrefix=html&identifier=AD0659972 Cited on page 36.

[42] R. J. Aspden and J. D. Campbell, "The effect of loading rate on the elasto-plastic flexure of steel beams," in *Proceedings of the Royal Society of London A: Mathematical, Physical and Engineering Sciences*, vol. 290, 1966, pp. 266–285. Cited on pages 36 and 37.

[43] H. Chen and J. Y. Liew, "Explosion and Fire Analysis of Steel Frames Using Mixed Element Approach," *Journal of Engineering Mechanics*, vol. 131, no. 6, pp. 606–616, Jun. 2005. [Online]. Available: http://ascelibrary.org/doi/abs/10.1061/%28ASCE%290733-9399%282005%29131%3A6%28606%29 Cited on pages 36 and 170.

[44] J. R. Liew, "Survivability of steel frame structures subject to blast and fire," *Journal of Constructional Steel Research*, vol. 64, no. 7-8, pp. 854–866, Jul. 2008. [Online]. Available: http://linkinghub.elsevier.com/retrieve/pii/S0143974X07001976 Cited on pages 36 and 170.

[45] A. A. Nassr, "Experimental and analytical study of the dynamic response of steel beams and columns to blast loading," Ph.D. dissertation, McMaster University, 2012. Cited on page 36.

[46] AISC, "Specification for structural steel buildings," American Institute of Steel Construction, Chicago, Tech. Rep., 2005. [Online]. Available: http://scholar.google.com/scholar?hl=en&btnG=Search&q=intitle: Specification+for+Structural+Steel+Buildings#9 Cited on page 37.

[47] E. C. N., "Eurocode 1: Actions on Structures - Part 1-7 General Actions - Densities, self-weight, imposed loads for buildings," *Brussels: European Standard EN*, 2002. Cited on page 39.

[48] A. S. C. E. Task committee on blast resistant design, "Design of blast-resistant buildings in petrochemical facilities," 1997, pp. 1–312. Cited on pages 39 and 41.

[49] R. J. Guyan, "Reduction of stiffness and mass matrices," *AIAA Journal*, vol. 3, no. 2, p. 380, Feb. 1965. [Online]. Available: http://dx.doi.org/10.2514/3.2874 Cited on page 42.

[50] C. C. Flanigan, "Implementation of the IRS dynamic reduction method in MSC/NASTRAN," in *1990 MSC/NASTRAN World Users Conference*, O. A. Mera A, Ed., 1990, pp. 1–10. Cited on page 42.

[51] N. Zhang, "Dynamic condensation of mass and stiffness matrices," *Journal of Sound and Vibration*, vol. 188, no. 4, pp. 601–615, 1995. Cited on page 42.

[52] M. Papadopoulos and E. Garcia, "Improvement in model reduction schemes using the system equivalent reduction expansion process," *AIAA Journal*, vol. 34, no. 10, pp. 2217–2219, 1996. [Online]. Available: http://www.scopus.com/inward/record.url?eid= 2-s2.0-0012762792&partnerID=40&md5=1f165897f005d2adce15d3affeb32578 Cited on page 43.

[53] Y. Shi, H. Hao, and Z.-X. Li, "Numerical derivation of pressure-impulse diagrams for prediction of RC column damage to blast loads," *International Journal of Impact Engineering*, vol. 35, no. 11, pp. 1213–1227, 2008. [Online]. Available: http://linkinghub.elsevier.com/retrieve/pii/S0734743X07001315 Cited on pages 48, 110, 113, 155, and 170.

[54] H. C. Yim and T. Krauthammer, "Mechanical properties of single-plate shear connections under monotonic, cyclic, and blast loads," *Engineering Structures*, vol. 37, pp. 24–35, Apr. 2012. [Online]. Available: http://linkinghub.elsevier.com/retrieve/pii/ S0141029611005244 Cited on page 48.

[55] C. K. Youngdahl, "Correlation parameters for eliminating the effect of pulse shape on dynamic plastic deformation," *Journal of Applied Mechanics*, vol. 37, no. 3, pp. 744–752, 1970. Cited on page 48.

[56] Q. M. Li and N. Jones, "Foundation of correlation parameters for eliminating pulse shape effects on dynamic plastic response of structures," *Journal of Applied*

Mechanics, vol. 72, no. 2, p. 172, 2005. [Online]. Available: http://appliedmechanics. asmedigitalcollection.asme.org/article.aspx?articleid=1415344 Cited on page 48.

[57] Q. M. Li and H. Meng, "Pressure-impulse diagram for blast loads based on dimensional analysis and single-degree-of-freedom model," *Journal of Engineering Mechanics*, vol. 128, no. 1, pp. 87–92, Jan. 2002. [Online]. Available: http://ascelibrary.org/doi/abs/ 10.1061/%28ASCE%290733-9399%282002%29128%3A1%2887%29 Cited on page 48.

[58] ——, "Pulse loading shape effects on pressure-impulse diagram of an elastic-plastic, single-degree-of-freedom structural model," *International Journal of Mechanical Sciences*, vol. 44, pp. 1985–1998, 2002. Cited on page 48.

[59] A. S. Fallah, E. Nwankwo, and L. a. Louca, "Pressure-impulse diagrams for blast loaded continuous beams based on dimensional analysis," *Journal of Applied Mechanics*, vol. 80, no. September, pp. 1–11, 2013. [Online]. Available: http://link.aip.org/link/doi/10.1115/1.4023639 Cited on pages 48, 105, and 168.

[60] K. Micallef, A. S. Fallah, D. J. Pope, and L. A. Louca, "The dynamic performance of simply-supported rigid-plastic circular steel plates subjected to localised blast loading," *International Journal of Mechanical Sciences*, vol. 65, no. 1, pp. 177–191, Dec. 2012. [Online]. Available: http://linkinghub.elsevier.com/retrieve/pii/S0020740312002202 Cited on page 48.

[61] ——, "Dynamic performance of simply supported rigid plastic circular thick steel plates subjected to localized blast loading," *Journal of Engineering Mechanics*, vol. 140, no. 1, pp. 159–171, 2013. Cited on pages 48 and 194.

[62] Q. M. Li and N. Jones, "Blast loading of fully clamped beams with transverse shear effects*," *Journal of Structural Mechanics*, vol. 23, no. 1, pp. 59–86, 1995. Cited on page 48.

[63] ——, "Shear and adiabatic shear failures in an impulsively loaded fully clamped beam," *International Journal of Impact Engineering*, vol. 22, no. 6, pp. 589–607, Jul. 1999. [Online]. Available: http://linkinghub.elsevier.com/retrieve/pii/S0734743X99000135 Cited on pages 48 and 144.

[64] Q. M. Li, Y. M. Liu, and G. W. Ma, "The anomalous region of elastic-plastic beam dynamics," *International Journal of Impact Engineering*, vol. 32, no. 9, pp. 1357–1369, 2006. Cited on page 48.

[65] Y. Liang, L. Louca, and R. Hobbs, "Corrugated panels under dynamic loads," *International Journal of Impact Engineering*, vol. 34, no. 7, pp. 1185–1201, Jul. 2007. [Online]. Available: http://linkinghub.elsevier.com/retrieve/pii/S0734743X0600090X Cited on page 48.

[66] G. Ma, H. Shi, and D. Shu, "P-I diagram method for combined failure modes of rigid-plastic beams," *International Journal of Impact Engineering*, vol. 34, no. 6, pp. 1081–1094, Jun. 2007. [Online]. Available: http://linkinghub.elsevier.com/retrieve/pii/S0734743X06000790 Cited on pages 48, 60, 113, and 144.

[67] R. Varizi, M. Olson, and D. Anderson, "Dynamic response of axially constrained plastic beams to blast loads," *International Journal of Solids and Structures*, vol. 23, no. 1, pp. 153–174, 1987. Cited on pages 48, 75, 93, and 175.

[68] G. K. Schleyer and S. S. Hsu, "A modelling scheme for predicting the response of elastic-plastic structures to pulse pressure loading," *International Journal of Impact Engineering*, vol. 24, no. 8, pp. 759–777, 2000. Cited on page 48.

[69] G. Langdon and G. Schleyer, "Modelling the response of semi-rigid supports under combined loading," *Engineering Structures*, vol. 26, no. 4, pp. 511–517, Mar. 2004. [Online]. Available: http://linkinghub.elsevier.com/retrieve/pii/S0141029603002979 Cited on page 48.

[70] ——, "Inelastic deformation and failure of profiled stainless steel blast wall panels. Part II: analytical modelling considerations," *International Journal of Impact Engineering*, vol. 31, no. 4, pp. 371–399, Apr. 2005. [Online]. Available: http://linkinghub.elsevier.com/retrieve/pii/S0734743X03002367 Cited on page 48.

[71] E. Nwankwo, A. S. Fallah, G. S. Langdon, and L. A. Louca, "Inelastic deformation and failure of partially strengthened profiled blast walls," *Engineering Structures*, vol. 46, pp. 671–686, Jan. 2013. [Online]. Available: http://linkinghub.elsevier.com/retrieve/pii/S0141029612004610 Cited on pages 48 and 142.

[72] A. S. Fallah and L. A. Louca, "Pressure-impulse diagrams for elastic-plastic-hardening and softening single-degree-of-freedom models subjected to blast loading," *International Journal of Impact Engineering*, vol. 34, no. 4, pp. 823–842, Apr. 2007. [Online]. Available: http://linkinghub.elsevier.com/retrieve/pii/S0734743X06000212 Cited on page 48.

[73] J. Dragos and C. Wu, "A new general approach to derive normalised pressure impulse curves," *International Journal of Impact Engineering*, vol. 62, pp. 1–12, Dec. 2013. [Online]. Available: http://linkinghub.elsevier.com/retrieve/pii/S0734743X13001115 Cited on pages 48, 130, and 192.

[74] L. Hamra, J.-F. Demonceau, and V. Denoël, "Pressure-impulse diagram of a beam developing non-linear membrane action under blast loading," *International Journal of Impact Engineering*, vol. 86, pp. 188–205, 2015. [Online]. Available: http://www.sciencedirect.com/science/article/pii/S0734743X15001578 Cited on page 49.

[75] M. Villette, *Critical analysis of the treatment of members subjected to compression and bending and propositions of new formulations (in French). Phd Thesis.* Liege University, 2004. Cited on page 52.

[76] Bentz, "Response-2000 program," 2000. Cited on page 52.

[77] J.-F. Demonceau, J.-P. Jaspart, R. Klinkhammer, R. Oerder, K. Weynand, F. Labory, and L.-G. Cajot, "Recent developments in composite connections," *Steel Construction*, vol. 1, no. 1, pp. 71–76, Sep. 2008. [Online]. Available: http://doi.wiley.com/10.1002/stco.200890012 Cited on page 52.

[78] J.-F. Demonceau and J.-P. Jaspart, "Experimental and analytical investigations on the response of structural building frames further to a column loss," in *Proceedings of the Structures Congress.*, 2009, pp. 1801–1810. Cited on pages 52 and 108.

[79] A. A. Nassr, A. G. Razaqpur, M. J. Tait, M. Campidelli, and S. Foo, "Strength and stability of steel beam columns under blast load," *International Journal of Impact Engineering*, vol. 55, pp. 34–48, May 2013. Cited on pages 53, 109, 110, 133, 140, 155, 161, 173, 176, and 192.

[80] J. Dragos and C. Wu, "Single-degree-of-freedom approach to incorporate axial load effects on pressure impulse curves for steel columns," *Journal of Engineering Mechanics*, vol. 141, no. 1, pp. 1–10, 2015. Cited on pages 53, 110, 133, 157, and 173.

[81] A. Depouhon, E. Detournay, and V. Denoël, "Accuracy of one-step integration schemes for damped / forced linear structural dynamics," *International Journal for Numerical Methods in Engineering*, vol. 99, no. 5, pp. 333–353, 2014. Cited on page 64.

[82] ——, "DE3: Yet another high-order integration scheme for linear structural dynamics," in *Proceedings of the 5th ECCOMAS Thematic Conference on Computational Methods in Structural Dynamics and Earthquake Engineering.*, 2015, pp. 1216–1223. Cited on page 64.

[83] T. Krauthammer, S. Astarlioglu, J. Blasko, T. Soh, and P. Ng, "Pressure-impulse diagrams for the behavior assessment of structural components," *International Journal of Impact Engineering*, vol. 35, no. 8, pp. 771–783, Aug. 2008. [Online]. Available: http://linkinghub.elsevier.com/retrieve/pii/S0734743X07001947 Cited on pages 67, 110, and 156.

[84] C. Huvelle, V.-L. Hoang, J.-P. Jaspart, and J.-F. Demonceau, "Complete analytical procedure to assess the response of a frame submitted to a column loss," *Engineering Structures*, vol. 86, pp. 33–42, Mar. 2015. [Online]. Available: http://linkinghub.elsevier.com/retrieve/pii/S0141029614007597 Cited on pages 75, 108, 170, 173, and 174.

[85] M. Géradin and D. J. Rixen, *Mechanical vibrations: theory and application to structural dynamics.* John Wiley & Sons, 2014. Cited on pages 78, 119, and 166.

[86] A. E. Taylor, "L'Hospital's Rule," in *The American Mathematical Monthly*, vol. 59, no. 1. JSTOR, 1952, pp. 20–24. Cited on page 80.

[87] N. M. Newmark, "A method of computation for structural dynamics," *Journal of Engineering Mechanics Division (ASCE)*, no. 85, pp. 67–94, 1959. Cited on pages 89, 120, 133, and 178.

[88] W. W. El-Dakhakhni, S. H. Changiz Rezaei, W. F. Mekky, and A. G. Razaqpur, "Response sensitivity of blast-loaded reinforced concrete structures to the number of degrees of freedom," *Canadian Journal of Civil Engineering*, vol. 36, no. 8, pp. 1305–1320, Aug. 2009. [Online]. Available: http://www.nrcresearchpress.com/doi/abs/10.1139/L08-140 Cited on page 93.

[89] A. A. Nassr, A. G. Razaqpur, M. J. Tait, M. Campidelli, and S. Foo, "Single and multi degree of freedom analysis of steel beams under blast loading," *Nuclear Engineering and Design*, vol. 242, pp. 63–77, 2012. [Online]. Available: http://linkinghub.elsevier.com/retrieve/pii/S0029549311008934 Cited on page 93.

[90] P. S. Symonds, "Elastic, finite deflection and strain rate effects in a mode approximation technique for plastic deformation of pulse loaded structures," *Journal of Mechanical Engineering Science*, vol. 22, no. 4, pp. 189–197, 1980. Cited on pages 105, 122, and 197.

[91] D. Izzuddin, B.A. and Vlassis, A.G. and Elghazouli, A.Y. and Nethercot, "Progressive collapse of multi-storey buildings due to sudden column loss - Part I: Simplified assessment framework," *Engineering Structures*, vol. 30, no. 5, pp. 1308–1318, 2008. Cited on pages 108 and 170.

[92] D. A. Vlassis, A. G. and Izzuddin, B. A. and Elghazouli, A. Y. and Nethercot, "Progressive collapse of multi-storey buildings due to failed floor impact," *Engineering Structures*, vol. 31, no. 7, pp. 1522–1534, 2009. Cited on pages 108 and 170.

[93] L. Comeliau, B. Rossi, and J.-F. Demonceau, "Robustness of steel and composite buildings suffering the dynamic loss of a column," *Structural Engineering International*, vol. 22, no. 3, pp. 323–329, 2012. Cited on pages 108 and 170.

[94] Z. P. Bažant and L. Cedolin, *Stability of structures: elastic, inelastic, fracture and damage theories.* World Scientific, 2010. Cited on page 109.

[95] S. P. Timoshenko and J. M. Gere, "Theory of elastic stability. 1961," *McGrawHill-Kogakusha Ltd, Tokyo*, 1961. Cited on page 109.

[96] C. J. Oswald, "Comparison of Response from Combined Axial and Blast Loads Calculated with SDOF and Finite Element Methods," DTIC Document, Tech. Rep., 2010. Cited on page 110.

[97] A. A. Nassr, A. G. Razaqpur, M. J. Tait, M. Campidelli, and S. Foo, "Dynamic Response of Steel Columns Subjected to Blast Loading," *Journal of structural engineering*, vol. 140, no. 7, pp. 1–15, 2014. Cited on page 110.

[98] C. Bedon, C. Amadio, and A. Sinico, "Numerical and analytical investigation on the dynamic buckling behavior of glass columns under blast," *Engineering Structures*, vol. 79, pp. 322–340, Nov. 2014. [Online]. Available: http://linkinghub.elsevier.com/retrieve/pii/S0141029614004957 Cited on page 110.

[99] R. L. Shope, "Response of Wide Flange Steel Columns Subjected to Constant Axial Load and Lateral Blast Load," *Civil Engineering*, vol. Doctor of, pp. 1–417, 2006. Cited on page 110.

[100] H. Al-thairy, "A modified single degree of freedom method for the analysis of building steel columns subjected to explosion induced blast load," *International Journal of Impact Engineering*, vol. 94, pp. 120–133, 2016. [Online]. Available: http://dx.doi.org/10.1016/j.ijimpeng.2016.04.007 Cited on page 110.

[101] S. Astarlioglu, T. Krauthammer, D. Morency, and T. P. Tran, "Behavior of reinforced concrete columns under combined effects of axial and blast-induced transverse loads," *Engineering Structures*, vol. 55, pp. 26–34, 2013. [Online]. Available: http://dx.doi.org/10.1016/j.engstruct.2012.12.040 Cited on page 110.

[102] S. Astarlioglu and T. Krauthammer, "Response of normal-strength and ultra-high-performance fiber-reinforced concrete columns to idealized blast loads," *Engineering Structures*, vol. 61, pp. 1–12, 2014. [Online]. Available: http://dx.doi.org/10.1016/j.engstruct.2014.01.015 Cited on page 110.

[103] L. Chernin, M. Vilnay, and I. Shufrin, "Blast dynamics of beam-columns via analytical approach," *International Journal of Mechanical Sciences*, vol. 106, pp. 331–345, 2016. [Online]. Available: http://dx.doi.org/10.1016/j.ijmecsci.2015.12.018 Cited on page 110.

[104] A. Montalva, E. Loukaides, M. Long, and S. Gallant, "Analysis of steel columns for air-blast loads," in *Proceedings of the international symposium on interaction of the effects of munitions with structures, Electronic Proceeding (CD) of the International Symposium on the Interaction of the Effects of Munitions with Structures (ISIEMS)*, vol. 12, 2007. Cited on page 110.

[105] K. Lee, T. Kim, and J. Kim, "Local response of W-shaped steel columns under blast loading," *Structural Engineering and Mechanics*, vol. 31, no. 1, pp. 25–38, 2009. Cited on page 110.

[106] Y. Shi, Z.-X. Li, and H. Hao, "A new method for progressive collapse analysis of RC frames under blast loading," *Engineering Structures*, vol. 32, no. 6, pp. 1691–1703, 2010. [Online]. Available: http://linkinghub.elsevier.com/retrieve/pii/S0141029610000593 Cited on pages 110 and 170.

[107] K.-C. Wu, B. Li, and K.-C. Tsai, "The effects of explosive mass ratio on residual compressive capacity of contact blast damaged composite columns," *Journal of*

Constructional Steel Research, vol. 67, no. 4, pp. 602–612, Apr. 2011. [Online]. Available: http://linkinghub.elsevier.com/retrieve/pii/S0143974X10002725 Cited on page 110.

[108] R. Jayasooriya, D. P. Thambiratnam, N. J. Perera, and V. Kosse, "Blast and residual capacity analysis of reinforced concrete framed buildings," *Engineering Structures*, vol. 33, no. 12, pp. 3483–3495, 2011. [Online]. Available: http://dx.doi.org/10.1016/j.engstruct.2011.07.011 Cited on pages 110 and 170.

[109] A. A. Mutalib and H. Hao, "Development of P-I diagrams for FRP strengthened RC columns," *International Journal of Impact Engineering*, vol. 38, no. 5, pp. 290–304, 2011. [Online]. Available: http://dx.doi.org/10.1016/j.ijimpeng.2010.10.029 Cited on page 110.

[110] L. Mazurkiewicz, J. Malachowski, and P. Baranowski, "Blast loading influence on load carrying capacity of I-column," *Engineering Structures*, vol. 104, pp. 107–115, 2015. [Online]. Available: http://linkinghub.elsevier.com/retrieve/pii/S0141029615005969 Cited on page 110.

[111] X. Bao and B. Li, "Residual strength of blast damaged reinforced concrete columns," *International Journal of Impact Engineering*, vol. 37, no. 3, pp. 295–308, 2010. [Online]. Available: http://dx.doi.org/10.1016/j.ijimpeng.2009.04.003 Cited on page 111.

[112] Y. Ding, M. Wang, Z.-X. Li, and H. Hao, "Damage evaluation of the steel tubular column subjected to explosion and post-explosion fire condition," *Engineering Structures*, pp. 1–12, Feb. 2012. [Online]. Available: http://linkinghub.elsevier.com/retrieve/pii/S0141029612000351 Cited on pages 111 and 155.

[113] L. Stewart and K. Morrill, "Residual capacity prediction of blast-loaded steel columns using physics-based fast running models," *International Journal of Safety and Security Engineering*, vol. 5, no. 4, pp. 289–303, 2015. [Online]. Available: http://www.witpress.com/doi/journals/SAFE-V5-N4-289-303 Cited on pages 111 and 155.

[114] Q. M. Li, Z. Q. Ye, G. W. Ma, N. Jones, and H. Y. Zhou, "The influence of elastic shear deformation on the transverse shear failure of a fully clamped beam subjected to idealized blast loading," *International Journal of Mechanical Sciences*, vol. 51, no. 6, pp. 413–423, Jun. 2009. [Online]. Available: http://linkinghub.elsevier.com/retrieve/pii/S0020740309000538 Cited on page 113.

[115] P. S. Symonds, "Finite elastic and plastic deformations of pulse loaded structures by an extended mode technique," *International Journal of Mechanical Sciences*, vol. 22, no. 10, pp. 597–605, 1980. Cited on page 122.

[116] J. M. Mosquera, H. Kolsky, and P. S. Symonds, "Impact tests on frames and elastic-plastic solutions," vol. 1, no. 11, pp. 1380–1401, 1986. Cited on page 122.

[117] P. Wriggers, *Nonlinear finite element methods.* Springer Science & Business Media, 2008. Cited on pages 125 and 191.

[118] P. S. Symonds and T. X. Yu, "Counterintuitive behavior in a problem of elastic-plastic beam dynamics," *Journal of Applied Mechanics*, vol. 52, no. 3, pp. 517–522, 1985. Cited on page 142.

[119] J.-F. Demonceau, "Steel and composite building frames : sway response under conventional loading and development of membrane effects in beams further to an exceptional action (Phd Thesis)," Ph.D. dissertation, University of Liège, Belgium, 2008. Cited on page 170.

[120] U.S. General Services Administration (GSA), "Alternate path analysis and design guidelines for progressive collapse resistance," Washington, DC, Tech. Rep., 2013. Cited on page 170.

[121] J.-F. Demonceau, M. D'Antimo, C. Huvelle, L. Hamra, V. L. Hoang, J.-P. Jaspart, N. Hoffmann, U. Kuhlmann, O. Vassart, F. Hanus, M. Charlier, S. Guezouli, A. Alhasawi, M. Hjiaj, B. Hoffmeister, J. Korndörfer, C. Colomer Segura, N. Baldassino, and R. Zandonini, "Simplified equivalent static approach and results for deriving structural requirements-Deliverables D. 11 and D. 12-Robustimpact," RFCS, Tech. Rep., 2016. Cited on page 170.

[122] P. Heng, M. Hjiaj, J.-M. Battini, and A. Limam, "A simplified model for nonlinear dynamic analysis of steel column subjected to impact," *International Journal of Non-Linear Mechanics*, vol. 86, pp. 37–54, 2016. [Online]. Available: http://linkinghub.elsevier.com/retrieve/pii/S0020746216300804 Cited on page 170.

[123] F. Fu, "Dynamic response and robustness of tall buildings under blast loading," *Journal of Constructional Steel Research*, vol. 80, pp. 299–307, 2013. [Online]. Available: http://dx.doi.org/10.1016/j.jcsr.2012.10.001 Cited on page 170.

[124] H. M. Elsanadedy, T. H. Almusallam, Y. R. Alharbi, Y. A. Al-Salloum, and H. Abbas, "Progressive collapse potential of a typical steel building due to blast attacks," *Journal of Constructional Steel Research*, vol. 101, pp. 143–157, 2014. [Online]. Available: http://dx.doi.org/10.1016/j.jcsr.2014.05.005 Cited on page 170.

[125] S. Jeyarajan, J. R. Liew, and C. Koh, "Vulnerability of simple braced steel building under extreme load," *The IES Journal Part A: Civil & Structural Engineering*, vol. 8, no. 4, pp. 219–231, 2015. [Online]. Available: http://www.tandfonline.com/doi/full/10.1080/19373260.2015.1068385 Cited on page 170.

[126] S. Jeyarajan, J. Y. R. Liew, and C. G. Koh, "Analysis of steel-concrete composite buildings for blast induced progressive collapse," *International Journal of Protective Structures*, vol. 6, no. 3, pp. 457–485, 2015. Cited on page 170.

[127] L. Song, B. A. Izzuddin, A. S. Elnashai, and P. J. Dowling, "An integrated adaptive environment for fire and explosion analysis of steel frames - Part I: analytical models," *Journal of Constructional Steel Research*, vol. 53, no. 1, pp. 63–85, 2000. Cited on page 170.

[128] B. A. Izzuddin, L. Song, A. S. Elnashai, and P. J. Dowling, "An integrated adaptive environment for fire and explosion analysis of steel frames - Part II : verification and application," *Journal of Constructional Steel Research*, vol. 53, no. 1, pp. 87–111, 2000. Cited on page 170.

[129] C. Faliang and Y. Tongxi, "Analysis of large deflection dynamic response of rigid-plastic beams," *Journal of Engineering Mechanics*, vol. 119, no. 6, pp. 1293–1301, 1993. Cited on page 175.

[130] B. Luccioni, D. Ambrosini, and R. Danesi, "Blast load assessment using hydrocodes," *Engineering Structures*, vol. 28, no. 12, pp. 1736–1744, 2006. Cited on page 177.